ISSN 1580-2949
UDK 669+666+678+53 MTAEC9, 45(6)501–659(2011)

MATER. TEHNOL.	LETNIK VOLUME 45	ŠTEV. NO. 6	STR. P. 501–659	LJUBLJANA SLOVENIJA	NOV.–DEC. 2011

VSEBINA – CONTENTS

IZVIRNI ZNANSTVENI ČLANKI – ORIGINAL SCIENTIFIC ARTICLES

STROKOVNI ČLANKI – PROFESSIONAL ARTICLES

UDK 54
Original scientific article/Izvirni znanstveni članek

ISSN 1580-2949
MTAEC9, 45(6)503(2011)

NEW DISCOVERED PARADOXES IN THEORY OF BALANCING CHEMICAL REACTIONS

NOVOODKRITI PARADOKSI V TEORIJI URAVNOTEŽENJA KEMIJSKIH REAKCIJ

Ice B. Risteski

2 Milepost Place # 606, Toronto, Ontario, Canada M4H 1C7
ice@scientist.com

»Failure to distinguish carefully between *mathematical* and *metamathematical* statements leads to paradoxes.«

M. Kac, S. M. Ulam, *Mathematics and Logic*, Dover Pub. Inc., Mineola 1992, p. 126.

Prejem rokopisa – received: 2011-01-24; sprejem za objavo – accepted for publication: 2011-09-21

In this work are given new paradoxes and fallacies discovered in the theory of balancing chemical reactions. All the counterexamples showed that so–called »*chemical procedures*« of balancing chemical reactions given in earlier chemical literature are inconsistent. Balancing chemical reactions is a mathematical procedure independent of chemistry. In order to avoid the appearance of paradoxes, chemical reactions must be considered as a formal system founded by virtue of well–defined mathematical model. The results obtained in this work affirmed that the usage of traditional ways of balancing chemical reactions is limited. They may be used only for balancing some elementary chemical equations. In other words, foundation of chemistry looks for a new approach of balancing chemical reactions, which must be completely different than current »*chemical procedures*«. This work is a collection and analysis of some paradoxes and fallacies which appeared in the theory of balancing chemical reactions.

Keywords: chemical reactions, paradoxes, balancing, fallacies

Predstavljeni so novi paradoksi in zmote, odkrite v teoriji uravnoteženje kemijskih reakcij. Vsi protiprimeri so pokazali, da so tako nekonsistentne tako imenovane kemijske procedure uravnoteženja kemijskih reakcij, navedene v zgodnjih virih. Uravnoteženje kemijskih reakcij je matematična procedura, neodvisna od kemije. Da bi se izognili nastajanju paradoksov, je treba kemijske reakcije formulirati kot formalen sistem na podlagi dobro definiranega matematičnega modela. Rezultati v tem delu potrjujejo, da je uporaba tradicionalnih načinov uravnoteženja kemijskih reakcij omejena. Uporabljamo jo le za uravnoteženje nekaterih elementarnih kemijskih reakcij. Z drugih besedami, temelj kemije išče nove približke za uravnoteženje kemijskih reakcij, ki se morajo razlikovati od sedanjih kemijskih procedur. To delo je izbor in analiza nekaterih paradoksov in zmote, ki so se pojavile v teoriji uravnoteženja kemijskih reakcij.

Ključne besede: kemijske reakcije, paradoksi, uravnoteženje, zmote

1 INTRODUCTION

In this section we shall discuss the balancing of chemical reactions from scientific viewpoint. It is an essential precondition for better understanding of our discourse about paradoxes connected with traditional ways of balancing chemical reactions.

Before opening this discussion about balancing chemical reactions, we would like to give a few remarks about the name of so–called course »*general chemistry*«. Why? The reply is very simple, because this course treats the balancing of chemical reactions as its subject. At the beginning of our exposition we want to say that the name »*general chemistry*« is not appropriately chosen. Generally speaking, »*general chemistry*« does not exist, and on top of all it is not possible to exist, because the principles of this particular chemistry are weak and do not hold for all parts of chemistry. They have only particular meaning and nothing more. In other words, it means that its principles are not general. This is just one thing. Another thing, chemistry is founded by virtue of mathematical principles, but also there not exists »*general mathematics*« and speaking more accurately it is not possible to exist.

For instance, in *mathematical logic* in the 20th century lots of paradoxes were discovered,[1] and mathematicians thought that only there are possible antinomies and that other parts of mathematics are in safety. Reality showed that it is not true. In *mathematical analysis* lots of counterexamples were found.[2,3] Also certain counterexamples were found in *probability & statistics.*[3,4] In *topology* as a contemporary mathematical discipline a great number of counterexamples were detected too.[5] It does not mean that other mathematical disciplines are without contradictions. No! Just the opposite, in almost all the branches of mathematics different kinds of counterexamples are detected[6]. These facts show that mathematical principles are not general, *i. e.*, they hold only in certain part of mathematics. These are the causes why there is not »*general mathematics*«. If we take into account the fact that chemical reaction is a basic issue in chemistry and according to its definition (see: Definition

2.2, in the section 2), then it follows that chemistry is founded on mathematical principles. If there is not »*general mathematics*«, then how is possible to exist »*general chemistry*«? Simply speaking, it is impossible!

In order to correct this irrational name of chemistry, it is necessary to choose an appropriate name which will be more suitable for that particular chemistry. For example, the names *basic chemistry* and *elementary chemistry* fit for that chemistry.

In chemical as well as mathematical journals there are lots of published papers which treat the problem of balancing chemical reactions. Specially, in chemical journals are considered many different so–called »*chemical ways*« for balancing chemical reactions, but unfortunately all of them offer only particular procedures for balancing of some simple chemical reactions. These »*chemical ways*« very often have negative consequences for chemistry. For instance, they produce fallacies or absurd results, because most of them work on *erroneous principles*, but not on true principles.

Balancing chemical reactions is not a simple procedure as some traditionally oriented chemists think or as they want to be. In[7] the author emphasized very clearly, that *balancing chemical reactions is not chemistry; it is just linear algebra.*

Balancing chemical reactions is a basic matter of chemistry, if not one of its most important issues, and it plays a main role in its foundation. Indeed, it is a subtle question, which deserves considerable attention.

This topic has always excited nature as deeply as no other question in chemistry. The balancing of chemical reactions has acted upon human mind in such stimulating and fruitful way as hardly any other idea, but also this subject needs an explanation as no other concept.

The concept of *balancing chemical reactions* in chemistry is tracked and transformed from traditionalism to intuitionism in the 19th century, from intuitionism to irrationalism in the first half of 20th century, from irrationalism to particularism in the second half of 20th century, while the particularism is sharpened by Moore–Penrose matrix[8, 9] concept into generalism and transformed into formalism, which takes on the status of a paradigm in the 21st century.

To the question of balancing chemical reactions the mathematicians, chemists and computer engineers with different conceptions will not always give the same answer. A mathematician, a chemist and a computer engineer will answer each in a different way. Some of them will admit that perhaps the others are right in a *certain sense* and will try to *reinterpret* the others' procedures in their own language. But in general everyone, more or less, will remain convinced that, in fact, still only he is right.

Since chemistry is not immune from contradictions, also we found several absurd results there when balancing chemical reactions. In this work only just these absurd contradictions are studied.

Sometimes the mistakes in reasoning come because our experience with one situation causes us to assume that the same reasoning will hold true in a related but different situation. This kind of mistake can occur at a very simple level or at a more complex one. At a simple level, the most common conclusion is that we know that we have to reject the reasoning, although it may be difficult to say why. At the more complex level, we may conclude that the reasoning must be accepted even when the results seem to contradict our notion of how the real world works.

Scientific research and experience have shown, when the results of reasoning and mathematics conflict with experience, then there is probably a *fallacy* of some sort involved[10].

In the literature[11–13] there are a great number of definitions for fallacy, but we shall mention merely few of them. For us is important only *deductive fallacy.* A *deductive fallacy* is a deductive reason that is illogical.

In philosophy, the term *logical fallacy* suitably refers to a *formal fallacy.* It is defined as *a defect in the structure of deductive reason*, *which makes the reason invalid*. Most textbooks echo the *standard treatment* of fallacy, as a reason, which *seems to be valid* but *is not* so[14]. According to Maxwell[15], a fallacy *leads by guile to a wrong but plausible conclusion*.

In mathematics the word *fallacy* could also refer to a truthful result obtained by wrong reasoning.

In looking at wrong thinking about easy ideas, we found some cases in which reasoning about balancing chemical equations is wrong.

As long as we cannot recognize what the *fallacy* is, the situation is a *paradox*. In some cases, as we shall see, the paradox is entirely inside chemistry. For most paradoxes that are inside chemistry, elimination of the fallacious reasoning produces a *purified* chemistry that is a better description of the real chemistry than the *contaminated* chemistry was.

In philosophy there is a bunch of different definitions of paradoxes.

According to Sainsbury,[16] *a paradox is an apparently unacceptable conclusion derived by apparently acceptable reasoning from apparently acceptable premises*. Rescher[17] defines a paradox as a *set of propositions that are individually plausible but collectively inconsistent*. Chihara[18] provides a similar definition: *a paradox is an argument that begins with premises that appear to be clearly true*, *that proceeds according to inference rules that appear to be valid*, *but ends in contradiction*. Quine[19], for example, offers the following definition (using the term antinomy, instead of a paradox): *An antinomy produces a self–contradiction by accepted ways of reasoning. It establishes that some tacit and trusted pattern of reasoning must be made explicit and hence–forward be avoided or revised*. In similar spirit, Koons[20] defines paradox as *an inconsistency among nearly nonrevisable principles that can be resolved only*

by recognizing some essential limitation of thought or language.

In the next section we shall consider the paradoxes which appeared in different parts of chemistry.

2 PRELIMINARIES

The word *paradox* in professional works has almost the same meaning as the word *contradiction*. Chemistry as other natural sciences is not immune of paradoxes. Unlike other natural sciences, in chemistry paradoxes appeared some time later, and it has some of them, while other sciences are overfull of such contradictions.

Now, we shall mention the well–known paradoxes in chemistry. They are:

□ The Prussian blue paradox:[21] *The reaction between ferric and ferrocyanide ions to form Prussian blue and ferrous and ferricyanide ions to form Turnbull's blue are profoundly influenced by the occurrence of the ionic redox equilibrium*:

$$Fe^{+3} + [Fe(CN)_6]^{-4} \rightleftharpoons Fe^{+2} + [Fe(CN)_6]^{-3},$$

which is largely displaced toward the right.

□ Feigl's paradoxes:[22]

- *Hydrogen peroxide as a reducing agent* (*Oxidizing agents undergo mutual reduction*)

$$2\ KMnO_4 + 3\ H_2O_2 \rightarrow 2\ KOH + 2\ MnO_2 + 2\ H_2O + 3\ O_2,$$

$$NaOCl + H_2O_2 \rightarrow NaCl + H_2O + O_2,$$

$$2\ [Fe(CN)_6]^{-3} + H_2O_2 + 2\ OH^- \rightarrow 2\ [Fe(CN)_6]^{-4} + 2\ H_2O + O_2,$$

$$Au^{+3} + 3\ H_2O_2 + 6\ OH^- \rightarrow 6\ H_2O + 3\ O_2 + Au.$$

- *Sulfurous acid brings about oxidations*

$$H_2SO_3 + 2\ H_2S \rightarrow 3\ H_2O + 3\ S,$$

or

$$SO_2 + 2\ H_2S \rightarrow 2\ H_2O + 3\ S,$$

or

$$2\ Ni(OH)_2 + SO_2{\cdot}O_2 \rightarrow NiSO_4 + Ni(OH)_4.$$

- *Nitric acid is not an oxidant*

$$HNO_2 + 3\ HN_3 \rightarrow 2\ H_2O + 5\ N_2.$$

- *Oxidation of aluminum at room temperature*

$$3\ HgCl_2 + 2\ Al \rightarrow 2\ AlCl_3 + 3\ Hg,$$

$$3\ HgI_2 + 2\ Al \rightarrow 2\ AlI_3 + 3\ Hg,$$

$$3\ HgS + 2\ Al \rightarrow Al_2S_3 + 3\ Hg.$$

- *Nonvolatile oxides of tin and antimony are made to disappear by heating them with a volatile compound*

$$SnO_2 + 4\ HI \rightarrow SnI_4 + 2\ H_2O.$$

- *An acid sets a base free from a salt*

$$H_3BO_3 + 4\ KF \rightarrow KBF_4 + 3\ KOH.$$

- *Permanganate is not capable of oxidizing oxalic acid*

$$5\ H_2C_2O_4 + 2\ KMnO_4 + 3\ H_2SO_4 \rightarrow 2\ MnSO_4 + 10\ CO_2 + K_2SO_4 + 8\ H_2O.$$

- *Ammonium polysulfide brings about an oxidation*

$$SnS + (NH_4)_2S_2 \rightarrow (NH_4)_2SnS_3.$$

$$(NH_4)_2SnS_3 + 2HCl \rightarrow 2\ NH_4Cl + H_2S + SnS_2.$$

□ Levinthal's paradox:[23] *The length of time in which a protein chain finds its folded state is many orders of magnitude shorter than it would be if it freely searched all possible configurations*.

□ Quantum chemistry paradoxes:[24]

- *Preponderant configurations*.
- *Relevant symmetry.*
- *Watson effect*.
- *High ionization energies of the partly filled shells*.
- *Continua of penultimate ionization*.
- *Continua of translational energy.*
- *Questions of time–scale*.
- *Quantum mechanics pretends to be valid for other systems than electrons*.
- *Assembly properties and repeated small entities.*

□ Campbell's paradoxes:[25]

- *A catalyst is a substance which increases the rate of a reaction without entering into it*.
- *System tends to a minimum in potential energy.*
- *The entropy of a shuffled deck of cards is greater than that of a new deck.*
- *Energy is the ability to do work*.

□ Paradoxes of spin–pairing energy in gadolinium (III)[26]: *The spin–pairing parameter* $D = 9E^1/8$ for $4f^q$ separates *the averages of all states* (S_0) *and* ($S_{0\text{-}1}$) *to the extent* $2DS_0$ *where* Gd^{+3} *has* $D = 0.80$ eV. *Hartree–Fock (flexible radial functions) have previously been performed for each of the four S, producing a value of* $D = 1.09$ eV *but the contributions to D from kinetic energy T, electron–nuclear attraction Q, and interelectronic repulsion C with ratios* – 1:6:(– 4) *distributed* T_c (3.5), T_f (– 4.5), Q_c (– 7), Q_f (13), C_{cc} (3.5), C_{cf} (– 7.9), C_{ff} (0.4) *indexed c* (*closed nl shells*) *and f* (4*f*). *Pragmatic* $D = 0.80$ eV *corresponds to* 1.84 *times the calculated contribution from* C_{ff} *and to* – 0.184 *times the sum of C integrals. Additional complications are expected from the correlation energy* –100 eV.

□ Structure–Activity Relationship (SAR) paradox[27]: *Exceptions to the principle that a small change in a molecule causes a small change in its chemical behavior are frequently profound*.

□ Helium paradoxes:[28] *The relatively high* $^4He/^{21}Ne$, $^3He/^{22}Ne$ *and* $^4He/CO_2$ *ratios in midocean ridge basalts suggest that it is the midocean ridge basalt reservoir that is He–rich and that the high ratio* $^3He/^4He$ *in midocean ridge basalts is due to excess* ^4He, *not a deficit in the 'primordial' isotope* ^3He.

□ Temperature dependence of $\Delta G°$ and the equilibrium constant K_{eq}:[29] *The sign of* $\Delta S°$ *determines the temperature dependence of* $\Delta G°$*, it is* $\Delta H°$ *that is responsible for the shift in* K_{eq} *with temperature.*

□ The *q*/*T* paradox:[30] *Which 'contains more heat', a cup of coffee at* 95 °C *or a liter of icewater*?

□ *pH* paradox:[31] $pH \equiv -lg[H^+]$.

□ Parrondo's paradox[32]: *A mathematical concept known as Parrondo's paradox is the unexpected situation in which two specific losing strategies can, by alternating between them, produce a winning outcome.*

□ Parrondo's paradox motivated the development of many new computational models of chemical systems, in which thermal cycling problem is studied.[33] By these kinetics systems compare the rates of formation of products under temperature–cycling and steady–state conditions. Also, these computational models of thermal cycling announce new applications in chemistry, biochemistry and chemical engineering. More essentially, by these models one obtains knowledge that some simple chemical systems might behave paradoxically, and that forced oscillating conditions may induce an outcome.

However, these paradoxes are not alone and there are more which appears in the theory of balancing of chemical equations. Just these paradoxes are main research object in this work.

3 A NEW CHEMICAL FORMAL SYSTEM

Chemists must introduce a whole set of auxiliary definitions to make the chemistry work consistently. The more abstract the theory is, the stronger the cognitive power is.

What does it mean a chemical equation? The reply of this question lies in the following descriptive definition given in a compact form.

Definition 2.1. *Chemical equation is a numerical quantification of a chemical reaction.*

Let $\mathscr{X}$ be a finite set of molecules.

Definition 2.2. *A chemical reaction on* $\mathscr{X}$ *is a pair of formal linear combinations of elements of* $\mathscr{X}$*, such that*

$$\rho: \sum_{j=1}^{r} a_{ij} x_j \rightarrow \sum_{j=1}^{s} b_{ij} y_j \ (1 \le i \le m) \tag{2.1}$$

with $a_{ij}, b_{ij} \ge 0$.

The coefficients x_j, y_j satisfy three basic principles (corresponding to a closed input–output static model)

- the law of conservation of atoms,
- the law of conservation of mass, and
- the reaction time–independence.

Definition 2.3. *Each chemical reaction* ρ *has a domain*

$$Dom\rho = \{x \in \mathscr{X} \mid a_{ij} > 0\} \tag{2.2}$$

Definition 2.4. *Each chemical reaction* ρ *has an image*

$$Im\rho = \{y \in \mathscr{X} \mid b_{ij} > 0\} \tag{2.3}$$

Definition 2.5. *Chemical reaction* ρ *is generated for some* $x \in \mathscr{X}$*, if both* $a_{ij} > 0$ *and* $b_{ij} > 0$.

Definition 2.6. *For the case as the previous definition, we say x is a generator* of ρ.

Definition 2.7. *The set of generators of* ρ *is thus* $Dom\rho \cap Im\rho$.

Often chemical reactions are modeled like pairs of multisets, corresponding to integer stoichiometric constants.

Definition 2.8. *A stoichiometrical space is a pair* ($\mathscr{X}$, $\mathscr{R}$), *where* $\mathscr{R}$ *is a set of chemical reactions on* $\mathscr{X}$. *It may be symbolized by an arc–weighted bipartite directed graph* $\Gamma(\mathscr{X}, \mathscr{R})$ *with vertex set* $\mathscr{X} \cup \mathscr{R}$, *arcs* $x \rightarrow \rho$ *with weight* a_{ij} *if* $a_{ij} > 0$, *and arcs* $\rho \rightarrow y$ *with weight* b_{ij} *if* $b_{ij} > 0$.

Let us now consider an arbitrary subset $\mathscr{A} \subseteq \mathscr{X}$.

Definition 2.9. *A chemical reaction* ρ *may take place in a reaction combination composed of the molecules in* $\mathscr{A}$ *if and only if* $Dom\rho \subseteq \mathscr{A}$.

Definition 2.10. *The collection of all feasible reactions in the stoichiometrical space* ($\mathscr{X}$, $\mathscr{R}$), *that can start from* $\mathscr{A}$ *is given by*

$$\mathscr{R}_A = \{\rho \in \mathscr{R} \mid Dom\rho \subseteq \mathscr{A}\}. \tag{2.4}$$

In[34] is proved the following proposition.

Proposition 2.11. *Any chemical equation may be presented in this form*

$$\sum_{j=1}^{r} x_j \prod_{i=1}^{m} \Psi_{aij}^{i} = \sum_{j=1}^{s} y_j \prod_{i=1}^{m} \Omega_{bij}^{i} \tag{2.5}$$

where x_j ($1 \le j \le r$) *and* y_j ($1 \le j \le s$) *are unknown rational coefficients,* Ψ^i *and* Ω^i ($1 \le i \le m$) *are chemical elements in reactants and products, respectively,* a_{ij} ($1 \le i \le m$; $1 \le j \le r$) *and* b_{ij} ($1 \le i \le m$; $1 \le j \le s$) *are numbers of atoms of elements* Ψ^i *and* Ω^i, *respectively, in j–th molecule.*

Definition 2.12. *The nullity of the reaction matrix* $\mathbf{A}$ *is*

$$nullity\mathbf{A} = n - r, \tag{2.6}$$

where n is the total number of reaction molecules and by $r = rank\mathbf{A}$ *the rank of the matrix* $\mathbf{A}$ *is denoted.*

Definition 2.13. *For any chemical reaction these criteria hold*:

1° *if* $nullity\mathbf{A} = 0$, *then the reaction is unfeasible*,

2° *if* $nullity\mathbf{A} = 1$, *then the reaction is unique, and*

3° *if* $nullity\mathbf{A} > 1$, *then the reaction is non–unique.*

We shall define a fallacy in this way.

Definition 2.14. *A wrong result attached with a seemingly logical explanation of why the result is correct is a fallacy.*

A new definition for a paradox should look like this.

Definition 2.15. *A paradox is a seemingly true assertion that leads to an inconsistency or a situation, which resists intuition.*

What does it mean the term non–stoichiometric? Briefly, it means that a substance may participate in two different reactions simultaneously, in which case the relative amounts of two products would bear no fixed ratio to one another.

According to this, now we can define a non–stoichiometric reaction as a real vector space.

Definition 2.16. *A non–stoichiometric reaction is a vector space in which a given set of vector–molecules as reactants gives final vector–molecules as products whose molecular proportions are variable in a continuous sense.*

4 NEW PARADOXES AND FALLACIES

In this section we shall present chronologically the new paradoxes and fallacies, which we discovered in the theory of balancing chemical reactions.

I. Steinbach gave this statement[35]: *While chemical equations may balance algebraically, they are not necessarily stoichimetrically exact*.

In order to illustrate the above statement, »*as the correct stoichiometric equations*«, he »*balanced*« the following chemical reactions

$$2\ KMnO_4 + 5\ H_2O_2 + 4\ H_2SO_4 \rightarrow 2\ KHSO_4 + 2\ MnSO_4 + 8\ H_2O + 5\ O_2, \quad (3.1)$$

$$K_2Cr_2O_3 + 5\ H_2O_2 + 5\ H_2SO_4 \rightarrow 2\ KHSO_4 + Cr_2(SO_4)_3 + 9\ H_2O + 4\ O_2, \quad (3.2)$$

$$NaOBr + H_2O_2 \rightarrow NaBr + H_2O + O_2, \quad (3.3)$$

$$KClO + KClO_2 \rightarrow KClO_3 + KCl, \quad (3.4)$$

$$3\ HClO_3 \rightarrow HClO_4 + Cl_2 + 2\ O_2 + H_2O, \quad (3.5)$$

$$4\ KClO_3 + 16\ HCl \rightarrow 4\ KCl + 7\ Cl_2 + 8\ H_2O + 2\ ClO_2. \quad (3.6)$$

He said: *Obviously there are an infinite number of solutions for the coefficients. Only a few of the total possible solutions are given*.

Next, he stated: *when equations are balanced by either the valence–change or the ion–electron methods, the coefficients obtained are the correct stoichiometric ones*.

He finished his article like this: *Equations* (3.1) ÷ (3.6) *have no stoichiometric meaning, and it is doubtful whether they have any real significance other than that they contain the short–hand suggestion of the reactants used and the products obtained. They do, however, have a definite suggestion that further investigation would be most desirable. It is by examples such as these that the wide divergence between the stoichiometric equation and the actual mechanism of a chemical reaction is so poignantly revealed*.

All the statements mentioned above are *paradoxical*. Why these statements are inconsistent will be explained in the following text.

Now, we shall make a very clean distinction what is what! The first statement is completely wrong, because the algebraic method has not any restriction of its usage. It holds for every chemical reaction, while other so–called »*chemical methods*« hold only for some particular cases.

From the general solution of the reaction (3.1),

$$x_1\ KMnO_4 + x_2\ H_2O_2 + 2x_1\ H_2SO_4 \rightarrow x_1\ KHSO_4 + x_1\ MnSO_4 + (3x_1/2 + x_2)\ H_2O + (5x_1/4 + x_2/2)\ O_2,$$

$$(\forall x_1, x_2 \in \Re)$$

we can see that it is a correct two–parametric stoichiometric reaction, but not as stated Steinbach. It is just one thing. Another thing, he »*offered*« only a particular solution of (3.1) for $x_1 = 2$ and $x_2 = 5$. Immediately, after publication of his article[35], Hall[36] pointed out, the statement for the reaction (3.1) that is a »*good*« example of variable coefficients is absolutely wrong. It has been known to be stoichiometric for many, many years and was studied by C. F. Schönbein, who found that particular reaction as expressed by (3.1).

Remark 3.1. *Schönbein's particular solution is obtained under certain experimental conditions and it does not mean that for other different condition other solutions will not be possible*!

Chemical reaction (3.2) is balanced incorrectly! The coefficients of the above reaction correspond to this chemical reaction

$$x_1\ K_2Cr_2O_7 + x_2\ H_2O_2 + 5x_1\ H_2SO_4 \rightarrow 2x_1\ KHSO_4 + x_1\ Cr_2(SO_4)_3 + (4x_1 + x_2)\ H_2O + (3x_1 + x_2)/2\ O_2,$$

$$(\forall x_1, x_2 \in \Re)$$

for $x_1 = 1$ and $x_2 = 5$. The reaction that is offered by Hall[36]

$$K_2Cr_2O_7 + 3\ H_2O_2 + 5\ H_2SO_4 \rightarrow 2\ KHSO_4 + 7\ H_2O + 3\ O_2,$$

is balanced wrongly too!

The general solution of the reaction (3.3) is

$$x_1\ NaOBr + x_2\ H_2O_2 \rightarrow x_1\ NaBr + x_2\ H_2O + (x_1 + x_2)/2\ O_2,\ (\forall x_1, x_2 \in \Re)$$

and Steinbach found a particular solution for $x_1 = x_2 = 1$. Again, we had not any limitations with the usage of the algebraically method. Also, in this case the method worked perfectly.

Chemical reaction (3.4) has this general solution

$$x_1\ KClO + x_2\ KClO_2 \rightarrow (x_1 + 2x_2)/3\ KClO_3 + (2x_1 + x_2)/3\ KCl,\ (\forall x_1, x_2 \in \Re)$$

and the above particular solution corresponds for $x_1 = x_2 = 1$.

The general solution of the chemical reaction (3.5) is

$$x_1\ HClO_3 \rightarrow x_2\ HClO_4 + (x_1 - x_2)/2\ Cl_2 + (5x_1 - 7x_2)/4\ O_2 + (x_1 - x_2)/2\ H_2O,\ (x_1 > 7x_2/5) \quad (3.7)$$

For $x_1 = 3$ and $x_2 = 1$, as a particular case from (3. 7) immediately follows (3. 5).

For $x_1 = x_2$, from (3.7) one obtains this elementary reaction

$$2\ HClO_3 + O_2 \rightarrow 2\ HClO_4.$$

For $x_1 = 7x_2/5$, chemical reaction (3.7) transforms into

$$7\ HClO_3 \rightarrow 5\ HClO_4 + Cl_2 + H_2O.$$

If $x_1 < x_2$, then (3.7) becomes

$$x_1\ HClO_3 + (x_2 - x_1)/2\ Cl_2 + (7x_2 - 5x_1)/4\ O_2 + (x_2 - x_1)/2\ H_2O \rightarrow x_2\ HClO_4,\ (x_1 < x_2).$$

If $x_2 < x_1 < 7x_2/5$, then chemical reaction (3.7) attains this form

$$x_1\ HClO_3 + (7x_2 - 5x_1)/4\ O_2 \rightarrow x_2\ HClO_4 + (x_1 - x_2)/2\ Cl_2 + (x_1 - x_2)/2\ H_2O,\ (x_2 < x_1 < 7x_2/5).$$

For the reactions (3.3), (3.4) and (3.5) Lehrman[37] with the mentioned particular cases gave a comprehensive construction of *ad infinitum* equations.

The last reaction (3.6), between potassium chlorate and hydrochloric acid, has a general solution

$$x_1\ KClO_3 + x_2\ HCl \rightarrow x_1\ KCl + (-3x_1 + 5x_2/2)/4\ Cl_2 + x_2/2\ H_2O + (3x_1 - x_2/2)/2\ ClO_2,\ (6x_1/5 < x_2 < 6x_1). \quad (3.8)$$

For $x_1 = 4$ and $x_2 = 16$ from the chemical reaction (3.8) as a particular solution follows (3. 6).

For $x_1 = 5x_2/6$, from (3.8) one obtains this elementary reaction

$$5\ KClO_3 + 6\ HCl \rightarrow 5\ KCl + 3\ H_2O + 6\ ClO_2.$$

For $x_1 = x_2/6$, then (3. 8) becomes

$$KClO_3 + 6\ HCl \rightarrow KCl + 3\ Cl_2 + 3\ H_2O.$$

If $x_1 > 5x_2/6$, then (3. 8) transforms into

$$x_1\ KClO_3 + x_2\ HCl + (3x_1 - 5x_2/2)/4\ Cl_2 \rightarrow x_1\ KCl + x_2/2\ H_2O + (3x_1 - x_2/2)/2\ ClO_2,\ (x_1 > 5x_2/6). \quad (3.\ 9)$$

We would like to emphasize here that all the reactions are balanced by the well–known algebraically method, and all the two–parametric coefficients are correct. It is completely different from the third Steinbach's statement given above, which gives advantage to the valence–change or the ion–electron methods.

If we take into account the very well–known rule that equations for consecutive reactions may be added and equations for concurrent reactions may not be added, then obviously Steinbach brings up the old, very old error involved in adding equations for concurrent reactions. It is his biggest mistake.

What happens when the reactions are not unique according to Steinbach? In that case, he »*balanced*« them as an infinite number of reactions, which do not express actual stoichiometric relations. They are »*derived*« by combining together the reactions for concurrent reactions, in which coefficients in each of the two or more reactions are previously multiplied by different numbers. Sure, these reactions are incorrect, as they do not correspond to the real stoichiometric relations among the substances, which are involved. In some cases, there is no constant relation among the quantities of substances expressed by his reactions. The ratio of the quantities will depend upon chemical conditions (concentration, temperature, etc.).

The above Steinbach's reactions, in fact, are oxidation–reduction reactions for which we found the general solutions by using of algebraic method. Every one of them in fact represents two chemical reactions, not one as Steinbach stated. Therefore, these reactions are not *non–stoichiometric reaction*! Standen in his article[38] named these Steinbach's reactions as *bizarre non–stoichiometric equations*.

McGavock in[39] gave a note on errata in the Steinbach's article[35].

In order to explain what a *non–stoichiometric reaction* represents, McGavock considered an example from his book[40].

Example 3.2. It is the cracking reaction

$$x_1\ C_8H_{18} \rightarrow x_2\ C_2H_4 + x_3\ C_3H_6 + x_4\ CH_4. \quad (3.10)$$

Now, we shall show that the above reaction (3.10) is not a *non–stoichiometric* reaction.

From the scheme given below

	$\nu_1 = C_8H_{18}$	$\nu_2 = C_2H_4$	$\nu_3 = C_3H_6$	$\nu_4 = CH_4$
C	8	2	3	1
H	18	4	6	4

follows this vector equation

$$x_1\boldsymbol{\nu}_1 = x_2\boldsymbol{\nu}_2 + x_3\boldsymbol{\nu}_3 + x_4\boldsymbol{\nu}_4,$$

i. e.,

$$x_1\ (8, 18)^T = x_2\ (2, 4)^T + x_3\ (3, 6)^T + x_4\ (1, 4)^T,$$

or

$$(8x_1, 18x_1)^T = (2x_2 + 3x_3 + x_4, 4x_2 + 6x_3 + 4x_4)^T.$$

From the system of linear equations

$$8x_1 = 2x_2 + 3x_3 + x_4,$$
$$18x_1 = 4x_2 + 6x_3 + 4x_4,$$

one obtains $x_4 = x_1$ and $x_3 = (7x_1 - 2x_2)/3$. Now, balanced chemical equation has this general solution

$$x_1\ C_8H_{18} \rightarrow x_2\ C_2H_4 + (7x_1 - 2x_2)/3\ C_3H_6 + x_1\ CH_4,\ (x_1 > 2x_2/7). \quad (3.11)$$

The vectors $\boldsymbol{v}_1$, $\boldsymbol{v}_2$, $\boldsymbol{v}_3$ and $\boldsymbol{v}_4$ of the molecules of the above chemical reaction are linearly dependent and they generate an *infinite number* of vector spaces V_∞ over $\Re$, *i. e.*, one obtains an *infinite number* of solutions $[x_1, x_2, (7x_1 - 2x_2)/3, x_1]$, $(x_1 > 2x_2/7)$, that means that the chemical reaction (3. 10) is non–unique.

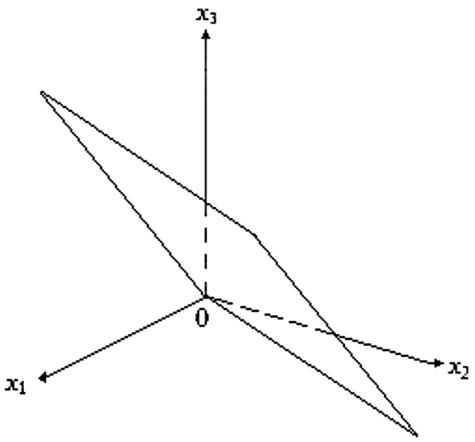

Figure 1: Plane $7x_1 - 2x_2 - 3x_3 = 0$ in $\Re^3$

However, it is not possible, either on an algebraic or empirical basis, to exclude nonintegral values for the coefficients. Each point of the plane $7x_1 - 2x_2 - 3x_3 = 0$, given on the **Figure 1**, represents a triad of positive, nonintegral values. Infinity of such points corresponding to infinity of triads of coefficients in the above equation exists. By virtue of this finding, it is asserted that this cracking reaction does not represent a *non–stoichiometric* reaction. It contradicts McGavock's statement.

McGavock in[39] obtained this reaction

$$C_8H_{18} \rightarrow 2\ C_2H_4 + C_3H_6 + CH_4. \quad (3.12)$$

Actually, the reaction (3.12) is a particular solution of (3.11), for $x_1 = 1$ and $x_2 = 2$. The above McGavock's »*non–stoichiometric*« reaction (3.12) according to Standen[38] can also be written as two reactions:

$$C_8H_{18} \rightarrow C_7H_{14} + CH_4,$$

$$C_7H_{14} \rightarrow 2\ C_2H_4 + C_3H_6.$$

Before the reaction (3.12) be regarded as a genuine *non–stoichiometric* reaction, it must be shown that it is one reaction. It might be a combination of these two reactions:

$$2\ C_8H_{18} \rightarrow 7\ C_2H_4 + 2\ CH_4,$$

$$3\ C_8H_{18} \rightarrow 7\ C_3H_6 + 3\ CH_4.$$

Also, this Standen's counterexample shows that chemical reaction (3.12) is not *non–stoichiometric* reaction.

By this and the Definition 2.16, we proved that McGavock's presentation for *non–stoichiometric reaction* is an ordinary fallacy.

II. Porges in his article[41] wrote: *After examinning a great many chemical equations*, *one concludes that most of them are of the type in which the number of compounds involved exceeds the number of elements by unity.*

This Porges' statement does not represent any criterion for balancing chemical equation and it is completely wrong. In fact, it is only an ordinary *paradox*! The counterexamples given below show it.

Example 3.3. Let us consider this elementary chemical reaction

$$x_1\ BiCl_3 + x_2\ H_2O \rightarrow x_3\ HCl + x_4\ BiClO.$$

Here, we have a case when the number of involved compounds does not exceed the number of elements by unity, *i. e.*, in this case four elements are involved in four molecules. The above chemical reaction reduces to a system of four linear equations in four unknown variables and the chemical reaction has a unique solution. The balanced reaction has this form

$$BiCl_3 + H_2O \rightarrow 2HCl + BiClO.$$

Example 3.4. For instance, in the chemical reaction

$$x_1\ Cu_2S + x_2\ HNO_3 \rightarrow x_3\ Cu_2SO_4 + x_4\ NO + x_5\ H_2O,$$

five elements are involved in five molecules. The above reaction has a unique solution $x_1 = 3$, $x_2 = 8$, $x_3 = 3$, $x_4 = 8$, $x_5 = 4$.

Example 3.5. In this particular reaction

$$x_1\ K_4Fe(CN)_6 + x_2\ K_2S_2O_3 \rightarrow x_3\ KCNS + x_4\ K_2SO_4 + x_5\ K_2S + x_6\ FeS,$$

are involved six elements and same number of molecules, *i. e.*, we have six linear equations in six unknown variables. The chemical reaction has a unique solution $x_1 = 2$, $x_2 = 12$, $x_3 = 12$, $x_4 = 9$, $x_5 = 1$, $x_6 = 2$.

Example 3.6. The chemical reaction

$$x_1\ AgPF_6 + x_2\ Re(CO)_5Br + x_3\ CH_3CN \rightarrow x_4\ AgBr + x_5\ [Re(CO)_5(CH_3CN)]PF_6,$$

contains nine elements in five molecules and it reduces to a system of nine linear equations in five unknown variables. The chemical reaction has a unique solution $x_1 = x_2 = \cdots = x_5 = 1$.

The mentioned four counterexamples contradict to the above Porges' statement. By this, we refuted his statement.

In the same article[41] there are *fallacies* too.

For instance, he reduced the chemical reaction

$$x_1\ FeCl_2 + x_2\ K_2Cr_2O_7 + x_3\ HCl \rightarrow x_4\ FeCl_3 + x_5\ KCl + x_6\ CrCl3 + x_7\ H_2O, \quad (3.13)$$

to the following system of linear equations

$$x_1 = x_4,\ 2x_1 + x_3 = 3x_4 + x_5 + 3x_6,$$
$$2x_2 = x_5,\ 2x_2 = x_6, \qquad (3.14)$$
$$7x_2 = x_7,\ x_3 = 2x_7.$$

Immediately from (3.14), he obtained

$$x_1 = 6x_2,\ x_2 = x_2,\ x_3 = 14x_2,\ x_4 = 6x_2,$$
$$x_5 = 2x_2,\ x_6 = 2x_2,\ x_7 = 7x_2. \qquad (3.15)$$

Next, he said: *It is evident that the general integral solution of* (3.14) *is derived from* $x_2 = k$, *where k is any positive integer, and consequently although* (3.14) *has an infinite number of integral solutions, all of them derive from* $x_2 = k$, *and consist merely of multiplies of values for the respective variables established by* (3.15). *All solutions other than for* $k = 1$, *are therefore trivial chemically as well as mathematically.*

Unfortunately, the above statement is fallacious! The last sentence *All solutions other than for* $k = 1$, *are therefore trivial chemically as well as mathematically*, is incorrect. Previous Porges stated that $x_2 = k$, where k is any positive integer, and after that he took $k = 1$. It is wrong! Why? To this question a very simple answer will follow like this. The reaction (3.13) has a unique solution. If we substitute (3.15) into (3.13), and after that if we divide the relation (3.13) by an arbitrary real number $x_2 \neq 0$, immediately follows

$$6\ FeCl_2 + K_2Cr_2O_7 + 14\ HCl$$
$$\rightarrow 6\ FeCl_3 + 2\ KCl + 2\ CrCl_3 + 7\ H_2O.$$

Actually, Porges considered the general solution (3.15) of the system (3.14) separately of (3.13), what is wrong. The reaction (3.13) and the general solution (3.15) of the system (3.14) must be considered as one whole, because they are connected with each other.

Obviously, we did not introduce any constant k, as it was done previously by Porges. Our approach is completely different than Porges' wrong way he used.

The same remark also holds for the second Porges' reaction

$$As_2S_3 + 3\ (NH_4)_2S \rightarrow 2\ (NH_4)_3AsS_3. \qquad (3.16)$$

considered in[41].

The third considered reaction in[41] is given by this expression

$$x_1\ HAuCl_3 + x_2\ K_4Fe(CN)_6$$
$$\rightarrow x_3\ KAu(CN)_4 + x_4\ KAu(CN)_2$$
$$+ x_5\ KAu(CN)_2Cl_2 + x_6\ KCl + x_7\ HCl$$
$$+ x_8\ [4Fe(CN)_3{\cdot}3Fe(CN)_2]. \qquad (3.17)$$

For its »*solution*« the author offered these expressions

$$x_1 = 12k - 2,\ x_2 = 7k,\ x_3 = 2,\ x_4 = 8k - 1,$$
$$x_5 = 4k - 3,\ x_6 = 16k + 2,$$
$$x_7 = 12k - 2,\ x_8 = k, \qquad (3.18)$$

where k takes on all positive integral values. Yet (3.18) is merely a particular solution, but it is not the general solution of (3.17).

The general solution of the reaction (3.17) is given by this expression

$$14x_1\ HAuCl_3 + 14x_2\ K_4Fe(CN)_6$$
$$\rightarrow (24x_2 - 14x_1)\ KAu(CN)_4$$
$$+ (7x_1 + 4x_2)\ KAu(CN)_2$$
$$+ (21x_1 - 28x_2)\ KAu(CN)_2Cl_2$$
$$+ (56x_2 - 14x_1)\ KCl + 14x_1\ HCl$$
$$+ 2x_2\ [4Fe(CN)_3{\cdot}3Fe(CN)_2],$$
$$(4x_2/3 < x_1 < 12x_2/7). \qquad (3.19)$$

The balanced reaction (3.19) is an expression of two parameters, but it is not one–parametric expression as it is given in[41]. In fact, it is another Porges' *fallacy.*

Remark 3.7. *Intentionally, we omitted from consideration other particular solutions of* (3.19) *because we had into account that our work has a limited size.*

Before ending his article[41], Porges posed the following three questions:

1° *Is there, for equations of this third type which admits infinitely many distinct, not multiple solutions, a* ***least action*** *principle similar to that in mechanics*?

2° *Of the unlimited number of ways of balancing such an equation as* (3.17), *is that corresponding to the solution in* ***least integer*** *of the linear equations the one invariably indicated by the laboratory work, which is, after all, the real criterion*?

3° *Further, what would a minimum solution be – that for which the square root of the arithmetic mean of the squares of the variables is less than for any other solution*?

To date we did not meet in chemical literature any reply on these questions. It is a challenge for us to try to give appropriate answers on the above questions. Sure, the answers will be given in a rough form, because a comprehensive replay looks for a special article dedicated only on that particular subject.

The answer on the first question should be like this. *No*! *In chemistry there is not a* ***least action*** *principle similar to that in mechanics, because the balancing chemical equation has not any tangent point with mechanics, just it is connected with linear algebra. In fact, balancing chemical equations is not chemistry; it is just linear algebra*[7]. *On the other hand, the term a* ***least action*** *associate on the dynamism of 18th century as metaphysics was traced by Leibniz and Boscovich. Later Boyle gave an explicit formulation of chemistry in a coherent metaphysical scheme. A comprehensive study about metaphysics of chemical reaction is given in*[42].

The second question is interesting for a discussion, and it can be answered negatively in this way. *Unlimited number of ways of balancing such a reaction as* (3.17) *is not corresponding to the solution in* ***least integer*** *of the linear equations the one invariably indicated by the laboratory work, which is, after all, the real criterion. This case, in fact, boils down to the continuum problem. It is an extremely hard problem, which is a stumbling block*

for mathematicians as well as chemists. In other words, this case can sink into the third question.

As the third question is posed, it contains a wrong formulation for minimum solution. It is one more Porges' fallacy. One can reply the last question like this. *When the question is posed it was unbelievable for that time. It was impossible because the mathematical methods needed for its proof were unknown. For instance, Moore–Penrose pseudoinverse matrix*[8,9] *was discovered ten years later in* 1955 *and its first application in chemistry*[43] *appeared more than two decades later in* 1978. *Also, then was unknown the general problem of balancing chemical equations*[44]. *From today viewpoint, by using of Moore–Penrose pseudoinverse matrix the minimal solution is obtained in*[45,46].

Now, a new question arises: *why not look for a topology of solutions of chemical equations, instead of finding minimal solutions*? It is a much better question, than non–unique equation to be reduced to a minimal case. The question is new, and it is extremely hard. Sure, it will be a challenge for the next research.

Porges finished his article[41] on this way: *In the very few equations of the third type encountered by the writer, the balancing in least integers was always that for which k was also least, and was identical with the laboratory balancing*; *but given a general solution not minimized by smallest admissible value of k – theoretically not impossible – then what*?

It represents one last Porges' fallacy! We shall build the reply to this question on the concept of the *continuum*. In fact, the word *continuum* is recognizable as the name used by Cantor to refer to the real line. From the expression (3. 19), we can see that this kind of chemical equations reduces to the *Cantor's continuum problem*. This problem is simply condensed in the following question: *How many points are there on the straight line in Euclidean space*? In other words, the question is: *How many different sets of integers do there exist*?[47] This problem is neither simple nor easy; it needs a wide explanation. It shows that balancing chemical equations is a main object in **Foundation of Chemistry**, which lies in an intertwined mixture of topology, abstract algebra, linear algebra, axiomatic set theory, mathematical logic, computability theory and proof theory. To explain a little more fully this idea we must first discuss the concept of a *formal system*. Why? Simply, chemical equation must be treated only as a *formal system*, if we like to avoid appearance of paradoxes. In an opposite case we shall have paradoxes as these mentioned in this section.

A formal chemical system consists of a finite set of symbols and of a finite number of rules by which these symbols can be combined into formulas or statements. That kind of formal system is given in second section of this work. A number of such statements are nominated as axioms and by repeated applications of the rules of the system one obtains an ever growing body of provable statements.

A proof of a given statement is a finite sequence of statements that starts with an axiom and ends with the preferred statement. The sequence is such that every transitional statement is either an axiom or is derivable by the rules of the system from statements that lead it. Thus, a statement that a sequence of formulas does or does not represent a proof of formula is »*not*« a statement in the formal system itself. It is a statement »*about*« the system and such statements are often referred to as »*metamathematical*«.

For the first time a formal generalized inverse matrix approach for balancing chemical equation is introduced in[44]. Balancing chemical equations as a matrix well–defined formal system is given in the works[45,46,48–50].

III. Another paradox in the theory of balancing chemical equations is the following Standen's statement[38]: *It would seem that examples could not be found where the number of mathematical equations actually exceeds the number of variables*; *for if the mathematical equations were inconsistent, the whole thing would be an impossibility, while if they were consistent it would indicate that the chemical equation had been appropriately broken down into its terms*.

To prove the above Standen's absurdity, we shall use the following counterexamples.

Example 3.8. The chemical reaction

$$x_1\ CoCl_2 + x_2\ Na_3PO_4 \rightarrow x_3\ NaCl + x_4\ Co_3(PO_4)_2,$$

contains five elements involved in four molecules, *i. e.*, in this case the chemical reaction reduces to a system of five linear equations in four unknown variables and the chemical reaction has a unique solution. The balanced reaction has this form

$$3\ CoCl_2 + 2\ Na_3PO_4 \rightarrow 6\ NaCl + Co_3(PO_4)_2.$$

Example 3.9. In this particular reaction

$$x_1\ Cu(NH_3)_4Cl_2 + x_2\ KCN + x_3\ H_2O \rightarrow x_4\ [K_2Cu(CN)_3{\cdot}NH_4Cl{\cdot}KCl] + x_5\ KCNO + x_6\ NH_3,$$

are involved seven elements in six molecules, *i. e.*, we have seven linear equations in six unknown variables. The chemical reaction has a unique solution $x_1 = 2$, $x_2 = 7$, $x_3 = 1$, $x_4 = 2$, $x_5 = 1$, $x_6 = 6$.

Example 3.10. For instance, the chemical reaction

$$x_1\ AgPF_6 + x_2\ Re(CO)_5Br + x_3\ CH_3CN + x_4\ K_2S_2O_3 \rightarrow x_5\ KBr + x_6\ [Re(CO)_5(CH_3CN)]PF_6 + x_7\ Ag_2S + x_8\ K_2O + x_9\ SO_2,$$

has eleven elements involved in nine molecules. The above chemical reaction reduces to a system of eleven linear equations in nine unknown variables, whose unique solution is $x_1 = 4$, $x_2 = 4$, $x_3 = 4$, $x_4 = 3$, $x_5 = 4$, $x_6 = 4$, $x_7 = 2$, $x_8 = 1$, $x_9 = 4$.

By the last three counterexamples we showed that the above Standen's[38] statement is an absurd.

IV. Next, we shall consider the Blakley's[51] paradox. Among other chemical reactions, he considered hydroly-

sis of two organic substances: *bradykinin* and *gramicidin–S*.

Example 3. 11. The following reaction

$$x_1\ C_2H_5NO_2 + x_2\ C_3H_7NO_3 + x_3\ C_6H_{14}N_4O_2 + x_4\ C_5H_9NO_2 + x_5\ C_9H_{11}NO_2 \rightarrow x_6\ H_2O + x_7\ C_{50}H_{73}N_{15}O_{11}. \quad (3.20)$$

was studied in[51]. Blakley considered balancing of the above chemical reaction by a matrix approach using a module basis.

He »*proved*« that »*hydrolysis* (3.20) *of bradykinin is unique*«. It represents only an empirical discovered relationship, which is wrong.

We shall prove the absurdity of his statement by using the well–known algebraic method for balancing chemical equations.

By the way, we shall show that this method is powerful and its usage is not limited as some traditional oriented chemists think.

Let us consider the scheme of the chemical reaction (3.20).

	$C_2H_5NO_2$	$C_3H_7NO_3$	$C_6H_{14}N_4O_2$	$C_5H_9NO_2$	$C_9H_{11}NO_2$	H_2O	$C_{50}H_{73}N_{15}O_{11}$
C	2	3	6	5	9	0	–50
H	5	7	14	9	11	–2	–73
N	1	1	4	1	1	0	–15
O	2	3	2	2	2	–1	–11

From the above scheme imediatelly follows the stoichiometric matrix

$$A = \begin{bmatrix} 2 & 3 & 6 & 5 & 9 & 0 & -50 \\ 5 & 7 & 14 & 9 & 11 & -2 & -73 \\ 1 & 1 & 4 & 1 & 1 & 0 & -15 \\ 2 & 3 & 2 & 2 & 2 & -1 & -11 \end{bmatrix}$$

with $r = rank\boldsymbol{A} = 4$.

Since $nullity\boldsymbol{A} = n - r = 7 - 4 = 3 > 1$, where n is the total number of reaction molecules, then the chemical reaction is possible and it has an infinite number of solutions. Let us prove it.

One can reduce the chemical reaction (3.20) to the following system of linear equations

$$\begin{aligned} 2x_1 + 3x_2 + 6x_3 + 5x_4 + 9x_5 &= 50x_7, \\ 5x_1 + 7x_2 + 14x_3 + 9x_4 + 11x_5 &= 2x_6 + 73x_7, \end{aligned} \quad (3.21)$$

$$\begin{aligned} x_1 + x_2 + 4x_3 + x_4 + x_5 &= 15x_7, \\ 2x_1 + 3x_2 + 2x_3 + 2x_4 + 2x_5 &= x_6 + 11x_7. \end{aligned}$$

The general solution of the system (3.21) is given by the following expressions

$$\begin{aligned} x_4 &= 66x_1/23 + 93x_2/23 - 45x_3/23, \\ x_5 &= -14x_1/23 - 26x_2/23 + 43x_3/23, \\ x_6 &= 95x_1/23 + 137x_2/23 - 24x_3/23, \\ x_7 &= 5x_1/23 + 6x_2/23 + 6x_3/23, \end{aligned} \quad (3.22)$$

where $x_i > 0$ $(1 \le i \le 3)$ are arbitrary real numbers.

After substitution of (3.22) in (3.20), one obtains a balanced chemical reaction

$$x_1\ C_2H_5NO_2 + x_2\ C_3H_7NO_3 + x_3\ C_6H_{14}N_4O_2 + (66x_1/23 + 93x_2/23 - 45x_3/23)\ C_5H_9NO_2 + (-14x_1/23 - 26x_2/23 + 43x_3/23)\ C_9H_{11}NO_2 \rightarrow (95x_1/23 + 137x_2/23 - 24x_3/23)\ H_2O + (5x_1/23 + 6x_2/23 + 6x_3/23)\ C_{50}H_{73}N_{15}O_{11}. \quad (3.23)$$

From (3.23) follows this system of inequalities

$$\begin{aligned} 22x_1 + 31x_2 - 15x_3 &> 0, \\ -14x_1 - 26x_2 + 43x_3 &> 0, \\ 95x_1 + 137x_2 - 24x_3 &> 0, \\ 5x_1 + 6x_2 + 6x_3 &> 0. \end{aligned} \quad (3.24)$$

From the first and the second inequality of (3.24) immediately follows this expression

$$14x_1/43 + 26x_2/43 < x_3 < 22x_1/15 + 31x_2/15. \quad (3.25)$$

The expression (3.25), the third and the fourth inequality of (3.24) are necessary and sufficient conditions for (3.23) to hold.

For instance, if we substitute $x_1 = x_2 = 1$ and $x_3 = 2$ in (3.23), then as a particular case appears this reaction

$$C_2H_5NO_2 + C_3H_7NO_3 + 2\ C_6H_{14}N_4O_2 + 3\ C_5H_9NO_2 + 2\ C_9H_{11}NO_2 \rightarrow 8\ H_2O + C_{50}H_{73}N_{15}O_{11},$$

for which Blakley[51] stated that it is unique, but it is not true.

Now, we shall give two more particular cases for which (3.23) holds.

Let $x_1 = x_2 = x_3 = 1$, then from (3.23) one obtains the reaction

$$23\ C_2H_5NO_2 + 23\ C_3H_7NO_3 + 23\ C_6H_{14}N_4O_2 + 114\ C_5H_9NO_2 + 3\ C_9H_{11}NO_2 \rightarrow 208\ H_2O + 17\ C_{50}H_{73}N_{15}O_{11}.$$

Let $x_1 = x_2 = 1$ and $x_3 = 3$, then (3.23) becomes

$$23\ C_2H_5NO_2 + 23\ C_3H_7NO_3 + 69\ C_6H_{14}N_4O_2 + 24\ C_5H_9NO_2 + 89\ C_9H_{11}NO_2 \rightarrow 160\ H_2O + 29\ C_{50}H_{73}N_{15}O_{11}.$$

The other particular cases of (3.23) are not considered, because we took into account the Remark 3.7.

Example 3.12. In[51] the hydrolysis of *gramicidin–S* was studied, given by the following reaction

$$x_1\ C_5H_9NO_2 + x_2\ C_5H_{11}NO_2 + x_3\ C_6H_{13}NO_2 + x_4\ C_9H_{11}NO_2 + x_5\ C_5H_{12}N_2O_2 \rightarrow x_6\ C_{60}H_{92}N_{12}O_{10} + x_7\ H_2O. \quad (3.26)$$

For the chemical reaction (3.26) if we write its stoichiometric scheme, then one obtains

	$C_5H_9NO_2$	$C_5H_{11}NO_2$	$C_6H_{13}NO_2$	$C_9H_{11}NO_2$	$C_5H_{12}N_2O_2$	$C_{60}H_{92}N_{12}O_{10}$	H_2O
C	5	5	6	9	5	–60	0
H	9	11	13	11	12	–92	–2
N	1	1	1	1	2	–12	0
O	2	2	2	2	2	–10	–1

from where follows the stoichiometric matrix

$$A=\begin{bmatrix} 5 & 5 & 6 & 9 & 5 & -60 & 0 \\ 9 & 11 & 13 & 11 & 12 & -92 & -2 \\ 1 & 1 & 1 & 1 & 2 & -12 & 0 \\ 2 & 2 & 2 & 2 & 2 & -10 & -1 \end{bmatrix}$$

with $r = rank\boldsymbol{A} = 4$.

Since $nullity\boldsymbol{A} = n - r = 7 - 4 = 3 > 1$, then chemical reaction is possible and it has an infinity number of solutions. Let us prove it.

The system of linear equations obtained from (3. 26) is

$$\begin{gathered} 5\,x_1 + 5\,x_2 + 6\,x_3 + 9\,x_4 + 5\,x_5 - 60\,x_6 = 0, \\ 9\,x_1 + 11\,x_2 + 13\,x_3 + 11\,x_4 \\ + 12\,x_5 - 92\,x_6 - 2\,x_7 = 0, \\ x_1 + x_2 + x_3 + x_4 + 2\,x_5 - 12\,x_6 = 0, \\ 2\,x_1 + 2\,x_2 + 2\,x_3 + 2\,x_4 \\ + 2\,x_5 - 10\,x_6 - 1\,x_7 = 0. \end{gathered} \tag{3.27}$$

The general solution of (3.27) is given by the expressions

$$\begin{gathered} x_1 = -4\,x_4 + 20\,x_6 - x_7, \\ x_2 = 7\,x_4 - 57\,x_6 + 9\,x_7/2, \\ x_3 = -4\,x_4 + 35\,x_6 - 5\,x_7/2, \\ x_5 = 7\,x_6 - x_7/2, \end{gathered} \tag{3.28}$$

where x_4, x_6 and x_7 are arbitrary real numbers.

After substitution of (3.28) in (3.26), the balanced chemical reaction has this form

$$\begin{gathered} (-4\,x_4 + 20\,x_6 - x_7)\ C_5H_9NO_2 \\ + (7\,x_4 - 57\,x_6 + 9\,x_7/2)\ C_5H_{11}NO_2 \\ + (-4\,x_4 + 35\,x_6 - 5\,x_7/2)\ C_6H_{13}NO_2 \\ + x_4\ C_9H_{11}NO_2 + (7\,x_6 - x_7/2)\ C_5H_{12}N_2O_2 \\ \rightarrow x_6\ C_{60}H_{92}N_{12}O_{10} + x_7\ H_2O, \end{gathered} \tag{3.29}$$

From (3.29) follows this system of inequalities

$$\begin{gathered} -4\,x_4 + 20\,x_6 - x_7 > 0, \\ 7\,x_4 - 57\,x_6 + 9\,x_7/2 > 0, \\ -4\,x_4 + 35\,x_6 - 5\,x_7/2 > 0, \\ 7\,x_6 - x_7/2 > 0. \end{gathered} \tag{3.30}$$

From the second and the third inequality of (3.30) immediately follows this expression

$$\begin{gathered} -14\,x_4/9 + 114\,x_6/9 < x_7 \\ < -8\,x_4/5 + 14\,x_6. \end{gathered} \tag{3.31}$$

The expression (3.31), the first and the fourth inequality of (3.30) are necessary and sufficient conditions for (3.29) to hold.

For instance, if we substitute $x_4 = 2$, $x_6 = 1$ and $x_7 = 10$ in (3.29), then as a particular case appears this reaction

$$\begin{gathered} 2\ C_5H_9NO_2 + 2\ C_5H_{11}NO_2 + 2\ C_6H_{13}NO_2 \\ + 2\ C_9H_{11}NO_2 + 2\ C_5H_{12}N_2O_2 \\ \rightarrow C_{60}H_{92}N_{12}O_{10} + 10\ H_2O. \end{gathered}$$

for which Blakley[51] stated that it is unique, but it is not true.

Now, we shall give more two particular cases for which holds (3.29).

Let $x_4 = x_6 = 9$ and $x_7 = 102$, then from (3.29) one obtains the reaction

$$\begin{gathered} 42\ C_5H_9NO_2 + 9\ C_5H_{11}NO_2 \\ + 24\ C_6H_{13}NO_2 + 9\ C_9H_{11}NO_2 + 12\ C_5H_{12}N_2O_2 \\ \rightarrow 9\ C_{60}H_{92}N_{12}O_{10} + 102\ H_2O. \end{gathered}$$

Let $x_4 = 27$, $x_6 = 21$ and $x_7 = 250$, then (3.29) becomes

$$\begin{gathered} 62\ C_5H_9NO_2 + 117\ C_5H_{11}NO_2 \\ + 2\ C_6H_{13}NO_2 + 27\ C_9H_{11}NO_2 + 22\ C_5H_{12}N_2O_2 \\ \rightarrow 21\ C_{60}H_{92}N_{12}O_{10} + 250\ H_2O. \end{gathered}$$

The other particular cases of (3.29) are not considered because we took into account the Remark 3.7.

V. Das in his article[52] applied the partial equation method for balancing chemical equations. There he wrote: *if the number of reactants and products is equal to or less* (*or at most one more*) *than the total number of elements involved in the chemical equation*, *then there will be only one way of balancing a chemical equation*.

For the first two cases this statement is a *paradox*! The next two counterexamples given below contradict to the above statement.

Example 3.13. The following chemical reaction

$$x_1\ NO_2 + x_2\ HClO \rightarrow x_3\ HNO_3 + x_4\ HCl,$$

has involved four elements in four molecules, but it has not a unique solution as stated above. It is an unfeasible reaction, because $x_1 = x_2 = x_3 = x_4 = 0$.

Now, we shall give another counterexample.

Example 3.14. In the reaction

$$x_1\ KIO_2 + x_2\ Pb(NO_3)_2 \rightarrow x_3\ KNO_3 + x_4\ PbI_2,$$

five elements are involved in four molecules. This reaction has only a trivial solution $x_1 = x_2 = x_3 = x_4 = 0$. It shows that this reaction is unfeasible.

VI. Next, we shall elaborate another very interesting *paradox*. García[53] gave a »*half–reaction method*« for balancing chemical equations. He described his »*method*« on this way. *The chemical reaction is divided into two half–reactions and each one is balanced independently. These two balanced half–reactions are added together to*

get the correct stoichiometry of the reaction. One half–reaction is formed with compounds that contain the same elements other than oxygen and hydrogen. The remaining compounds, and others if it is necessary, constitute the other half–reaction.

Example 3.15. This chemical reaction

$$x_1\ FeS_2 + x_2\ HNO_3 \rightarrow x_3\ Fe_2(SO_4)_3 + x_4\ NO + x_5\ H_2SO_4, \quad (3.32)$$

he »*balanced*« like this

$$2\ FeS_2 + 10\ HNO_3 \rightarrow Fe_2(SO_4)_3 + 10\ NO + H_2SO_4 + 4\ H_2O. \quad (3.33)$$

Unfortunately reaction (3.33) is quantitatively and qualitatively different from the reaction (3.32). Actually, the reaction (3.33) is augmented reaction (3.32) by four water molecules. Reactions (3.32) and (3.33) belong to different types of reactions, and according to it, they are incompatible. The reaction (3.32) belongs to the type of unfeasible reactions, because its vectors of molecules do not generate a vector space V over $\Re$.

For our next analysis we shall use the newest method[7] for balancing chemical equations founded by virtue of theory of complex finite dimensional vector spaces. We chose it, because in this particular Garcia's case, it was the most suitable method for comparative analysis of chemical reactions which belong to different classes. Application of this method confirmed its scientific supremacy.

From (3.32) one obtains the scheme given below

	$\boldsymbol{v}_1 = FeS_2$	$\boldsymbol{v}_2 = HNO_3$	$\boldsymbol{v}_3 = Fe_2(SO_4)_3$	$\boldsymbol{v}_4 = NO$	$\boldsymbol{v}_5 = H_2SO_4$
Fe	1	0	2	0	0
S	2	0	3	0	1
H	0	1	0	0	2
N	0	1	0	1	0
O	0	3	12	1	4

The vector equation of reaction (3.32) is

$$x_1\boldsymbol{v}_1 + x_2\boldsymbol{v}_2 = x_3\boldsymbol{v}_3 + x_4\boldsymbol{v}_4 + x_5\boldsymbol{v}_5,$$

i. e.,

$$x_1\ (1, 2, 0, 0, 0)^T + x_2\ (0, 0, 1, 1, 3)^T = x_3\ (2, 3, 0, 0, 12)^T + x_4\ (0, 0, 0, 1, 1)^T + x_5\ (0, 1, 2, 0, 4)^T,$$

or

$$(x_1, 2x_1, x_2, x_2, 3x_2)^T = (2x_3, 3x_3 + x_5, 2x_5, x_4, 12x_3 + x_4 + 4x_5)^T.$$

The system of linear equations

$$x_1 = 2x_3,\ 2x_1 = 3x_3 + x_5,\ x_2 = 2x_5,\ x_2 = x_4,\ 3x_2 = 12x_3 + x_4 + 4x_5,$$

is inconsistent, because one obtains the contradiction $x_5 = x_1/2$ and $x_5 = -x_1$. It means that the vectors $\boldsymbol{v}_1$, $\boldsymbol{v}_2$, $\boldsymbol{v}_3$, $\boldsymbol{v}_4$ and $\boldsymbol{v}_5$ of molecules of the chemical reaction (3.32) are linearly independent and they do not generate a vector space V over $\Re$. By this we showed that the chemical reaction (3.32) is unfeasible.

On the other hand, the rank of the reaction matrix $\boldsymbol{A}$ of the chemical reaction (3.32) is

$$r = rank\boldsymbol{A} = rank\begin{bmatrix} 1 & 0 & 2 & 0 & 0 \\ 2 & 0 & 3 & 0 & 1 \\ 0 & 1 & 0 & 0 & 2 \\ 0 & 1 & 0 & 1 & 0 \\ 0 & 3 & 12 & 1 & 4 \end{bmatrix} = 5$$

According to the algebraic criterion (2.6) for balancing chemical reactions, the reaction (3.32), has *nullity*$\boldsymbol{A}$ $= n - r = 5 - 5 = 0$, that means that the reaction (3.32) is unfeasible. Both proofs, vector and algebraic, confirmed the same, that the reaction (3.32) is unfeasible. It contradicts the García's »*procedure*« named as »*half–reaction method*« for balancing chemical reactions.

Now, we shall consider the reaction (3.33) in its unbalanced form

$$x_1\ FeS_2 + x_2\ HNO_3 \rightarrow x_3\ Fe_2(SO_4)_3 + x_4\ NO + x_5\ H_2SO_4 + x_6\ H_2O \quad (3.34)$$

Now, we need the stoichiometric scheme for the above chemical reaction. From this particular reaction (3.34), we shall derive very easy required stoichiometric scheme

	$\boldsymbol{v}_1 = FeS_2$	$\boldsymbol{v}_2 = HNO_3$	$\boldsymbol{v}_3 = Fe_2(SO_4)_3$	$\boldsymbol{v}_4 = NO$	$\boldsymbol{v}_5 = H_2SO_4$	$\boldsymbol{v}_6 = H_2O$
Fe	1	0	2	0	0	0
S	2	0	3	0	1	0
H	0	1	0	0	2	2
N	0	1	0	1	0	0
O	0	3	12	1	4	1

From the above scheme one obtains this vector equation

$$x_1\boldsymbol{v}_1 + x_2\boldsymbol{v}_2 = x_3\boldsymbol{v}_3 + x_4\boldsymbol{v}_4 + x_5\boldsymbol{v}_5 + x_6\boldsymbol{v}_6,$$

i. e.,

$$x_1\ (1, 2, 0, 0, 0)^T + x_2\ (0, 0, 1, 1, 3)^T = x_3\ (2, 3, 0, 0, 12)^T + x_4\ (0, 0, 0, 1, 1)^T + x_5\ (0, 1, 2, 0, 4)^T + x_6\ (0, 0, 2, 0, 1)^T,$$

or

$$(x_1, 2x_1, x_2, x_2, 3x_2)^T = (2x_3, 3x_3 + x_5, 2x_5 + 2x_6, x_4, 12x_3 + x_4 + 4x_5 + x_6)^T.$$

The solution of the system of linear equations

$$x_1 = 2x_3,\ 2x_1 = 3x_3 + x_5,\ x_2 = 2x_5 + 2x_6,$$
$$x_2 = x_4,\ 3x_2 = 12x_3 + x_4 + 4x_5 + x_6,$$

is

$$x_2 = 5x_1,\ x_3 = x_1/2,\ x_4 = 5x_1,$$
$$x_5 = x_1/2 \text{ and } x_6 = 2x_1. \qquad (3.35)$$

If we substitute (3.35) in (3.34), and after that, if we divide the reaction by $x_1/2$ one obtains (3.33). The vectors $\boldsymbol{v}_1$, $\boldsymbol{v}_2$, $\boldsymbol{v}_3$, $\boldsymbol{v}_4$, $\boldsymbol{v}_5$ and $\boldsymbol{v}_6$ of reaction molecules are linearly dependent and they generate a vector space V over $\Re$. By this we confirmed that the reaction (3.33) has a unique solution.

Similarly as in the previous equation analysis, now we can go to the next step. Now we can calculate the rank of the reaction matrix $\boldsymbol{A}$ of the reaction (3.33).

Therefore, we can express its rank in this way

$$r = rank\boldsymbol{A} = rank\begin{bmatrix} 1 & 0 & 2 & 0 & 0 & 0 \\ 2 & 0 & 3 & 0 & 1 & 0 \\ 0 & 1 & 0 & 0 & 2 & 2 \\ 0 & 1 & 0 & 1 & 0 & 0 \\ 0 & 3 & 12 & 1 & 4 & 1 \end{bmatrix} = 5$$

According to the algebraic criterion (2.6) for balancing chemical equations, the reaction matrix $\boldsymbol{A}$ has $nullity\boldsymbol{A} = n - r = 6 - 5 = 1$. By this, again we showed that chemical reaction (3.33) has a unique solution. The analysis of the reaction (3.33), established that it belongs to the type of solvable equations, which have a unique solution.

This comparative analysis confirmed that García's half–reaction simple »*method*«[53] is completely wrong. Generally speaking, his so–called »*method*« cannot recognize the type of reaction, and much less to decide if the chemical equation is solvable or not. To support it, we shall give a dozen of counterexamples, where water molecules in García's procedure of reaction extension (3.33), may be substituted by other molecules of the elements involved in the reaction (3.32), as it is exposed by the following reactions

$$2\ FeS_2 + 8\ HNO_3 \rightarrow Fe_2(SO_4)_3 + 8\ NO + H_2SO_4 + 3\ H_2,$$
$$2\ FeS_2 + 14\ HNO_3 \rightarrow Fe_2(SO_4)_3 + 14\ NO + H_2SO_4 + 6\ H_2O_2,$$
$$10\ FeS_2 + 34\ HNO_3 \rightarrow 5\ Fe_2(SO_4)_3 + 22\ NO + 5\ H_2SO_4 + 12\ NH_2,$$
$$14\ FeS_2 + 50\ HNO_3 \rightarrow 7\ Fe_2(SO_4)_3 + 38\ NO + 7\ H_2SO_4 + 12\ NH_3,$$
$$10\ FeS_2 + 34\ HNO_3 \rightarrow 5\ Fe_2(SO_4)_3 + 22\ NO + 5\ H_2SO_4 + 6\ N_2H_4,$$
$$10\ FeS_2 + 34\ HNO_3 \rightarrow 5\ Fe_2(SO_4)_3 + 26\ NO + H_2SO_4 + 4\ (NH_4)_2SO_3,$$
$$14\ FeS_2 + 50\ HNO_3 \rightarrow 7\ Fe_2(SO_4)_3 + 38\ NO + H_2SO_4 + 6\ (NH_4)_2SO_4,$$
$$4\ FeS_2 + 16\ HNO_3 \rightarrow 2\ Fe_2(SO_4)_3 + 13\ NO + 2\ H_2SO_4 + 3\ NH_4O,$$
$$34\ FeS_2 + 130\ HNO_3 \rightarrow 17\ Fe_2(SO_4)_3 + 106\ NO + 17\ H_2SO_4 + 12\ (NH_4)_2O.$$

Neither one of the above reactions nor chemical reaction (3.33) is equivalent to the chemical reaction (3.32). Therefore, reactions (3.32) and (3.33) are incompatible.

In a similar way, García considered the following two reactions[53].

Example 3. 16. The following chemical reaction

$$x_1\ CrI_3 + x_2\ KOH + x_3\ Cl_2 \rightarrow x_4\ K_2CrO_4 + x_5\ KIO_3 + x_6\ KCl, \qquad (3.36)$$

he »*balanced*« like this

$$2\ CrI_3 + 52\ KOH + 21\ Cl_2 \rightarrow 2\ K_2CrO_4 + 6\ KIO_3 + 42\ KCl + 26\ H_2O. \qquad (3.37)$$

On top of all he said: *This method is appropriate to balance any kind of reaction, even those that include complex ions or reactions of compounds with oxidation numbers difficult to determine.*

By the same analysis which we used in the previous counterexample, very easy we shall show the absurdity of his statement.

Reaction (3.36) belongs to the type of unfeasible reaction. Its stoichiometric matrix $\boldsymbol{A}$ has rank $r = rank\boldsymbol{A} = 6$ and its $nullity\boldsymbol{A} = n - r = 6 - 6 = 0$ verifies that it is an unfeasible reaction. Also, this reaction generates an inconsistent system of linear equations which has only a trivial solution $x_i = 0$, $(1 \leq i \leq 6)$. Thus, this algebraic criterion verifies that the reaction (3.36) is unfeasible too.

Reaction (3. 37) generates a consistent system of linear equations which has a unique solution given in (3.37). Also, the $nullity\boldsymbol{A} = n - r = 7 - 6 = 1$, shows that this equation has a unique solution. Therefore, reactions (3.36) and (3.37) are incompatible, because they are two completely different types of reactions – the first one is an unfeasible reaction, while the second one is a unique reaction.

Now, we shall mention just two chemical reactions, where water molecules in García's »*procedure*« of reaction extension (3.37), are substituted by other molecules of the elements involved in the reaction (3.36):

$$2\ CrI_3 + 26\ KOH + 8\ Cl_2 \rightarrow 2\ K_2CrO_4 + 6\ KIO_3 + 16\ KCl + 13\ H_2,$$
$$2\ CrI_3 + 26\ KOH + 21\ Cl_2 \rightarrow 2\ K_2CrO_4 + 6\ KIO_3 + 16\ KCl + 26\ HCl.$$

Neither one of the above reactions nor chemical reaction (3.37) is equivalent to the chemical reaction (3.36). Therefore, reactions (3.36) and (3.37) are incompatible.

In the same paper, García considered two ionic reactions too. Unfortunately, also in these particular cases the same absurdity appears again.

Example 3.17. For example, he »*balanced*« an unfeasible reaction

$$x_1\ IO_3^- + x_2\ Br^- \rightarrow x_3\ IO_2^- + x_4\ Br_2, \qquad (3.38)$$

where $x_i = 0$ $(1 \leq i \leq 4)$ as a unique reaction

$$IO_3^- + 2\ Br^- + 2\ H^+ \rightarrow IO_2^- + Br_2 + H_2O. \quad (3.39)$$

Reactions (3.38) and (3.39) are two completely different reactions and they are incomparable!

A second ionic example that García considered is given in the next example.

Example 3.18. The reaction

$$x_1\ ClO^- + x_2\ P_4 \rightarrow x_3\ H_2PO_4^- + x_4\ Cl^-, \quad (3.40)$$

is »*balanced*« like this

$$10\ ClO^- + P_4 + 2\ H_2O + 4\ OH^- \rightarrow 4\ H_2PO_4^- + 10\ Cl^-. \quad (3.41)$$

Where is the hydrogen atom in the left side of (3.40)? Reaction (3.40) is an *absurd*, because it does not contain hydrogen atom in its left side. **With this kind of reactions current chemistry does not work!**

Reaction (3.41) does not dependent on (3.40) and it represents a solvable equation. In other words, reactions (3.40) and (3.41) are completely different types of reactions and they are incompatible.

VII. In[54] the so–called »*formal balance numbers*« (FBN) are introduced like this: *Formal balance numbers are an aid that may grossly facilitate the problem of balancing complex redox equations. They may be chosen as being equal to the traditional values of oxidation numbers, but not necessarily. An inspection of the redox equation may suggest the optimal values that are to be assigned to formal balance numbers. In most cases, these optimal values ensure that only two elements will* '*change their state*' (*i. e. the values of the formal balance numbers*), *allowing the use of the oxidation number technique for balancing equations, in its simplest form. Just as for oxidation numbers, the algebraic sum of the formal balance numbers in a molecule/neutral unit is* 0, *while in an ion it is equal to its charge* (*the sum rule*).

It was quickly detected that the »*procedure*« given in[54] boils down to using of well–known *unconventional oxidation numbers*, which previously were advocated by Tóth[55] and Ludwig[56].

Consider this sentence from previous definition: *They may be chosen as being equal to the traditional values of oxidation numbers, but not necessarily.* It is a *paradox*! If the »*formal balance numbers*« can be the same as *oxidation numbers* or not, then the whole definition is illogical. This definition represents only a contradictory premise, which does not have any correlation with balancing chemical equations. It is just one thing.

Another thing, the above definition does not speak anything about balancing chemical reactions in a chemical sense of the word, or their solution in a mathematical sense.

Recent research[7] confirmed that **a chemical equation can be balanced if and only if it generates a vector space**. That is a necessary and sufficient condition for balancing a chemical equation!

The so–called **called** »*formal balance numbers*«, which actually are the same as the well–known *oxidation numbers*, **do not represent any criterion for balancing chemical equations**.

Also the author of[54] asserted that his »*procedure*« *is probably the fastest of all possible* ***methods***! Obviously the author omitted to *prove* it. **Perhaps, his statement is valid (if he can prove it?) in some metachemistry, but from a viewpoint of current mathematics and chemistry it is not true**. Why? The reason is very simple. In mathematics, as well as in chemistry there is neither a definition for speed of equation solution nor its unit, and according to it, it is impossible to compare which method is faster. It is just one thing; another thing is that the definition of so–called »*formal balance numbers*« (FBN)[54] is paradoxical and it produces only inconsistent procedure for balancing chemical equations. According to it, the author's assertion of[54] is an absurd.

The »*procedure*«[54] founded by virtue of so–called »*formal balance numbers*« (FBN), with several counterexamples was refuted in[7].

VIII. Ten Hoor in[57] obtained this result:

$$C + x\ O_2 \rightarrow 2(1 - x)\ CO + (2x - 1)\ CO_2, \quad (3.42)$$
$$(1/2 \leq x \leq 1)$$

if the coefficient of a product is allowed to be equal to zero. Taking x equal to its smallest or largest extreme value, equation (3.42) *reduces to*

$$C + 1/2\ O_2 \rightarrow CO, \quad (3.43)$$

or

$$C + O_2 \rightarrow CO_2, \quad (3.44)$$

respectively.

The above statement is wrong. The reaction (3.42) holds if only if $1/2 < x < 1$, like it is shown on Fig. 2, but not as it is given in[57].

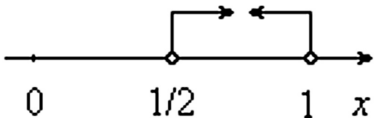

Figure 2: The interval $1/2 < x < 1$

In (3.42) x does not have any extreme value, because it is presented by the following linear functions: x, $2 - 2x$ and $2x - 1$. None of these functions have extrema, since their second derivatives are equal to zero. Then on what basis ten Hoor[57] states that for smallest or largest extreme value of x the reaction (3.42) reduces to (3.43) and (3.44) respectively?

The chemical reaction (3.42) has two subgenerators $2 - 2x$ and $2x - 1$ which generate the following particular cases:

1° For $x = 1$, then (3.42) reduces to

$$C + O_2 \rightarrow CO_2.$$

2° For $x = 1/2$, then (3.42) becomes

$C + 1/2\ O_2 \rightarrow CO$.

3° For $x < 1/2$, then (3.42) transforms into

$$C + x\ O_2 + (1 - 2x)\ CO_2 \rightarrow 2(1 - x)\ CO,$$

4° For $x > 1$, then from (3.42) one obtains

$$C + x\ O_2 + (2x - 2)\ CO \rightarrow (2x - 1)\ CO_2,$$

5° For $1/2 < x < 1$, holds this reaction

$$C + x\ O_2 \rightarrow 2(1 - x)\ CO + (2x - 1)\ CO_2.$$

Next, for the reaction (3.42) we shall determine its minimal coefficients by using of Moore–Penrose generalized inverse matrix[46].

From the chemical reaction (3.42) follows this scheme

	C	O	CO	CO_2
C	1	0	–1	–1
O	0	2	–1	–2

According to the above scheme, the reaction matrix $\boldsymbol{A}$ of (3.42) has this form

$$\boldsymbol{A} = \begin{bmatrix} 1 & 0 & -1 & -1 \\ 0 & 2 & -1 & -2 \end{bmatrix}$$

The Moore–Penrose generalized inverse matrix $\boldsymbol{A}^+$ is

$$\boldsymbol{A}^+ = \boldsymbol{A}^{\mathrm{T}}(\boldsymbol{A}\,\boldsymbol{A}^{\mathrm{T}})^{-1} = \begin{bmatrix} 1/2 & -1/6 \\ -1/3 & 1/3 \\ -1/3 & 0/0 \\ -1/6 & -1/6 \end{bmatrix}$$

The reaction (3.42) reduces to this matrix form

$$\boldsymbol{A}\boldsymbol{x} = \boldsymbol{0}, \qquad (3.\ 45)$$

where $\boldsymbol{x} = (x_1, x_2, x_3, x_4)^{\mathrm{T}}$ is the vector of the coefficients of (3.42), $\boldsymbol{0} = (0, 0)^{\mathrm{T}}$ is the zero vector and T denoting transpose.

The general solution of the matrix equation (3.45) is

$$\boldsymbol{x} = (\boldsymbol{I} - \boldsymbol{A}^+\boldsymbol{A})\boldsymbol{a}, \qquad (3.46)$$

where $\boldsymbol{a}$ is an arbitrary vector and $\boldsymbol{I}$ is a unite matrix. For $\boldsymbol{a} = (1, 1, 1, 1)^{\mathrm{T}}$, one obtains

$$\boldsymbol{x}_{min} = (4/3,\ 1,\ 2/3,\ 2/3)^{\mathrm{T}}.$$

Then the reaction (3.42) with its minimal coefficients attains this form

$$4/3\ C + O_2 \rightarrow 2/3\ CO + 2/3\ CO_2,$$

but not as ten Hoor asserted in[57]. By this proof we have shown that his statement is paradoxical.

Also, the assumptions 1 and 2 which ten Hoor used in[57] are completely wrong, because carbon burns according to the Boudouard's reaction[58]. Wrong suppositions can not lead to correct results.

IX. Authors of the article[59] studied several chemical reactions, but unfortunately there are given lots of erroneous results.

Let us mention them. In their article[59] they provided the following wrong definition: *a chemical equation is a written representation of a chemical reaction, showing the reactants and products, they physical states, and the direction in which the reaction proceeds*.

According to the above definition a chemical equation will show like this

$$a\ A_{(s)} + b\ B_{(g)} \rightarrow c\ C_{(s)} + d\ D_{(g)}. \qquad (3.47)$$

For instace, if $r = s = 2$ in (2.1), then as a particular case appears the reaction (3.47). Actually, *it is not a definition for a chemical equation*, just opposit it is *a definition for a chemical reaction*. Obviously the authors can not distinguish what is a *chemical reaction* and what is its *chemical equation*. These two things are different entities given by the Definitions 2.2 and 2.1 (in a descriptive form), *i.e.*, 2.11 (in an analitical form), respectively. It is just one reason what the above definition is wrong.

In order to be balanced certain chemical reaction is not necessary to be known its reactants and products as it is described in the above definition! It holds if only if reaction is given in a conventional form, but in an opposite case it does not hold. For instace, the chemical reaction (3.47) given in a convntional form can be presented in an algebrical free form too

$$a\ A_{(s)} + b\ B_{(g)} + c\ C_{(s)} + d\ D_{(g)} = 0. \qquad (3.48)$$

After determination of its coefficients, one obtains that some of them have a negative sign and others have a positive sign. Positive coefficients stay in front of reactants and negative coefficients stay in front of products of reaction, that means that chemical reaction is self–adaptive. For example, in[48] are balanced chemical reactions given in an algebrical free form.

Next, we shall give an another reason why the above definition is wrong.

Chemical equation does not have arrow mark as a reaction, just sign for equality. It is a main difference between chemical reaction and chemical equation.

More accurately speaking, **any chemical reaction has a chemical equation, but the opposite does not hold**. Why?

Next, we shall give an explanation about it by a new example. Let us balance the following chemical reaction

$$x_1\ Pb_2O_3 + x_2\ C \rightarrow x_3\ Pb_{0.987}O + x_4\ Pb_3O_4 + x_5\ CO + x_6\ CO_2. \qquad (3.49)$$

From the above reaction follows this system of linear equations

$$\begin{gathered} 2\ x_1 = 0.987\ x_3 + 3\ x_4, \\ 3\ x_1 = x_3 + 4\ x_4 + x_5 + 2\ x_6, \\ x_2 = x_5 + x_6. \end{gathered} \qquad (3.50)$$

In order to avoid fractional coefficients of the system (3.50), we shall multiply its first equation by 1000, such that one obtains this system of linear equations

$$\begin{gathered} 2000\ x_1 = 987\ x_3 + 3000\ x_4, \\ 3\ x_1 = x_3 + 4\ x_4 + x_5 + 2\ x_6, \\ x_2 = x_5 + x_6. \end{gathered} \tag{3.51}$$

The systems (3.50) and (3.51) are equivalent and they have same solution.

Now, according to the system (3.51) the chemical reaction (3.49) will transform into this particular form

$$\begin{gathered} x_1\ Pb_{2000}O_3 + x_2\ C \rightarrow x_3\ Pb_{987}O \\ + x_4\ Pb_{3000}O_4 + x_5\ CO + x_6\ CO_2. \end{gathered} \tag{3.52}$$

Do the expression (3.52) is a correct chemical reaction? No! It represents only an ordinary chemical absurd, because the molecules $Pb_{2000}O_3$, $Pb_{987}O$ and $Pb_{3000}O_4$ do not exist in chemistry. This is the cause why from chemical equation does not follow chemical reaction.

Chemical reactions (3.49) and (3.52) in a mathematical sense both are equivalent reactions, since they reduce to the same system of linear equations, but in a chemical sense they are not equivalent reactions. That means, that

math. equivalency ≠ chem. equivalency.

In other words, from a mathematical point of view, the systems (3.50) and (3.51) both are equivalent, but from a chemical view point they are not, since they generate different chemical reactions.

The above explanation, we can articulate roughly on this way: performing of reaction is a chemical subject, and its balancing is a mathematical topic. This is the reason why balancing of chemical reactions is pure mathematical matter, but not a chemical issue.

Next, we shall continue with the balancing of the reaction (3.49), because its general solution is necessary for a comparative analysis of other particular chemical reactions.

The general solution of the system (3.50) is

$$\begin{gathered} x_4 = 2\ x_1/3 - 0.329\ x_3, \\ x_5 = -\ x_1/3 + 2\ x_2 - 0.316\ x_3, \\ x_6 = x_1/3 - x_2 + 0.316\ x_3, \end{gathered} \tag{3.53}$$

where x_i, $(1 \leq i \leq 3)$ are arbitrary real numbers.

Balanced reaction has this form

$$\begin{gathered} x_1\ Pb_2O_3 + x_2\ C \rightarrow x_3\ Pb_{0.987}O \\ + (2\ x_1/3 - 0.329\ x_3)\ Pb_3O_4 \\ + (-\ x_1/3 + 2\ x_2 - 0.316\ x_3)\ CO \\ + (x_1/3 - x_2 + 0.316\ x_3)\ CO_2, \end{gathered} \tag{3.54}$$

where x_i, $(1 \leq i \leq 3)$ are arbitrary real numbers.

Since x_4, x_5 and x_6 are > 0, then from (3.54) one obtains this system of inequalities

$$\begin{gathered} 2\ x_1/3 - 0.329\ x_3 > 0, \\ -\ x_1/3 + 2\ x_2 - 0.316\ x_3 > 0, \\ x_1/3 - x_2 + 0.316\ x_3 > 0. \end{gathered} \tag{3.55}$$

From (3.55), we obtain this relation

$$3\ x_2 - 0.948\ x_3 < x_1 < 6\ x_2 - 0.948\ x_3. \tag{3.56}$$

The inequality (3.56) is necessary and sufficient condition to hold the general reaction (3.54).

Now, we can analyze the general reaction (3.54) for all possible values of x_1, x_2 and x_3. As particular reactions of (3.54) we shall derive the following cases.

1° For $x_1 = 3$, $x_2 = 2.4$ and $x_3 = 4.5$, from (3.53) follows $x_4 = 0.5195$, $x_5 = 2.378$ and $x_6 = 0.022$, *i.e.*, one obtains this particular reaction

$$\begin{gathered} 3\ Pb_2O_3 + 2.4\ C \rightarrow 4.5\ Pb_{0.987}O \\ + 0.5195\ Pb_3O_4 + 2.378\ CO \\ + 0.022\ CO_2. \end{gathered} \tag{3.57}$$

2° For $x_1 = 0$, the reaction (3.54) transforms into this particular reaction

$$\begin{gathered} 0.329\ x_3\ Pb_3O_4 + x_2\ C \rightarrow x_3\ Pb_{0.987}O \\ + (2\ x_2 - 0.316\ x_3)\ CO \\ + (-\ x_2 + 0.316\ x_3)\ CO_2, \\ (0.158\ x_3 < x_2 < 0.316\ x_3). \end{gathered} \tag{3.58}$$

3° For $x_2 = 0.158\ x_3$, from (3.58) one obtains

$$\begin{gathered} 0.329\ Pb_3O_4 + 0.158\ C \rightarrow Pb_{0.987}O \\ + 0.158\ CO_2. \end{gathered} \tag{3.59}$$

4° For $x_2 = 0.316\ x_3$, the reaction (3.58) becomes

$$\begin{gathered} 0.329\ Pb_3O_4 + 0.316\ C \rightarrow Pb_{0.987}O \\ + 0.316\ CO. \end{gathered} \tag{3.60}$$

5° For $x_2 < 0.158\ x_3$, from (3.58) follows

$$\begin{gathered} 0.329\ x_3\ Pb_3O_4 + x_2\ C + (0.316\ x_3 - 2\ x_2)\ CO \\ \rightarrow x_3\ Pb_{0.987}O + (-\ x_2 + 0.316\ x_3)\ CO_2, \end{gathered} \tag{3.61}$$

where x_2 and x_3 are arbitrary real numbers.

6° For $x_2 > 0.316\ x_3$, the reaction (3.58) becomes

$$\begin{gathered} 0.329\ x_3\ Pb_3O_4 + x_2\ C + (x_2 - 0.316\ x_3)\ CO_2 \\ \rightarrow x_3\ Pb_{0.987}O + (2\ x_2 - 0.316\ x_3)\ CO, \end{gathered} \tag{3.62}$$

where x_2 and x_3 are arbitrary real numbers.

7° For $x_2 = 0$, from (3.54) one obtains this particular reaction

$$\begin{gathered} x_1\ Pb_2O_3 + (x_1/3 + 0.316\ x_3)\ CO \\ \rightarrow x_3\ Pb_{0.987}O + (2\ x_1/3 - 0.329\ x_3)\ Pb_3O_4 \\ + (x_1/3 + 0.316\ x_3)\ CO_2, \end{gathered} \tag{3.63}$$

where x_1 and x_3 are arbitrary real numbers.

From (3.63) follows these inequalities

$$x_1/3 + 0.316\ x_3 > 0 \text{ and } 2\ x_1/3 - 0.329\ x_3 > 0.$$

From this system follows this inequality

$$-\ x_1/0.048 < x_3 < 2\ x_1/0.987. \tag{3.64}$$

The reaction (3.63) holds if only if the inequality (3.64) is satisfied.

8° For $x_1 < 0.4935\ x_3$, from (3.63) follows

$$\begin{gathered} x_1\ Pb_2O_3 + (0.329\ x_3 - 2\ x_1/3)\ Pb_3O_4 + (x_1/3 + \\ 0.316\ x_3)\ CO \rightarrow x_3\ Pb_{0.987}O \\ + (x_1/3 + 0.316\ x_3)\ CO_2, \end{gathered} \tag{3.65}$$

where x_1 and x_3 are arbitrary real numbers.

9° For $x_1 = 0.4935\ x_3$, from (3.63) follows

$$\begin{gathered} 0.4935\ Pb_2O_3 + 0.4805\ CO \\ \rightarrow Pb_{0.987}O + 0.4805\ CO_2. \end{gathered} \tag{3.66}$$

10° For $x_3 = 0$, from (3.54) one obtains this particular reaction

$$x_1\ Pb_2O_3 + x_2\ C \rightarrow (2\ x_1/3)\ Pb_3O_4 + (-\ x_1/3 + 2\ x_2)\ CO + (x_1/3 - x_2)\ CO_2, \quad (3.67)$$
$$(3\ x_2 < x_1 < 6\ x_2).$$

11° For $x_1 = 3\ x_2$, from (3.67) follows

$$3\ Pb_2O_3 + C \rightarrow 2\ Pb_3O_4 + CO. \quad (3.68)$$

12° For $x_1 = 6\ x_2$, from (3.67) one obtains

$$6\ Pb_2O_3 + C \rightarrow 4\ Pb_3O_4 + CO_2. \quad (3.69)$$

13° For $x_1 < 3\ x_2$, from (3.67) follows

$$x_1\ Pb_2O_3 + x_2\ C + (x_2 - x_1/3)\ CO_2 \rightarrow (2\ x_1/3)\ Pb_3O_4 + (-\ x_1/3 + 2\ x_2)\ CO, \quad (3.70)$$

where x_1 and x_2 are arbitrary real numbers.

14° For $x_1 > 6\ x_2$, the reaction (3.67) transforms into

$$x_1\ Pb_2O_3 + x_2\ C + (x_1/3 - 2\ x_2)\ CO \rightarrow (2\ x_1/3)\ Pb_3O_4 + (x_1/3 - x_2)\ CO_2, \quad (3.71)$$

where x_1 and x_2 are arbitrary real numbers.

The authors of the article[59] gave this statement: *Balancing the chemical equation* (*with three molecules*) *means finding the* ***smallest whole*** *numbers* x_1, x_2 *and* x_3 (*as its coefficients*).

The above statement does not hold for every reaction. It has just particular meaning and holds if only if a chemical reaction has atoms with integers, in an opposite case, when the reaction contains atoms with fractional oxidation numbers, it does not hold. For example, see the previous reactions (3.57), (3.58) and so on.

Also, in the article[59] is »*balanced*« this reaction

$$x_1\ Cu + x_2\ HNO_3 \rightarrow x_3\ Cu^{+2} + x_4\ NO_2 + x_5\ NO_3^- + x_6\ H_2O, \quad (3.72)$$

like this

$$3\ Cu + 4\ HNO_3 \rightarrow 3\ Cu^{+2} + 2\ NO + 2\ NO_3^- + 2\ H_2O. \quad (3.73)$$

The last reaction (3.73) is wrong.

The correct form of balanced reaction (3.72) is

$$x_1\ Cu + x_2\ HNO_3 \rightarrow x_1\ Cu^{+2} + (x_2/2)\ NO_2 + (x_2/2)\ NO_3^- + (x_2/2)\ H_2O, \quad (3.74)$$

where x_1, $x_2 > 0$ are arbitrary real numbers.

Next reaction was »*balanced*« in[59] too

$$x_1\ OH^- + x_2\ SnO_2^{-2} + x_3\ Bi(OH)_3 \rightarrow x_4\ Bi + x_5\ SnO_3^{-2} + x_6\ H_2O, \quad (3.75)$$

in this form

$$0\ OH^- + 3\ SnO_2^{-2} + 2\ Bi(OH)_3 \rightarrow 2\ Bi + 3\ SnO_3^{-2} + 3\ H_2O. \quad (3.76)$$

The general form of the reaction (3.75) is

$$x_1\ OH^- + x_2\ SnO_2^{-2} + (2x_2/3 - x_1/3)\ Bi(OH)_3 \rightarrow (2x_2/3 - x_1/3)\ Bi + x_2\ SnO_3^{-2} + x_2\ H_2O,\ (x_1 < 2x_2). \quad (3.77)$$

For $x_1 = 0$ and $x_2 = 3$, from (3.77) immediately follows (3.76), like a particular reaction.

Another reaction is »*balanced*« in[59]

$$x_1\ CH_3CH_2OH + x_2\ Cr_2O_7^{-2} + x_3\ H^+ \rightarrow x_4\ CH_3CO_2H + x_5\ Cr^{+3} + x_6\ H_2O, \quad (3.78)$$

in this form

$$3\ CH_3CH_2OH + 2\ Cr_2O_7^{-2} + 16\ H^+ \rightarrow 3\ CH_3CO_2H + 4\ Cr^{+3} + 11\ H_2O. \quad (3.79)$$

The general form of the reaction (3.78) is

$$x_1\ CH_3CH_2OH + x_2\ Cr_2O_7^{-2} + (-\ 4x_1 + 14\ x_2)\ H^+ \rightarrow x_1\ CH_3CO_2H + 2x_2\ Cr^{+3} + (-\ x_1 + 7\ x_2)\ H_2O, \quad (3.80)$$
$$(0 < x_1 < 7x_2/2).$$

For $x_1 = 3$ and $x_2 = 2$, from (3.80) immediately follows (3.79), like a particular reaction.

In[59] the authors only determined the particular reactions (3.76) and (3.79), but considered reactions (3.75) and (3.78) have general forms with two arbitrary parameters, given by (3.77) and (3.80), respectively.

X**.** As a last paradox we discovered in the theory of balancing chemical equations is the case considered below. The authors of the article[60] studied this chemical reaction

$$CH_{0.686}O_{0.32} + w\ H_2O + m\ O_2 + 3.76\ m\ N_2 \rightarrow x_1\ H_2 + x_2\ CO + x_3\ CO_2 + x_4\ H_2O + x_5\ CH_4 + 3.76\ m\ N_2. \quad (3.81)$$

Immediately from (3.81) we have seen its absurdity. In this reaction H_2O appears as a reactant and as a product at the same time. Is it logical? No! It is just one thing.

Another illogical thing is not reacted N_2. Nitrogen appears in (3.81) as reactant $3.76m\ N_2$ and $3.76m\ N_2$ as a product at the same time.

Also, the treatment of hydrogen as a product is illogical. Burning of $CH_{0.686}O_{0.32}$ presented by (3.81) does not give H_2 as a product!

We think that the reaction

$$x_1\ CH_{0.686}O_{0.32} + x_2\ O_2 + x_3\ N_2 \rightarrow x_4\ CO + x_5\ CO_2 + x_6\ H_2O + x_7\ CH_4 + x_8\ N_2O_3, \quad (3.82)$$

which represents a correct version of (3.81) is very interesting for chemistry.

From (3.82) one obtains this scheme

	$CH_{0.686}O_{0.32}$	O_2	N_2	CO	CO_2	H_2O	CH_4	N_2O_3
C	1	0	0	–1	–1	0	–1	0
H	0.686	0	0	0	0	–2	–4	0
O	0.32	2	0	–1	–2	–1	0	–3
N	0	0	2	0	0	0	0	–2

Reaction matrix $\boldsymbol{A}$ of (3.82) has this form

$$\boldsymbol{A} = \begin{bmatrix} 1.000 & 0 & 0 & -1 & -1 & 0 & -1 & 0 \\ 0.686 & 0 & 0 & 0 & 0 & -2 & -4 & 0 \\ 0.320 & 2 & 0 & -1 & -2 & -1 & 0 & -3 \\ 0.000 & 0 & 2 & 0 & 0 & 0 & 0 & -2 \end{bmatrix}$$

The reaction (3.82) reduces to the following system of linear equations

$$\begin{gathered} x_1 = x_4 + x_5 + x_7, \\ 0.686\ x_1 = 2\ x_6 + 4\ x_7, \\ 0.32\ x_1 + 2\ x_2 = x_4 + 2\ x_5 + x_6 + 3\ x_8, \\ 2\ x_3 = 2\ x_8. \end{gathered} \tag{3.83}$$

The general solution of the system (3.83) is

$$\begin{gathered} x_5 = 1.977\ x_1/4 + x_2/2 - 3\ x_3/4 - 3\ x_4/4, \\ x_6 = -\ 1.337\ x_1/2 + x_2 - 3\ x_3/2 + x_4/2, \\ x_7 = 2.023\ x_1/4 - x_2/2 + 3\ x_3/4 - x_4/4, \\ x_8 = x_3, \end{gathered} \tag{3.84}$$

where $x_i > 0$ $(1 \le i \le 4)$ are arbitrary real numbers.

Since $x_i > 0$ $(5 \le i \le 8)$, then from (3.84) one obtains this system of inequalities

$$\begin{gathered} 1.977\ x_1 + 2\ x_2 - 3\ x_3 - 3\ x_4 > 0, \\ -\ 1.337\ x_1 + 2\ x_2 - 3\ x_3 + x_4 > 0, \\ 2.023\ x_1 - 2\ x_2 + 3\ x_3 - x_4 > 0. \end{gathered} \tag{3.85}$$

From (3.85) immediately follows this inequality

$$1.337\ x_1 - x_4 < 2\ x_2 - 3\ x_3 < 2.023\ x_1 - x_4. \tag{3.86}$$

Reaction (3.82) holds if and only if the condition (3.86) is satisfied.

The reaction (3.82) contains three subgenerators which induce a topology of its solutions, but we omitted it, since it will be a subject of the author's next research.

The other particular cases of (3.82) are not considered because we took into account the Remark 3.7.

For instance, for $x_1 = 2$, $x_2 = 4$, $x_3 = 2$ and $x_4 = 1$, from (3.84) one obtains this particular solution $x_5 = 0.7385$, $x_6 = 0.163$, $x_7 = 0.2615$ and $x_8 = 2$. Then (3.82) becomes

$$\begin{gathered} 2\ CH_{0.686}O_{0.32} + 4\ O_2 + 2\ N_2 \rightarrow CO \\ + 0.7385\ CO_2 + 0.163\ H_2O \\ + 0.2615\ CH_4 + 2\ N_2O_3. \end{gathered}$$

Now, we shall determine the minimal coefficients of the reaction (3.82). The Moore–Penrose generalized matrix $\boldsymbol{A}^+$ will have this form

$$\boldsymbol{A}^+ = \begin{bmatrix} 0.334436538275454 & -0.037800281937753 \\ -0.164755899838609 & 0.019118215665491 \\ 0.123566924878957 & -0.014338661749118 \\ -0.338363333974391 & 0.077822527216911 \\ -0.255985384055086 & 0.068263419384166 \\ 0.257141220018618 & -0.145193039626989 \\ -0.071214743695069 & -0.183886228538830 \\ 0.123566924878957 & -0.014338661749118 \end{bmatrix}$$

$$\begin{bmatrix} -0.048377720464309 & 0.036283290348232 \\ 0.171516759260828 & -0.128637569445621 \\ -0.128637569445621 & 0.346478177084216 \\ -0.003380429711109 & 0.002535322283332 \\ -0.089138809341523 & 0.066854107006142 \\ -0.104876595295905 & 0.078657446471929 \\ 0.044141518588323 & 0.033106138941242 \\ -0.128637569445621 & -0.153521822915784 \end{bmatrix}$$

The reaction (3.82) reduces to the matrix form (3.45), whose general solution is given by the expression (3.46).

For $\boldsymbol{a} = (1, 1, 1, 1, 1, 1, 1, 1)^T$, one obtains

$$\boldsymbol{x}_{min} = (x_1, x_2, x_3, x_4, x_5, x_6, x_7, x_8)^T,$$

where

$$\begin{gathered} x_1 = 1.241594646560723466, \\ x_2 = 1.574780831709873263, \\ x_3 = 0.568914376217595052, \\ x_4 = 0.721001830633894027, \\ x_5 = 0.433611414778957395, \\ x_6 = 0.251904161474584061, \\ x_7 = 0.086981401147872044, \\ x_8 = 0.568914376217595052. \end{gathered}$$

5 DISCUSSION

We cannot always trust chemical experiments! We cannot always trust mathematics either, for it can mislead us unless we define away the problem area. However, we surely can trust pure logic – no questionable experiments or unusual mathematical operations.

Are they *methods* when somebody can find counterexamples on every step? Obviously, the answer is negative! It is merely a pale picture of the old chemically irrational traditionalism of the past chemistry.

As it is showed by all counterexamples given in this work the traditional procedures for balancing chemical reactions are inconsistent. These particular procedures, we hope that they are the last traditional unsuccessful approach of balancing chemical reactions. Long time ago chemistry lost the battle with mathematics in sense of balancing chemical reactions.

Before we finish this discussion, we would like to stress here, that our facts for arguing are founded by virtue of scientific results.

From current view point of balancing chemical equations, we feel free to tell that traditional approach of balancing chemical reactions is only a history, and Jones' problem[44], which was as one of the hardest problems of balancing chemical reactions is completely solved[45].

There exists a completely satisfactory ways of avoiding paradoxes[7,34,45,46,48–50]. The theory used is based on the idea of formal approach of balancing chemical reactions. In these works completely new general highly sophisticated methods are developed for balancing chemical reactions and their stability by virtue of the theory of generalized matrix inverse using Moore–Penrose, Drazin and von Neumann matrices. By these methods chemistry is cleaned from old traditional inconsistent procedures for balancing chemical reactions, such that is open a brand new direction for development of this topic in chemistry and its foundation on genuine principles. That is the newest trend in chemistry about this issue, which showed that traditionalism in chemistry is over.

6 CONCLUSION

By this work the consideration of paradoxes in chemistry will begin very seriously as a special object and in any way it will increase researchers' carefulness to avoid the appearance of paradoxes. Sure, no perfect science! Appearance of paradoxes is always possible.

It is more than certain, that this work opened doors for the next research in chemistry for its diagnostic of paradoxes and their resolution. It will accelerate the newest contemporary research in chemistry and it will destroy all barriers which hamper the development of chemistry and lay its foundation on genuine scientific principles.

This work affirms:

- that all formally provable mathematical methods are true if chemical reactions are considered as a consistent formal system,
- that all mathematical truths can be formally provable, and
- that the new branch **Foundation of Chemistry** proves the consistency and completeness of the formal approach of balancing chemical reactions and that it will be a special kind of chemistry, *i.e.*, it will be a finite theory which contains only perfectly well known concepts with true axioms and positive conclusions. It affirms that the principles used in the mathematical approach of balancing chemical reactions, will not lead to contradictions.

After that, what is proven about the paradoxes in this work is there a *general chemistry*? Or it should be refounded on genuine principles as *elementary chemistry*?

The replies to these two questions are looking for deep reform in chemistry in a formalistic way, because in the opposite case paradoxes will be a stumbling block for a long time. To avoid this awkward position, reforms in chemistry are needed as soon as possible.

Sure, that the above topic is considered in a rough form, but it happens with every pioneer's job.

ACKNOWLEDGEMENT

The author would like to thank Prof. Dr Valery C. Covachev, from Bulgarian Academy of Sciences for reading the work and for his remarks which improved the quality of this work.

REFERENCES

[1] H. B. Curry, *Foundations of Mathematical Logic*, 2nd Ed., Dover Pub. Inc., New York 1977, pp. 3–8
[2] B. R. Gelbaum, J. M. H. Olmsted, *Counterexamples in Analysis*, Dover Pub. Inc., New York 2003
[3] G. L. Wise, E. B. Hall, *Counterexamples in Probability and Analysis*, Oxford Univ. Press, Oxford 1993
[4] J. P. Romano, A. F. Siegel, *Counterexamples in Probability and Statistics*, Chapman & Hall, New York – London 1986
[5] L. A. Steen, J. A. Seebach, Jr., *Counterexamples in Topology*, Dover Pub. Inc., New York 1995
[6] B. R. Gelbaum, J. M. H. Olmsted, *Theorems and Counterexamples in Mathematics*, Springer Vlg. New York, Inc., New York 1990
[7] I. B. Risteski, *A new complex vector method for balancing chemical equations*, Mat. & Technol. 44 (**2010**), 193–203
[8] E. H. Moore, *On the reciprocal of the general algebraic matrix*, Bull. Amer. Math. Soc. 26 (**1920**) 394–395
[9] R. Penrose, *A generalized inverse for matrices*, Proc. Cambridge Phil. Soc. 51 (**1955**), 406–413
[10] B. Bunch, *Mathematical Fallacies and Paradoxes*, Van Nostrand, New York 1982, p. 2
[11] J. W. Oliver, *Formal fallacies and other invalid arguments*, Mind 76 (**1967**), 463–478
[12] D. H. Sanford, *Contraries and subcontraries*, Noûs 2 (**1968**), 95–96
[13] E. J. Barbeau, *Mathematical Fallacies, Flaws, and Flimflam,* Math. Assoc. Amer., Washington DC 2000
[14] C. L. Hamblin, *Fallacies*, Methuen, London 1970, p. 12
[15] E. A. Maxwell, *Fallacies in Mathematics*, Cambridge Univ. Press, Cambridge 1959, p. 9
[16] R. M. Sainsbury, *Paradoxes*, 2nd Ed., Cambridge Univ. Press, Cambridge 2002, p. 1
[17] N. Rescher, *Paradoxes: Their Routs, Range and Resolution*, Open Court, Chicago 2001, p. 6
[18] Ch. S. Chihara, *The semantic paradoxes: A diagnostic investigation*, Philos. Rev. 88 (**1979**), 590–618
[19] W. V. Quine, *The Ways of Paradoxes*, Harvard Univ. Press, Cambridge Mass. 1966, p. 7
[20] R. A. Koons, *Paradoxes of Belief and Strategic Rationality*, Cambridge Univ. Press, Cambridge 1992, p. 8
[21] D. Davidson, *The Prussian blue paradox*, J. Chem. Educ. 14 (**1937**), 238–241
[22] F. Feigl, *Spot reaction experiments, Part VII: Chemical paradoxes*, J. Chem. Educ. 21 (**1944**), 347–353
[23] C. Levinthal, *Are there pathways for protein folding*? J. Chim. Phys. 65 (**1968**), 44–45
[24] C. K. Jørgensen, *Models and paradoxes in quantum chemistry*, Theor. Chim. Acta 34 (**1974**), 189–198
[25] J. A. Campbell, *Paradigms and paradoxes*, J. Chem. Educ. 57 (**1980**), 41–42

[26] C. K. Jørgensen, *New paradoxes of spin–pairing energy in gadolinium* (III), J. Less Common Metals 148 (**1989**), 147–150
[27] G. A. Patani, E. J. LaVoie, *Bioisosterism: A rational approach in drug design*, Chem. Rev. 96 (**1996**), 3147–3176
[28] D. L. Anderson, *The helium paradoxes*, Proc. Nat. Acad. Sci. USA 95 (**1998**), 4822–4827
[29] F. H. Chapple, *The temperature dependence of* ΔG° *and the equilibrium constant,* K_{eq}*; Is here a paradox*? J. Chem. Educ. 75 (**1998**), 342
[30] E. Vitz, M. J. Schuman, *The q/T paradox: which 'contains more heat', a cup of coffee at* 95°C *or a liter of icewater*? J. Chem. Educ. 82 (**2005**), 856–860
[31] Ch. G. McCarty, E. Vitz, *pH Paradoxes: demonstrating that it is not true that* $pH \equiv -\log[H^+]$, J. Chem. Educ. 83 (**2006**), 752–757
[32] J. M. R. Parrondo, in *EEC HC&M Network on Complexity and Chaos*, ISI, Torino, Italy, 1996, (unpublished)
[33] D. C. Osipovitch, C. Barratt, P. M. Schwartz, *Systems chemistry and Parrondo's paradox: computational models of thermal cycling*, New J. Chem. 33 (**2009**), 2022–2027
[34] I. B. Risteski, *A new pseudoinverse matrix method for balancing chemical equations and their stability*, J. Korean Chem. Soc. 52 (**2008**), 223–238
[35] O. F. Steinbach, *Non–stoichiometric equations*, J. Chem. Educ. 21 (**1944**), 66, 69
[36] W. T. Hall, *Non–stoichiometric equations*, J. Chem. Educ. 21 (**1944**), 201–202
[37] A. Lehrman, *Non–stoichiometric equations,* J. Chem. Educ. 21 (**1944**), 202–203
[38] A. Standen, *Some simple balancing*, J. Chem. Educ. 22 (**1945**), 461–462
[39] W. C. McGavock, *Non–stoichiometric equations*, J. Chem. Educ. 22 (**1945**), 269–270
[40] W. C. McGavock, *Organic Oxidation–Reduction Reactions*, 2nd Ed. San Antonio 1945, p. 135
[41] A. Porges, *A question of balancing*, J. Chem. Educ. 22 (**1945**), 266–267
[42] R. Harré, *Some presuppositions in the metaphysics of chemical reactions*, Found. Chem. 10 (**2008**) 19–38
[43] E. V. Krishnamurthy, *Generalized matrix inverse for automatic balancing of chemical equations,* Int. J. Math. Educ. Sci. Technol. 9 (**1978**), 323–328
[44] M. Jones, *Problem 71–25**: *Balancing chemical equations*, SIAM Rev. 13 (**1971**), 571
[45] I. B. Risteski, *A new approach to balancing chemical equations*, SIAM Problems & Solutions, (**2007**), 1–10
[46] I. B. Risteski, *The new algebraic criterions to even out the chemical reactions*, 22nd Oct. Meeting of Min. & Metall., Collection of Papers, Oct. 1–2, 1990, Bor, 313–318
[47] K. Gödel, *What is Cantor's continuum problem?* Amer. Math. Monthly 54 (**1947**), 515–527
[48] I. B. Risteski, *A new non–singular matrix method for balancing chemical equations and their stability*, Int. J. Math. Manuscripts 1 (**2007**), 180–205
[49] I. B. Risteski, *A new generalized matrix inverse method for balancing chemical equations and their stability*, Bol. Soc. Quím. Méx. 2 (**2008**), 104–115
[50] I. B. Risteski, *A new singular matrix method for balancing chemical equations and their stability*, J. Chin. Chem. Soc. 56 (**2009**), 65–79
[51] G. R. Blakley, *Chemical equations balancung*, J. Chem Educ. 59 (**1982**), 728–734
[52] S. C. Das, *A mathematical method of balancing a chemical equation*, Int. J. Math. Educ. Sci. Technol. 17 (**1986**), 191–200
[53] A. García, *A new method to balance chemical equations*, J. Chem Educ. 64 (**1987**), 247–248
[54] V. M. Petruševski, *A fast solution to the problem of balancing redox equations: Numbers introducing formal balance*, Glas. hem. tehnol. Makedonija 17 (**1998**), 141–145
[55] Z. Tóth, *On balancing 'redox challenges' by unconventional oxidation numbers*, J. Chem. Educ. 74 (**1997**), 1270
[56] O. Ludwig, *Balancing chemical equations*, J. Chem. Educ. 74 (**1997**), 1270–1271
[57] M. J. ten Hoor, *Chemical equations with a non–unique balance*, Chem NZ 105 (**2006**), 7–10
[58] A. F. Holleman, E. Wiberg, *Inorganic Chemistry*, Academic Press, Berlin – New York **2001**, pp. 810–811
[59] J. Croteau, W. P. Fox, K. Varazo, *Mathematical modeling of chemical stoichiometry*, PRIMUS 17 (**2007**), 301–315
[60] M. V. Ramanan, E. Lakshmanan, R. Sethumadhavan, S. Renganarayanan, *Performance prediction and validation of equilibrium modeling for gasification of cashew nut shell char*, Braz. J. Chem. Eng. 25 (**2008**), 585–601

UDK 669.14.018:620.172.251
Original scientific article/Izvirni znanstveni članek

ISSN 1580-2949
MTAEC9, 45(6)523(2011)

CHARACTERISTICS OF CREEP IN CONDITIONS OF LONG OPERATION

ZNAČILNOSTI LEZENJA PRI DOLGOTRAJNI UPORABI

Nikolay A. Katanaha[1], Leonid B. Getsov[2]

[1]Saint-Petersburg State Polytechnical University, Saint-Petersburg 194 021 Hlopina 13, Russia
NPO CKTI, 195213 St. Petersburg, 195213 Zanevski pr. 43 apt. 89, Russia
katanaha@mail.ru, guetsov@yahoo.com

Prejem rokopisa – received: 2011-07-28; sprejem za objavo – accepted for publication: 2011-10-20

The creep of materials is considered in various temperature ranges: at low, at elevated and at high temperatures. Different approaches of extrapolation of experimental data for creep curves are shown. For the available isochronous curves of steels R2M and EP291, the coefficients for the upgraded formula Soderberg were obtained. The isochronous creep curves and the curves with a partition into first and second stages were constructed by using the coefficients obtained. Calculation of the coefficients was performed using the computational mathematics package MathCad and OriginPro. The Arrhenius equation for description of the temperature dependence of creep rate in a narrow temperature range is presented.

The results of this work are a new method of determining the extrapolated values of material creep resistance relating to long-life, a verification of this method for experimental data of the steels R2M and EP291.

Key words: steel, creep, isochronous curves, creep curve, Norton formula, Soderberg formula, Arrhenius equation for a creep rate, steels R2M, EP291, 20Cr12WNiMoV

Lezenje materialov je obravnavano za različna območja temperatur: pri nizki, povišani in visoki temperaturi. Prikazani so različni načini ekstrapolacije eksperimentalnih podatkov s krivulj lezenja. Za razpoložljive izohrone krivulje za jekli R2LM in EP291 so bili določeni koeficienti za izboljšavo Soderbergove enačbe. Izohrone krivulje in krivulje z delitvijo na prvo in drugo stopnjo so oblikovane z upoštevanjem prve in druge faze in z uporabo določenih koeficientov. Koeficienti so izračunani z uporabo matematičnih izračunov na podlagi matematičnih paketov MathCad in OriginPro. Arheniusova enačba za odvisnost hitrosti lezenja od temperature je prikazana za ozko območje temperature.

Rezultati tega dela sta nova metoda za določanje ekstrapoliranih vrednosti odpornosti materiala proti lezenju pri dolgi uporabi in verifikacija metode na podlagi eksperimentalnih podatkov za jekli R2M in EP291.

Ključne besede: jeklo, lezenje, izohrone krivulje, krivulje lezenja, Nortonova enačba, Soderbergova enačba, Arheniusova odvisnost za hitrost lezenja, jekla R2M, EP291, 20Cr12WNiMoV

1 INTRODUCTION

The use of isochronous curves of creep in the strength calculations of details for power plants and necessary demands of increasing resource of these details up to 300 000 h or more, requires the need of resolving of several problems connected with the processing of experimental data of creep.

Considering the features of the steel creep in conditions of insignificant residual strain, the stress change over time can be neglected.

In these conditions creep should be considered in various temperature ranges:

a) At low temperatures. Creep is characterized by the first stage of transient creep. For example, further course of the creep process is almost inhibited with increasing time, leading to a lack of long damage at stresses less than the yield stress (**Figure 1a**);
b) At elevated temperatures. As test results of various materials show the rate of steady creep depends on the duration of tests: more time, lower slope of the creep curve. In this connection it should be recognized, that the adequacy of isochronous creep curves, obtained by extrapolation, is very low (**Figure 1b**). The corresponding curves are lower than those, which were obtained by direct experiment. It gives a conservative estimate of the deformation process details by soft loading. However, when the processes of stress relaxation are defined (hard load – uneasiness strain) and when the durability assessment is determined in accordance with the equivalent stress, we find higher values of durability and safety margins. These conditions are the material behavior at stress raisers, the stress relaxation at the high temperature fasteners, the redistribution of stresses in the steam pipeline bending, in the blades and turbine disks;
c) At high temperatures, as it is well known, the processes of diffusion creep take place without the first stage of creep (**Figure 1c**).

The second stage of creep is followed by the third (the stage of accelerated creep) depending on the deformation ability of the material and the stress level at the elevated and high temperatures.

2 EXPERIMENTAL

Consequently, using the experimental data of creep at the terminal duration, different approaches for the extrapolation should be taken into account.

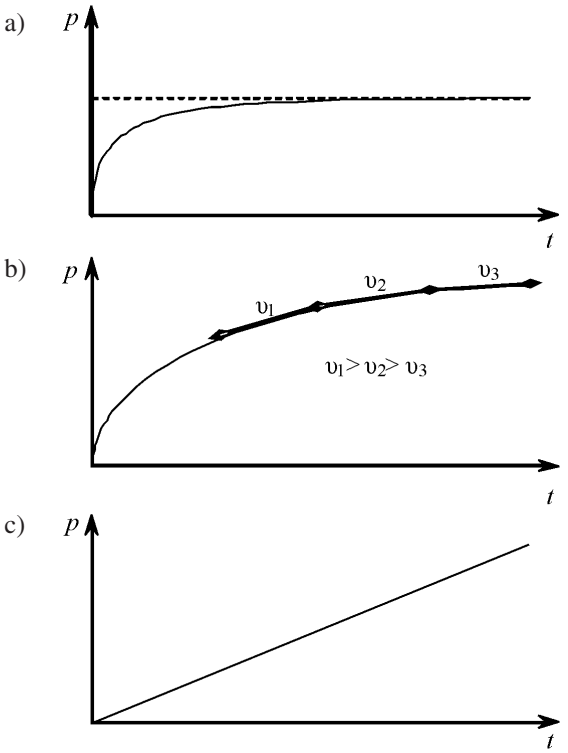

Figure 1: Schematic diagram of creepa) at low b) at elevated c) at high temperature
Slika 1: Shematična krivulja lezenja a) pri nizki, b) pri povišani in c) pri visoki temperature

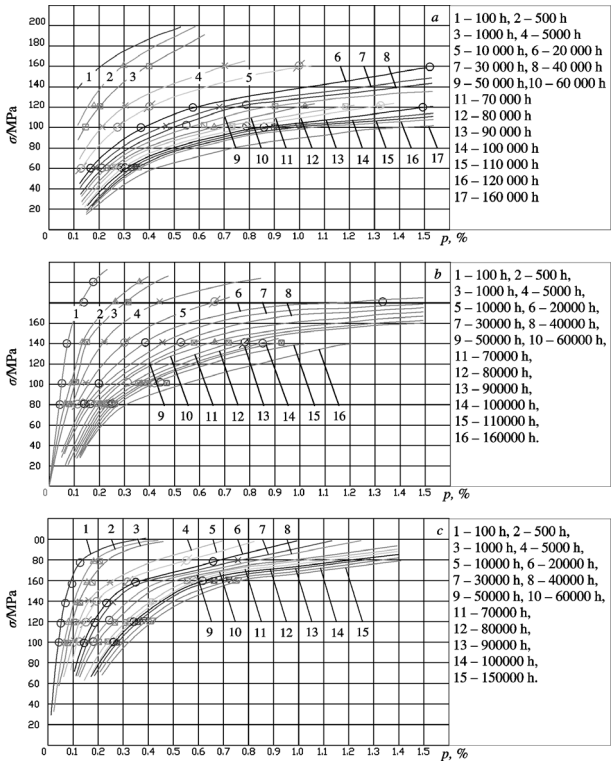

Figure 2: Approximation of the experimental creep data of the steel R2M at 500 °C (a), 525 °C (b) and 550 °C (c), presented in [1]
Slika 2: Aproksimacija eksperimentalnih podatkov za jeklo R2M pri 500 °C (a), 525 °C (b) in 550 °C, ref. [1]

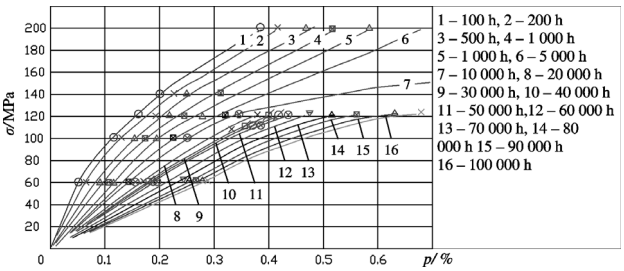

Figure 3: Approximation of the experimental creep data of the steel EP291 at 550 °C, presented in [1]

An adequate description of creep at low temperatures can be obtained by using the expression:

$$\dot{p} = a \cdot c \cdot \exp(-c \cdot t) \tag{1}$$

where: $a = A \cdot \sigma^{k}$, $c = C \cdot \sigma^{l}$ (σ – stress, t – time, A, C, k, l – constants, depending on temperature). For high temperatures, the Norton formula gives the consistent results:

$$\dot{p} = b \tag{2}$$

where: $b = B \cdot \sigma^{m}$ (σ – stress, B, m – constants, depending on temperature).

3 THE RESEARCH RESULTS

At elevated temperatures, at which details power plants operate usually, the use of sum (1) and (2) for determining the rate of creep:

$$\dot{p} = a \cdot c \cdot \exp(-c \cdot t) + b \tag{3}$$

is possible for time not exceeding the experimental. To solve the problem of extrapolation of the creep data of long duration, the experimental data of long duration have been used. These data have been received by A. A. Chizhik for the steel R2M pearlitic at 50 °C, 525 °C, 550 °C (**Figure 2**), the steels of martensitic class 18Cr11MoVNbNi (EP291) (**Figure 3**) and 20Cr12WNiMoV (**Figure 4**) at 550 °C [1].

Dependence of the duration of the first and second stages of creep has been determined in accordance with the test base for steel R2M (**Figure 5**) as well as for steel EP291.

Taking this in consideration, the use of the Norton formula with coefficients derived from a relatively short

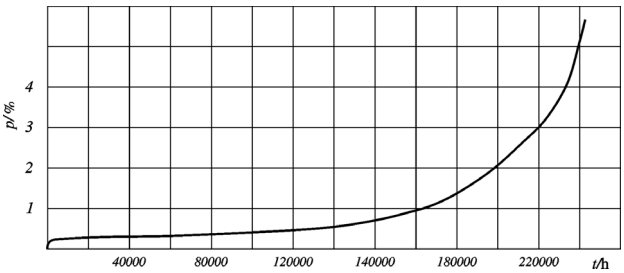

Figure 4: Creep curve of the steel 20Cr12WNiMoV at 550 °C
Slika 4: Krivulja lezenja za jeklo 20Cr12WNiMoV pri 550 °C

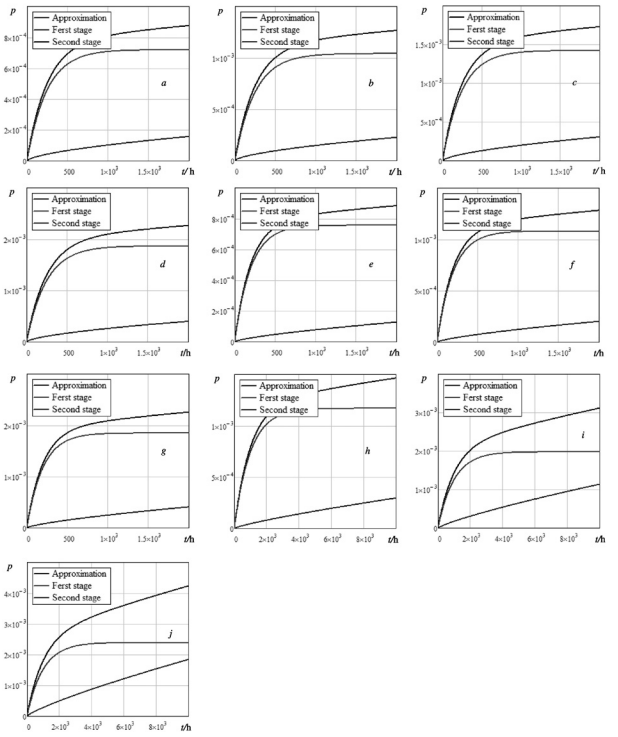

Figure 5: Duration of the first and second stages of creep for the steel R2M at 500 °C (*a* – 100 MPa, *b* – 120 MPa, *c* – 140 MPa, *d* – 160 MPa), 525 °C (*e* – 80 MPa, *f* – 100 MPa, *g* – 120 MPa), 550 °C (*h* – 60 MPa, *i* – 100 MPa, *j* – 120 MPa)

Slika 5: Trajanje prve in druge faze lezanja za jeklo R2M pri 500 °C (a- 100 MPa, b- 120 MPa, c- 140 MPa, d- 160 MPa), 525 °C (e- 80 MPa, f- 100 MPa, g- 120 MPa), 550 °C (h- 6a MPa, i- 100 MPa, j- 120 MPa)

duration of data, can give very significant errors in the calculation regarding the operation of equipment with very long lifetime (more than 100 000 h) both due to the neglect of the first stage of creep and the overrated values of the exponent *m*. The various attempts of description of this phenomenon led to the need to modify the Soderberg formula as:

$$p = a_1 \cdot \sigma^{a_2} \cdot (1 - \exp(-c_1 \cdot \sigma^{c_2} \cdot t)) + b_1 \cdot t^{b_2} \cdot \sigma^{b_2} \cdot t \quad (4)$$

where: (σ – stress, t – time, a_1, a_2, b_1, b_2, b_3, c_1, c_2 – constants depending on temperature).

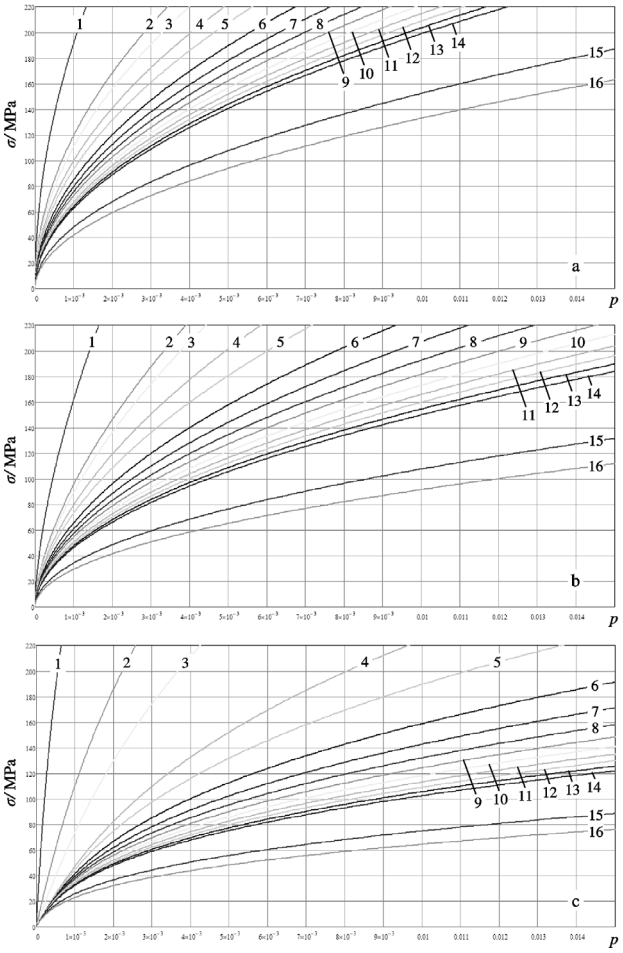

Figure 6: Isochronous curves of steel R2M at 500 °C (*a*), 525 °C (*b*) and 550 °C(*c*) 1 – 100 h; 2 – 500 h; 3 – 1 000 h; 4 – 5 000 h; 5 – 10 000 h; 6 – 20 000 h; 7 – 30 000 h; 8 – 40 000 h; 9 – 50 000 h; 10 – 60 000 h; 11 – 70 000 h; 12 – 80 000 h; 13 – 90 000 h; 14 – 100 000 h; 15 – 300 000 h; 16 – 500 000 h.

Slika 6:. Izohrone krivulje za jeklo R2M pri 500 °C (a), 525 °C (b), in 550 °C (c). 1 – 100 h; 2 – 500 h; 3 – 1 000 h; 4 – 5 000 h; 5 – 10000 h; 6 – 20 000 h; 7 – 30 000 h; 8 – 40 000 h; 9 – 50 000 h; 10 – 60 000 h; 11 – 70 000 h; 12 – 80 000 h; 13 – 90 000 h; 14 – 100 000 h; 15 – 300 000 h; 16 – 500 000 h.

The expression for the creep rate is:

$$\dot{p} = a_1 \cdot \sigma^{a_2} \cdot c_1 \cdot \sigma^{c_2} \cdot (1 - \exp(-c_1 \cdot \sigma^{c_2} \cdot t)) + b_1 \cdot t^{b_2} \cdot \sigma^{b_2} \quad (5)$$

Table 1: Values of the coefficients of equation (4)
Tabela 1: Vrednosti koeficientov enačbe (4)

	R2M						18Cr11MoVNbNi (EP291)	
	500 °C		525 °C		550 °C		550 °C	
	I	II	I	II	I	II	I	II
a_1	6.322E-8	1.402E-7	6.942E-7	1.314E-6	1.717E-5	1.043E-5	7.383E-6	6.626E-6
a_2	2.028	1.854	1.596	1.448	1.031	1.126	1.202	1.203
b_1	1.435E-10	8.803E-11	5.510E-11	9.066E-11	3.217E-12	4.293E-12	1.768E-7	2.059E-7
b_2	–3.752E-1	–3.915E-1	–2.784E-1	–2.914E-1	–1.843E-1	–1.554E-1	–5.973E-1	–6.215E-1
b_3	1.988	2.121	2.091	2.017	2.643	2.515	1.070	1.087
c_1	9.341E-5	6.374E-5	1.181E+8	6.662E-7	1.016E-3	1.175E-3	1.294E-5	2.718E-5
c_2	7.793E-1	8.868E-1	-5.270	-5.148	0	0	1.214	1.197
SD	1.937E-2	1.776E-2	2.796E-2	2.718E-2	1.290E-2	1.088E-2	6.917E-2	7.044E-2

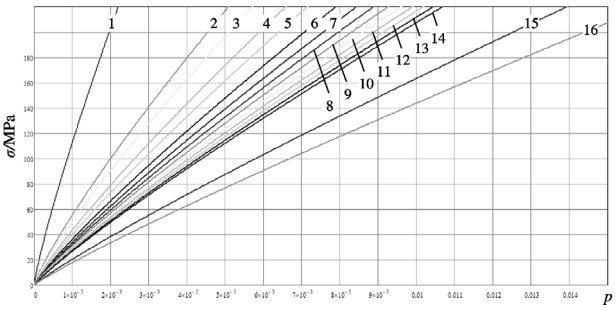

Figure 7: The isochronous curves of steel EP291 at 550 °C 1 – 100 h; 2 – 500 h; 3 – 1 000 h; 4 – 5 000 h; 5 – 10 000 h; 6 – 20 000 h; 7 – 30 000 h; 8 – 40 000 h; 9 – 50 000 h; 10 – 60 000 h; 11 – 70 000 h; 12 – 80 000 h; 13 – 90 000 h; 14 – 100 000 h; 15 – 300 000 h; 16 – 500 000 h

Slika 7: Izohromne krivulje za jeklo EP291 pri 550 °C 1 – 100 h; 2 – 500 h; 3 – 1 000 h; 4 – 5 000 h; 5 – 10 000 h; 6 – 20 000 h; 7 – 30 000 h; 8 – 40 000 h; 9 – 50 000 h; 10 – 60 000 h; 11 – 70 000 h; 12 – 80 000 h; 13 – 90 000 h; 14 – 100 000 h; 15 – 300 000 h; 16 – 500 000 h

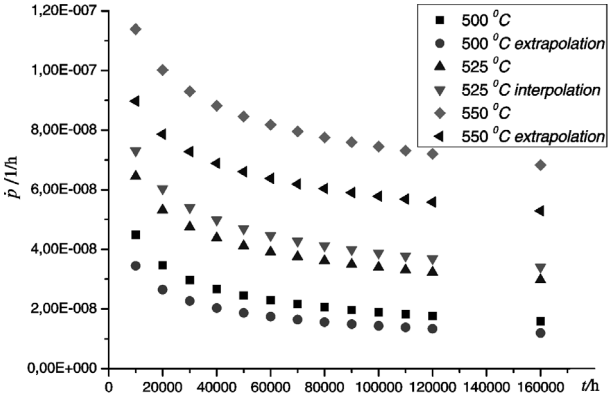

Figure 8: Comparison of experimental values of creep rate for the steel R2M with the extrapolated and interpolated values

Slika 8: Primerjava eksperimentalnih hitrosti lezenja za jeklo R2M z ekstrapoliranimi in interpoliranimi vrednostmi

The values of the coefficients of equation (4) for the investigated materials are given in **Table 1**. The coefficients are calculated in accordance with the minimum standard deviation for the experimental points and the proposed approximation. Calculation of the coefficients has been performed by means of the computational mathematics package MathCad and OriginPro.

The standard deviation has been used for comparing the results obtained during the calculation of the creep deformation with the original data calculated from:

$$SD = \frac{1}{n} \cdot \sum_{i=1}^{n} \left(\frac{y_i - y}{y_i} \right)^2 \qquad (6)$$

In some cases, the dependence (4) for certain values of the coefficients may give an inadequate representation of the isochronous curves of creep that has double bends. For example, this situation occurred during processing the experimental data for the steel R2M at 550 °C. In case of these incorrect results on the basis of the analysis, it is necessary to use of $c_2 = 0$ in equation (4).

Data in **Table 1** show, that SD values are at low level. The isochronous creep curves of steel have been built according to the values of the coefficients listed in **Table 1** (**Figure 6**).

Comparing **Figures 2 and 3** with **Figures 6 and 7**, we can see significant differences in the type of curves. It is related to the effectiveness of the proposed approximation by means of the dependence (4) and the use directly the experimental points for finding the values of the coefficients, rather than curves.

Unfortunately, methods of calculation that have been used for the calculated construction of the isochronous creep curves, were based on the unique experimental data of long duration obtained for a metal melting and these methods didn't make provision for the scatter of

Table 2: Creep rate

Tabela 2: Hitrost lezenja

t/ h	100 MPa					
	T = 500 °C	*T* = 500 °C extrapolation	*T* = 525 °C	*T* = 525 °C interpolation	*T* = 550 °C	*T* = 550 °C extrapolation
100	2,876E-07	1,538E-07	5,725E-07	7,713E-07	1,891E-06	1,070E-06
500	1,448E-07	2,392E-08	1,923E-07	4,535E-07	1,280E-06	2,490E-07
1 000	1,073E-07	1,590E-08	1,258E-07	3,124E-07	8,251E-07	1,454E-07
5 000	5,821E-08	4,107E-08	7,823E-08	9,236E-08	1,405E-07	1,023E-07
10 000	4,488E-08	3,451E-08	6,450E-08	7,310E-08	1,139E-07	8,969E-08
20 000	3,460E-08	2,650E-08	5,318E-08	6,039E-08	1,002E-07	7,860E-08
30 000	2,972E-08	2,270E-08	4,750E-08	5,401E-08	9,296E-08	7,276E-08
40 000	2,668E-08	2,034E-08	4,385E-08	4,990E-08	8,816E-08	6,888E-08
50 000	2,454E-08	1,867E-08	4,121E-08	4,693E-08	8,461E-08	6,602E-08
60 000	2,291E-08	1,742E-08	3,917E-08	4,463E-08	8,182E-08	6,376E-08
70 000	2,163E-08	1,642E-08	3,752E-08	4,278E-08	7,952E-08	6,192E-08
80 000	2,057E-08	1,561E-08	3,615E-08	4,123E-08	7,759E-08	6,036E-08
90 000	1,968E-08	1,492E-08	3,499E-08	3,992E-08	7,592E-08	5,903E-08
100 000	1,892E-08	1,433E-08	3,397E-08	3,878E-08	7,446E-08	5,785E-08

the data depending on the characteristics of melting and the variations in the mode of heat treatment. Thus the use of these methods in practice requires the application of certain stocks in the deformations (or the stresses).

Next step was getting a universal dependence of isochronous curves on temperature for any values (in a relatively narrow temperature range). The Arrhenius equation was used to describe the temperature dependence of creep rate in a narrow temperature range.

$$\dot{p}^{c} = \dot{p}_0 e^{-\frac{U}{RT}} \quad (7)$$

where
U – activation energy of creep,
$R = 8{,}32 \cdot 10^{-3}$ kJ/mol·K – gas constant,
$\dot{p}_0$ – constant.

Table 2 and **Figure 8** show the values of creep rate obtained in the experiment by means of extrapolation and interpolation on temperature.

The comparison of the experimental values of the creep rate with the extrapolated and interpolated values on temperature in dependence on time, showed that their differences were 3–30 % and quite acceptable.

4 CONCLUSION

The new method of determining the extrapolated values of material creep resistance related to long-life was proposed.

The verification techniques relating the experimental data obtained previously for the steels R2M and EP291 by A. A. Chizhik were made.

5 REFERENCES

[1] A. A. Lanin, V. S. Balina. Heat-resistant metals and alloys. EnergoTeh. Saint-Petersberg, 2006, 221 p.

[2] L. B. Getsov, H. A. Katanaha, I. P. Popova. Methods of calculation of the creep characteristics at the first and second stages on the basis of the test results on relaxation using a limited number of isochronous creep curves. Problems of mechanical engineering, 13 (**2010**) 6, 35–41

UDK 669.131.2:536.7
Original scientific article/Izvirni znanstveni članek

ISSN 1580-2949
MTAEC9, 45(6)529(2011)

A THERMODYNAMIC AND KINETIC STUDY OF THE SOLIDIFICATION AND DECARBURIZATION OF MALLEABLE CAST IRON

TERMODINAMIČNA IN KINETIČNA ANALIZA STRJEVANJA IN RAZOGLJIČENJA BELEGA LITEGA ŽELEZA

Miran Pirnat[1], Primož Mrvar[2], Jože Medved[2]

[1]SIJ, Acroni, d. o. o, Jesenice, Slovenia,
[2]University of Ljubljana, Faculty of Natural Sciences and Engineering, Department of Materials and Metallurgy, Aškerčeva 6, 1000 Ljubljana, Slovenia
miran.pirnat@acroni.si

Prejem rokopisa – received: 2011-04-05; sprejem za objavo – accepted for publication: 2011-10-05

An analysis of the solidification and decarburization of white-heart malleable cast iron (MCI) is presented. The solidification and decarburization courses were examined with simple and differential scanning calorimetry. The microstructure characteristics and the physical properties of the white-heart malleable cast iron changed during the decarburization process. Also, the electrical resistivity changed with the change of carbon contents and the macro-and microstructures. Based on this hypothesis, a measuring method for simultaneous measurements of the electrical resistivity and dimensional variations during the decarburization process of white-heart malleable cast iron was developed. In addition, a physico-mathematical model was developed to follow the carbon concentration and to determine the depths of the decarburization zone during the decarburization process. The decarburization process was presented as a function of the specific electrical conductivity, the carbon concentration and the decarburization time.

Keywords: white-heart malleable cast iron (MCI), thermal analysis,electrical resistivity, specific electrical resistivity, decarburization time, depth of decarburization zone

Članek opisuje spremljanje strjevanja in razogljičenja belega litega železa. Potek strjevanja in razogljičenja sta bila preiskana z enostavno in diferenčno vrstično kalorimetrijo. Med procesom razogljičenja belega litega železa se spreminjajo značilnosti zgradbe in fizikalne lastnosti. Prav tako se zaradi spremembe koncentracije ogljika ter makro- in mikrostrukture spreminja tudi električna upornost. Na tej hipotezi je bila razvita merilna metoda istočasnega merjenja električne upornosti in dimenzijskih sprememb med procesom razogljičenja belega litega železa. Razvit je fizikalno-matematični model, s katerim je možno med procesom razogljičenja spremljati koncentracijo ogljika in določiti globino razogljičenja. Potek procesa razogljičenja je prikazan kot funkcija specifične električne upornosti, koncentracije ogljika in časa razogljičenja.

Ključne besede: belo lito železo, termična analiza, električna upornost, specifična električna upornost, čas razogljičenja, globina razogljičenja

1 INTRODUCTION

White-heart malleable cast iron (MCI) was prepared from a chilled hypoeutectic iron alloy. Afterwards, it was decarburized to achieve adequate mechanical properties. The morphology of the solidified phases, the temperature regions of the corresponding reactions and the formed phases were determined with a thermodynamic analysis of the MCI solidification and decarburization process. The fraction of pearlite and the heat treatment[1] are essential to obtain the desired properties of the MCI. The following methods were used to examine the solidification process and solid-state transformations: simple thermal analyses (TA), dilatometric analyses, and simultaneous thermal analyses (DSC). An "in situ" measuring apparatus, as a part of the laboratory equipment, was also developed to follow the electrical resistivity during the decarburization process. The goal of the examination was to design a model for the "in situ" monitoring of the decarburization process by determining the carbon concentrations and the depths of decarburization zone. The thermal analyses could be used for the quality control of the MCI, since it made it possible to determine the metallurgical quality of the cast iron in the shortest possible time. The chemical composition and the nucleation conditions determined the obtained microstructure.[2–7] The simple thermal analysis made it possible to determine the reference liquidus temperature and the temperatures of the transformations and to forecast the latter properties of the castings.[8] In the solidification of the MCI it was important that all the remnant melt solidified entirely as a chill in the form of a cementite eutectic. The simple thermal analysis and dilatometric curves helped to examine the solidification process and the cooling of spheroidal-graphite cast iron (**Figure 1**).[9]

The as-cast MCI was decarburized in approximately 40 h in an oxidizing atmosphere at 1050 °C, when the cast microstructure changed with the reactions:

1. Formation of austenite:

$$(\alpha_{Fe} + Fe_3C) \rightarrow \gamma_{Fe}$$

2. Decomposition of cementite:

$$Fe_3C \rightarrow 3\gamma_{Fe} + C_{(malleablizedgraphite)}$$

3. Decarburization process:

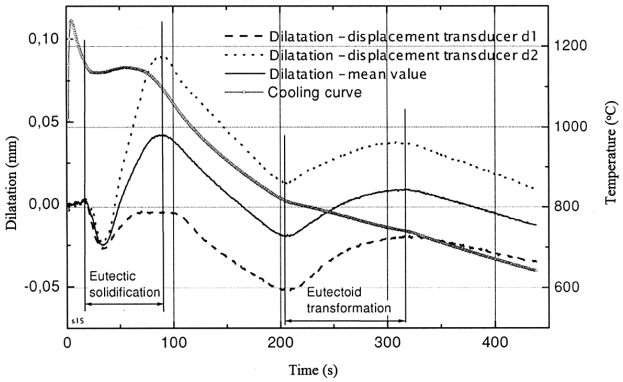

Figure 1: Cooling curve and dilatometric curves of slightly hypo-eutectic spheroidal graphite cast iron[9]

Slika 1: Ohlajevalna krivulja in dilatometrske krivulje podevtektske sive litine s kroglastim grafitom[9]

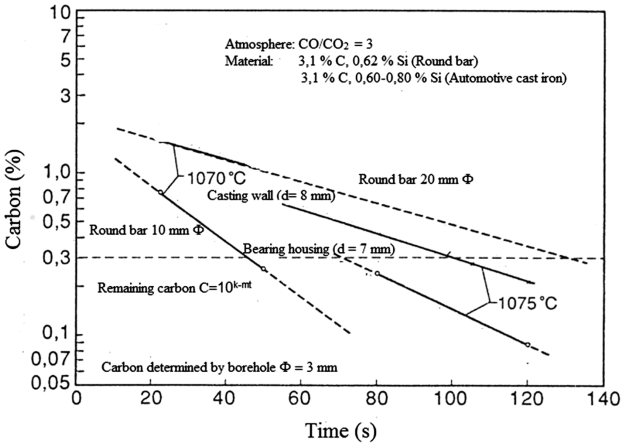

Figure 2: Relationship between the mass fraction of carbon and the decarburization time[12]

Slika 2: Odvisnost masnega deleža ogljika od časa razogljičenja[12]

$C_{(malleablized\ graphite)}$ and $[C]_{\gamma} + H_2O_{(g)} = CO_{(g)} + H_{2(g)}$

4. Precipitation of ferrite:

$$\gamma_{Fe} \rightarrow \alpha_{Fe}$$

5. Formation of pearlite:

$$\gamma_{Fe} \rightarrow (\alpha_{Fe} + Fe_3C)$$

6. Precipitation of graphite:

$$\alpha_{Fe} \rightarrow Graphite_{(tertiary)}$$

The decarburization proceeded predominantly by the reactions:

$$[C]_{\gamma\text{–}Fe} + H_2O_{(g)} = CO_{(g)} + H_{2(g)} \quad (1)$$

and

$$C_{malleablized\ graphite} + H_2O_{(g)} = CO_{(g)} + H_{2(g)} \quad (2)$$

The decarburization process of steel, such as electrical steel,[10,11] proceeded by the decarburization reaction (1). The decarburization process of MCI started with a carbon loss in austenite, $[C]_{\gamma\text{–}Fe}$ (reaction 1), and then it was continued by $C_{malleablized\ graphite}$ loss according to reaction (2) after the cementite decomposed according to reaction:

$$Fe_3C = 3\gamma_{Fe} + C_{malleablized\ graphite} \quad (3)$$

The decarburization process depends on the chemical composition of the decarburized material (steel or MCI), on the applied atmosphere,[10,11] the temperature and first of all on the wall thickness of the casting. For MCI it was also essential to know how the microstructure was influenced by the wall thickness.[12] The relationship between the mass fraction of carbon and the decarburization time is presented in **Figure 2**. The decarburization was achieved by annealing in the temperature range from 1070 °C to 1075 °C in a gas atmosphere with water vapor ($H_2O_{(g)}$), and the process consisted of carbon diffusion from the interior towards the surface of the MCI casting, of the water vapor transport to the surface of the MCI casting, the oxidation of MCI carbon on the surface of the MCI casting where proceeded and also the oxidation of iron and of the other elements. The relations between the decarburization time and the remaining carbon concentration in the MCI are represented by the following equations:[12]

$$\lg C = k - m \cdot t \quad (4)$$

$$C = 10^{k - m \cdot t} \quad (5)$$

$$t = \frac{k - \lg C}{m} \quad (6)$$

with:

C – remaining carbon concentration,

t – time,

k, m – constants

The microstructural characteristics and the physical properties of the malleable cast iron changed during the decarburization process. Due to changed carbon concentrations and changed macro- and microstructures the electrical resistivity also varied. The relationship between the electrical resistivity and the specific electrical resistivity applied for the calculations of the specific electrical resistivity during the MCI decarburization process are described with the equation:

$$\rho = R\frac{A}{l}\ (\Omega\ \text{m}) \quad (7)$$

where:

ρ = specific electrical resistivity of the specimen (Ω m)

R = electrical resistivity of the specimen (Ω)

A = cross-section of the specimen (mm^2)

l = length (mm)

Matthiessen's rule[13] describes the relation between the specific electrical resistivity and the temperature, as follows:

$$\rho(T) = \rho_0 + \rho_G(T) \quad (8)$$

where ρ_0 is a term that is independent of the temperature and takes into account the influence of the alloying elements and $\rho_G(T)$ is a temperature-dependent term.

2 EXPERIMENTAL

"In-situ" simple thermal and dilatometric analyses of the same alloy were made in industrial conditions. The "in-situ" measuring equipment is presented in **Figure 3**.[14]

A sample for chemical analysis was taken after each measurement and for laboratory decarburization. For an easier comparison, some of those specimens were decarburized together with industrial castings in industrial conditions, while the others were prepared only for laboratory decarburization tests. The chemical analyses of the as-cast cast irons and of the decarburized specimens were made after "in-situ"dilatometrical measurements, thermal analyses and differential scanning calorimetry to follow how the electrical resistivity varied during the laboratory decarburization process.The chemical compositions of the as-cast cast iron samples were evaluated and are presented in **Tables 1 and 2**.

The measurements of the electrical resistivity and of the dimensional changes were performed with laboratory equipment to follow the variations of the electrical resistivity of the MCI specimens during the decarburization process at 1050 °C, 1075 °C and 1100 °C for periods of (12, 24 and 48) h in atmospheres of argon, CO_2, N_2 and $N_2 + H_2O$. **Figure 4** shows the used equipment.

The Olympus BX 1 optical microscope with the DP 70 video camera and the analySIS 5.0 software for analyzing micrographs was used in the metallographic examinations. Multiple image alignment (MIA), a method of stitched overview, was applied to determine the microstructural constituents and the variation of their fractions with the distance from the surface of the specimens. The microstructural components were determined across the specimen's cross-section from the center (x = 0) towards the edge (x = 2 500 μm). The distance from the center to the edge of the specimens decarburized in laboratory conditions was divided into five sections, each was 500 μm long. The microstructural changes and the variations in the microstructural constituents were determined in each section. Afterwards, the single pictures were stitched into a joint picture.

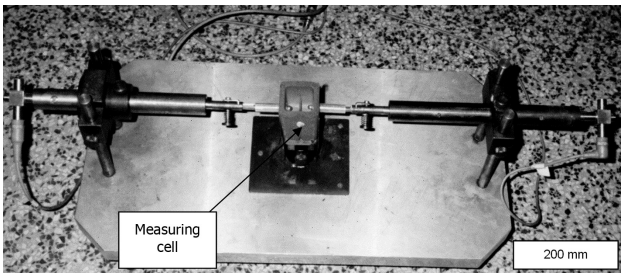

Figure 3: Equipment for "in situ" simple thermal and dilatometric analyses with the measuring cell[14]

Slika 3: Naprava za enostavno termično in dilatometrijsko analizo z merilno celico[14] "in situ"

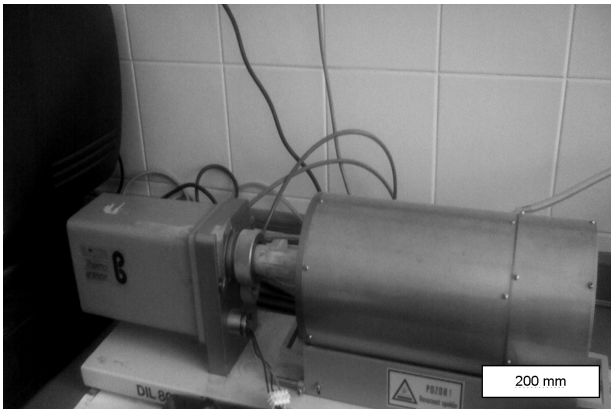

Figure 4: Laboratory equipment for measuring electrical resistivity, and performing dilatometric analyses during the decarburization process

Slika 4: Posnetek naprave za izvedbo meritev električne upornosti in dilatometrijske analize pri razogljičenju

3 RESULTS AND DISCUSSION

The simple thermal analysis was applied to record the cooling curves and the curves of the dimensional changes of specimens Nos. 1, 2, 3 and 4. In addition, characteristic temperatures of the solidification and of the transformations were determined, too. The cooling curve with the marked characteristic temperatures for the

Table 1: Chemical compositions of as-cast cast iron samples, including the C+Si sum and the Mn/S ratio *w*/%

Tabela 1: Kemijska sestava vzorcev 1, 2, 3, 4, vsota C + Si in Mn/S v masnih deležih

Chemical composition in mass fractions, *w*/%									
Sample	C	Si	Mn	S	Al	P	Cr	C+Si	Mn/S
1.	2.8405	0.9174	0.5026	0.1952	0.0010	0.0321	0.0395	3.7579	2.5748
2.	3.0633	0.9549	0.5005	0.1879	0.0024	0.0321	0.0396	4.0182	2.6637
3.	3.0032	0.9305	0.4991	0.2132	0.0009	0.0323	0.0398	3.9337	2.3410
4.	3.0259	0.9368	0.5045	0.1818	0.0004	0.0312	0.0040	3.9627	2.7750

Table 2: Chemical compositions of as-cast cast iron samples prepared for laboratory decarburization, including the C+Si sum and the Mn/S ratio

Tabela 2: Kemijska sestava vzorcev belega litega železa za razogljičenje z vsoto C + Si in razmerjem Mn/S v masnih deležih, *w*%

Chemical composition in mass fractions, *w*/%								
C	Si	Mn	S	Al	P	Cr	C+Si	Mn/S
2.99	0.85	0.49	0.17	0.004	0.0321	0.04	3.84	2.88

specimen No. 3 is presented in **Figure 5**. It shows that the solidification started at 1280 °C with the precipitation of primary austenite (L → γ_{Fe}) and continued until the temperature of the eutectic reaction (L → (γ_{Fe} + Fe_3C)) at 1154 °C. After the eutectic reaction was completed, the cooling continued in the solid state down to the eutectoid reaction (γ_{Fe} → (α_{Fe} + Fe_3C)) at 740 °C. Afterwards, the cooling continued and no further changes were detected on the cooling curve. The liquidus and solidus temperatures of all the specimens, i.e., of Nos. 1, 2, 3 and 4, were collected and are presented in **Table 3** with the results of the differential scanning calorimetry. Next to characteristic temperatures, the reaction enthalpies were determined also.

Figure 6a presents the heating curves of industrially cast specimens, i.e., of the initial specimen, and of the decarburized specimen with 0.18 % C. Both curves exhibit the exothermic and endothermic peaks of the eutectoid transformation (γ_{Fe} → α_{Fe} + Fe_3C); (α_{Fe} + Fe_3C → γ_{Fe}) at 757 °C and 752 °C. Both peaks were much more pronounced with the initial specimen since the enthalpy of transformation was –16.48 J/g, while the enthalpy of transformation in the decarburized specimen was much smaller, only –3.632 J/g. The melting of the initial specimen (blue line) commenced at 1139 °C with the solidification of the (γ_{Fe} + Fe_3C → L) eutectic, and it continued with the melting of the primary austenite (γ_{Fe} → L) at 1188 °C.

The melting enthalpy was at –1 34.2 J/g. In the decarburized specimen (red line) no melting of the eutectic (γ_{Fe} + Fe_3C → L) was detected. After the eutectoid transformation (α_{Fe} + Fe_3C → γ_{Fe}) at 752 °C, the heating was continued until the primary austenite melted (γ_{Fe} → L) at 1 331 °C, then the peritectic reaction (γ_{Fe} + L → δ_{Fe}) proceeded at 1 452 °C and the δ-ferrite melted (δ_{Fe} → L) at 1 479 °C.

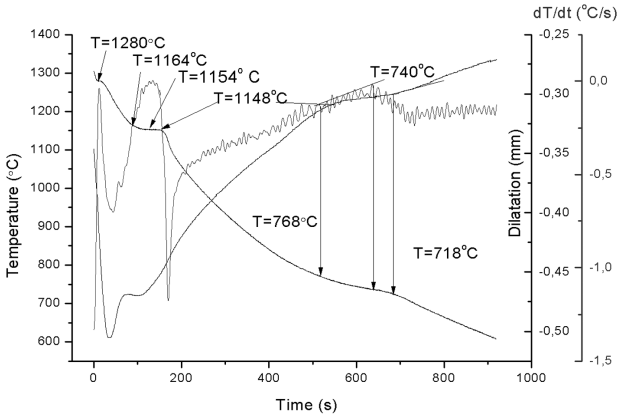

Figure 5: Dilatometric and cooling curve and derivative of the cooling curve with marked temperatures of the solidification start, of the eutectic solidification and of the eutectoid transformation for sample No. 3

Slika 5: Dilatometrijska in ohlajevalna krivulja z odvodom ohlajevalne krivulje s temperaturami začetka in evtektičnega strjevanja ter evtektoidne premene za vzorec 3

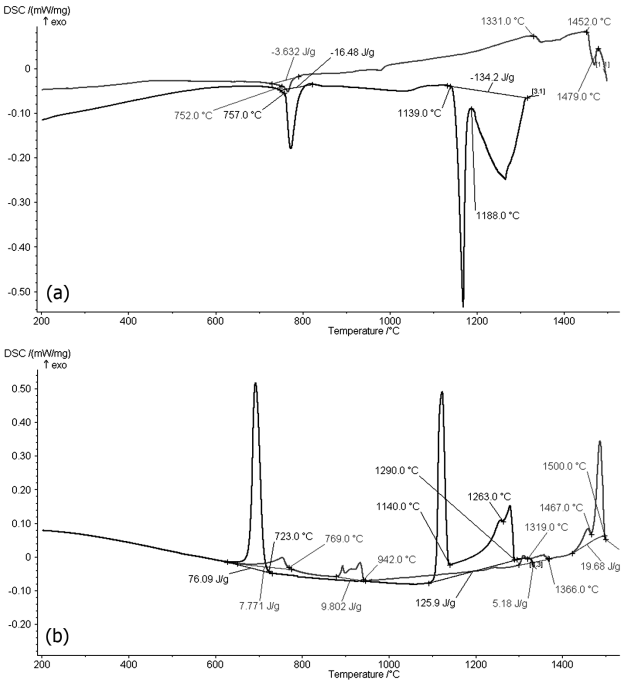

Figure 6: Heating (a) and cooling curves (b) of the as-cast specimen (blue), and specimen with mass fraction of C 0.18 %, decarburized in industrial conditions (red), obtained by differential scanning calorimetry

Slika 6: a) Segrevalni in b) ohlajevalni krivulji diferenčne vrstične kalorimetrije; modro: izhodno lito stanje; rdeče: industrijsko razogljičeni vzorec z masnim deležem C 0,18 %

Figure 6b presents the cooling of the initial (blue line) and of the decarburized specimen (red line). The solidification of the decarburized specimen started at 1500 °C with precipitation of the δ-ferrite (L → δ_{Fe}). The peritectic reaction (δ_{Fe} + L→ γ_{Fe}) at 1467 °C, at 1366 °C the peak of formation of primary austenite (L → γ_{Fe}), at 942 °C the peak of formation of hypoeutectoid ferrite from austenite (γ_{Fe} → α_{Fe}) and at 769 °C a smaller peak of eutectoid transformation (γ_{Fe} → α_{Fe} + Fe_3C) were detected. The melting enthalpy was 19.68 J/g, and of eutectoid transformation 7.771 J/g.

The solidification of the basic specimen started at 1290 °C with the precipitation of the primary austenite (L → γ_{Fe}) and it was completed at 1140 °C with eutectic reaction or the solidification of the eutectic (L → γ_{Fe} + Fe_3C), respectively. At 723 °C a big exothermic peak of eutectoid transformation (γ_{Fe} → α_{Fe} + Fe_3C) appeared. The enthalpy of solidification was 125.9 J/g, and of eutectoid transformation was 76.09 J/g.

Figure 7 shows the results of measurements of the electrical resistivity and of the dimensional changes during decarburization of specimen No. 8. The decarburization proceeded at 1100 °C for 12 hours in the N_2+H_2O atmosphere. The obtained value of the electrical resistivity after heating to the decarburization temperature of 1100 °C was 0.2725 Ω and it was constantly dropping as the decarburization continued. After 40 000 s of decarburization, the electrical resistivity dropped to 0.2525 Ω.

Table 3: Characteristic temperatures obtained with simple thermal analysis (TA) and differential scanning calorimetry (DSC) in °C
Tabela 3: Značilne temperature TA in DSC v stopinjah Celzija

	Temperatures of solidification and phase transformations in solid state					
	TA				DSC	
Solidification and phase transformations in solid state	Specimen				Decarburized specimen in industrial conditions, containing mass fraction of C 0.18 %	As-cast specimen
	1	2	3	4		
$L \rightarrow \delta_{Fe}$					1 500	
$\delta_{Fe} + L \rightarrow \gamma$					1 467	
$L \rightarrow \gamma_{Fe}$		1 280	1 280	1 281	1 366	1 290
$L \rightarrow (\gamma_{Fe} + Fe_3C)$	1 158	1 154	1 154	1 154		1 140
$\gamma_{Fe} \rightarrow \alpha_{Fe}$					942	
$\gamma_{Fe} \rightarrow \alpha_{Fe} + Fe_3C)$	740	738	740	733	769	723

With a lowering of the electrical resistivity dimensional changes occurred. The dimensional changes dropped from 400 µm at the beginning of the decarburization process to 120 µm at the end of the process.

Figure 8 presents the changes of the microstructure and of the fractions of the microstructural constituents as a function of the distance x from the center of the specimen to its edge. The stitched metallographic image presents the microstructures and the fractions of the microstructural constituents, i.e., pearlite, ferrite, and graphite. The fractions of microstructural constituents are also presented graphically as a function of the distance x from the specimen center to its edge. The fraction of microstructural constituents changed from the center to the edge and greater changes of the microstructural constituents were detected at adistance of 1 000 µm to 1 500 µm from the center. The fraction of graphite was reduced to 1 % and the fraction of pearlite to 70 %. In contrast, the fraction of ferrite was constantly increasing and the share of ferrite was 25 % at adistance of 1 500 µm, while its share at the edge of the specimen reached as high as 90 %.

Based on measurements of the electrical resistivity and the changed lengths of specimens during the decarburization of white-heart cast iron and applying a physico-mathematical model of white-heart cast iron decarburization, variations of the carbon concentrations and the specific electrical resistivity during the decarburization process were evaluated as a function of the decarburization time. The variations of the carbon concentrations were calculated for (12, 24, 36, 48 and 60) h of decarburization at a temperature T = 1 000 °C for specimens that were decarburized in various atmospheres. These relations are presented in **Figure 9**. The relations between the decarburization time and the depths of the decarburized zone are shown in **Figure 10**. It is evident from the plot in **Figure 9** that the greatest variations of the specific electrical resistivity and of the carbon concentration occurred between 12 h and 24 h of decarburization. A similar behavior was also found with measurements of the electrical resistivity of laboratory specimens, where the corresponding time interval was between 11.1 h and 22.2 h. The course of the decarburization process in **Figure 9**, i.e., the relation between the carbon concentrations and the time of decarburi-

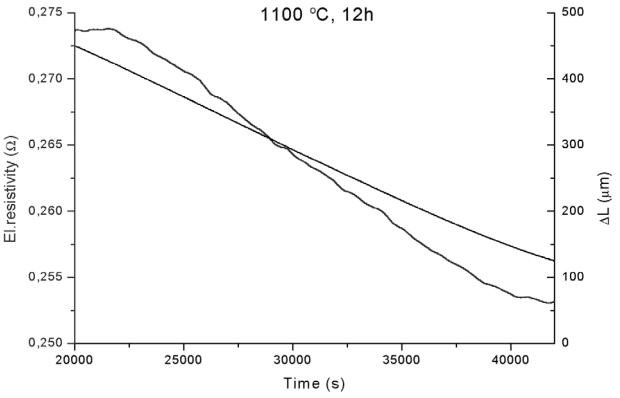

Figure 7: Variations of electrical resistivity and dimensional changes with time during decarburization of the specimen, decarburized in laboratory conditions (T_3 t_1); T = 1 100 °C, 12 h, $N_2 + H_2O$ mixture,
Slika 7: Električna upornost in dimenzijske spremembe v odvisnosti od časa razogljičenja za vzorec (T_3 t_1); T = 1 100 °C;12 h; $N_2 + H_2O$

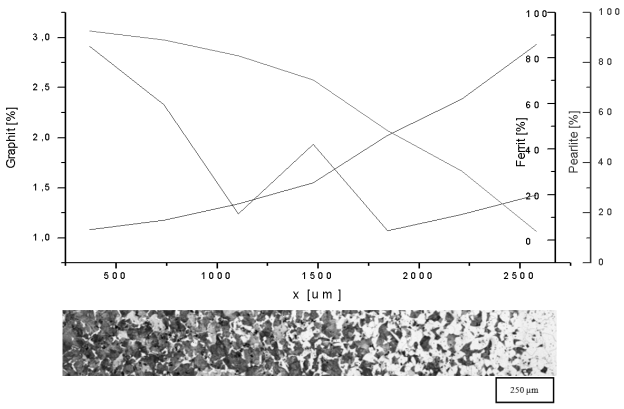

Figure 8: Micrograph with microstructural constituents in the specimen (T_3 t_1);T = 1 100 °C; 12 h; $N_2 + H_2O$ mixture
Slika 8: Posnetek mikrostrukture in deleži mikrostrukturnih sestavin vzorca (T_3 t_1) ; T = 1 100 °C; 12 h; $N_2 + H_2O$

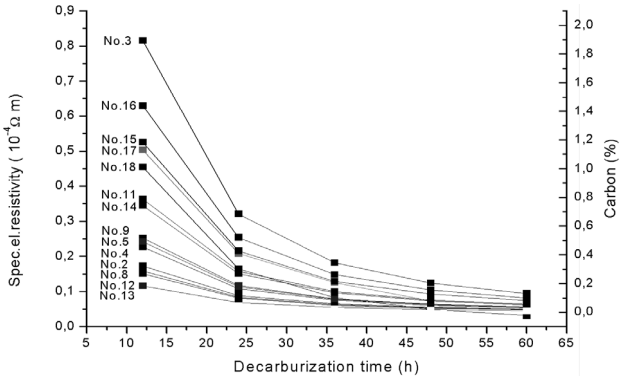

Figure 9: Variation of the carbon concentration and of the specific electrical resistivity during the decarburization process at T = 1 100 °C

Slika 9: Sprememba koncentracije ogljika in specifične električne upornosti v odvisnosti od časa razogljičenja pri temperaturi T = 1 100 °C

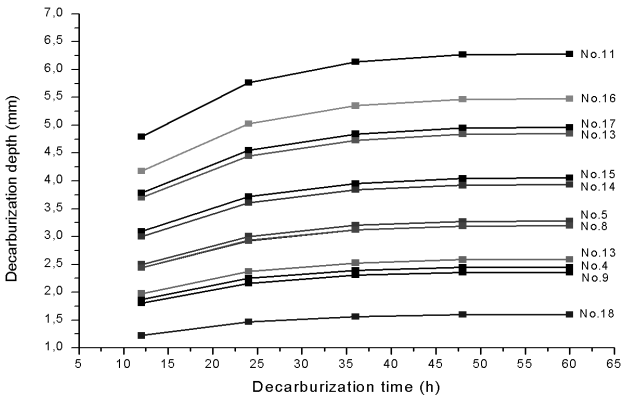

Figure 10: Variation of the depth of the decarburization zone during the decarburization process at T = 1 100 °C

Slika 10: Sprememba globine razogljičenja v odvisnosti od časa razogljičenja pri temperaturi T = 1 100 °C

zation, was similar to that described where the decarburization of the electrical sheet was investigated[15]. Furthermore, **Figure 10** shows that an increased decarburization rate in the time interval between 12 h and 24 h of decarburization resulted in greater depths of the decarburized zone that varied between 1 mm and 6 mm, depending on the decarburization time and the decarburization conditions. The relationships between the wall thickness of the casting and the decarburization time at T = 1 000 °C are presented, showing that a depth of the decarburization zone of 5 mm was reached after 50 h of decarburization.[12]

The temperature of the solidification and of the phase transformations were determined by analyzing the course of the MCI solidification and decarburization by physico-metallurgical means. Among those temperatures, the essential in the MCI decarburization process is the temperature of eutectoid transformation ($\gamma_{Fe} \rightarrow \alpha_{Fe}$ + Fe_3C) at 752 °C.

The mechanism of the MCI decarburization process was determined. This process started at $T \geq 752$ °C by carbon loss in the austenite, $[C]_{\gamma\text{-Fe}}$, and was continued by $C_{\text{malleablized graphite}}$ loss, described with the reactions:

$$[C]_{\gamma\text{-Fe}} + H_2O_{(g)} = CO_{(g)} + H_{2(g)}, \text{ and}$$

$$C_{\text{malleablized graphite}} + H_2O_{(g)} = CO_{(g)} + H_{2(g)}$$

4 CONCLUSIONS

In the first part of the research, the MCI decarburization was investigated with the thermal analyses, chemical analyses, and differential scanning calorimetric analyses of as-cast malleable samples. The thermal analyses revealed the entire course of the solidification process, the course of the cooling, and reactions relating to how the austenite, cementite eutectic and pearlite were formed. Differential scanning calorimetry of the as-cast specimens confirmed the course of the reactions that were determined by the thermal analysis.

Further examinations were focused on a laboratory examination of the malleablizing process from the thermodynamic and kinetic points of view and the dilatometric analyses of specimens during the malleablizing process were performed. The measurements of the electrical resistivity were added to follow the decarburization process more precisely. Electrical resistivity changes during the decarburization process of the specimens decarburized in laboratory conditions were confirmed by an assessment of the changes in the microstructures.

5 REFERENCES

[1] P. V. Hübner, G. Pusch, O. Liesenberg, O.; R. Döpp, R., Bruchmechanische Kennwerte von entkohlendgeglühtemTemperguss, Giesserei, 90 (**2003**) 5, 82–92

[2] M. J. Oliveira, L. F. Malheiros, C. A. Silva Ribeiro, Evaluation of the heat of solidification of cast irons from continuous cooling curves, Journal of Materials Processing Technology, 92–93 (**1999**), 25–30

[3] P. Mrvar, M.Trbižan, J. Medved, Solidification of Aluminium Cast Alloys investigated by the Dilatation Analysis, Metalurgija, 40 (**1985**), 81–84

[4] P. Mrvar, J. Medved, A. Križman, Control of Microstructure during the Eutectoid Transformation in the As-cast Spheroidal Graphite Cast Iron with "in-situ" Dilatation Analysis and Quenching Experiments, Steel Research Int., 77 (**2006**) 5, 353–361

[5] J. Medved, P. Mrvar, Thermal Analysis of the Mg-Al Alloys, Materials Science Forum, 508 (**2006**), 603–608

[6] P. Mrvar, M. Trbižan, J. Medved, A. Križman, Study of the Eutectoid Transformation in the As-cast Spheroidal Graphite Cast Iron with »in-situ« Dilatation Analysis-Method for Quality control, Materials Science Forum, 508, (**2006**), 287–294

[7] E. Guhl, O. Liesenberg, R. Döpp, Qualitätskontrolleniedriglegierter-Gußeisenschmelzen durchrechnergestütztethermische Analyse, Giessereiforschung, 46 (**1994**) 2/3, 62–70

[8] W. Menk, M. O. Speidel, R. Döpp, Die thermische Analyse in der Praxis der Eisen- und Tempergießerei, Giessereiforschung 44 (**1992**) 2, 66–79

[9] P. Mrvar, M. Trbižan, J. Medved, Dilatation analysis of the eutectoid transformation of the as-cast spheroidal graphite cast iron, Scandinavian Journal of Metallurgy, 31 (**2002**), 393–400

[10] D. Steiner Petrovič, Non-oriented electrical steel sheets, Mater. Tehnol., 44 (**2010**), 317–325

[11] D. Steiner Petrovič, B. Markoli, M. Čeh, The nanostructure of non-oriented electrical steel sheets, Journal of Magnetism and Magnetic Materials, doi 10.1016/j.jmmm.2010.05.026

[12] J. Beer, H. Hocke, Das Glühen von schweißbarem Temperguß – EinBerichtaus der Praxis, Giesserei 82 (**1995**) 3, 87–90

[13] E. Hornbogen, H. Warlimont, Metallkunde, Aufbau und Eigenschaften von Metallen und Legirungen, 2. Auflage, Springer Verlag, Berlin, Heidelberg, New York, (1996)

[14] P. Mrvar, M. Trbižan, J. Medved, Investigation of cast iron solidification with dilatation analysis, Kovine Zlit. Tehnol. 33, (**1999**) 1–2, 45–49

[15] K. M. Marra, E. A. Alvarenga, V. T. L. Buono, Decarburization kinetics during annealing of a semi-processed electrical steel, ISIJ International, 44 (**2004**) 3, 618–622

UDK 669.715.017:621.771
Original scientific article/Izvirni znanstveni članek

ISSN 1580-2949
MTAEC9, 45(6)537(2011)

MODELLING AND PREPARATION OF CORE FOAMED Al PANELS WITH ACCUMULATIVE HOT-ROLL BONDED PRECURSORS

NAČRTOVANJE IN IZDELAVA Al-PANELOV S SREDICO IZ Al-PEN NA OSNOVI VEČSTOPENJSKO TOPLO VALJANIH PREKURZORJEV

Varužan Kevorkijan[1], Uroš Kovačec[2], Irena Paulin[3], Srečo Davor Škapin[4], Monika Jenko[3]

[1]Independent Researcher, Betnavska cesta 6, 200 Maribor, Slovenia
[2]Impol Aluminium Industry, Partizanska 38, 2310 Slovenska Bistrica, Slovenia
[3]Institute of Metals and Technology, Lepi pot 11, 1000 Ljubljana, Slovenia
[4]Institut "Jožef Stefan", Jamova 39, 1000 Ljubljana, Slovenia
varuzan.kevorkijan@impol.si

Prejem rokopisa – received: 2011-08-29; sprejem za objavo – accepted for publication: 2011-10-25

In this paper, laboratory and semi-industrial processes for the preparation of aluminium foam samples and core-foamed panels with closed porosity were investigated. The samples were prepared starting from the accumulative hot-roll bonded precursors, with titanium hydride (TiH_2) or dolomite ($Ca_{0.5}Mg_{0.5}CO_3$) powder added as the foaming agent. The formation of the precursors was performed in three steps. In the initial stage, titanium dihydride or dolomite particles were deposited on a single side of a selected number of aluminium strip samples made from the alloy AA 1050. In the second step, by putting together in pairs, single-sided coated strips, precursors with a two-layered structure were prepared. The samples were hot-rolled to a final thickness of 1.9–3.8 mm, introducing a total deformation of about 45–49 % by a process well-known as accumulative hot-roll bonding. In the third stage of the precursor's formation, the desired multilayered precursor's structure was achieved by hot-roll multi-passing, i.e., by repeating (with 2–16 passes) the accumulative hot-roll bonding procedure. The obtained precursors were foamed in an electrical furnace, under different foaming conditions, based on the initial temperature of the thermal decomposition of the foaming agent. The microstructure of the obtained foam samples was investigated with optical and scanning electron microscopy. According to the accumulated experimental results, one can conclude that the usage of dolomite powder as a foaming agent with a higher temperature of thermal decomposition (>750 °C) compared to TiH_2, which thermally decomposed even at the temperature of hot-rolling (>350 °C), enabling the formation of multilayered precursors at higher temperatures of hot-rolling without any intermediate annealing. This consequently increases the productivity of the foamed core panel production without influencing their final quality.

Key words: Al foams, core foamed Al panels, precursors preparation, accumulative hot-roll bonding, comparison of different foaming agents, characterisation

V delu opisujemo razvoj laboratorijskih in polindustrijskih postopkov priprave vzorcev aluminijskih pen in panelov iz Al-pen z zaprto poroznostjo. Vzorce panelov smo izdelovali na osnovi večstopenjsko toplo valjanih prekurzorjev, ki so kot sredstvo za penjenje vsebovali delce titanovega dihidrida (TiH_2) ali dolomitnega prahu ($Ca_{0.5}Mg_{0.5}CO_3$). Postopek priprave večplastnih prekurzorjev je potekal v treh fazah. V začetni fazi smo delce titanovega dihidrida ali dolomita nanašali na izbrano stran aluminijevega traku zlitine AA 1050. Sledila je priprava

dvoplastnega prekurzorja. Po dva in dva premazana trakova smo zložili tako, da sta se premazani stranici stikali ter dvojček vroče zvaljali na 1,9–3,8 mm s skupno deformacijo med 45–49 %. Postopek smo v sklepni fazi izdelave prekurzorjev ponavljali do želene večplastnosti (od 2- do 16-krat). S postopkom večkratnega valjanja in podvajanja plasti penilnega sredstva smo dosegli enakomerno porazdelitev penilnega sredstva skozi celoten prerez izdelanih prekurzorjev. Dobljene prekurzorje smo nato penili v električni peči pri različnih pogojih glede na temperaturo termičnega razkroja sredstva za penjenje. Mikrostrukturo dobljenih vzorcev pen smo analizirali z optično in vrstično elektronsko mikroskopijo. Z raziskavami smo potrdili, da uporaba dolomitnega prahu kot penilnega sredstva z višjo temperaturo termičnega razkroja (>750 °C) v primerjavi s TiH_2, ki se termično razkraja že pri temperaturi toplega valjanja (>350 °C), omogoča izdelavo večplastnih prekurzorjev pri višjih temperaturah toplega valjanja brez vmesnega žarjenja in posledično povišuje produktivnosti brez vpliva na kakovost končnega izdelka.

Ključne beside: Al-pene, Al-paneli s penasto sredico, priprava prekurzorjev, večstopenjsko toplo valjanje, primerjava različnih sredstev za penjenje, karakterizacija

1 INTRODUCTION

Accumulative Roll Bonding (ARB) is a new and promising manufacturing process for closed-cell aluminium foams and core-foamed panels [1–3]. The ARB process, as one of the severe plastic deformation processes, has been applied to many metals and alloys to produce an ultra-fine crystal grains structure. The processing procedure is presented in **Figure 1**.

Instead of aluminium powder, Al sheet is applied as a starting material, making this processing route cost-effective and promising for further industrialization. During the first stage, two aluminium strips are stacked with the appropriate amount of selected blowing-agent powder of the proper morphology. Second, the strip is roll-bonded by a 50 % reduction and cut into two. After repeatedly covering the surface with blowing agent, the two strips are stacked to be the initial dimension, and then roll-bonded again. Since these procedures can be repeated indefinitely, the desired multilayered precursor's structure could be achieved. By multiplying the foaming-agent layers, its uniform distribution across the entire cross-section of the prepared precursor can be achieved. Finally, the obtained precursors are foamed to the end products: foamed aluminium sheet or core-foamed panels.

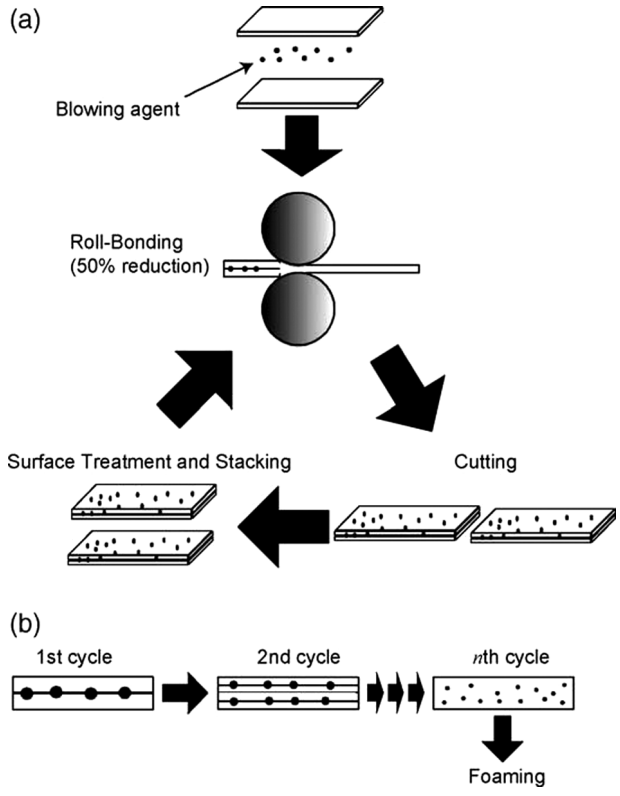

Figure 1: (a) Schematic illustration of the manufacturing process of a precursor sheet using the ARB process. (b) Prediction of gradual distribution of added foaming-agent particles [3].

Slika 1: (a) Shematski prikaz postopka večstopenjskega toplega valjanja prekurzorja; (b) prikaz porazdelitve delcev penila v večplastnem prekurzorju [3].

Investigations performed in the past few years have confirmed the great potential of the ARB processing route in the cost-effective and highly productive fabrication of foamed aluminium sheets and various core-foamed panels by TiH_2 as a foaming agent [3, 4]. An additional reduction in cost can be achieved by replacing the expensive TiH_2 with alternative, inexpensive foaming agents, particularly carbonates, among which natural carbonates such as $CaCO_3$ marble powder or $CaMg(CO_3)_2$ dolomite powder are particularly attractive.

Successfully replacing the TiH_2 with carbonates in the foaming precursor fabricated by the powder metallurgical or stir-casting route has been reported by several authors [5–9]. However, similar investigations of replacing the TiH_2 foaming agent with dolomite particles in accumulative hot-roll bonded precursors are still not completed. Therefore, the purpose of this work was to investigate the possible benefits of replacing TiH_2 with dolomite particles in multilayered precursors made by ARB.

2 EXPERIMENTAL PROCEDURE

The samples were prepared by starting from the accumulative hot-roll bonded precursors, with titanium hydride (TiH_2) or dolomite ($Ca_{0,5}Mg_{0,5}CO_3$) powder added as the foaming agent.

The formation of the precursors was performed in three steps. In the initial stage, titanium dihydride or dolomite particles were deposited on a single side of a selected number of aluminium strip samples (100 mm in width, 200 mm in height and with a thickness of approx. 2–4 mm) made from the alloy EN AW 1050. The suspension of the powdered foaming agent (TiH_2 or $MgAl_3O_4$) in acetone was spread out on the strip with a painter's roll. Titanium hydride (supplier: AG Materials Inc.) and dolomite powders (supplier: Granit, d. o. o., Slovenska Bistrica, Slovenia) of five different average particle sizes were applied as foaming agents. The average particle size of the powders used in the experiments is listed in **Table 1**. The particle size distribution of the a powdered foaming agents was measured using laser particle analyzer (Malvern Mastersizer 2000). The relative error of the measurement was within ±1 %.

The surface concentration of the foaming agent achieved after removing the acetone was between approximately 2.5×10^{-3} and 3.75×10^{-3} mg/mm^2. In the second step, by putting together in pairs single-sided coated strips, precursors with a two-layered structure were prepared. The samples were hot-rolled to a final thickness of 1.9–3.8 mm, introducing a total deformation of about 45–49 % by a process that is well known as accumulative hot-roll bonding. It was found that the consistency of the obtained precursors (the adhesion between two layers) was strongly affected by the parameters of the hot-rolling (the strip deformation and the temperature of the hot-rolling). These were signifi-

Table 1: The average particle size and the cumulative particle size distribution of the TiH_2 and dolomite powder applied as foaming agents
Tabela 1: Povprečna velikost delcev in porazdelitev delcev po velikosti TiH_2 in dolomitnega prahu, uporabljenih kot sredstvo za penjenje

TiH_2 powder	TIH-0420
Average particle size (μm)	20.4
Cumulative particle size distribution (μm	
D_{10}	13.1
D_{25}	17.4
D_{50}	20.4
D_{75}	23.7
D_{90}	41.4
Uniformity of particle size distribution (μm)	
D_{90}–D_{10}	28.3
Dolomite powder	D-4
Average particle size (μm)	20.8
Particle size distribution	
D_{10}	11.2
D_{25}	15.9
D_{50}	20.8
D_{75}	23.1
D_{90}	27.2
Uniformity of particle size distribution (μm)	
D_{90}–D_{10}	16.0

cantly limited by the technical possibilities of the existing mini hot-rolling mill. The diameter of the working rolls was only 200–450 mm. However, by carefully selecting the optimal power of the hot-rolling mill unit (about 18–50 kW) for the proper deformation of the strip and the temperature of the hot-rolling (between 300–350 °C), the complete recrystallization of the strip was achieved, avoiding in that way any possible hardening of the wrought aluminium alloy. In the third stage of the precursor's formation, the desired multilayered precursor's structure was achieved by hot-roll multi-passing, i.e., by repeating (with 2–16 passes) the accumulative hot-roll bonding procedure. By the multiple accumulative hot-roll bonding and by doubling the layers of the foaming agent, its uniform distribution was achieved across the entire cross-section of the prepared precursors.

The precursors were foamed in a conventional batch electrical furnace with air-atmosphere circulation under various experimental conditions (time, temperature) and by applying the same cooling method. Before foaming, the individual precursors were placed on a ceramic plate covered by a boron nitride layer. The plate dimensions and the precursor size 100 mm × 100 mm were selected to allow the complete expansion of the precursor to foam. The arrangement was placed inside a pre-heated batch furnace at a selected temperature and held for the selected holding time. In samples with TiH_2, thermal decomposition was observed, starting from approximately 350 °C. These samples were foamed at 700–750 °C, for 3–18 s. Samples with the dolomite foaming agent, for which the thermal decomposition is initiated above 750 °C, were foamed at 780 °C for 2–5 min. After that, the sample was removed from the furnace and the foaming process was stopped by rapid cooling with pressurised air to room temperature. The thermal history of the foam sample was recorded, using a thermocouple located directly in the precursor material. The density of the foam was calculated using Archimedes' method. The porosity of the manufactured foam was calculated using the rate: 1-(foam density/aluminium density). Macro and microstructural examinations were performed on sections obtained by wire precision cutting across the samples and on samples mounted in epoxy resin, using optical and scanning electron microscopy (SEM/EDS). The average particle size of the pores in the foams was estimated by analysing optical and scanning electron micrographs of the as-polished foam bars using the point-counting method and image analysis and processing software.

3 MODELLING OF THE SURFACE CONCENTRATION AND MORPHOLOGY OF THE FOAMING AGENT IN ARB PRECURSORS

In precursors fabricated by the ARB processing route, the proper surface concentration and morphology of the foaming agent are crucial for the development of high-quality foams with closed cells and a uniform microstructure. Because of that, it was very important to correlate by the model developed in this work the surface concentration and morphology of the foaming agent with an average cell size and microstructure of the foam.

The particles of foaming agent are, as much as possible, homogeneously dispersed on the surface of the aluminium sheet, as is evident in **Figure 2**.

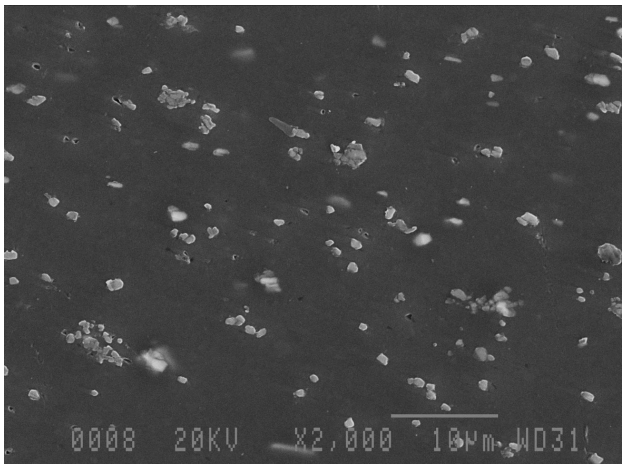

Figure 2: SEM micrograph of the surface of an aluminium sheet after the first cycle of ARB, with homogeneously distributed dolomite particles
Slika 2: SEM-posnetek površine aluminijskega traku po prvem prehodu večstopenjskega toplega valjanja s homogeno porazdeljenimi delci dolomita

The neighbouring particles of foaming agent are mutually apart for an average minimum distance X_{min}. As will be demonstrated in the model, this distance is determined by the surface concentration of the foaming agent C and its average particle size d_{50}.

The surface concentration of the foaming agent is defined as follows:

$$C = m/S \quad (1)$$

Here, m is the total mass of the foaming agent and S is the surface of the aluminium sheet. The molar surface concentration C' is defined as:

$$C' = m/(MS) \quad (2)$$

where M represents the molar mass of the selected foaming agent. Finally, the particle surface concentration C'' is introduced as:

$$C'' = N/S = 1/X_{min}^2 \quad (3)$$

N is the total number of particles of foaming agent:

$$N = m_p/M = d_{50}^3\pi\rho/6M \quad (4)$$

In Eq. 4, m_p represents the mass of an average particle of foaming agent, d_{50} is the average particle size and ρ is the theoretical density of the foaming agent.

Therefore, by combing Eqs.1–4 we can derive, for the particle surface concentration, the following expression:

$$C'' = 6C/(d_{50}^3\pi\rho) \quad (5)$$

and, consequently, for X_{min}:

$$X_{min} = [(d_{50}^3\ \pi\rho)/6C]^{1/2} \quad (6)$$

Applying, for the bubbles' growth, a simple, stoichiometric model, in which the complete thermal decomposition of an individual foaming agent particle provides a gas phase for the bubble's nucleation and growth, the maximum bubble diameter D_{max} can be determined with the ideal gas equation:

$$p_{max}V = nRT \quad (7)$$

where n corresponds to the number of moles of gas phase inside the bubble, V is the bubble volume, R is the universal gas constant and T is the temperature.

p_{max} can be calculated by applying Laplace's equation:

$$p_{max} = (2\sigma_{lg}/r) + \rho gh + p_0 \quad (8)$$

The maximum bubble pressure p_{max} is the sum of the capillary ($2\sigma_{lg}/r$), hydrostatic (ρgh) and atmospheric (p_0) pressures. The capillary pressure depends on the surface tension σ_{lg} at the gas-liquid interface and the bubble radius (r); the hydrostatic pressure is determined by the immersion depth (h) and the density of the molten aluminium alloy (ρ).

By considering a spherical bubble and by combining Eqs. (7) and (8), we can calculate:

$$[(2\sigma_{lg}/r) + \rho gh + p_0]\ (4/3)r_{max}^3\pi = nRT \quad (9)$$

During an early stage of the bubble's growth, only the capillary pressure ($2\sigma_{lg}/r$) should be considered, while in the final stage of the bubble's growth the only important pressure is the atmospheric (p_0). Note that for laboratory conditions, the hydrostatic pressure (ρgh) is always negligible.

Based on this, in the case considered by the model:

$$p_{max} = p_0 \quad (10)$$

Therefore, the maximum bubble diameter D_{max} is finally determined by the formula:

$$D_{max} = d_{50}[(kRT\rho)/p_0M]^{1/3} \quad (11)$$

Here, k represents the stoichiometric constant (k = 1 for TiH_2 and k = 2 for dolomite), R is the universal gas constant, T is temperature, ρ is the density of the foaming agent, p_0 is the atmospheric pressure and M is the molar mass of the foaming agent. In **Tables 2 and 3**, the calculated values for the maximum bubble radius for cells grown from the TiH_2 and dolomite particles of different initial particle size are listed.

Table 2: Maximum bubble radius for a cell grown from TiH_2 particles with different initial particle sizes (d_{50}).
Tabela 2: Maksimalni premer pore iz TiH_2 delcev različne začetne velikosti (d_{50})

The average particle size of TiH_2 (μm)	3	20	40	75	140
Maximum bubble diameter, D_{max} /μm	54	360	808	1.352	2.526

Table 3: Maximum bubble radius for bubbles created by dolomite particles of different initial particle sizes (d_{50})
Tabela 3: Maksimalni premer pore iz delcev dolomita različne začetne velikosti (d_{50})

The average particle size of dolomite (μm)	3	5	10	20	35
Maximum bubble diameter, D_{max}/μm	40	68	132	268	468

According to the theoretical prediction based on Eq. 11 and the calculated values reported in Tables 2 and 3, at the same initial particle size of the applied foaming agents (3 μm or 20 μm) and the same foaming conditions (temperature, time), the bubbles created by TiH_2 should be coarser.

In order to obtain a stable foam microstructure, with isolated closed cells, it is necessary that:

$$X_{min} > D_{50} \quad (12)$$

By combining Eqs. 6, 11 and 12, the condition (12) leads to the required correlation between the surface concentration and the foaming-agent morphology:

$$C < \text{const.}\ (d_{50}/T)^{2/3} \quad (13)$$

Based on the model, it is evident that for the selected morphology of the foaming agent d_{50} and foaming temperature T the surface concentration of the foaming agent C cannot be selected arbitrarily, but, in order to achieve a

foam microstructure with stable individual closed cells, it should fulfil the condition expressed by Eq.13.

4 RESULTS AND DISCUSSION

4.1 Foam properties as a function of the composition of accumulative roll-bonded precursors

The results of the investigation of the foam properties (density and cell size distribution) achieved by applying various types (TiH_2 or dolomite) and surface concentrations of foaming agents are reported in **Tables 4 and 5**.

Table 4: The experimentally measured density and cell-size distribution of the aluminium foam samples at various concentrations of TiH_2 foaming agent. The foaming conditions: 700 °C, 120 s.

Tabela 4: Eksperimentalno izmerjene vrednosti gostote in porazdelitve velikosti por v vzorcih aluminijske pene, izdelanih pri različni koncentraciji delcev TiH_2, uporabljenega kot penila. Pogoji penjenja: 700 °C, 120 s.

Surface concentrations of TiH_2 (mg/mm^2)	2.5×10^{-3}	3.0×10^{-3}	3.5×10^{-3}
Density of Al foam (% T. D.)	25.9 ± 1.3	23.8 ± 1.2	21.2 ± 1.1
Cell size distribution (mm)			
D_{10}	2.6 ± 0.3	3.2 ± 0.3	3.3 ± 0.3
D_{25}	2.7 ± 0.3	3.5 ± 0.3	3.8 ± 0.3
D_{50}	2.8 ± 0.3	3.7 ± 0.4	5.1 ± 0.5
D_{75}	3.0 ± 0.3	4.2 ± 0.3	5.5 ± 0.6
D_{90}	4.6 ± 0.5	8.4 ± 0.3	10.4 ± 1.0
Uniformity of cell size distribution (μm)			
D_{90}–D_{10}	2.0 ± 0.2	5.2 ± 0.6	7.1 ± 0.7

Table 5: The experimentally measured density and cell-size distribution of aluminium foam samples at various concentrations of dolomite foaming agent. The foaming conditions: 700 °C, 120 s.

Tabela 5: Eksperimentalno izmerjene vrednosti gostote in porazdelitve velikosti por v vzorcih aluminjske pene, izdelanih pri različni koncentraciji delcev dolomite, uporabljenega kot penila. Pogoji penjenja: 700 °C, 120 s.

Surface concentrations of dolomite (w/%)	2.5×10^{-3}	3.0×10^{-3}	3.5×10^{-3}
Density of Al foam (% T.D.)	15.4 ± 0.8	12.8 ± 0.6	11.1 ± 0.6
Cell size distribution (mm)			
D_{10}	2.0 ± 0.2	2.4 ± 0.2	2.9 ± 0.3
D_{25}	2.3 ± 0.2	2.9 ± 0.3	3.3 ± 0.3
D_{50}	2.5 ± 0.3	3.2 ± 0.3	4.7 ± 0.5
D_{75}	2.7 ± 0.3	4.8 ± 0.6	5.1 ± 0.5
D_{90}	5.8 ± 0.6	7.6 ± 0.8	9.7 ± 1.0
Uniformity of cell size distribution (μm)			
D_{90}-D_{10}	3.8 ± 0.4	5.2 ± 0.5	6.8 ± 0.7

Generally, the panels foamed with the dolomite foaming agent were with a more uniform cell-size distribution and lower average bubble size. The most uniform cell-size distribution was achieved in foam samples foamed with the minimum surface concentration (2.5×10^{-3} mg/mm^2) of dolomite powder, **Figure 3**.

The experimentally determined values of the average bubble radius in the foamed panels were at least for one order of magnitude higher that those predicted by the model. The reason for that difference is in effects limiting the stability of the individual bubbles, which are not considered by the model. These effects are as follows: bubble flow, drainage, rupture or coalescence, and coarsening.

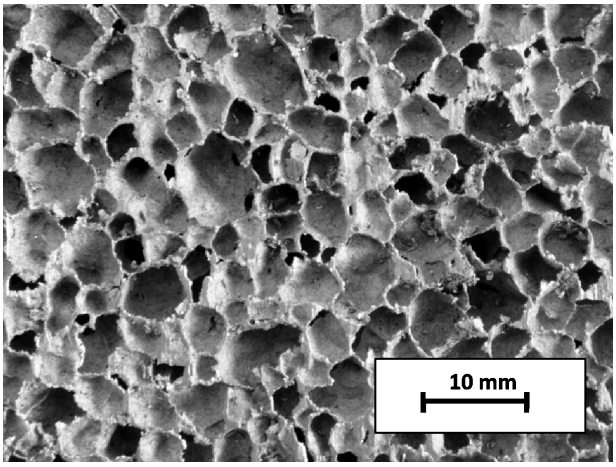

Figure 3: The homogeneous microstructure of the Al foam made from the ARB precursor with dolomite particles as the foaming agent. The ARB precursor was made by four roll-bonding cycles.

Slika 3: Homogena mikrostruktura vzorca Al-pene iz prekurzorja, izdelanega po postopku večstopenjskega toplega valjanja

From the difference between the theoretically predicted and experimentally determined values of the bubble radius, it is possible to estimate the stability of the real foam systems considered in this work. The experimental findings clearly confirm that coarser bubbles are more stable that finer ones. In addition, it is also evident that the stability of the bubbles is much higher in foams created by dolomite particles than in the counterparts foamed by TiH_2. However, in both cases the average bubble sizes are proportional to the average initial size of the foaming particles – finer foaming particles lead to finer bubbles, while coarser ones lead to larger bubbles, as was predicted by the model.

On the other hand, the density of the aluminium foam samples was inversely proportioned to the bubble radius: the foam samples with finer bubbles had the higher density and, in contrast, the foam samples with larger bubbles were specifically lighter. At the same time and under the same foaming conditions (temperature, time), the foams made with the dolomite were with a significantly lower density than the samples with similar cell size foamed by the TiH_2.

As is evident from the cell-size distribution data listed in **Tables 3 and 4**, an increase of the foaming-agent surface concentration (either TiH_2 or dolomite) leads to the formation of foams with larger bubbles and a lower density. However, also in that case, the samples foamed with dolomite were with smaller bubbles and lower densities.

The experimentally developed foam microstructures were mostly influenced by the degree of foam movement slowing down (i.e., the foam stability) attained in particular trials. In addition, the microstructure of foams was also influenced in some cases by the layered structure of the ARB precursors.

The slowing down of the movement of the foam includes the prevention of flow (the movement of bubbles with respect to each other caused either by external forces or changes in the internal gas pressure during foaming), drainage (flow of liquid metal through the foam), coalescence (sudden instability in a bubble wall leading to its disappearance) and coarsening (slow diffusion of gas from smaller bubbles to bigger ones).

The layered structure of the ARB precursors caused, in some samples, the appearance of so-called "line segregation", i.e., the flow of liquid metal across the line, **Figure 4**. Such segregation is most probably involved in the non-sufficient and/or different plastic deformation of individual layers during various roll-bonding cycles.

Generally, the foam stability in the liquid and semi-solid state of an aluminium alloy is improved by increasing the thickness of the bubble wall, decreasing the surface tension of the molten metal and increasing its viscosity. Simultaneously decreasing the surface tension and increasing the viscosity of molten aluminium can be achieved by introducing to the molten metal some amount of ceramic particles, e.g., formed in situ, by the thermal decomposition of the foaming agent at the interface between molten aluminium and the gas phase.

Quantitatively, the foam stability in the liquid and semi-solid state might be expressed by a dimensionless foam-stability factor (FSF), which we defined as:

$$FSF = X_0\eta/(\sigma t) \qquad (14)$$

where X_0 is the average distance between neighbouring bubbles (which is proportional to the wall thickness), η is the dynamic viscosity of the slurry, σ is the surface tension at the interface molten or semi-solid aluminium-gas and t is the foaming time.

Evidently, a higher FSF means better foam stability. Unfortunately, in practice, it is not easy to determine the viscosity and the surface tension of the slurry of the molten aluminium alloy and the foaming agent particulates as well as the wall thickness of bubbles during their growth. Because of that, the usage of FSF is mostly limited to theoretical and, to some level, qualitative considerations.

The main differences between the TiH_2 and the dolomite foaming agent, which influences the foam microstructure development, are the following: (i) in the nature and reactivity of products of its thermal decomposition and (ii) the temperature interval of thermal decomposition.

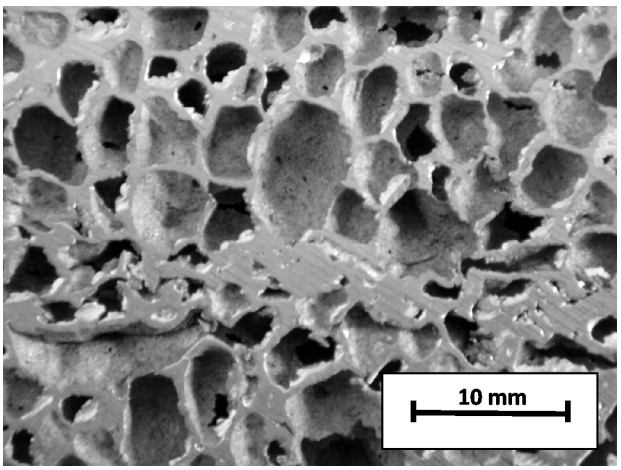

Figure 4: The characteristic "line segregation" in the samples of aluminium foams made from ARB precursors using dolomite as a foaming agent

Slika 4: Značilno "linijsko izcejanje" v vzorcih aluminijske pene z dolomitom kot sredstvom za penjenje. Vzorci pene so iz prekurzorjev, izdelanih po postopku večkratnega toplega valjanja

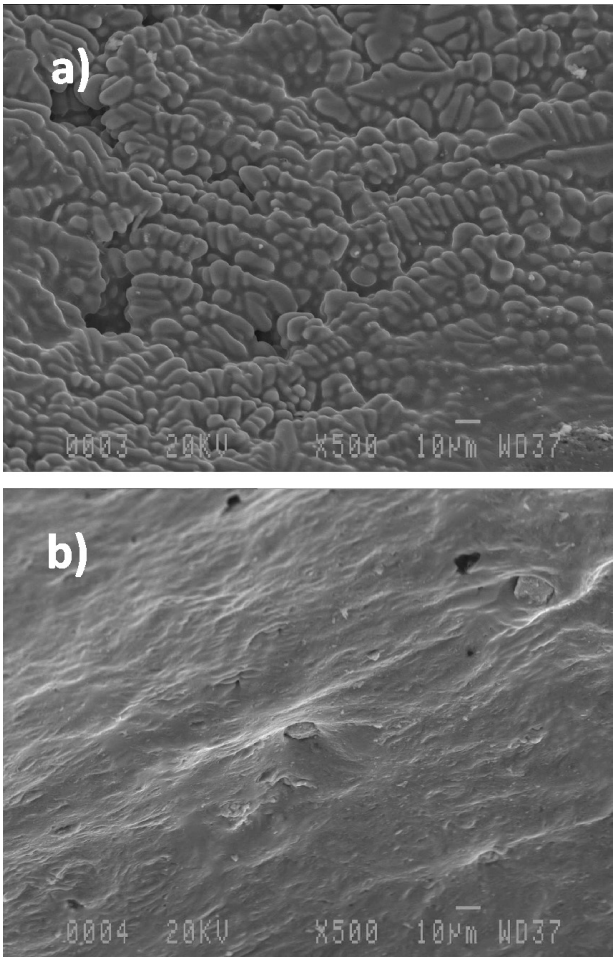

Figure 5: SEM micrograph of the internal surface of the bubble wall: a) bubble wall fully covered by Al_2O_3, CaO and MgO particles in bubbles foamed by dolomite and b) clean internal surface in bubbles foamed by TiH_2

Slika 5: SEM-posnetek notranje površine por: a) nastale z razkrojem dolomita ter povsem prevlečene z delci Al_2O_3, CaO in MgO in b) neprevlečene, nastale z razkrojem TiH_2

In ARB precursors with TiH_2, the thermal decomposition of the foaming agent was observed starting from approximately 350 °C. The TiH_2 decomposes to $Ti_{(s)}$ and $H_{2(g)}$, Eq. 15, which do not tends to react with molten aluminium in the way of creating secondary ceramic phases making it possible to slow down the movement of the foam. Because of that, the internal surface of the bubble wall foamed by the TiH_2 is clean (**Figure 5b**).

$$TiH_{2(s)} = Ti_{(s)} + H_{2(g)} \quad (15)$$

In contrast to this, the thermal decomposition of the dolomite foaming agent, Eq. (16), proceeded above 700 °C, resulting in highly reactive products: $MgO_{(s)}$, $CaO_{(s)}$ and $CO_{2(g)}$ [7].

$$CaMg(CO_3)_{2(s)} = CaO_{(s)} + MgO_{(s)} + 2CO_{2(g)} \quad (16)$$

CaO and MgO are in the form of solid particulate aggregates, appearing at the molten metal-$CO_{2(g)}$ interface, while $CO_{2(g)}$ reacts with the molten aluminium in a bubble covering bubble internal surface with a thin, mostly continuous, film of Al_2O_3 (**Figure 5a**). Therefore, all the products of the dolomite thermal decomposition (MgO, CaO and Al_2O_3) are very effective in slowing down the foam movement, decreasing the surface tension and increasing the local viscosity of the slurry. Due to the limited foam movement, bubbles in solidified samples remain significantly finer, resulting in foams with a higher density (a lower volume fraction of bubbles).

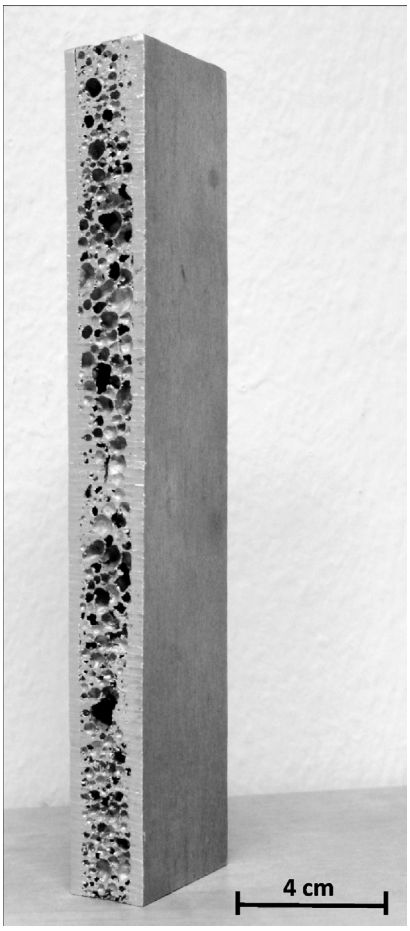

Figure 6: The cross-section of the prototype core-foamed panel made from ARB precursor with dolomite particles as the foaming agent.

Slika 6: Prečni prerez prototipnega panela s sredico iz aluminijske pene. Panel je izdelan iz večstopenjsko toplo valjanega prekurzorja z dolomitom kot sredstvom za penjenje

4.2 Fabrication of prototype core-foamed aluminium panels

Accumulative hot-roll bonded precursors with dolomite particles as a foaming agent were successfully foamed to core-foamed panels with a wall thickness of about 2 mm and a thickness of the foamed core of about 10 mm. The flat panel samples (approx. 150 mm long and 80 mm wide) were routinely foamed from the ARB precursors using the existing laboratory capabilities, **Figure 6**.

5 CONCLUSION

Our experimental findings confirmed that the ARB procedure is very promising (semi)-industrial route for the production of precursors for core-foamed aluminium panels. By combining a pair of AA1050 aluminium alloy strips and various foaming agents (TiH_2 or dolomite powders), several foaming precursors were prepared through two to four cycles of ARB and successfully foamed into core-foamed aluminium panels.

The use of dolomite powder as a foaming agent with a higher temperature of thermal decomposition (>700 °C) compared to TiH_2, which thermally decomposed even at the temperature of hot-rolling (>350 °C), enabled the formation of multilayered precursors at higher temperatures of the hot-rolling without any intermediate annealing. This significantly improved the productivity of the production of core-foamed aluminium panels without influencing their final quality.

The microstructure uniformity and stability of the foams made from ARB precursors depend on the surface concentration and morphology of the foaming agent as well as on the foaming temperature.

Acknowledgement

This work was supported by funding from the Public Agency for Research and Development of the Republic of Slovenia, as well as the Impol Aluminium Company and Bistral, d. o. o., from Slovenska Bistrica under contract No. 2410-0206-09.

6 REFERENCES

[1] N. Tsuji, Y. Saito, S. H. Lee, Y. Minamino, Adv. Eng. Mater., 5 (**2003**) 5, 338

[2] Y. Saito, H. Utsumonia, N. Tsuji, T. Sakai, Acta Mater., 47 (**1999**), 579

[3] K. Kitazono, E. Sato, K. Kuribayashi, Scripta Mater., 50 (**2004**), 495

[4] K. Kitazono, E. Sato, Materials Science Forum, 475–479 (**2005**), 433
[5] L. E. G. Cambonero, J. M. R. Roman, F. A. Corpas, J. M. R. Prieto, Journal of Materials Processing Technology, 209 (**2009**), 1803
[6] D. P. Papadopoulos, H. Omar, F. Stergioudi, S. A. Tsipas, N. Michailidis, Colloidal and Surfaces A: Physiochem. Eng. Aspects, 382 (**2011**), 118
[7] V. Gergely, D. C. Curran, T. W. Clyne, Composites Science and Technology, 63 (**2003**), 2301
[8] V. Kevorkijan, S. D. Škapin, I. Paulin, B. Šuštaršič, M. Jenko, Mater. Tehnol., 44 (**2010**) 6, 363
[9] US Pat. No. 7.452.402 issued on November 18, 2008

UDK 621.771:519.68
Original scientific article/Izvirni znanstveni članek

ISSN 1580-2949
MTAEC9, 45(6)545(2011)

NUMERICAL SOLUTION OF HOT SHAPE ROLLING OF STEEL

NUMERIČNA REŠITEV VROČEGA VALJANJA JEKLA

Umut Hanoglu, Siraj-ul-Islam, Božidar Šarler

Laboratory for Multiphase Processes, University of Nova Gorica, Vipavska 13, SI-5000 Nova Gorica, Slovenia
umut.hanoglu@ung.si

Prejem rokopisa – received: 2011-02-02; sprejem za objavo – accepted for publication: 2011-07-29

The modeling of hot shape rolling of steel is represented by using a meshless method. The physical model consists of coupled thermal and mechanical models. Both models are numerically solved by using a strong formulation. The material is assumed to behave ideally plastic. The model decomposes the 3D geometry of the steel billet into a traveling 2D cross section which lets us analyze the large shape reductions by a sequence of small steps. A uniform velocity over each of the cross-sections is assumed. The meshless method, based on collocation with radial basis functions is used to solve the thermo-mechanical problem. The node distribution is calculatedby elliptic node generation at each deformation step to the new form of the billet. The solution is calculated in terms of temperatures and displacements at each node. Preliminary numerical examples for the new rolling mill in Štore Steel are shown.

Keywords: steel, hot rolling, radial basis functions, meshless numerical method

Modeliranje vročega valjanja je predstavljeno z uporabo brezmrežne numerične metode. Fizikalni model je sestavljen iz sklopljenega termičnega in mehanskega modela. Oba sta numerčno rešena z uporabo močne formulacije. Predpostavljamo, da se material vede idealno plastično. V modelu razstavimo 3D-geometrijo jeklene gredice v premikajoč 2D-prerez, ki omogoča analizo velikih sprememb oblike v majhnih korakih. Predpostavimo uniformno hitrost preko vsakega prereza. Za rešitev termo-mehanskega problema je uporabljena brezmrežna numerična metoda, ki temelji na kolokaciji z radialnimi baznimi funkcijami. Distribucijo diskretizacijskih točk smo za vsako novo obliko prereza gredice izračunali na podlagi eliptičnega generatorja diskretizacijskih točk. Rešitev je podana kot temperatura in premik v vsaki točki. Prikazani so preliminarni numerični primeri za novo valjarsko progo v podjetju Štore Steel.

Ključne besede: jeklo, vroče valjanje, radialne bazne funkcije, brezmrežna numerična metoda

1 INTRODUCTION

The main aim of this paper is elaboration of the coupled thermo-mechanical computational model developed for hot shape rolling of steel. The output of the thermal model is the temperature field and mechanical model the displacement (deformation). Shape rolling is a 3D process, however it is analyzed with 2D imaginary slices which is denoted as a slice model. The coordinate system of a 2D slice is based on Langrangian description where the slice travels across the rolling contact. The third axis, the rolling direction, is based on the Eularian description where there is a constant inflow and outflow of steel through the rolling direction. This is considered as a mixed Eularian-Langrangian model. It was discussed previously by many authors [1,2].

In many publications of rolling Finite Element Method (FEM) was used which is based on a mesh. A novel numerical method used in this paper to solve the involved partial differential equations is the Local Radial Basis Function Collocation Method (LRBFCM). This is a completely meshless procedure. LRBFCM has been recently used in highly sophisticated simulations like multi-scale solidification modeling [3], convection driven melting of anisotropic metals [4], continuous casting of steel [5]. This paper is organized in a way that, first the thermal model and afterwards the mechanical model are developed. Overall it becomes a coupled thermo mechanical model. The flow chart of the process is shown in **Figure 1**.

2 THERMAL MODEL

The thermal model of the shape rolling process is aimed to calculate the temperature field of the steel slab during the rolling process. The three dimensional domain Ω^{3D} with boundary Γ^{3D} is considered. The solution procedure is based on Cartesian coordinate system with axes x, y, z. Slices coincide with coordinates and the rolling direction is z. The steady state temperature distribution in the rolled product is defined through the following equation,

$$\nabla\cdot(\rho c_p \mathbf{v}T)=\nabla\cdot(k\nabla T)+S\ ;\ \mathbf{p}\in\Omega^{3D}\quad (x,y,z) \qquad (1)$$

Since we analyze the process with 2D slices perpendicular to the rolling direction and assume thata uniform velocity over the slices (homogenous compression) takes place. The Equation (1) can be transferred into

$$\rho c_p \frac{\partial T}{\partial t}=\nabla\cdot(k\nabla T)+S\ ;\ \mathbf{p}\in\Omega^{2D}\quad (x,y)$$

$$p_z(z,t)=\int v\mathrm{d}t = v_{\text{entry}} A_{\text{entry}} \int \frac{1}{A(z)}\mathrm{d}t \qquad (2)$$

with $\mathbf{p}$, ρ, t, c_p, T, k, v_{entry}, A_{entry}, $(A)z$ and S standing for position vector, density, time, specific heat, temperature, thermal conductivity, entry speed of billet, entry cross sectional area, instant cross sectional area and internal heat generation due to plastic deformation. It is assumed in the slice model that the heat transport takes place only in the direction perpendicular to the rolling direction and that the homogenous deformation takes place. The Neumann boundary condition on the part of the boundary denoted as Γ^N, Robin boundary condition on the part of the boundary denoted as Γ^R are taken into consideration ($\Gamma = \Gamma^N \cup \Gamma^R$) which are described below,

$$-k\nabla T(\mathbf{p})\cdot\mathbf{n}_\Gamma = -k\frac{\partial T(\mathbf{p})}{\partial \mathbf{n}_\Gamma} = q\ ;\ \mathbf{p}\in\Gamma^N \tag{3}$$

$$-k\nabla T(\mathbf{p})\cdot\mathbf{n}_\Gamma = -k\frac{\partial T(\mathbf{p})}{\partial \mathbf{n}_\Gamma} = h\left[T(\mathbf{p}) - T_\Gamma^R(\mathbf{p})\right]\ ;\ \mathbf{p}\in\Gamma^R \tag{4}$$

The N_Ω nodes at the domain and N_Γ nodes at the boundary are used to discretize the temperature in LRBFCM where for each node $\mathbf{p}_n = \{p_x, p_y\}^T$. For each node there is a defined influence domain with N_ω neighboring nodes. For each influence domain a radial basis function in terms of multiquadric is written

$$y_i = \sqrt{(p_x - p_{xn})^2/x_{\max} + (p_y - p_{yn})^2/y_{\max} + c^2}$$

The temperature can now be interpolated as

$$T = \sum_{n=1}^{N_\omega}\psi_n\alpha_n$$

with the collocation coefficients to be determined. The main equation in 2D can be rewritten by using the explicit time stepping,

$$\rho c_p\frac{T_{i+1}-T_i}{\Delta t} = \nabla k_i\cdot\sum_{n=1}^{N_\omega}(\nabla\psi_n)\alpha_n + \left(k_i\cdot\sum_{n=1}^{N_\omega}(\nabla\psi_n)\alpha_n\right) + S\ ;\ \mathbf{p}\in\Omega^{2D} \tag{5}$$

3 MECHANICAL MODEL

A strong form is chosen here for analysis due to its compatibility with LRBFCM. Adomain Ω with boundary Γ, $\Gamma = \Gamma^U \cup \Gamma^T$ is considered where Γ^U is the essential and Γ^T represents the natural boundary conditions. The strong formulation of the static metal deformation problems is:

$$\mathbf{L}^T\sigma + \mathbf{b} = \mathbf{0} \tag{6}$$

In the calculations, in order to avoid complications of a 3D solution, the slab is analyzed, compatible with the thermal model, with imaginary traveling 2D slices that are perpendicular to the rolling direction. For a 2D slice method, $\mathbf{L}$ is the 3×2 derivative matrix with elements $L_{11} = \partial/\partial p_x$, $L_{12} = 0$, $L_{21} = 0$, $L_{22} = \partial/\partial p_y$, $L_{31} = \partial/\partial p_y$ and $L_{32} = \partial/\partial p_y$, $\boldsymbol{\sigma} = [\sigma_x, \sigma_y, \sigma_{xy}]^T$ is the stress vector,

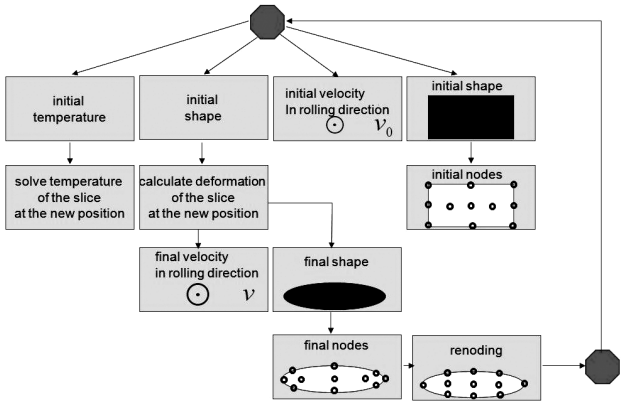

Figure 1: Flow chat of the coupled thermo mechanical model.
Slika 1: Bločni diagram sklopljenega termo-mehanskega modela

and $\mathbf{b} = [b_x, b_y]^T$ is the body force. At the essential boundary Γ^U

$$\mathbf{u}(\mathbf{p}) = \bar{\mathbf{u}}(\mathbf{p})\ ;\ \mathbf{p}\in\Gamma^U \tag{7}$$

where $\mathbf{u}(\mathbf{p})$ is displacement vector and $\bar{\mathbf{u}}(\mathbf{p})$ is the prescribed displacement vector. At the naturalboundary condition Γ^T

$$\mathbf{N}^T\boldsymbol{\sigma} = \bar{\boldsymbol{\tau}}\ ;\ \mathbf{p}\in\Gamma^T \tag{8}$$

is valid, where $\bar{\boldsymbol{\tau}}$ is the prescribed surface traction $\bar{\boldsymbol{\tau}} = [\bar{\tau}_x, \bar{\tau}_y]^T$, $\mathbf{N}$ is the 2×3 matrix of direction cosines of the normal direction at the boundary which can be defined as $N_{11} = N_{32} = n_x$, $N_{12} = N_{21} = 0$, $N_{31} = N_{22} = n_y$ (n_x,n_y) represent correlation of the normal at the boundary). In a 2D system the equations for mechanical model can be written as,

$$\frac{\partial\sigma_x}{\partial p_x} + \frac{\partial\sigma_{xy}}{\partial p_y} + b_x = 0,\ \frac{\partial\sigma_y}{\partial p_y} + \frac{\partial\sigma_{xy}}{\partial p_x} + b_y = 0 \tag{9, 10}$$

The discretization is made in terms of displacement on x and y axes for each slice,

$$u_x(\mathbf{p}) = \sum_{n=1}^{N_\omega}\psi_n(\mathbf{p})\alpha_{xn},\ u_y(\mathbf{p}) = \sum_{n=1}^{N_\omega}\psi_n(\mathbf{p})\alpha_{yn} \tag{11, 12}$$

Since the strain vector $\varepsilon = [\varepsilon_x,\varepsilon_y,\varepsilon_{xy}]^T$ can be written in terms of displacement as $\boldsymbol{\varepsilon} = \mathbf{Lu}$, the strain vector σ can be expressed as a stress vector by using 6×6 stiffness matrix $\mathbf{C}$ which depends on the material characteristic assumption such as elastic, elastic-plastic or ideally plastic.

$$\sum_{n=1}^{N_\omega}\alpha_{xn}\left[C_{11}\frac{\partial^2\psi_n}{\partial p_x^2} + C_{33}\frac{\partial^2\psi_n}{\partial p_y^2} + (C_{13}+C_{31})\frac{\partial^2\psi_n}{\partial p_y\partial p_x}\right] + \sum_{n=1}^{N_\omega}\alpha_{yn}\left[(C_{12}+C_{33})\frac{\partial^2\psi_n}{\partial p_y\partial p_x} + C_{13}\frac{\partial^2\psi_n}{\partial p_x^2} + C_{32}\frac{\partial^2\psi_n}{\partial p_y^2}\right] + b_x = 0 \tag{13}$$

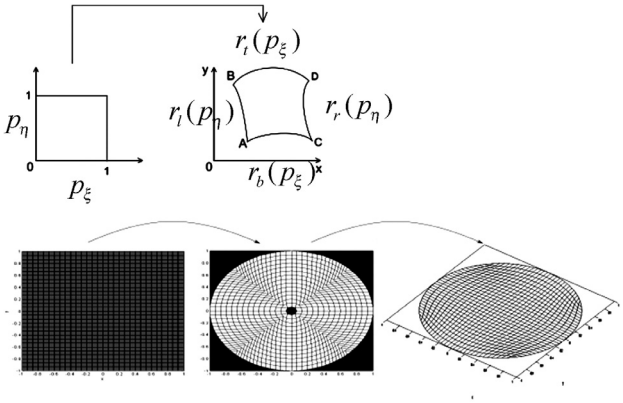

Figure 2: Transformation from computational domain to physical domain (left), TFI and nodes displacement through ENG (right). The collocation points are put on the intersection of grid lines.

Slika 2: Transformacija izračunskega območja v fizično območje (levo) TFI in premik točk preko ENG (desno). Kolokacijske točke so postavljene v prerez mrežnih linij.

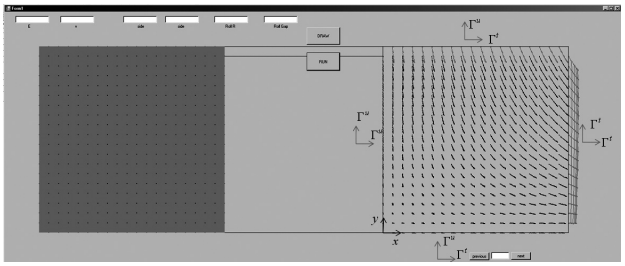

Figure 3: Simulation of flat rolled (180 × 180) mm cross sectioned 16MnCrS5 steel at 1100 °C with Young's modulus E = 97362.21 MPa and Poisson's ratio ν = 0.35678. The total reduction is 16.66 % and preliminary analyzed with 5 slices by using elastic stiffness matrix [7]. Arrows represents the displacement vector for each slice. The exit speed is equal to 1.14389 times the entry speed of the billet. Due to symmetry only the top right part of the billet is considered.

Slika 3: Simulacija prereza (180 × 180) mm ploščatega valjanja za jeklo16MnCrS5 pri 1100 °C z Youngovim modulom E = 97362.21 MPa in Poissonovim razmerjem ν = 0.35678. Skupno zmanjšanje je 16,66 % in predhodno analizirano s 5 rezinami z uporabo elastične togostne matrike [7]. Puščice pomenijo vektor premika za vsako rezino. Izhodna hitrost je enaka 1.14389-kratniku vhodne hitrosti gredice. Zaradi simetrije je upoštevana samo zgornja polovica gredice.

$$\sum_{n=1}^{N_\omega} \alpha_{xn}\left[(C_{21}+C_{33})\frac{\partial^2\psi_n}{\partial p_y \partial p_x}+C_{31}\frac{\partial^2\psi_n}{\partial p_x^2}+C_{23}\frac{\partial^2\psi_n}{\partial p_y^2}\right]+ \\ +\sum_{n=1}^{N_\omega} \alpha_{yn}\left[C_{22}\frac{\partial^2\psi_n}{\partial p_y^2}+(C_{23}+C_{32})\frac{\partial^2\psi_n}{\partial p_y \partial p_x}+C_{33}\frac{\partial^2\psi_n}{\partial p_x^2}\right]+b_y=0 \quad (14)$$

4 TRANSFINITE INTERPOLATION (TFI)

This technique is used to generate initial grid which is confirming to the geometry encountered in different stages of plate and shape rolling. Suppose that there exists a transformation $\mathbf{r}(p_\xi, p_\eta) = \{p_x(p_\xi, p_\eta), p_y(p_\xi, p_\eta)\}^T$ which maps the unit square, $0 < p_\xi < 1$, $0 < p_\eta < 1$ in the computational domain onto the interior of the region ABCD in the physical domain such that the edges p_ξ = 0,1 map to the boundaries AB, CD and the edges p_η = 0,1 are mapped to the boundaries AC, BD. The transformation is used for this purpose is defined as

$$\mathbf{r}(p_\xi,p_\eta) = (1-p_\eta)\mathbf{r}_l(p_\eta) + \xi\mathbf{r}_r(p_\eta)\mathbf{r}_b(p_\xi) + \\ p_\eta\mathbf{r}_t(p_\xi) - (1-p_\xi)(1-p_\eta)\mathbf{r}_b(0) - (1-p_\xi)p_\eta\mathbf{r}_t(0) - \\ (1-p_\eta)p_\xi\mathbf{r}_b(1) - p_\xi p_\eta\mathbf{r}_t(1) \quad (15)$$

Where $\mathbf{r_b}$, $\mathbf{r_t}$, $\mathbf{r_l}$, $\mathbf{r_r}$ represent the values at the bottom, top, left and right edges respectively. The initial grid is refined through ENG [6]. **Figure 2** shows initial node generation through TFI and its correlation with ENG.

5 CONCLUSION

In this paper the thermal and mechanical formulations are given for hot shape rolling. The numerical method for the solution of the problem is based on meshfree LRBFCM. The preliminary result of mechanical model for elastic case is presented in **Figure 3**. The future work will include plastic deformation in a sequence of 10 rolling stands as recently installed in Štore –Steel Company.

6 REFERENCES

[1] J. Synka and A. Kainz, International Journal of Mechanical Sciences, 45 (**2003**), 2043–2060

[2] M. Glowacki, Journal of Materials Processing Technology,168 (**2005**), 336–343

[3] B. Šarler, G. Kosec, A. Lorbiecka and R. Vertnik, Mater. Sci. Forum, 649 (**2010**), 211–216

[4] G. Kosec and B. Šarler, Int. J. Cast. Met. Res., 22 (**2009**), 279–282

[5] R. Vertnik and B. Šarler, Int. J. Cast. Met. Res., 22 (**2009**), 311–313

[6] J. F. Thompson, B. K. Soni and N. P. Weatherill, Handbook of grid generation, 1st ed., CRC Press, USA 1999

[7] W. F. Chen and D. J. Han, Plasticity for Structural Engineers, 1st ed., Springer-Verlag, USA 1988, p. 606

UDK 669.715:620.17
Original scientific article/Izvirni znanstveni članek

ISSN 1580-2949
MTAEC9, 45(6)549(2011)

SOLIDIFICATION AND PRECIPITATION BEHAVIOUR IN THE AlSi9Cu3 ALLOY WITH VARIOUS Ce ADDITIONS

STRJEVANJE IN IZLOČANJE V ZLITINI ALSI9CU3 PRI RAZLIČNIH DODATKIH Ce

Maja Vončina, Stanislav Kores, Primož Mrvar, Jožef Medved

University of Ljubljana, Faculty of Natural Sciences and Engineering, Department of Materials and Metallurgy, Aškerčeva 12, 1000 Ljubljana, Slovenia
maja.voncina@omm.ntf.uni-lj.si

Prejem rokopisa – received: 2011-03-07; sprejem za objavo – accepted for publication: 2011-08-12

The effect of Ce additions on the AlSi9Cu3 alloy was investigated using an equilibrium thermodynamic calculation, thermal analysis, differential scanning calorimetry (DSC) and scanning electron microscopy (SEM). The purpose was to study the variations that occur during solidification and precipitation with different Ce additions, as well as theireffect on the mechanical properties.

The results show that Ce additions shift the temperature of the eutectic solidification (α_{Al} + Al_2Cu) and the solidus temperature to higher values. It was found that the precipitation reaction is more intense when the specimen is previously cooled with a higher cooling rate. Moreover, when the fraction of the precipitates regarding the temperature at different cooling rates was taken into account, it was found that the precipitation is faster when Ce is added and also when the specimen was cooled faster. Ce also changed the morphology of the eutectic Al_2Cu phase. Furthermore, the Ce phase was detected, indicating the Al–Ce–Cu–Si ($Al_9Ce_2Cu_5Si_3$) phase. The mechanical properties, such as hardness and tensile strength, increase with larger Ce additions.

Keywords: AlSi9Cu3 alloy, Ce addition, reaction kinetics, solidification and precipitation, mechanical properties

Vpliv dodatka Ce v zlitini AlSi9Cu3 je bil preiskan z uporabo izračuna ravnotežnega strjevanja, termične analize, diferenčne vrstične kalorimetrije (DSC) ter vrstične elektronske mikroskopije (SEM). Namen je bil preiskati spremembe, ki nastopijo pri strjevanju in izločanju v zlitini z različnimi dodatki Ce ter njegov vpliv na mehanske lastnosti.

Rezultati so pokazali, da dodatek Ce zviša temperaturo strjevanja evtektika (α_{Al}+ Al_2Cu) in solidus temperature k višjim vrednostim. Ugotovljeno je bilo, da reakcija izločanja poteče intenzivnejše, ko je vzorec predhodno ohlajen z večjo hitrostjo ohlajanja. Pri preiskavi deleža izločkov glede na različne temperature se pokaže, da poteče izločanje hitreje, ko zlitini dodamo Ce, ter prav tako, ko je vzorec predhodno hitreje ohlajen. Ce v zlitini AlSi9Cu3 spreminja tudi morfologijo evtektske faze Al_2Cu. Analizirali smo Ce fazo AlCeCuSi ($Al_9Ce_2Cu_5Si_3$). Mehanske lastnosti, kot sta trdota ter natezna trdnost, se povečujejo z dodatkom Ce v zlitini AlSi9Cu3.

Ključne besede: zlitina AlSi9Cu3, dodatek Ce, reakcijska kinetika, strjevanje ter izločanje, mehanske lastnosti

1 INTRODUCTION

Al–Si–Cu alloys are widely used for thin-wall castings[1] in automobile, aircraft and in the chemical industry. The AlSi9Cu3 alloy is a heat-treatable alloy with good castability. These alloys usually contain copper and often magnesium as the main alloying element, together with various other alloying elements or impurities, such as Fe, Mn or Cr.[2] Cu in the AlSi9Cu3 alloy reduces the corrosion resistance and improves the mechanical properties. A controlled cooling process and/or optimal alloying with Ce makes it possible to achieve suitable mechanical properties, like tensile strength and hardness. A small amount of Mg causes the formation of the Mg_2Si phase[3,4] and additionally it increases the mechanical properties in Al–Si–Cu alloys.[5,6,7,8,9] The microstructure in Al–Si alloys dictates the mechanical and technological properties of the castings. For this reason a specific microstructure and the mechanical properties must be achieved. This can be established with a smaller grain size and with a modification of the (α_{Al} + β_{Si}) eutectic and/or with high cooling rates.

Rare-earth metals, such as cerium (Ce), have been found to improve the mechanical properties of Al–Si castings by modifying their microstructure and enhancing their tensile strength[10] and ductility[11], heat resistance and extrusion behaviour.[12] It was reported that Ce-phases may act as nucleation sites for (Al) or (Si) crystals in both hypo- and hypereutectic Al-Si alloys.[13] Cerium has a high activity in an aluminium melt because of its specific electron structure. It forms a quaternary intermetallic compound with aluminium, silicon and copper and this leads to the formation of an Al–Ce–Cu–Si phase between the dendrite structure. The cerium phase acts as a barrier for dislocation movement that increases the mechanical properties of the material.[14].

This paper treats the influence of Ce addition on the course of the solidification, precipitation and cooling, and also of the cooling rate, on the solidification and precipitation and on the mechanical properties of the AlSi9Cu3 alloy.

2 EXPERIMENTAL

A commercial AlSi9Cu3 alloy was melted in an electric induction furnace.Various concentrations (w(Ce) = 0, 0.01, 0.02, 0.05 and 0.1) of pure (99.9 %) Ce were added. After 10 min the melt was poured into a measuring cell with a controlled cooling system (simple thermal analysis-STA) with the purpose of recording the cooling curves at different cooling rates. A new measuring cell for the controlled cooling of specimens from the melt to low temperatures was designed in order to obtain various cooling rates. Simultaneously, the specimens for the tensile tests were also cast into a mould made according to the DIN50125 standard. The characteristic solidification temperatures were determined from the cooling curves, and the influence of Ce was defined.

Differential scanning calorimetry (DSC) using a Jupiter 449c, NETZSCH, was applied to analyse the solidification process and to determine the characteristic temperatures of single reactions and the produced or consumed enthalpies. The measurements were carried out under a protective Ar atmosphere according to the temperature program: heating rate 10 °C/min up to 710 °C → holding at 710 °C for 10 min → cooling rate 10 °C/min. Moreover, the DSC curves were plotted, the temperatures of the precipitation were marked and the formation enthalpies of the precipitates were determined. The precipitation kinetics connected to the Ce addition and the cooling rate was also determined.

Light and electron microscopy were applied to analyse the microstructures. Single microstructural phases were determined quantitatively with the system for analysing images. A quantitative analysis for the identification of the phases was performed by energy-dispersive and wave length-dispersive X-ray spectroscopy. A cerium phase was identified. The hardness was measured using a universal Brinell hardness tester and the tensile strength was defined on as-cast specimens made according to the EN 10002-1 standard using a GLEEBLE 1500D simulator of thermomechanical states.

3 RESULTS AND DISCUSSION

The chemical composition of the investigated samples is presented in **Table 1**.

From the chemical composition, equilibrium solidification and calculated equilibrium the vertical cross-section diagrams were simulated using the Thermo-Calc program TCW5 and database COST507 (**Figure 1a**). The course of the equilibrium solidification was determined (**Figure 1b**).

The equilibrium solidification of the AlSi9Cu3 alloy proceeds as follows (**Figure 1**): Si_2Ti, AlFeSi-β, primary crystals of α_{Al}, AlMnSi-α, eutectic ($\alpha_{Al} + \beta_{Si}$) and just below the solidus temperature the Ce phase Al_8Ce. Under the solidus, the Mg_2Si and Al_2Cu-θ phase also precipitated.

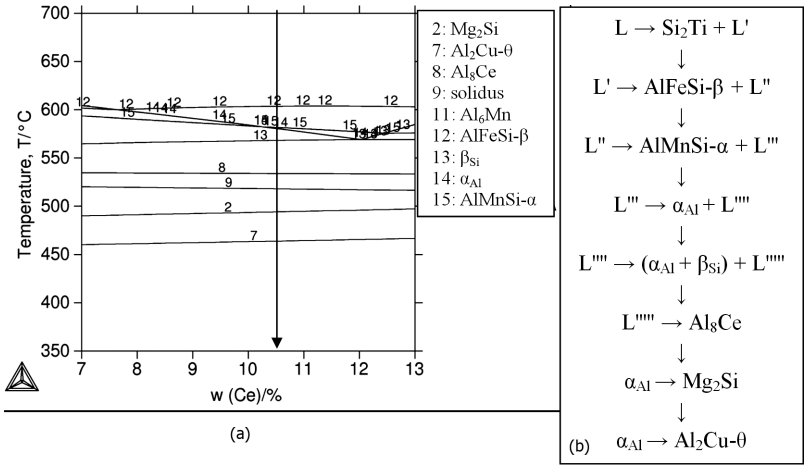

Figure 1: Equilibrium phase diagram (a) and schematic representation of equilibrium solidification of AlSi9Cu3 alloy (b) with w = 0.02 % Ce
Slika 1: Ravnotežni fazni diagram (a) ter shematski prikaz ravnotežnega strjevanja zlitine AlSi9Cu3 (b) z w = 0,02 % Ce

Table 1: Chemical composition of AlSi9Cu3 alloy, *w*/%
Tabela 1: Kemijska sestava zlitine AlSi9Cu3, *w*/%

Specimen	Mg	Mn	Cu	Ti	Fe	Si	Ce (nominal)	Ce (actual)	Al
AlSi9Cu3	0.35	0.242	2.61	0.04	0.694	10.72	0		rest
AlSi9Cu3 + 0.01 % Ce	0.34	0.27	2.55	0.04	0.75	10.60	0.01		rest
AlSi9Cu3 + 0.02 % Ce	0.35	0.29	2.685	0.04	0.80	10.66		0.015	rest
AlSi9Cu3 + 0.05 % Ce	0.32	0.29	2.565	0.04	0.81	10.59		0.043	rest

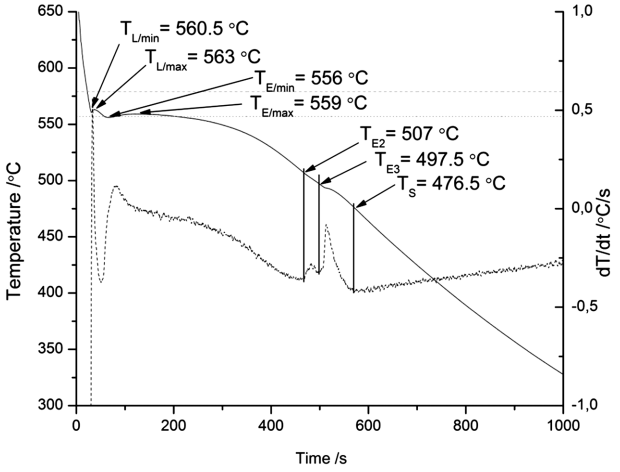

Figure 2: Cooling curve and differential cooling curve of AlSi9Cu3 alloy with w = 0.02 % Ce and with the theoretical calculated equilibrium liquidus and eutectic temperature (horizontal line)
Slika 2: Ohlajevalna in diferencirana ohlajevalna krivulja zlitine AlSi9Cu3 z w = 0,02 % Ce ter z vrisanima teoretično izračunanima ravnotežno likvidus in evtektsko temperaturo (vodoravne črte)

Figure 2 shows a typical cooling curve together with a differential cooling curve of the investigated AlSi9Cu3 alloy with 0.02 % Ce. The characteristic solidification temperatures were determined in all the specimens with various Ce additions (**Table 2**). The striped line indicates the theoretical, with the Thermo-Calc calculated, liquidus temperature calculated from the chemical composition:

$$T_{\text{L teor.}} = 656.38468 - 6.78571 \cdot w(\text{Si}) - 1.42857 \cdot w(\text{Cu}) + 1.34798 \cdot 10\text{–}10 \cdot w(\text{Fe}) - 1.04224 \cdot 10\text{–}10 \cdot w(\text{Mn}) - 3.15848 \cdot w(\text{Mg}) - 2.24953 \cdot w(\text{Zn})$$

The dotted line in **Figure 2** indicates the theoretically calculated eutectic temperature calculated from the chemical composition:

$$T_{\text{Eteor.}} = 574.2834 - 0.57134 \cdot w(\text{Si}) - 2.57143 \cdot w(\text{Cu}) - 3 \cdot w(\text{Fe}) - 1.14639 \cdot 10^{-10} \cdot w(\text{Mn}) - 5.73489 \cdot w(\text{Mg}) - 1.38954 \cdot w(\text{Zn})$$

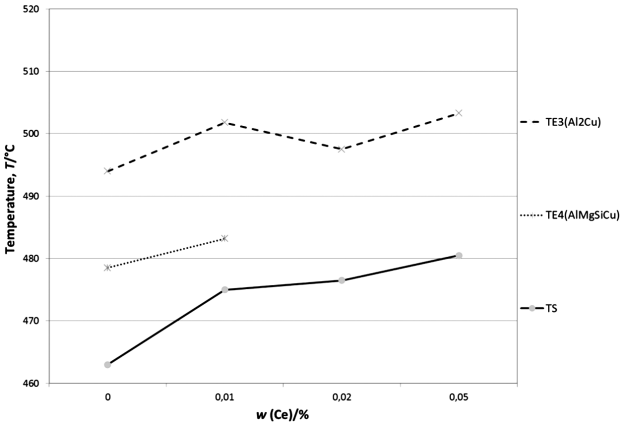

Figure 3: Comparison of some characteristic solidification temperatures for AlSi9Cu3 alloy with respect to Ce addition
Slika 3: Primerjava nekaterih karakterističnih temperature pri strjevanju zlitine AlSi9Cu3 glede na dodatek Ce

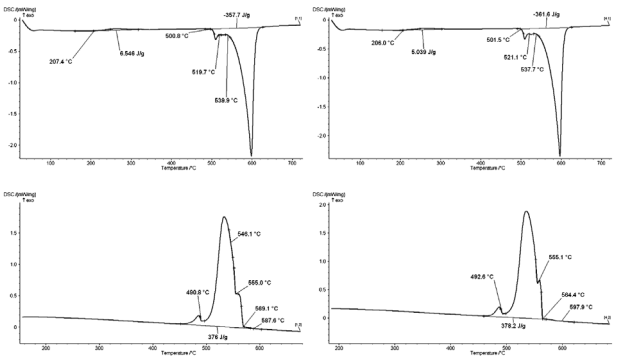

a) *b)*

Figure 4: Heating and cooling DCS curves of AlSi9Cu3 alloy without Ce (a) and with w = 0.02 % Ce (b)
Slika 4: Segrevalne in ohlajevalne DSC-krivulje zlitine AlSi9Cu3 brez Ce (a) in z w = 0,02 % Ce (b)

Table 2 and **Figure 3** represent the characteristic solidification temperatures with respect to the Ce addition. The temperature of the eutectic solidification (α_{Al} + Al_2Cu) and the solidus temperature shift to higher temperatures. The temperature of the eutectic solidification (α_{Al} + AlCuMgSi) could not be detected when larger

Table 2: Characteristic solidification temperatures for AlSi9Cu3 after STA
Tabela 2: Značilne temperature strjevanja zlitine AlSi9Cu3 po STA

w(Ce)/%	T_{Lteor}/°C	$T_{\text{L/min}}$/°C	$T_{\text{L/max}}$/°C	$\Delta T_{\text{L p.}}$/°C	$\Delta T_{\text{L r.}}$/°C
0	578.8	561	564	17.81	3
0.01	579.7	562	566.8	17.71	4.8
0.02	579.1	560.5	563	18.6	2.5
0.05	579.9	563.7	565.9	16.1	2.2

w (Ce)/%	$T_{\text{Eteor.}}$ /°C	$T_{\text{E/min}}$ /°C	$T_{\text{E/max}}$ /°C	$\Delta T_{\text{E p.}}$ /°C	$\Delta T_{\text{E r.}}$ /°C	$T_{\text{E2(Mg2Si)}}$ /°C	$T_{\text{E3(Al2Cu)}}$ /°C	$T_{\text{E4(AlCuMgSi)}}$ /°C	T_{S} /°C
0	557.4	556.5	559	0.9	2.5	512	494	478.5	463
0.01	557.5	563.9	564.7	–6.4	0.8	520.1	501.8	483.2	475
0.02	556.9	556	559	0.9	3	507	497.5		476.5
0.05	557.4	563.4	564.4	–6.0	1	523.2	503.3		480.5

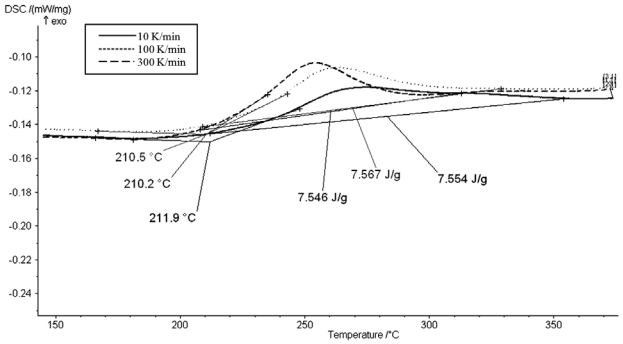

Figure 5: DSC curves of the precipitation region of AlSi9Cu3 alloy at different cooling rates

Slika 5: DSC-krivulje s področja izločanja zlitine AlSi9Cu3 pri različnih hitrostih ohlajanja

concentrations of Ce were added, presumably because these elements combined with Ce.

The DSC analysis was made on all the specimens after the STA. From the heating (**Figure 4a**) and cooling (**Figure 4b**), all the characteristic temperatures during heating/cooling were determined, including the melting/solidification and precipitation enthalpies with various Ce additions.

When the precipitation kinetics was investigated, it was found that the precipitation reaction is more intense

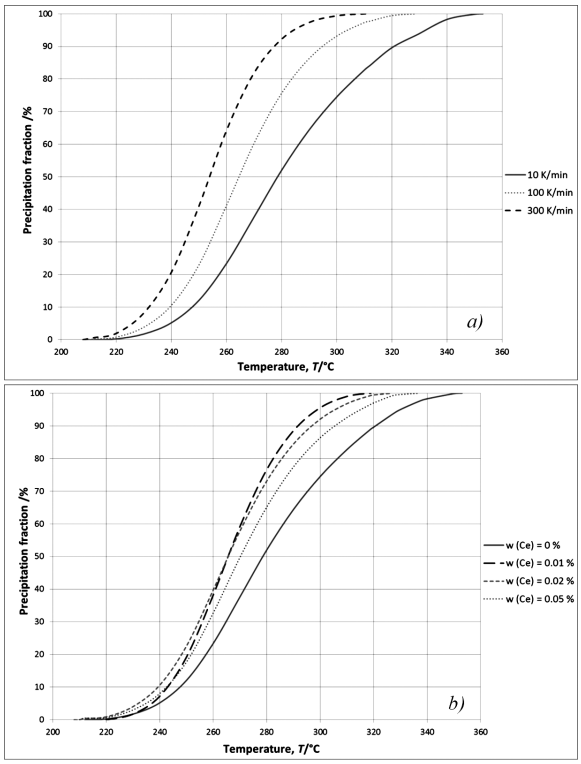

Figure 6: Fraction of Al_2Cu precipitates with respect to the temperature in the AlSi9Cu3 alloy at various cooling rates (a) and at various concentrations of Ce (b)

Slika 6: Delež izločkov Al_2Cu v odvisnosti od temperature v zlitini AlSi9Cu3 po različnih hitrostih ohlajanja (a) ter pri različnih koncentracijah Ce (b)

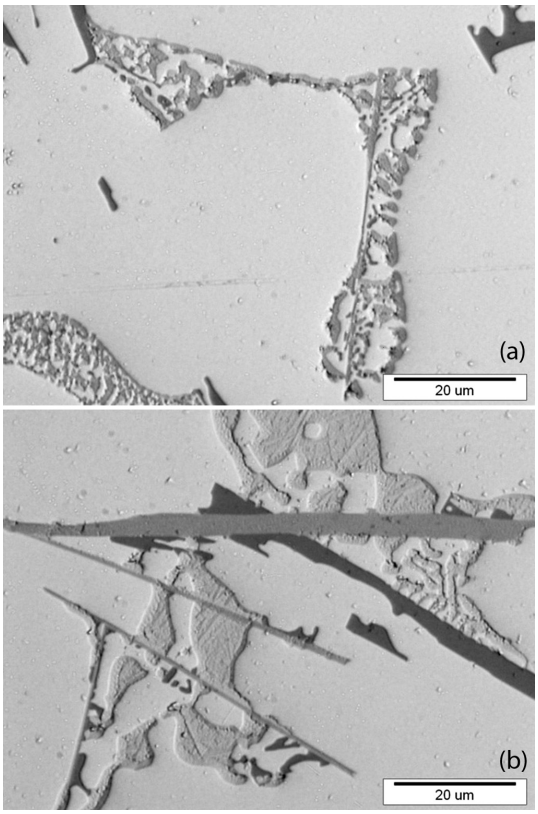

Figure 7: Microstructure of Al_2Cu phase without Ce (a) and with w = 0.05 % Ce (b)

Slika 7: Mikrostrukturni posnetek faze Al_2Cu brez Ce (a) in z w = 0,05 % Ce (b)

when the specimen is previously cooled faster (**Figure 5**). This is a consequence of a more supersaturated solid solution. Moreover, when the fraction of the precipitates regarding the temperature at different cooling rates was taken into account, it was found that the precipitation ki-

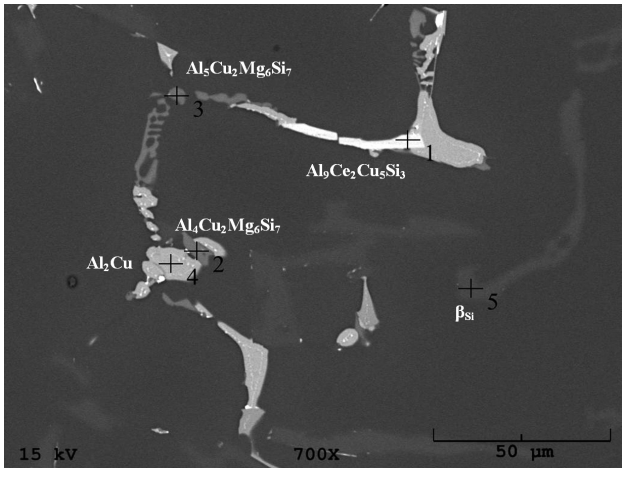

Figure 8: Microstructure (SEM) of AlSi9Cu3 + 0.02 % Ce with EDS analysis

Slika 8: Mikrostruktura (SEM) zlitine AlSi9Cu3 + 0,02 % Ce z EDS-analizo

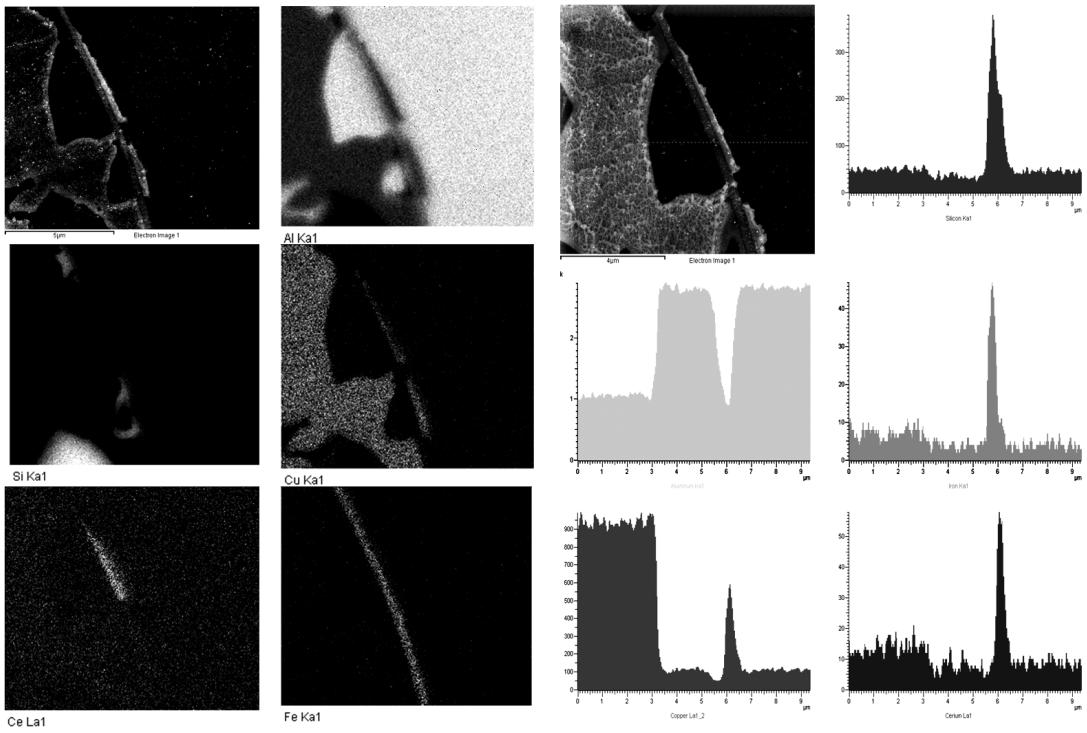

Figure 9: Mapping (a) and line analyses (b) of (α_{Al} + Al_2Cu) eutectic in AlSi9Cu3 alloy with w = 0.02 % Ce
Slika 9: Površinska porazdelitev elementov ter linijska analiza (b) evtektske faze (α_{Al} + Al_2Cu) v zlitini AlSi9Cu3 z w = 0,02 % Ce

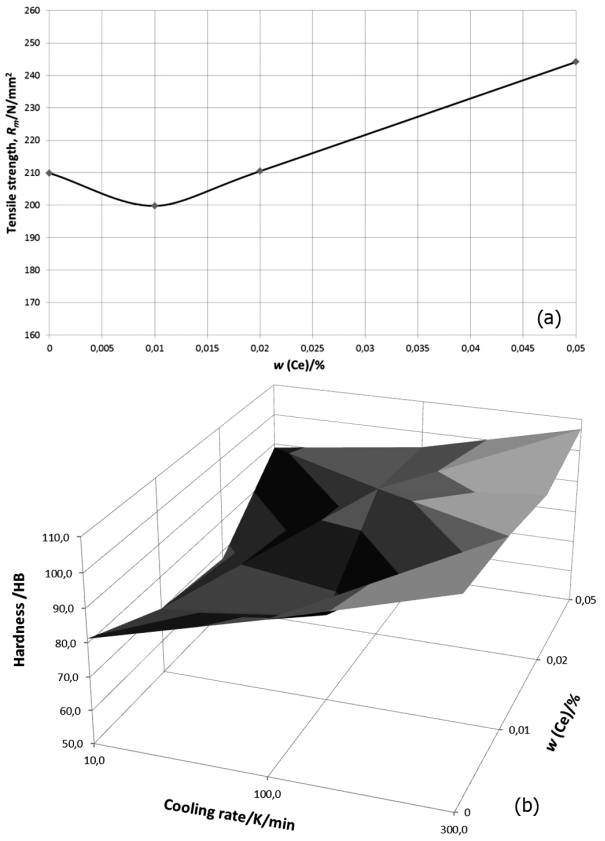

Figure 10: Tensile strength (a) and hardness (b) of AlSi9Cu3 alloy for various Ce additions
Slika 10: Natezna trdnost (a) ter trdota (b) zlitine AlSi9Cu3 pri različnih koncentracijah Ce

netics is faster when Ce is added (**Figure 6a**) and also when the specimen was cooled faster (**Figure 6b**).

When the microstructure was investigated, no influence on the size and distribution of the microstructure components was detected, only the morphology of the Al_2Cu phase changed. In the alloy without Ce, the eutectic phase Al_2Cu appears to be "crumbled" (**Figure 7a**), but when Ce was added the Al_2Cu phase was fully formed (**Figure 7b**).

Besides the usual phases that occur in these types of alloys, the Ce phase was also detected with the EDS analyser, indicating the Al–Ce–Cu–Si (calculated stoichiometry was $Al_9Ce_2Cu_5Si_3$, **Figure 8**) phase. This phase forms in a needle shape. To establish what happens with the Al_2Cu, mapping (**Figure 9a**) and line analyses (**Figure 9b**) through the Al_2Cu were made. It was proved that the Ce is bound to the Al_2Cu eutectic phase.

The tensile strength and Brinell hardness of the AlSi9Cu3 alloy with respect to Ce are presented in **Figure 10a and 10b**. The tensile strength for a small amount of Ce is slightly reduced and at a higher concentration of Ce it is increased, probably because of the modified Al_2Cu eutectic phase. The hardness due to the Ce addition was investigated for different cooling rates. For the smaller cooling rate (10 K/min) the hardness slightly decreased when 0.01 % Ce was added to the alloy, but it increased as well as the tensile strength for higher Ce additions. With higher cooling rates the hardness increased because the influence of the Ce was reduced.

4 CONCLUSION

The effects of Ce content on the solidification sequence, microstructure and mechanical properties of the AlSi9Cu3 alloy were investigated. Moreover, the reaction kinetics of the precipitation in the AlSi9Cu3 alloy was studied also. The results can be summarized as follows:

The equilibrium solidification of the AlSi9Cu3 alloy proceeds as follows: Si_2Ti, AlFeSi-β, primary crystals of α_{Al}, AlMnSi-α, eutectic ($\alpha_{Al} + \beta_{Si}$) and just below the solidus temperature the Ce phase Al_8Ce is precipitated. Below the solidus the Mg_2Si and Al_2Cu-θ phases are precipitated also. The data base should be complemented with multicomponent phases with Ce.

The temperature of the eutectic solidification (α_{Al} + Al_2Cu) and the solidus temperature are shifted to higher temperatures with the addition of Ce. The temperature of the eutectic solidification (α_{Al} + AlCuMgSi) could not be detected when greater concentrations of Ce were added.

When the precipitation kinetics was investigated it was found that the precipitation reaction is more intense for the specimen that was previously cooled faster. Moreover, when the fraction of the precipitates depending on the temperature at different cooling rates was taken into account, it was found that the precipitation is faster when Ce is added and also when the specimen was cooled faster.

Ce changed the morphology of the eutectic Al_2Cu phase with building into the Al_2Cu phase. Furthermore, the Ce phase was detected, indicating the Al–Ce–Cu–Si ($Al_9Ce_2Cu_5Si_3$) phase. This phase forms in a needle shape.

The tensile strength and the hardness vs. slower cooling for a small amount of Ce were slightly reduced. However, they were increased when a greater concentration of Ce is added, probably because of the modification of the Al_2Cu eutectic phase. With higher cooling rates the hardness increased and the influence of Ce is reduced.

Acknowledgements

The authors would like to thank dr. Franc Zupanič, University of Maribor, Faculty of Mechanical Engineering, and dr. Aleš Nagode, University of Ljubljana, Faculty of Natural Sciences and Engineering, for work on the SEM.

5 REFERENCES

[1] ASM Metals HandBook Volume 15 – Casting, 1988

[2] L. Lasa, J. M. Rodriguez-Ibabe, Characterization of the dissolution of the Al2Cu phase intwo Al–Si–Cu–Mg casting alloys using calorimetry, Materials Characterization 48 (2002), 371–378

[3] G. Terjesen, Effect of elevated temperature on tensile properties and fracture toughness of an AlSi10Mg alloy. Aluminium, 79 (**2003**) 9, 748–754

[4] B. K. Shah, S. D. Kumar, D. K. Dwivedi, Aging temperature and abrasive wear behaviour of cast Al-(4 %, 12 %, 20 %)Si-0.3 % Mg alloys, Materials and Design, 28 (**2007**), 1968–1974

[5] L. Bäckerud, G. Chai, J. Tamminen,Solidification Characteristics of Aluminum Alloys. Volume 2, Foundry Alloys. AFS/SKANALUMINIUM.Department of Structural Chemistry – Arrhenius Laboratory, University of Stockholm, 1990

[6] S. Esmaeili, D. J. Lloyd, W. J. Poole, Modelling of precipitation hardening for the naturally aged Al-Mg-Si-Cu alloy AA6111, ActaMaterialia, 51 (**2003**), 3467–3481

[7] S. Esmaeili, D. J. Lloyd, Modelling of precipitation hardening in pre-aged AlMgSi(Cu) alloys, ActaMaterialia, 53 (**2005**), 5257–5271

[8] Q. G. Wang, C. J. Davidson, Solidification and precipitation behaviour of Al-Si-Mg casting alloys, Journal of material science, 36 (**2001**), 739–750

[9] C. Vorge, M. Jucgues, M. P. Schmidt., Corrosion of Aluminium, 2001

[10] M. Vončina, S. Kores, J. Medved, Influence of Ce addition on the solidification and mechanical properties of AlSi10Mg alloy, Tofa 2010 discussion meeting on Thermodynamics OF Af, Book of abstracts and Programme, Faculdade de Engenharia da Universidade do Porto, Portugal, 2010, 75

[11] H. R. Ammar, C. Moreau, A. M. Samuel, F. H. Samuel, H. W. Doty, Influences of alloying elements, solution treatment time and quenching media on quality indices of 413-type Al–Si casting alloys, Materials Science and Engineering A, 20 (**2008**), 426–438

[12] Y. Wu, J. Xiong, R. Lai, X. Zhang, Z. Guo, The microstructure evolution of an Al–Mg–Si–Mn–Cu–Ce alloy during homogenization, Journal of Alloys and Compounds, 475 (**2009**) 1–2, 332–338

[13] J. Gröbner, D. Mirković, R. Schmid - Fetzer, Thermodynamic Aspects of the Constitution, Grain Refining, and Solidification Enthalpies of Al-Ce-Si Alloys, metallurgical and materials transactions A, 35A (**2004**), 3349–3362

[14] Y. G. Zhao, Q. D. Qin, W. Zhou, Y. H. Liang, Microstructure of the Ce-modified in situ Mg2Si/Al–Si–Cu composite, Journal of Alloys and Compounds, 389 (**2005**), L1–L4

UDK 669.14.018.44:539.37
Original scientific article/Izvirni znanstveni članek

ISSN 1580-2949
MTAEC9, 45(6)555(2011)

EFFECT OF CHANGE OF CARBIDE PARTICLES SPACING AND DISTRIBUTION ON CREEP RATE OF MARTENSITE CREEP RESISTANT STEELS

VPLIV SPREMEMBE RAZDALJE MED KARBIDNIMI IZLOČKI IN NJIHOVE PORAZDELITVE NA HITROST LEZENJA MARTENZITNIH JEKEL, ODPORNIH PROTI LEZENJU

Danijela A. Skobir Balantič, Monika Jenko, Franc Vodopivec, Roman Celin

Institute of Metals and Technology, Lepi pot 11, SI-1000 Ljubljana, Slovenia
danijela.skobir@imt.si

Prejem rokopisa – received: 2011-10-04; sprejem za objavo – accepted for publication: 2011-10-25

The creep rate dependence of particles coarsening and spacing as well as distribution in analysed considering quoted equations. A simple method for assessment of particle spacing is proposed. Accelerated creep rates at 580 °C for CrV and CrVNb steel after different tempering times at 800 °C and 650 °C are calculated and determined experimentally. The rate of microstructural processes increases the creep rate at 800 °C in the CrV steel by 36 times and in the CrVNb by 57 times greater.

Key words: creep resistant steel, creep rate, carbide particles, particles spacing, distribution of particles, tempered martensite

Matematično smo analizirali odvisnost hitrosti lezenja od rasti izločkov in njihove medsebojne razdalje ter porazdelitve. Predlagali smo preprosto metodo za oceno medsebojne razdalje med izločki. Izračunali in eksperimentalno smo določili pospešene hitrosti lezenja pri 580 °C za jekli CrV in CrVNb po različnih časih žarjenja pri 800 °C in 650 °C. Mikrostrukturni procesi, ki vplivajo na zvišano hitrost lezenja, potekajo v jeklu CrV 36-krat hitreje in v jeklu CrVNb 57-krat hitreje pri 800 °C.

Ključne besede: jekla odporna proti lezenju, hitrost lezenja, karbidni izločki, razdalja med karbidnimi izločki, porazdelitev izločkov, popuščeni martenzit

1 INTRODUCTION

Modern creep resistant steels have a microstructure consisting of a distribution of carbide particles in ferrite with a significant content of chromium and molybdenum in solid solution.[1,2] In these steels particles of intermetallic (Lawes) phases are also found,[3,4] depending on steel composition and tempering temperature. These particles are generally much coarser than carbide particles,[3,4] have a minor effect on creep rate and will be omitted in further discussion. The great majority of particles consists of carbides with different stability at increased temperatures, mostly of $M_{23}C_6$ and MC particles. The composition of $M_{23}C_6$ particles depends on annealing temperature, however, the content of chromium is always much higher than the contents of iron and molybdenum.[5,6] MC particles are mostly vanadium and niobium carbides that may also have a minor content of nitrogen.

The effect of temperature on the solubility of carbide phases is given by the general relation:

$$lg\ [M]\ [C] = A + (B/T) \qquad (1)$$

with $[M]$ and $[C]$ mass fractions of elements in solid solution in ferrite, A and B – constants and T/K – temperature.

At low solubility, particles are more stable and coarse slower because, according to the LSW equation (2), the coarsening rate depends of volume diffusion transport, which is smaller by low content of carbide forming elements in substitutional solution in ferrite. The solubility products for carbides in ferrite were established for VC and NbC in structural steels with a much lower content of chromium.[7,8] These products can not be used reliably for creep resisting steels with much higher content of chromium which is a strong carbide forming element and may affect the solubility of MC carbides. Based on a thermodynamic analysis and on solubility product of VC in structural steel, it was calculated that at 873 K (600 °C) the solubility of NbC particles in ferrite was for one order of magnitude lower than for VC carbide.[9] The solubility can be deduced also by Thermocalc analysis.

The coarsening rate of carbide particles is calculated applying the Lifshitz-Slyozov-Wagner[10] (LSW) equation:

$$\Delta d^3 = d_t^3 - d_0^3 = 8\ S\gamma\Omega Dt\ /\ 9k_BT \qquad (2)$$

With d_t – particles size at tempering time t, d_0 – initial particles size, S – content of carbide constituting metal in solution in the matrix, γ – carbide particle matrix interfacial energy, Ω – volume of diffusing atoms, k_B – Boltzmann constant, D – diffusion coefficient and T – temperature in K. In ref.[11] the exponent 2 was proposed for coarsening of grain boundary particles.

For the 0.18C-11.7Cr-1Mo-0.29V steel, the experimental coarsening rate based on the assessment of particles size after tempering of steel specimens up to 1356 h

at 800 °C was $k_{ce} = 1.48 \times 10^{-26}$ m^3 s^{-1} and in acceptable agreement with the coarsening rate $d^3_{cc} = 7.25 \times 10^{-27}$ m^3 s^{-1} deduced applying the LSW equation.[12] The increase of size of particles at a determined temperature can be calculated using the simple relation:[11,12,13,14]

$$\Delta d^3 = k_{ci} t \tag{3}$$

with k_{ci} – isothermal coarsening rate.

Based on the acceptable agreement of calculated and experimental coarsening rate at 800 °C, assuming that by change of temperature in equation (1) only the diffusion constant changed and using as base the coarsening rate calculated for the temperature 800 °C, for the calculation of coarsening rate of $M_{23}C_6$ particles in range 550 °C to 800 °C the relation was obtained:[12]

$$d^3_{cc,T} = k_{cc,Cr,1073} (D_{Cr,T}/D_{Cr,1073}) (T/1073)\, t \tag{4}$$

with k_{cc} – calculated coarsening rate at 800 °C, T/K – temperature, D – diffusion constant, t/s – time.

The coarsening rate of 2.89×10^{-27} m^3 s^{-1} at 750 °C was calculated for $M_{23}C_6$ particles in the steel 0.18C-11.7Cr-1Mo-0.29V using this equation and $S = 0.277$ J m^{-2} very similar to that reported in ref.[15] of 2.82×10^{-27} m^3 s^{-1} calculated using a model based on equations (1) and (2). At low temperature the differences obtained using equation (4) and experimental data on assessment particle size may be affected by the simultaneous coarsening of particles of different carbides.

For the calculation of the coarsening rate for VC particles at the temperature of 650 °C a modification of equation (4) was proposed with introducing of proper ratio of parameters for chromium and vanadium[12] in equation (1), thus:

$$k_{cc,VC,} = k_{cc,Cr} (S_V D_{V,K} \gamma_{M23C6} \Omega_V / S_{Cr} D_{Cr,K} \gamma_{MC} \Omega_{Cr})$$
$$k_{cc,v,923\ K} = 4.77 \times 10^{-29} \times 0.01623 =$$
$$= 1.28 \times 10^{-31} \text{ m}^3 \text{ s}^{-1} \tag{5}$$

For the 0.18C-11.7Cr-1Mo-0.29V steel and the temperature of 650 °C the calculated coarsening rate for VC particles was for about two orders of magnitude lower than for $M_{23}C_6$ particles.[12]

Creep increases the number of mobile dislocations in steel and for the calculation of the density of these dislocations the relation was proposed[12,16]:

$$\rho = \sigma/\alpha\, MGb \tag{6}$$

with σ/MPa – stress, $\alpha = 0.4$ – constant $M = 3$ (Taylor factor), G – shear modul at creep temperature and b – Burgers vector.

By creep tests at 923 K by 80 MPa stress of a 0.14C-12Cr-1.5Mo-0.2V-0.05Nb-0.05N steel the size of MX particles was assessed in grip and in gauge of tested specimens.[17] Using the simplified relation $\Delta d^3 = k_{ci}\, t$ it was deduced that the coarsening rate was 3.73 times greater in the gauge than in the grip part of specimens and, according to equation (6), the density of mobile dislocations[12] in the gauge part of specimen was of 2.40×10^{13} m^{-2}. The increased coarsening of particles in gauge part of specimens in ascribed to higher density of mobile dislocations.

For the dependence of creep rate on different physical parameters related to the tested steel the equation was proposed:[18, 19]

$$\dot{\varepsilon} = \left(\frac{b^2}{k_B TG} \right) \lambda \rho \sigma^2 D \tag{7}$$

with: $\dot{\varepsilon}$ – creep rate, b – Burgers vector, k_B – Boltzmann constant, T/K – temperature, G – shear modulus, σ – acting stress, D – diffusion coefficient and ρ – density of mobile dislocations.

A better fit to experimental values of creep rate was found by modification of equation (7) with introduction of a constant (A) accounting also for particles spacing, a stress exponent $n > 2$, the rationalisation of the stress σ with the shear modulus and yield stress at creep temperature and the threshold stress σ_{th}, below which, theoretically, no creep could occur[20]:

$$\dot{\varepsilon} = A \left(\frac{DGb}{k_B T} \right) \left(\frac{\sigma - \sigma_{th}}{G} \right)^n \tag{8}$$

In the detachment concept of interaction of particles and mobile dislocations the particle size is included, as parameter of a real microstructure:[21, 22, 23, 24]

$$E = Gb^2 r \left[(1-k) \left(1 - \frac{\sigma}{\sigma_d} \right) \right]^{3/2} \tag{9}$$

$$\dot{\varepsilon} = \left(\frac{6\lambda\rho}{k_B T} \right) \cdot \exp\left(-\frac{E}{k_B T} \right) \tag{10}$$

with E – creep activation energy, σ_d – detachment stress, r – average particles size and the relaxation parameter $k = T_p/T_m$, with T_m – dislocation line energy in the matrix and $T_{2\,-}$ the dislocation line energy decreased by the attraction force precipitate – dislocation. The value of the parameter k is $(0 < k < 1)$.

Theoretically, creep and self diffusion activation energies for pure α iron are about 300 kJ/mol.[25] On the base of lifetime of specimens tested at different temperatures,[26] creep activation energies of about 600 kJ/mol were calculated.[27,28] In ref.[29] it is suggested that the difference may be related partially to the increase of creep rate due to the change of distribution of particles during creep tests.

The differences in creep rate for 0.18C-11.7Cr-1Mo-0.29V tempered for 672 h and 1356 h at 800 °C calculated according to equation (7) and experimental creep rate were of 1.53 and 2.26 times, while it was of several sizes of magnitudes greater if calculated according to equation (9). This indicates as unreliable the detachment model of interaction of a mobile dislocation and carbide particles in creep resistant steels with the microstructure of tempered martensite.[29] In all quoted equations it is assumed that the distribution of particles in ferrite is uniform. However, in steels the particles dis-

tribution is not uniform, since by tempering of martensite carbide particles are precipitated at grain boundaries and subboundaries and in the interior of grains and the coarsening rate is greater for particles situated at grain boundaries, where the diffusion rate is greater.

In investigations on 0.18C-11.7Cr-1Mo-0.29V steel tempered for 2 h to 1356 h at 800 °C [30] it was found that the average $M_{23}C_6$ particles size (d) increased with tempering time (t) as $d^3 = 1.48 \times 10^{-26} \times t$ m^3 s^{-1}, which is much slower than the rate of decrease of the number of carbide stringers of $n_s = 3.15 \times 10^{-17}$ m^2 s^{-1}. The difference is related to the difference in volume and boundary diffusion rate. Accordingly, the delaying effect of stringers on creep rate, which is very strong by sufficient stringers density, is ended relatively fast and by a critical stringers density of about 0.5×10^2 mm^{-2} the creep rate is increased for about one order of magnitude (**Figure 1**).

The particle spacing (λ) can be calculated from the relation[18]:

$$\lambda = (4d/\pi \cdot f^{A/3}) \quad (11)$$

with f – volume share of carbides in the investigated steel.

Assuming that carbide particles are uniformly distributed in the micrograph and situated in the centre of a square with the side equal to particles spacing, the spacing could be deduced without prior assessment of particles size and knowledge of the volume fraction of the carbide phases with the relation:

$$\lambda = (F/N)^{1/2} \quad (12)$$

with F – as surface of a micrograph with N carbide particles.

As mentioned earlier, the creep rate for the 0.18C-11.7Cr-1Mo-0.29V steel was calculated using equation (7) for two points in **Figure 1** below the critical stringers density using the particles spacing deduced according to relation (11), the calculated volume of $M_{23}C_6$ carbide content and experimentally assessed average particles size.

Specimens of a 0.18C-11Cr-0.94Mo-0.31V (steel a) and 0.10C-7.9Cr-0.98Mo-0.23V-0.11Nb (steel b) steels with microstructure in **Figures 2, 3** and **4** were cut out

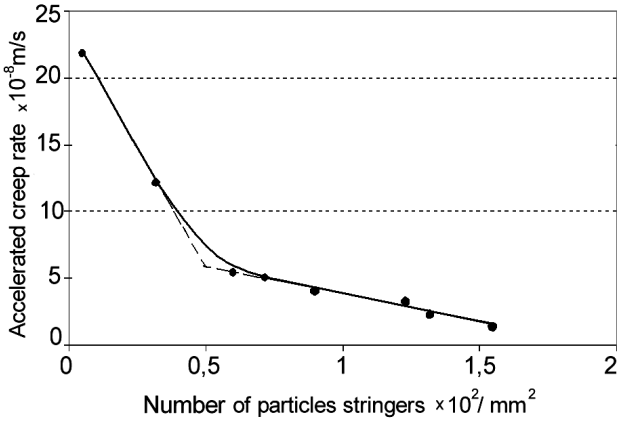

Figure 1: 0.18C-11.7Cr-1Mo-0.29V steel. Dependence of accelerated creep rate on the number of grain boundary stringers of carbide particles in tempered martensite[29]

Slika 1: Jeklo 0.18C-11.7Cr-1Mo-0.29V. Odvisnost pospešene hitrosti lezenja od števila nizov karbidnih izločkov po mejah zrn v popuščenem martenzitu[29]

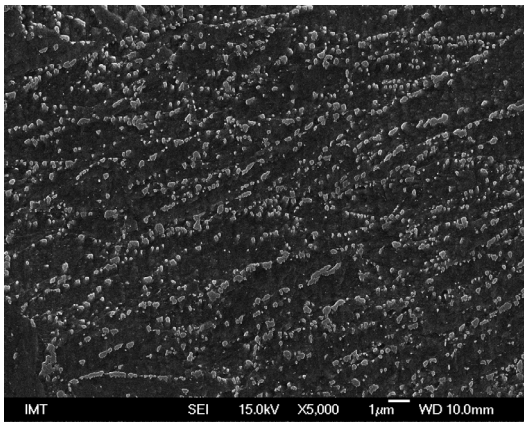

Figure 2: Initial microstructure of steel (a)

Slika 2: Izhodna mikrostruktura jekla (a)

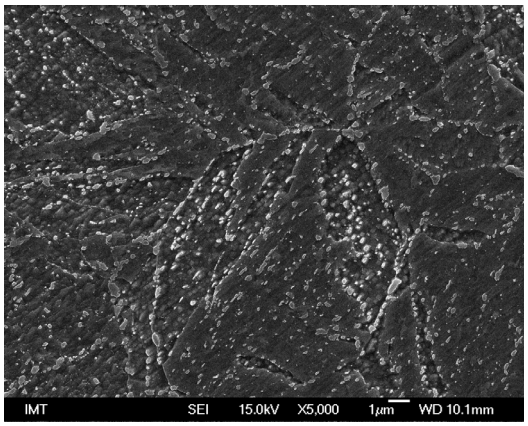

Figure 3: Initial microstructure of steel (b)

Slika 3: Izhodna mikrostruktura jekla (b)

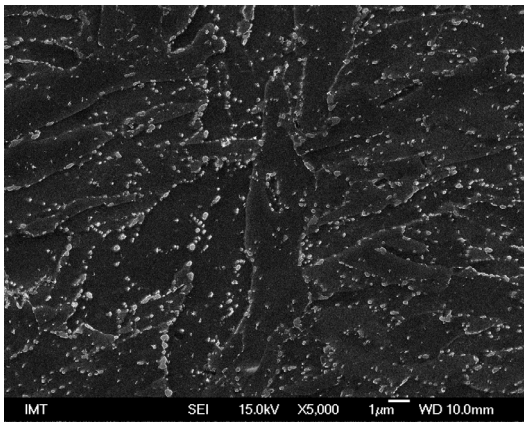

Figure 4: Microstructure of steel (b) after 1 year of tempering at 650 °C

Slika 4: Mikrostruktura jekla (b) po enem letu žarjenja na 650 °C

Table 1: Experimental and calculated creep rate for specimens of steels a) 0.18C-11.7Cr-1Mo-0.29V, b) 0.2C-11Cr-0.94Mo-0.31V and c) 0.10C-7.9Cr-0.98Mo-0.23V-0.11Nb tempered for different times at 800 °C and 650 °C. Test temperature 580 °C, stress 170 MPa and time 100 h.
Tabela 1: Eksperimentalne in izračunane vrednosti hitrosti lezenja za vzorce jekel a) 0.18C-11.7Cr-1Mo-0.29V, b) 0.2C-11Cr-0.94Mo-0.31V in c) 0.10C-7.9Cr-0.98Mo-0.23V-0.11Nb, žarjene različno dolgo pri 800 °C in 650 °C. Temperatura preskušanja 580 °C, napetost 170 MPa in čas 100 h.

Tempering	Particles spacing λ (10^{-6} m)	Creep rate (s^{-1}) experimental	calculated	Exp./cal.
800 °C, 672 h, a	1.24	12.2×10^{-8}	7.93×10^{-8}	1.53
800 °C, 1356 h, a	1.50	21.8×10^{-8}	9.62×10^{-8}	2.26
650 °C, 2h, b	0.53	4.76×10^{-8}	3.39×10^{-8}	1.41
650 °C, 8760 h, b	0.61	10.2×10^{-8}	3.90×10^{-8}	2.61
650 °C, 2 h, c	0.507	1.47×10^{-8}	3.24×10^{-8}	0.45
650 °C, 8760 h, c	0.508	2.03×10^{-8}	3.25×10^{-8}	0.62

from industrial tubes and tempered for up to 8760 h (1 year) at 650 °C. [31] For both steels the accelerated creep rate was determined with 100 h static test at 580 °C and the load of 170 MPa, as for the earlier mentioned steel.[30] For the steel (a), the particles spacing was calculated using equation (11) and particles size assessed on SE micrographs at magnification 10^4 and 2×10^4 times, while the particles spacing for steels (b) and (c) was calculated using equation (12) and particles counting on SE micrographs at magnification of 5×10^3 times, where only particles with size of about 0.1 μm (about 20 nm) and more were discernible, sufficiently clearly.

In **Table 1** particles spacings, calculated as well as experimental creep rates are given.

By steel (a) and (b) the ratio of experimental and calculated creep rate is above 1 for both tempering temperature, while it is below 1 for the steel (c) tempered at 650 °C. The different ratio of calculated and experimental rate for the steel (c) may be explained assuming that after both tempering temperatures by steels (a) and (b) on used SE micrographs the great majority of both kinds of carbide particles ($M_{23}C_6$ and VC) was visible, while the resolution of micrographs of steel (c) was too small for NbC particles. This explanation is supported by the different stability of carbides, since after tempering at 800 °C in steel (a) consisted only of $M_{23}C_6$ particles, in steel (b) at 650 °C of $M_{23}C_6$ and VC and in steel (c) of $M_{23}C_6$, VC and NbC particles. Data in **Table 1** indicate that the difference between calculated and experimental creep rate is greater after longer tempering time at both temperatures and independent of particles spacing. As the creep rate is related to the density of particles stringers, it is concluded, that also by longer tempering at 650 °C creep rate was changed by decrease of the effect of stringers of particles.

3 CONCLUSIONS

The following conclusions on the effect of changes in microstructure, i.e. changes in spacings and distribution of carbide particles, are based on data from quoted references and on results of investigations of three creep resistant steels.

- a simple method for assessment of particles spacing was devised based on the assumption that all particles in a micrographs are situated in the centre of a square with the side equal to particles spacing;
- the creep rate delaying effect of stringers of carbide particles at grain and subgrain boundaries is significantly stronger than the effect of particles distributed uniformly in the grains interior;
- when by tempering of the steel the density of particles stringers (number of stringers per unity of the examined surface) is diminished rapidly below a critical level, the creep rate is increased strongly, for about one order of magnitude, in case of tempering the 0.18C-11.7Cr-1Mo-0.29V steel at 800 °C;
- the creep rates determined experimentally and calculated using the Ashby equation with the stress exponent $n = 2$ agree acceptably and differences of both rates depend also on the distribution of particles. The effect of distribution of particles was confirmed for steels with the microstructure with only $M_{23}C_6$ as well as microstructures with $M_{23}C_6$, VC and NbC particles.
- at 650 °C the effect of tempering time on change of distribution of particles is much lower than at 800 °C. In the first case the creep rate was increased 12.1 times after 1356 h of tempering, while at 650 °C, the creep rate was increased for 2.14 times for the CrV steel and 1.38 times for the CrVNb steel after 8760 h of tempering. Thus the processes occurring in microstructure by tempering at 800 °C decrease the CrV creep resistance for about 36 times faster for the CrV steel and 57 times for the CrVNb steel than processes at the for 150 °C lower temperature of 650 °C.

4 REFERENCES

[1] K. H. Mayer, F. Masuyama: The development of creep resistant steels; Ed. F. Abe, T-U. Kern, R. Viswanathan: Creep resistant steels, Woodhead Publ. LTD., Cambridge, England, (**2008**), 15–77
[2] F. Abe: Strengthening mechanisms in steel for creep and creep rupture; Ed. F. Abe, T-U. Kern, R. Viswanathan: Creep resistant steels, Woodhead Publ. LTD., Cambridge, England, (**2008**), 279–304
[3] K. Yamamoto, Y. Kimura, Y Mishima: ISIJ Intern. 42 (**2003**), 1253–1259

[4] A. Aghajani, F. Richter, C. Somsen, S. G. Fries, I. Steinbach, G., Eggeler: Scripta Mater., 61 (**2009**), 1068–1071
[5] D. A. Skobir, Dr. thesis, Univ. of Ljubljana, **2003**
[6] D.A. Skobir, F. Vodopivec, M. Jenko, S. Spaić, B. Markoli: Zeit. Metallkunde, 95 (**2004**), 1020–1024
[7] K. Narita: Trans. ISIJ, (**1975**), 15, 145–151
[8] F. Vodopivec, Kovine, zlitine, tehnologije 26 (**1992**), 319–328
[9] F. Vodopivec, M. Jenko, J. V. Tuma: Metalurgija (Metallurgy) 45 (**2006**), 147–153
[10] J. W. Martin, R. D. Doherty, B. Cantor: Stability of microstructure in metallic systems; Ed. Cambridge Un. press, U.K., 1997. p. 242 and 272
[11] K. Maruyama, K. Sawada, J. Koike: ISIJ Intern.41 (2001), 641–653. Fundamental aspects of creep deformation and deformation mechanism map; Ed. F. Abe, T-U. Kern, R. Viswanathan: Creep resistant steels, Woodhead Publ. LTD., Cambridge, England, (**2008**), 265–278
[12] F. Vodopivec, D. A. Skobir, B. Zuzek, M. Jenko: ISIJ Intern., Submitted for publication
[13] W. Blum: Mechanisms of creep deformation in steel; in F. Abe, T-U. Kern, R. Wiswanathan: Creep resistant Steels, Woodhead publ., Cambridge, 2008, 366–400
[14] J. Hald, L. Korcakova: ISIJ Intern.43 (**2003**), 420–427
[15] A. Gustafson, J. Agren: ISIJ Intern. 41 (**2001**), 356–360
[16] K. Maruyama: Fundamental aspects of creep deformation and deformation mechanism map; Ed. F. Abe, T-U. Kern, R. Viswanathan: Creep resistant steels, Woodhead Publ. LTD., Cambridge, England, (**2008**), 265–278
[17] M. Taneike, M. Kondo, T. Morimoto: ISIJ Intern. 41 (**2001**), S111–S 115
[18] E. Hornbogen: Einfluss von Teilchen einer zweiter Phase aus das Zeitverhalten; W. Dahl, W. Pitch: Festigkeits- und Bruchverhalten bei höheren Temperaturen, Verl. Stahleisen, Düsseldorf, (**1980**), 31–52
[19] M.F. Asby: Proc. Sec. Int. Conf. On Strength of Metals and Alloys, (1970), Am. Soc. Metals, ASM, Metals Park, Ohio, Ca, 507. Loc. Cit. ref. 15
[20] B. Wilshire, H. Burt: Scripta mater. 53 (**2005**), 909–914
[21] J.H. Schröder, E. Artz: Scripta metall., 19 (**1985**), 1129–1134
[22] J. Rösler, E. Artz: Acta metal., 38 (**1990**), 671–683
[23] E. Artz, D.S. Wilkinson: Acta metall., 34 (**1986**), 1893–1898
[24] E. Artz, J. Rösler: Acta metal., 36 (**1988**), 1053–1060
[25] R. W. K. Honeycombe: The Plastic deformation of Metals, 2nd Ed., E. Arnold, 1985, 372
[26] J. Čadek, V. Šustek, M. Pahutová: Mat. Sci. Eng. A225, (**1997**), 22–28
[27] A. Nagode, B. Ule, M. Jenko, L. Kosec: Steel Res. Int. (**2007**), 638–642
[28] B. Ule, A. Nagode: Mat. Sci. Techn. 23 (**2007**), 1367–1374
[29] F. Vodopivec, J. Vojvodič-Tuma, B. Šuštaršič, R. Celin, M. Jenko: Mat. Sci.Techn. 27 (**2011**), 937–942
[30] D. A. Skobir, F. Vodopivec, L. Kosec, M. Jenko, J.Vojvodič-Tuma: Steel Res. Int. 75 (**2004**), 196–202
[31] J. Vojvodič-Gvardjančič, D. Kmetič, R. Celin, B. Arzenšek, F. Vodopivec: Report NCRI 377/2007, Institute of Metals and Technology, Ljubljana, Slovenia

UDK 616.31:539.3
Original scientific article/Izvirni znanstveni članek

ISSN 1580-2949
MTAEC9, 45(6)561(2011)

STRESS-STRAIN ANALYSIS OF AN ABUTMENT TOOTH WITH REST SEAT PREPARED IN A COMPOSITE RESTORATION

NAPETOSTNO-DEFORMACIJSKA ANALIZA OPORNEGA ZOBA Z ZAPORNIM SEDEŽEM, IZDELANA S KOMPOZITNIM POPRAVILOM

Ljiljana Tihaček Šojić[1], Aleksandra M Lemić[1], Dragoslav Stamenković[1], Vojkan Lazić[1], Rebeka Rudolf[2,1], Aleksandar Todorović[1]

[1]Faculty of stomatology, University of Belgrade, Dr. Subotića 8, 11000 Beograd, Serbia
[2]University of Maribor, Faculty of Mechanical Engineering, Smetanova 17, 2000 Maribor, Slovenia
saskam@eunet.rs

Prejem rokopisa – received:2011-02-02 ; sprejem za objavo – accepted for publication: 2011-04-06

Placing a composite restoration on abutments for the removable of partial dentures gives favorable aesthetic results with minimal intervention. The objective of this paper is to analyze the stress distribution of a tooth with occlusal rest-seat preparation in the composite and compare it to the biomechanical behavior of an intact tooth, assuming that the stress and strain distribution throughout the intact tooth provides the control scenario. For this finite-element study two different models were designed. The first model was the three-dimensional (3D) model of an intact tooth, and the other one was a 3D model of a tooth with a composite restoration and an appropriate occlusal rest-seat preparation. Load stimulations were performed when the rest was fully seated on its corresponding rest seat and abutment tooth in order to obtain data about the biomechanical behavior of the abutment tooth compared to the intact tooth's stress-distribution pattern. The results of our analyses are presented and analyzed qualitatively. The occlusal loading effect along the sound tooth exhibits a wider high-stress area, localized in correspondence with the occlusal enamel, than the restored teeth. This is due to the rigidity of the enamel. The reduction in the stress values occurs in the composite restoration, which is less rigid. Its lower rigidity allows larger cusp movements. The stress-distribution pattern of the restored tooth with the rest seat showed that introducing an occlusal restoration does not differ from the intact tooth globally, but locally. Our findings indicate that the composite rest-seat restoration absorbs the loading, so reducing the stresses inside the tooth's structure.

Key words: composite rest seat, abutment tooth, stress distribution, finite element method (FEM)

Postavitev kompozitnega popravila opore za odstranljive dele zobovja daje dobre estetske rezultate z minimalno intervencijo. Cilj tega članka je analizirati porazdelitev napetosti na zobu z zapornim sedežem s kompozitno zaporo in jo primerjati z biomehanskim vedenjem intaktnega zoba s predpostavko, da odloča razdelitev napetosti in deformacije intaktnemu zobu. Za to študijo sta bila na podlagi končnih elementov razvita dva različna modela. Prvi je tridimenzionalen (#D) model intaktnega zoba, drugi pa je 3D-model zoba s kompozitno restoracijo in ustrezno pripravo zapornega sedeža, da bi tako dobili podatke o biomehanskem vedenju mostičnega opornika in o porazdelitvi napetosti v intaktnem zobu. Rezutati so prikazanai in analizirani kvalitativno. Zaporna obremenitev povzroči široko področje visoke napetosti v zdravem zobu zaradi stika s sklenino in ne restoriranega zoba. To je posledica velike togosti sklenine. Manjše so napetosti v manj togi kompozitni restoraciji, kar omogoča večje premik opornega vrha. Porazdelitev napetosti restoriranega zoba z opornim sedežem kaže, da uporaba zaporne restoracije ne vpliva globalno, ampak lokalno. Ugotovitve kažejo, da popravilo zob z oporo absorbira obremenitev, ker zmanjša napetosti v strukturi zoba.

Ključne besede: kompozitna opora, oporni zob, porazdelitev napetosti, FEM

1 INTRODUCTION

The preparation of occlusal rest seats on the supporting, corresponding surfaces of the abutment teeth is widely recommended as a way of promoting axial load[1]. A removable partial denture (RPD) designed and manufactured in that manner fulfils the functional, prophylactic and aesthetic demands placed upon it. Occlusal rest-seat preparation demands cutting the enamel tissue in order to achieve "spoon-shaped" depressions with the proper dimensions.[2] The integrity of the remaining tooth structure is deteriorated from the biomechanical point of view with a resultant change in the intact tooth's pattern of stress and strain distribution. The change of the natural tooth's biomechanical balance could lead to increased potential for further trauma and eventual loss of the remaining tooth's structure. Although many studies with different methodologies have been implemented and performed, no clear cut and clinically relevant conclusions were drawn for the minimal dimensions of the cavity preparation that would minimize the tooth-fracture potential when subjected to occlusal loading. In particular, when an RPD abutment tooth is considered where most occlusal forces are distributed to the abutment from the occlusal rest to the rest seats in the tooth/tooth- or tooth/mucosa-supported RPD. When planning prosthetic restorations one is facing the presence of two different biological tissues and the need for an even distribution of the occlusal and other forces on the periodontal tissue of the remaining teeth, and in the mucoperiosteum on the edentulous alveolar ridge. The stress distribution throughout an RPD

and the supporting tissues may be evaluated easily using the finite-element method (FEM) [3].

In order to manufacture an RPD that fulfills both the functional and prophylactic demands, a non-invasive modality treatment for preparing the abutment tooth may be suggested. It is a good option for preparing the supporting dental tissues for receiving the elements of the RPD. The minimal appropriate intervention in that case could be placing a composite restoration, as stated by Shimizu & Takahashi [4]. Using a highly filled composite resin for the restoration of an abutment preparation for removable partial dentures gives favorable aesthetic results with the minimum intervention.[4]

The discussed treatment modality highlights the objective of this paper, which is to analyze the stress-strain distribution of the tooth with an occlusal rest-seat preparation in a composite filling and compare it to the biomechanical behavior of an intact tooth, assuming that the stress-strain distribution throughout the intact tooth provide the control scenario.

2 MATERIALS AND METHODS

The problem of the biomechanical behavior of a complex structure with irregular geometry such as a tooth could be analyzed using the finite-element method (FEM). Applications of the FEM are expanding rapidly, not only in the field of engineering but in science globally, especially as it appears that the FEM is a useful and convenient method for solving problems related to macrostructures, but also might give a precise insight into the problems related to microstructures.[5]

For this study two different models were created. The first model was a three-dimensional (3D) model of an intact tooth – **Model 1** (**Figure 1**), and the other was a 3D model of a tooth with a composite filling and an appropriate occlusal rest-seat preparation – **Model 2** (**Figure 2**). The 3D model of the second upper premolar was generated by combining the inner and outer geometry profiles obtained from literature data.[6,7] The mentioned morphologic details and dimensions were used to define a series of planes at different levels with the outlines of the tooth cross-section at each level. (**Figure 1**) The distance between the sliced planes was three slices in one mm, where over two hundred planes were generated. As this was time-consuming data for the software processing, the distance between the slices was increased afterwards to 2 mm for the crown portion of the model, and 3 mm for the root portion of the model.

The PRO-ENGINEER (Parametric Technology Corporation / Needham Massachusetts) and SOLID WORKS (Solid Works Corporation) software packages were employed for these procedures. The next step was to describe the relations between the planes, from where the solid model was constructed by connecting these contours. The dentine part of the tooth structure's crown and root portions were modeled separately from the enamel shell. Afterwards, the enamel and dentine were assembled into the final model of the intact tooth (**Figure 2**).

Subsequently, a model of a tooth with a composite filling and an appropriate occlusal rest seat was obtained, where additional cutting planes were defined in order to perform the cavity preparation. The occlusal rest preparation's size and location were chosen to conform to the standard cavity-design recommendations for a rest seat. The rest seat was 1.5 mm deep, occupying one half of the mesio-distal dimensions of the tooth crown and was approximately one third of the crown in the bucco-lingual direction. The recommended dimensions were adopted from literature recommendations.[8] The final FEM model of the restored tooth was realized by

Figure 1: Solid model of an intact tooth
Slika 1: Trdni model intaktnega zoba

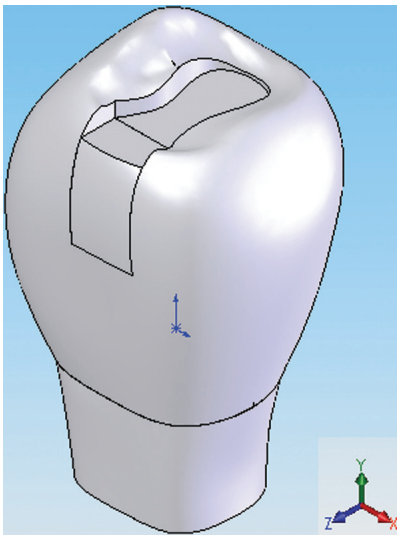

Figure 2: Solid model of a tooth with rest-seat preparation in a composite
Slika 2: Trdni model zoba z opornim sedežem iz kompozita

changing the element material properties in the zone of the cavity preparation.

Table 1: Young's modulus and Poisson's ratio of the materials used in this study[9,10]

Tabela 1: Youngov modul in Poissonovo razmerje za materiale, uporabljene v tej raziskavi[9,10]

	Young's modulus	Poisson's ratio
Enamel	84.1 GPa	0.33
Dentin	14.7 GPa	0.31
Composite resin	10.0 GPa	0.30
Co-Cr alloy	154.0 GPa	0.33

All the materials were considered to be isotropic and homogeneous and were assigned the appropriate physical properties according to literature data[9,10].The material properties are listed in **Table 1**. The dental pulp was modeled as a void because of its negligible stiffness and strength.[11] The cement was not included in the models due to its small dimensions and because it had no influence on the analysis.[12] Perfect bonding was considered between the enamel and the composite.

Both models were constrained at the top, 2 mm from the cement-enamel junction, representing the normal level of the alveolar crest and, in that way, the boundary conditions in this stress-strain analysis were defined. Therefore, the influence of the periodontal ligament (PDL) was not involved in the study.

Creating the finite-element mesh (pre-processing) for the described models was performed using the NASTRAN program (Noran Engineering Inc / Westminster Ca), where all the subsequent procedures (processing and post-processing) were done. The intact tooth-model mesh consisted of 15 092 finite elements with 23 300 nodes, while the mesh for the second model had 15 089 finite elements with 23 334 nodes. Each model was meshed by structurally solid elements defined by 10 nodes and having three degrees of freedom in tetrahedral bodies.

The loads were determined with an emphasis on load intensity, the direction and the point of the loading. Because of the variety of occlusal forces (differing among individuals, types of food chewing, conditions of occlusion) this study adopted vertical loading with 250 N in intensity. The existence of possible horizontal forces were ignored, where the RPD was assumed to be a rigid and stable appliance resisting the horizontal component of the masticatory forces[13]. As the analysis was considered linear in nature, sliding and friction phenomena that might occur between a rest and an abutment tooth were also ignored. Load stimulations were performed when the rest was fully seated on its corresponding rest seat and abutment tooth. The loads for both models were applied vertically at right angles to the inner aspects of the cusp slopes, away from the cusp tip. The simulated direction and intensity of the loads represent the loading pattern found in the centric occlusion, as stated by Rees and Jacobsen [16].

3 RESULTS

Based on the assumptions involved in the study and the fact that computer simulations simplified the real problems, the results of the study might be different to the values of stresses encountered by teeth in real situations. Therefore, the results were presented and considered qualitatively, not quantitatively, in order to offer more insight into the general influence of the prosthetic devices placed on teeth.

The results of the study are presented graphically as maps of the stress distribution within both investigated models. The total displacement (translation), maximum principal stress σ_{max}, and minimum principal stress σ_{min} were evaluated for each of the models.

The total displacement of the intact tooth after occlusal loading is shown in **Figure 3**. The largest displacement values are recorded at the cusp tip, due to tooth structure deformation encountered as a result of loading. Obviously, a lot of deformation happens in the points where the load is applied and therefore the greatest displacement values are observed there. Moving away from the loading point along the longitudinal axis of the tooth in an apical direction, the displacement decreases. This is probably the mechanism for the occlusal load amortization within the intact tooth's structure. Such findings are partly recognized as a consequence of the applied boundary conditions.

The values for σ_{max} and σ_{min} are also found to be the highest at the occlusal portion of the tooth. The concentration of stresses is higher at the location of the loading. These stresses rapidly decrease in the occluso-gingival direction. Close to the cement-enamel junction (CEJ) the stresses again increase and concentrate at that location. The pattern of stress distribution throughout the rest of the tooth structure shows a reasonably symmetrical distribution with the exception of the occlusal surface and the location close to the CEJ. (**Figures 4 and 5**)

As shown in **Figure 6**, the total translational displacement of the tooth with rest seat preparation is greatest at the cusp tip, as a result of the whole structure deformation. The occlusal loading of the model with rest-seat preparation induced a large deformation of the tooth structure. The observed total displacement values are similar to the values obtained for the intact tooth model. Similarly, as with the intact tooth model, the total displacement values are the largest at the location of the loading where great deformation happens. The displacement decreases in an apical direction as the distance from the loading location increases.

The general trend of stress distribution through the tooth with a rest-seat preparation is similar to that of an intact tooth, but some regional variations were observed.

The concentration of the stresses σ_{max} and σ_{min} is higher occlusally at the location of the loading, but very high stresses are concentrated at the bottom (pulpal

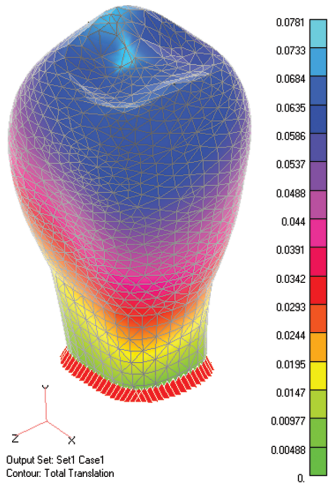

Figure 3: Total translational displacement of the intact tooth model
Slika 3: Totalni premik modela intaktnega zoba

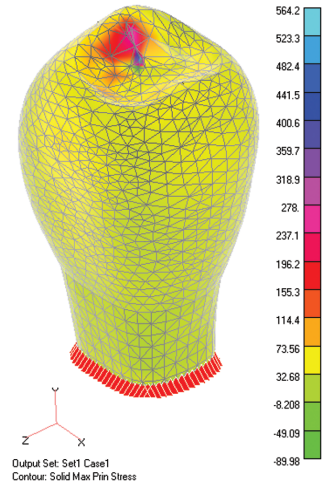

Figure 4: Distribution of the maximum principal stress of the intact tooth model
Slika 4: Porazdelitev največjih glavnih napetosti v modelu intaktnega zoba

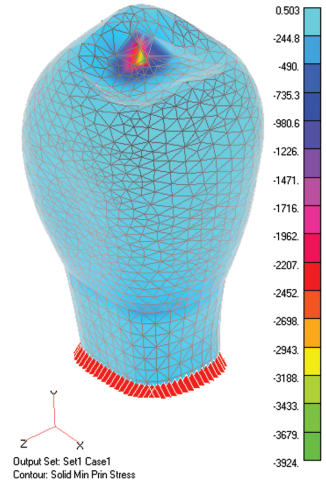

Figure 5: Distribution of the minimum principal stress of the intact tooth model
Slika 5: Porazdelitev najmanjših glavnih napetosti v modelu intaktnega zoba

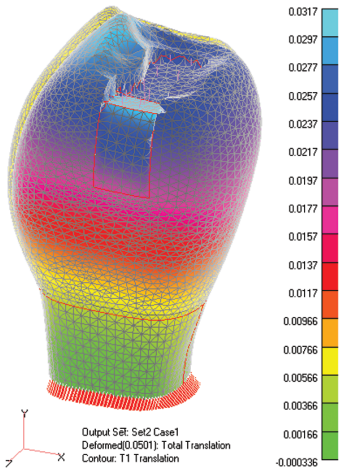

Figure 6: Total translational displacement of the tooth with occlusal rest-seat preparation in a composite
Slika 6: Popoln premik zoba z opornim sedežem, izdelanim iz kompozita

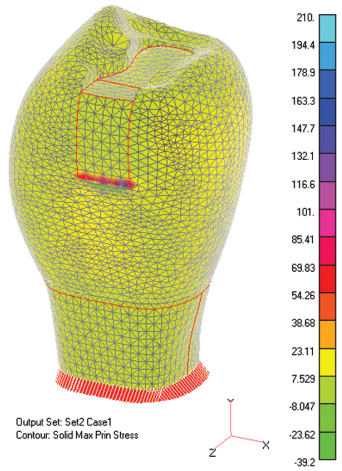

Figure 7: Distribution of the maximum principal stress of the tooth with the occlusal rest-seat preparation in the composite restoration
Slika 7: Porazdelitev največjih maksimalnih napetosti v zobu z zapornim sedežem in kompozitno restoracijo

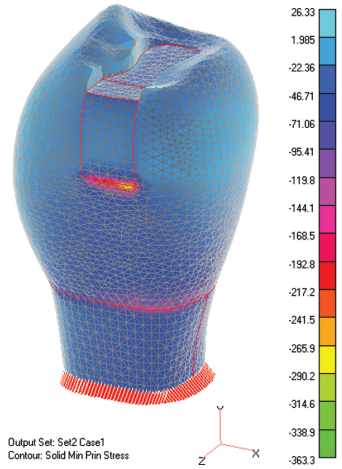

Figure 8: Distribution of the minimum principal stress of the tooth with the occlusal rest-seat preparation in the composite restoration
Slika 8: Porazdelitev najmanjših glavnih napetosti v zobu z opornim sedežem s kompozitno restoracijo

floor) of the rest-seat preparation (**Figures 7 and 8**). The trend of a symmetrical stress distribution through the rest of the tooth structure with decreasing intensity is also observed in this model. Again, the stresses rapidly increase close to the CEJ and reach their highest peak concentration at the CEJ. The stresses σ_{max} and σ_{min} resulting from the application of the occlusal load on the tooth with rest-seat preparation have lower values than those obtained after the intact tooth loading.

4 DISCUSSION

This investigation was focused on the mechanical behavior of a critical system such as the second upper premolar restored by a class II cavity preparation (where an accordant amount of dentine and enamel tissue is lost and the integrity of the structure is altered by placing an occlusal rest).

The relative behavior of composite restoration and the abutment tooth under the mastication load is shown, although some assumptions were made in order to simplify the calculations. Despite their intrinsic anisotropic nature, dentine and enamel can be assumed to be homogeneous and isotropic because their anisotropy belongs to the microscopic scale, whereas the tooth model is macroscopic.[14,15] Furthermore, all the materials were considered to be elastic throughout the entire deformation, which is a reasonable assumption for brittle materials in non-failure conditions.[16]

From the mechanical point of view, considering dentine as elastic and isotropic is an acceptable assumption, while enamel does not show such behavioral characteristics. Enamel is a more anisotropic material and some authors have modeled the enamel as anisotropic[14,16] Although such enamel modeling was more orthotropic, where the principal material axes coincided with the direction of enamel prisms, they were assumed to be perpendicular to the enamel-dentine junction. Following the recommendations of Darendeliler [14] and Versluis [15], materials which comprise the tooth structure could be modeled as isotropic and homogeneous,[14,18] especially because there is still no competent literature data on dental structure inhomogeneity and anisotropy.

Considering the occlusal loading effect alone, the sound tooth exhibits a wider high stress area, localized in correspondence to the occlusal enamel, than the restored teeth. This is due to the rigidity of the enamel. The reduction in stress occurs in the composite restoration, which is less rigid, and its lower rigidity allows greater cusp movements. The composite restoration will only cause deformation of the surrounding tooth structure through a well-bonded interface. So, the average stress in the entire structure is lower, but the stress values in the buccal and lingual cusps are higher. However, placement of a composite restoration with included a rest seat does not deteriorate the tooth's ability to withstand occlusal loading. The tooth with a composite restoration was less sensitive to occlusal loading than the intact one, probably due to the cusp reinforcement achieved by dentine and enamel bonding.

However, the concentration of stresses along the pulpal floor must undoubtedly be considered. The presence of cracks in the enamel introduced during cavity preparation may be a primary factor contributing to the stress concentration and eventual restoration failure. Also, some variance in the enamel mineralization between the surface and deep portions might interfere in homogeneous stress distribution throughout the restored tooth. The degree of enamel mineralization decreases as one approaches the amelo-dentinal junction, with a decreased elastic modulus[19]. Therefore, it seems that the peak stresses found in the tooth model with composite restoration with an included rest seat may be attributed to different causes.

These preliminary considerations, however, do not take into account setting composite shrinkage. These findings correlate with the statement of Ausiello [20] that more rigid composites lead to lower cusp movements under occlusal loading, but exhibit a higher pre-loading effect. A good composite for restoration has to balance the two opposite effects. In this way, a low pre-load on the cusps can be accepted in order to reach a sufficient restoration rigidity.[20] The size and configuration of the composite restoration affects the amount of tooth deformation due to resin polymerization shrinkage. In a small restoration (Class I and small Class II), deformation could hardly be visualized, which means that it was consistently lower or close to the measurement resolution.[21] The cavity designed for the rest seat in the study was of smaller dimensions than the standard Class II restoration, allowing us to speculate that the obtained deformation was a consequence of the applied loading by the occlusal rest and may not be partly the result of resin polymerization shrinkage. The study adopted the absolute bonding between the tooth and composite restoration, which may be the reason for the high stress concentration found along the pulpal floor. An infinitely rigid interface layer produces high stress areas all around the tooth-restoration interface. Accompanied by the polymerization shrinkage, stress and occlusal load stress exists as a very complex biomechanical system. An appropriate way to limit the intensity of all the stress transmitted to the remaining tooth tissues under occlusal loading by the rest would be the proper selection of the adhesive layer. Ausiello[22] stated that a substantially thicker layer of a more flexible adhesive (lower elastic modulus) would partially absorb the composite deformation.[22]

5 CONCLUSION

Within the limitations of the finite-element simulation study, the results suggest that a composite restoration with a rest seat included reduces the generation of

stresses inside the tooth structure. Findings indicate that a composite restoration absorbs the loading and, due to its resilient nature, acts as a cushion beneath the occlusal rest. The simplifications used in the study have also been shown to affect the results. The detailed modeling of dental hard-tissue anisotropy, along with the more precise modeling of the adhesive interface, should be considered as a goal for any future study on this topic.

The potential of the system composite-occlusal rest seat is that it represents the minimum intervention procedure and acts as an absorbent of occlusal loading. Furthermore, the eventual use of a composite restoration may be suggested as a way of preparing abutments for receiving elements of the RPD. However, clinical trials are required to ensure that a composite restoration with rest seat included can survive under long-term clinical conditions.

6 REFERENCES

[1] O'Grady J, Sheriff M, Likeman P. A finite element analysis of a mandibular canine as a denture abutment. European Journal of Prosthodontics and Restorative Dentistry, 4 (**1996**) 3, 117–121

[2] Sato Y, Shindoi N, Koretake K, Hosokawa R. The effect of occlusal rest size and shape on yield strength. Journal of Prosthetic Dentistry, 89 (**2003**), 503–507

[3] Todorovic A, Radovic K, Grbovic A, Rudolf R, Maksimovic I, Stamenkovic D. Stress analysis of a unilateral complex partial denture using the finite-element method. Mater. Tehnol., 44 (**2010**) 1, 41–47

[4] Shimizu H, Takahashi Y. Highly filled composite partial coverage restorations with lingual rest seats and guide planes for removable partial dentures. Journal of Prosthetic Dentistry, 99 (**2008**),73–74

[5] Avdiaj S, Setina J, Syla N. Modeling of the piezoelectric effect using the finite-element method (FEM.) Mater. Tehnol., 43 (**2009**) 6, 283–291

[6] Ash MM, Nelson SJ. Wheeler's Dental Anatomy, Physiology and Occlusion. Eighth edition Elsevier Science, **2003**, 230–238

[7] Schillinburg HT, Jacobi R, Brackett SE. Fundamentals of Tooth Preparations. Second printing Quintessence Publishing Co. **1991**, 13–15

[8] Biomaterials Properties Database, University of Michigan Quintessence Publishing, **1996**. Available from World WideWeb: http://www.lib.umich.edu/libhome/Dentistry.lib/Dental_tables.html

[9] Ensaff, H., D. M O'Doherty and P. H. Jacobsen. The influence of the restoration-tooth in light cured composite restoration: a finite element analysis. Biomaterials, 22 (**2001**), 3097–3103

[10] Rubin C., Krishnamurthy N., Capilouto E., Yi H. Stress analysis of the human tooth using a three-dimensional finite element model. Journal of Dental Research, 62 **(1983**), 82–86 2

[11] Tanaka M, Naito T, Yokota M, Kohno M. Finite element analysis of the possible mechanism of cervical lesion formation by occlusal force. J Oral Rehabilitation, 30 (**2003**), 60–67

[12] Rees JS. The effect of variation in occlusal loading on the development of abfraction lesions: a finite element study. J Oral Rehabilitation, 29 (**2002**), 188–193

[13] Muraki H, Wakabayashi N, Park I, Ohyama T. Finite element contact stress analysis of the RPD abutment tooth and periodontal ligament. Journal of Dentistry, 32 (**2004**), 659–665

[14] Darendeliler, S. Y., Alacam, T., Yaman, Y., Analysis of stress distribution in a maxillary central incisor subjected to various post and core applications. Journal of Endodontics, 24 (**1998**), 107–111

[15] Versluis, A., Douglas, W. H., Cross, M, Sakaguchi, R. L. Does an incremental filling technique reduce polymerization shrinkage stresses? Journal of Dental Research, 3 (**1996**), 871–878

[16] Rees, J. S., Jacobsen, P. H. Modelling the effects of enamel anisotropy with the finite element method. Journal of Oral Rehabilitation, 22 (**1995**), 451–454

[17] Yettram A. L., Wright K. W. J. Pickard H. M. Finite element stress analysis of the crowns of normal and restored teeth Journal of Dental Research, 55 (**1976**) 6, 1004–1011

[18] Versluis A. Does an incremental filling technique reduce polymerisation shrinkage stresses? Journal of Dental Research, 75 (**1996**), 871–878

[19] Meredith N, Sheriff DJ, Setchell DJ. Measurement of the microhardness and young's modulus of human enamel and dentine using an indentation technique. Archives of Oral Biology, 41 (**1996**), 539–541

[20] Ausiello P., Apicella A. Davidson C. L., Rengo S. 3D-finite element analyses of cusp movements in a human upper premolar, restored with adhesive resin-based composites Journal of Biomechanics, 34 (**2001**), 1269–1277

[21] Tantbirojn D., Versluis A., Pintado M. R., DeLong R., Douglas W H. Tooth deformation patterns in molars after composite restoration. Dental Materials, 20 (**2004**), 535–542

[22] Ausiello P., Apicella A. Davidson CL. Effect of adhesive layer properties on stress distribution in composite restoration – a 3D finite element analysis. Dental Materials, 18 (**2002**), 295–303

UDK 669.018.9:620.1/.2
Original scientific article/Izvirni znanstveni članek

ISSN 1580-2949
MTAEC9, 45(6)567(2011)

IDENTIFICATION AND VERIFICATION OF THE COMPOSITE MATERIAL PARAMETERS FOR THE LADEVÈZE DAMAGE MODEL

IDENTIFIKACIJA IN VERIFIKACIJA PARAMETROV KOMPOZITNEGA MATERIALA ZA MODEL LADEVÈZE

Václav Kleisner, Robert Zemčík, Tomáš Kroupa

University of West Bohemia in Pilsen, Department of Mechanics, Univerzitní 22, 306 14, Plzeň, Czech Republic
kleisner@kme.zcu.cz

Prejem rokopisa – received:2011-02-01 ; sprejem za objavo – accepted for publication: 2011-04-14

In this investigation we examine the properties of a layered composite material and verify the Ladevèze material model implemented in PAM-CRASH software. The complex material model incorporates plasticity, failure and damage mechanisms and is suitable for dynamic phenomena, such as crash tests. The experimental tests were performed on appropriate laminated specimens made from unidirectional, pre-impregnated, composite fiber (prepregs) – coupons with axially oriented fibers, coupons with fibers at 45°, and ±45° cross-ply laminates. The tests included simple tensile tests to fracture and cyclic tensile tests. Numerical models were created for the finite-element analysis using shell elements. A mathematical optimization was then used to minimize the error between the experimental and numerical results in terms of load-displacement curves for all the tested configurations by varying the material characteristics.

Keywords: composite, identification, carbon, fiber, epoxy, plasticity, experiment, finite-element analysis

Identifikacija lastnosti plastastega kompozitnega materiala in verifikacja modela Ladeveze za material s PAM-CRASH-sofverom. Kompleksen model materiala vključuje plastičnost, prelom in mehanizem poškodbe ter je primeren za dinamične fenomene kot preizkus trka. Preizkusi so bili izvršeni na primernih laminatnih vzorcih, izdelanih iz enosmernih predimpregniranih kompozitnih vlaken (prepreg) – kuponov z osno orientiranimi vlakni, kuponov z vlakni pod kotom 45° in križnimi laminati ±45°. Preizkusi so obsegali enostavne raztržne in ciklične natezne preizkuse. Pripravljeni so bili numerični modeli za analizo po metodi končnih elementov z uporabo lupinastih elementov. Matematična optimizacija je bila nato uporabljena za zmanjšanje napak med eksperimentalnimi in numeričnimi rezultati s krivuljami obremenitev – pomik za vse preizkušene konfiguracije s spremembami karakteristik materiala.

Ključne besede: kompozit, identifikacija, ogljikova vlakna, epoksi, plastičnost, preizkusi, končna elementna analiza

1 INTRODUCTION

Composite materials are modern materials with advantageous strength- and stiffness-to-mass ratios compared to classical materials, such as steel or aluminum [1,2]. Namely, the carbon-fiber-reinforced plastic composites consisting of continuous carbon fibers and a matrix can have similar or better strength than steel structures and they can have similar or less weight than aluminum structures. As their properties are highly oriented (generally anisotropic), the greatest strength is achieved in the direction of the fibers. This can be utilized especially in the case of the design of components with excessive loading in a specific direction.

Composite materials are increasingly used in the aerospace and automotive industries for the reason mentioned above. Numerical simulations help to design the desired components or complex structures, including the possibility to optimize the fiber orientations or lay-ups. Nevertheless, it is important to know the correct material parameters and to use the appropriate material model. This material data must be obtained from experimental measurements. An integral part of any material model is the failure/damage prediction possibility. Many material models have been proposed so far, but none of them is perfect or universal [6]. The basic failure criteria, such as the maximum stress, maximum strain and others, are not interactive criteria. This means that there is no relation between the stress components in different directions. In this respect, the so-called interactive criteria, such as Tsai-Wu [1], are more suitable for crash simulations. On the other hand, the disadvantage is that we cannot distinguish between the matrix and fiber failure, which is important in an impact simulation. The most recent failure criteria (the so-called direct mode criteria), such as Puck [8] or LaRC [3], use the advantages of both types [9].

The Ladevèze material model [5] in the PAM-CRASH software [7] is implemented only for a multi-layered, thin shell element and transient analysis (i.e., the explicit code). It includes the following modes of failure of a composite material: debonding, micro-cracking, delamination, and fiber breaking. The Ladevèze damage model also includes inelastic material deformations caused by the matrix-dominated loading. The plasticity of the matrix cannot be neglected in general and the effect is best seen, for example, in the case of cyclic loading.

2 MATERIAL AND DAMAGE MODELS

The constitutive relationship for materials with a linear response is usually written in the form of the extended Hooke's law [1]. The constitutive relationship of the Ladevèze material model can be written with similar formulae, except that elastic constants are herein modified by additional damage parameters or functions [4,5]. The crucial relations are summarized in **Table 1**. The superscript 0 denotes the initial values (damage free) of the material constants. The quantities d_{11}, d_{22} and d_{22} represent the fiber damage in tension, matrix damage, and fiber-matrix debonding damage, respectively. The effect of d_{12} is shown in the relation of the actual (G_{12}) and initial (G^0_{12}) values of the shear moduli. The shear damage function Y_{12} is derived from the strain energy E_d for an anisotropic material, where Y_C and Y_0 are the critical shear damage limit and the initial shear damage threshold, respectively. The parameter Y_R represents the shear failure.

Another important improvement to the composite material model is obtained by the inclusion of the matrix plasticity behavior. This is incorporated by changing the yield stress during the cyclic loading. The yield stress is given by $R(\varepsilon^P)$, which is a function of the initial yield stress R_0, the plastic deformation ε^P and the hardening coefficients β, m. This represents a power-law approximation of the experimental curve.

The fiber tensile damage (longitudinal damage) is characterized by the initial (ε^i_{11}) and ultimate (ε^u_{11}) fiber tensile damage strains.

3 EXPERIMENT AND SIMULATIONS

In this study, laminated composite coupons made of HexPly 913C prepregs with Tenax HTS 5631 carbon fibers are tested (see **Figures 1–3**). The material characteristics needed for the numerical models are obtained from the experimental data. The detailed description of the measurement can be found in [7]. It consists of three types of tests:

- simple tensile test on $[0]_8$ laminates,
- simple tensile test with load/unload cycles on $[\pm45]_{2S}$ laminates,
- simple tensile test on $[45]_8$ laminates.

Figure 1: Fractured $[0]_8$ specimen
Slika 1: Prelomljen vzorec $[0]_s$

Figure 2: Fractured $[\pm45]_{2S}$ specimen. The position and orientation of the cracks is emphasized
Slika 2: Prelomljen vzorec $[\pm45]_{2s}$. Poudarjena sta položaj in orientacija razpok

Figure 3: Fractured $[45]_8$ specimen
Slika 3: Prelomljen vzorec $[45]_8$

Simple [0] tensile test

The tensile test was conducted on UD composite coupons with the $[0]_8$ fiber composition (see **Figure 1**). The coupons were loaded by displacement (speed 1 mm/min) until rupture. The force–displacement curve was measured, see **Figure 4**.

The initial Young's modulus E^0_{11}, the initial fiber failure value ε^i_{11} and the critical fiber failure value ε^u_{11} were assessed from the data obtained using Hooke's law.

The averaged experimental results were used directly in the material model within the corresponding numerical simulation. The results of the simulation are in a good

Tabela 1: Relacije modela Ladevèze za lupinaste elemente[4,5]
Table 1: Ladevèze model relations for shell elements [4,5]

$$\begin{bmatrix} \varepsilon_{11} \\ \varepsilon_{22} \\ \varepsilon_{12} \\ \varepsilon_{23} \\ \varepsilon_{13} \end{bmatrix} = \begin{bmatrix} \frac{1}{E^0_{11}(1-d_{11})} & \frac{-\nu^0_{12}}{E^0_{11}(1-d_{11})} & 0 & 0 & 0 \\ \frac{-\nu^0_{12}}{E^0_{11}(1-d_{11})} & \frac{1}{E^0_{22}(1-d_{22})} & 0 & 0 & 0 \\ 0 & 0 & \frac{1}{G^0_{12}(1-d_{12})} & 0 & 0 \\ 0 & 0 & 0 & \frac{1}{G^0_{23}(1-d_{12})} & 0 \\ 0 & 0 & 0 & 0 & \frac{1}{G^0_{12}(1-d_{12})} \end{bmatrix} \begin{bmatrix} \sigma_{11} \\ \sigma_{22} \\ \sigma_{12} \\ \sigma_{23} \\ \sigma_{13} \end{bmatrix}$$

$$G_{12} = G^0_{12}(1-d_{12}), \qquad d_{12} = 1 - \frac{G_{12}}{G^0_{12}}$$

$$E_d = \frac{1}{2}\left[\frac{\sigma^2_{11}}{E^0_{11}} - \frac{2\nu^0_{12}}{E^0_{11}}\sigma_{11}\sigma_{22} + \frac{\langle\sigma_{22}\rangle^2_+}{E^0_{22}(1-d_{22})} + \frac{\langle\sigma_{22}\rangle^2_-}{E^0_{22}} + \frac{\sigma^2_{12}}{G^0_{12}(1-d_{12})}\right]$$

$$Z_d = \frac{\partial E_d}{\partial d_{12}} = \frac{1}{2}\frac{\sigma^2_{12}}{G^0_{12}(1-d_{12})^2}, \; Y_{12} = \sqrt{Z_d}$$

$$Y_{12} = Y_C d_{12} + Y_0$$

$$Y_R = \sup(Y_{12})$$

$$R(\varepsilon_P) = R_0 + \beta(\varepsilon^P)^m$$

$$\varepsilon^i_{11} \leq \varepsilon_{11} < \varepsilon^u_{11}$$

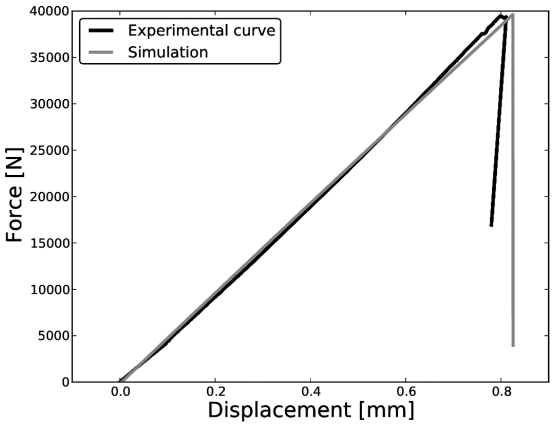

Figure 4: Load–displacement curves from the $[0]_8$ test
Slika 4: Krivulji obremenitev – pomik za preizkus $[0]_8$

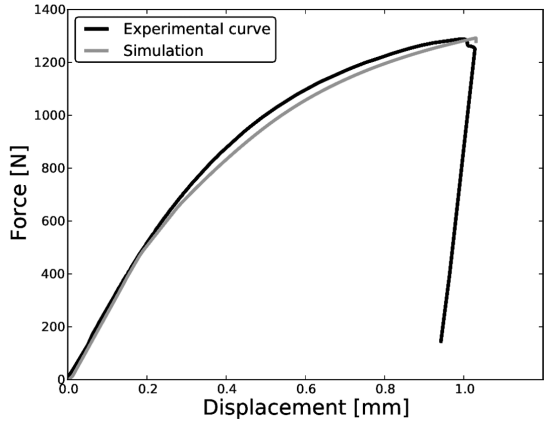

Figure 5: Load–displacement curves from the $[45]_8$ test
Slika 5: Krivulji obremenitev – pomik za preizkus $[45]_8$

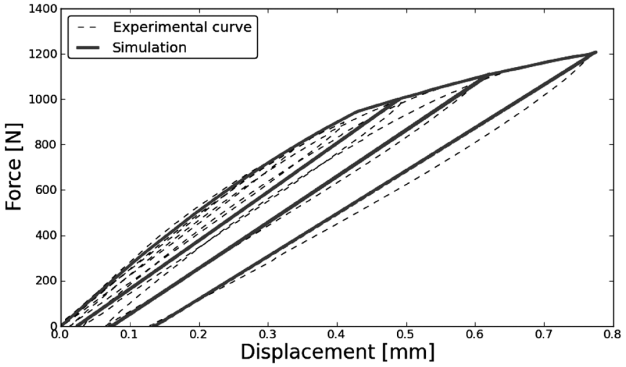

Figure 6: Load–displacement curves from $[\pm45]_{2S}$ test
Slika 6: Krivulji obremenitev – pomik za preizkus $[\pm45]_{2S}$

agreement with the experimental data (see **Figure 4**). The constants $\varepsilon^i{}_{11}$ and $\varepsilon^u{}_{11}$ have similar values as the whole cross-section ruptured at the same time.

Cyclic [±45]$_{2S}$ tension test

The composite coupons (**Figure 2**) were loaded by a cyclic loading – 6 cycles (load/unload) with increasing load amplitude (700 N, 800 N, 900 N, 1000 N, 1100 N and 1200 N) and the force–displacement curves were obtained. The nonlinear behavior and the plasticity of the composite material can be clearly seen from the results. This phenomenon is given by the plastic behavior of the matrix or fiber-matrix interface. The stress and strain vectors in the principal material directions (the fiber direction and the transverse fiber direction) must be calculated from the experimental data using the relations for the stress/strain transformation for each lamina. Consequently, it is possible to calculate the actual shear modulus G_{12}.

Tabela 2: Identificirane karakteristike materiala
Table 2: Identified material characteristics

Parameter	Symbol	Value
Elastic properties		
Young's modulus in fiber direction	E^0_{11}	125.295 [GPa]
Young's modulus in transverse direction	E^0_{22}	7.446 [GPa]
Shear modulus in plane 12	G^0_{12}	3.720 [GPa]
Shear modulus in plane 23	G^0_{23}	3.720 [GPa]
Poisson's ratio	ν^0_{12}	0.3126 [-]
Failure properties		
Initial fiber failure	ε^i_{11}	0.01366 [-]
Critical fiber failure	ε^u_{11}	0.013661 [-]
Shear failure	Y_R	0.036 [GPa]$^{1/2}$
Damage properties		
Critical shear damage	Y_C	0.0655 [GPa]$^{1/2}$
Initial shear damage	Y_0	0.0040 [GPa]$^{1/2}$
Plastic properties		
Yield stress	R_0	0.049 [GPa]
Hardening parameter β	β	0.85 [GPa]
Hardening parameter α	α	0.24 [-]

The material parameters responsible for the nonlinear response of the numerical model were optimized using the PAM-OPT tool to minimize the error between the simulated and experimental data. Relatively good agreement between the experimental and the simulated curves was obtained; however, the maximum force in this case was not correctly predicted.

Simple [45]$_8$ tension test

For the validation of the shear failure parameter Y_R a simple tension test on the $[45]_8$ laminate was performed (**Figure 3**). This parameter will ensure that the material fails when the load exceeds a certain limit **Figure 5**.

Recalculation of the cyclic test with the new shear failure parameter in the material model led to a significant improvement of the correlation with the experimental data. The comparison of the resulting curves is shown in **Figure 6**. The resulting values of all the parameters of the Ladevèze model used are summarized in **Table 2**.

4 CONCLUSION

The combination of three types of experimental measurements and numerical simulations in the finite-element code PAM-CRASH was performed. A

mathematical optimization was used to obtain the parameters of the used Ladevèze material model that incorporates plasticity, damage and failure. The resulting comparison of the numerical and experimental data in terms of load–displacement curves shows a very good agreement.

In future work, a similar investigation will be performed on textile composites. The applicability of the Ladevèze model will thus be tested on a material with even more complex behavior.

Acknowledgement

The work has been supported by the research project GA CR 101/08/0299 and the research project GA CR 101/08/P091.

5 REFERENCES

[1] Berthelot, J. M. (1999). Composite materials, Springer, New York

[2] Daniel I. M., Ishai O.: Engineering mechanics of composite materials, Oxford University Press, Inc. (1994)

[3] Dávila, C. G., Camanho, P. P. (2003). Failure Criteria for FRP Laminates in Plane Stress, NASA/TM-2003-212663 report, NASA

[4] Greve L., Pickett A. K.: Modelling damage and failure in carbon/epoxy non-crimp fabric composites including effects of fabric pre-shear, Composites Part A: Applied Science and Manufacturing, 37 (**2006**), 11, 1983–2001

[5] Ladevèze P., Le Dantec E.: Damage Modelling of the elementary ply for laminated composites, Compos. Sci. Technol., 43 (**1992**) 3, 257–2671

[6] Laš V., Zemčík R.: Progressive damage of unidirectional composite panels, Journal of Composite Materials, 42 (**2008**) 1, 25–44

[7] PAM-CRASH 2007. Solver Notes Manual. ESI-Group, Paris

[8] Puck, A., Schurmann, H., Failure analysis of FRP laminates by means of physically based phenomenological models. Composites Science and Technology, 58 (**1998**), 1045–1067

[9] Soden, P. D., Kaddour, A. S., Hinton, M. J., Recommendations for Designers and Researchers Resulting from the World-wide Failure Exercise, Composites Science and Technology, 64 (**2004**), 589–604

UDK 666.97:620.181
Original scientific article/Izvirni znanstveni članek

ISSN 1580-2949
MTAEC9, 45(6)571(2011)

EVALUATION OF THE STRENGTH VARIATION OF NORMAL AND LIGHTWEIGHT SELF-COMPACTING CONCRETE IN FULL SCALE WALLS

OCENA VARIACIJE TRDNOSTI NORMALNEGA IN LAHKEGA VIBRIRANEGA BETONA V POLNIH STENAH

M. M. Ranjbar[1], M. Hosseinali Beygi[2], I. M. Nikbin[3] , M. Rezvani[4], A. Barari[5]

[1]Department of Civil Engineering, Guilan University, Rasht, Iran
[2]Department of Civil Engineering, Babol University of Technology, Babol, Iran
[3]Department of Civil Engineering Islamic Azad University, Rasht Branch, Rasht
[4]Institute of Material Science, University of Duisburg-Essen, Universitätstrasse 15, 45141 Essen, Germany
[5]Department of Civil Engineering, Aalborg University, Sohngardsholmsvej 57, 9000 Aalborg, Aalborg, Denmark
ab@civil.aau.dk, amin78404@yahoo.com

Prejem rokopisa – received: 2011-03-26; sprejem za objavo – accepted for publication: 2011-06-10

The strength of cast concrete along the height and length of large structural members might vary due to inadequate compaction, segregation, bleeding, head pressure, and material type. The distribution of strength within a series of full scale reinforced concrete walls was examined using non-destructive testing. Self-compacting concrete (SCC) and lightweight self-compacting concrete (LWSCC) with different admixtures were tested and compared with normal concrete (NC). The results were also compared with results for standard cubic samples. The results demonstrate the effect of concrete type on the in situ strength variation and the relationship to the strength of standard cube samples. Investigation of the strength variation along the height of the wall showed that SCC mixes had better strength uniformity and that the NC mix had the greatest strength variation. There were no significant strength differences between mixtures along the length of the walls. Furthermore, different admixture replacements did not have a meaningful effect on the strength distribution.

Keywords: strength variation, self-compacting concrete, lightweight aggregate, ultrasonic pulse velocities, compressive strength, structural walls.

Trdnost litega betona po višini in dolžini večjih gradbenih elementov lahko variira zaradi neprimernega vibriranja, segregacije, iztekanja (solzenja), pritiska glave in vrste materiala. Porazdelitev trdnosti v seriji železobetonskih cementnih sten je bila preiskana z uporabo neporušnih preizkusov. Vibrirani beton (SCC) in lahek vibrirani beton (LWSCC) iz različnih zmesi sta bila primerjana z normalnim betonom (NC). Rezultati so bili primerjani tudi z rezultati za standardne kockaste vzorce. Rezultati dokazujejo učinek vrste betona na *in situ* variacijo trdnosti in odvisnost od trdnosti standardnih kockastih vzorcev. Raziskava trdnosti vzdolž višine stene je pokazala, da različne zmesi ne vplivajo pomembno na porazdelitev trdnosti.

Ključne besede: variacija trdnosti, vibrirani beton, lahek agregat, hitrost ultrazvočnega impulza, tlačna trdnost, zidovi konstrukcij

1 INTRODUCTION

In the past two decades, self-compacting concrete (SCC) has been developed to build concrete structures. Practical applications of SCC vary widely and have been accompanied by numerous research studies. SCC is a flowable concrete that fills spaces, especially in sections with highly congested reinforced members and restricted shapes.[1] SCC has less stringent working and safety requirements because of its negligible vibration factor. The weight of SCC is the main cause of its compaction. Its significant advantages, such as favorable mechanical properties and durability, have made SCC a high-performance concrete. Most of the probable bleeding and segregation can be reduced with viscosity-modifying agents in SCC mixes. Consequently, due to the elimination of any voids, the maximum density, material strength and concrete-steel rebar bonding are improved. Furthermore, SCC provides easier transition and pumping. Hence, the casting process is faster for huge structural members.[1,2,3]

Structural lightweight concrete has a lower density in place compared to normal weight concrete. The concrete mixture is made with a lightweight aggregate. The main application of structural lightweight concrete is to decrease the dead load of concrete structures such as high-rise buildings and long-span bridges, which then allows the structural designer to reduce the size of piers, footings, walls and other load-bearing elements.[4] Furthermore, it can decrease the applied dynamic loads, such as earthquake forces, which are directly related to the dead load of a structure. It has been shown that a decrease in the dimensions of structural members compensates for the higher cost of lightweight concrete.[5]

Variations in the strength of concrete in a structure and control samples of a similar age are fundamentally due to differences in curing conditions and compaction. These factors also affect the strength variations within the depth of the members. Variations in a concrete supply are due to the variety of batching, materials, placing and handling methods, which are often restricted by the quality control of a production, such as the

compliance testing of control samples. These factors are clearly not related to the member type involved but lead to random in situ variations. Previous research has shown positional differences along the height of concrete members cast in a deep form, and the lowest strength occurred at higher positions due to the concrete pressure head, aggregate settlement, bleeding and pores, which cause inadequate compaction. Another reason for this type of variation is the upward movement of water through concrete while the material is still plastic and the fact that upper layers protect the lower layers of concrete from rapid drying.[6–9]

Considering the nature of self-compacting concretes, which have a high consistency and flow ability, the homogeneity of these concretes in comparison to normal concrete that is compacted traditionally has been evaluated. Previous studies performed by Zou and Khayat on reinforced concrete beams, columns at large scales and un-reinforced walls relative to small scale walls made of self-compacting and normal concretes showed that the members made of self-compacting concrete had higher homogeneity but some discrepancies within and between them.[10,11]

On the other hand, in many situations, the standard cube sample strength may not indicate the actual strength of the concrete members. Therefore, the concrete strength of full scale reinforced concrete walls in service sites was evaluated. The ultrasonic pulse velocity test was used to investigate the strength variation and uniformity of in situ concrete strength.

2 EXPERIMENTAL PROGRAM

To study the homogeneity of normal weight self-compacting concretes and lightweight self-compacting concretes, five (2.0 × 2.0 × 0.2) m reinforced concrete walls were cast. The strength distribution in the structural walls and their variations with the normal weight concrete (NC) were also studied. The walls contained reinforcing steel 12 mm in diameter and 25 cm in length. Steel reinforcement details for the walls are given in **Figure 1**. This reinforcement configuration was selected to assess the effect of steel bars on the compaction of self-compacting concretes.

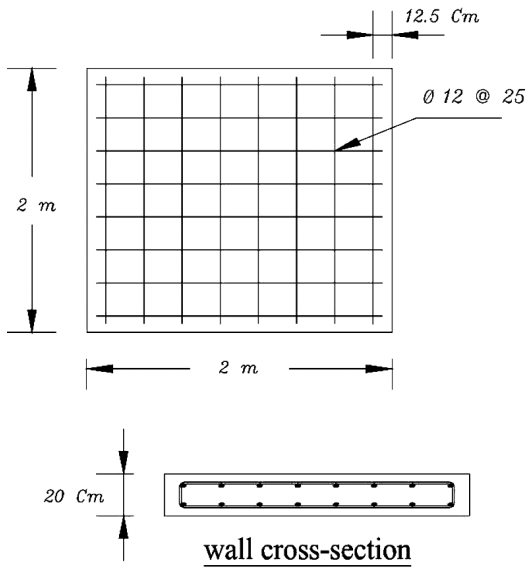

Figure 1: Details of reinforcement for the walls
Slika 1: Detajli utrditve stene

Concrete mix with a specified cube strength of 28 MPa was considered, and Type I Portland cement conforming to BS12 was used throughout the tests. The lightweight aggregate used in this research was Leca with a 24 h water absorption of 14 %. Other research has shown that domestic Leca has lower levels of resistance compared to its foreign counterparts.[11] Hence, Leca was used as a fine aggregate and substitute for part of the natural sand. The natural river sand, 1.46 % water absorption, was the other part of the fine aggregate. It was washed before use in the mixture procedures. The normal coarse aggregate was crushed stone with a maximum size of 20 mm and 0.8 % water absorption, except for the lightweight concretes, where the maximum size was 10 mm with 0.5 % water absorption. Limestone powder was used to maintain the viscosity of the fresh mix and hence to reduce the segregation phenomena. The chemical characteristics of the cement and mineral admixture are presented in **Table 1**. Superplasticizer Viscocrete 1 was introduced into the mixes. The properties of the concrete mix used in this study and the properties of the fresh concrete are shown in **Tables 2 and 3**, respectively. SSCC and SLWSCC (Light weight self-compacting concrete containing silica fume) produced mixtures containing 7.0% silica fume by weight of cement content. NSCC and NLWSCC (Light weight self-compacting concrete containing nano-sized SiO_2) had mixtures containing nano-sized SiO_2 with a particle size of 15 nm in the amount of 3.0 % by weight of cement content.

Full scale walls were cast in steel molds. To simulate the site construction, workshop executives and technical

Table 1: Chemical properties of cement and mineral admixtures
Tabela 1: Kemična sestava cementnih in mineralnih zmesi

	mass fractions, *w*/%			
	Cement	Silica fume	Limestone filler	Nano SiO_2
SiO_2	22.02	96.4	–	99.9
Al_2O_3	4.40	1.32	–	–
Fe_2O_3	3.20	0.87	–	–
CaO	64.9	0.49	–	–
MgO	1.42	0.97	–	–
SO_3	1.67	0.10	–	–
Na_2O	0.27	0.31	–	–
LOI	1.30	–	–	0.1
P_2O	–	0.16	–	–
$MgCO_3$	–	–	1.10	–
$CaCO_3$	–	–	98.1	–

Table 2: Mixture proportions
Tabela 2: Sestava zmesi

Coarse Agg	Fine Agg. (kg/m^3)	Leca 0–3 mm (kg/m^3)	Limestone powder (kg/m^3)	Water (kg/m^3)	Superplasticizer (kg/m^3)	Nano SiO_2 (kg/m^3)	Silica fume (kg/m^3)	Cement (kg/m^3)	Mixture Type	
									10–20 mm (kg/m^3)	5–10 mm (kg/m^3)
648	349	815	–	–	200	–	–	–	320	NC
384	469	873	–	270	181	8	–	22.4	300	SSCC
384	469	873	–	270	166	8.5	9.6	–	310	NSCC
–	250	382	245	290	198	9.8	–	30.8	440	SLW-SCC
–	250	382	245	290	205	10.2	14.1	–	456	NLW-SCC

Table 3: Fresh properties
Tabela 3: Lastnosti svežih vzorcev

Mix Type	Slump flow		*V*/s Funnel	*L*-Box (h_2 / h_1)	Unit weight (kg/m^3)
	T_{50}/s	*D*/cm Final			
NC	–	–	–	–	2395
SSCC	2.2	68	7.2	0.93	2373
NSCC	2.5	65	7.8	0.94	2362
SLW-SCC	3.8	69	8.1	0.91	1840
NLW-SCC	4.2	63	7.9	0.90	1831

staff were involved. The concrete was supplied in four 0.3 m^3 batches. During the concreting of the reinforced concrete walls, the different concretes were poured directly from the top of the walls without any external vibration into the framework except for the wall made of normal concrete, which was compacted with a common vibrator. Specimens were cured under wet textiles and polythene sheets for 7 d. Five 100 mm cubes were also cast from each of the four batches. Half of the cubic specimens were subjected to curing conditions similar to those of the walls, and other half were treated with the standard curing regime.

3 TEST PROCEDURES

3.1 Ultrasonic Pulse Velocity (UPV) Test

Non-destructive tests of concrete are preferred because measurements can be obtained without destructive forces. The most generally used method is the ultrasonic pulse velocity method. The test procedure is based on the fact that the velocity of an ultrasonic pulse wave in solid bodies depends on the modulus of elasticity, Poisson's ratio and the density of the material. When the uniformity, density and homogeneity of the concrete are good, ultrasonic pulse waves of higher velocity can be observed. Generally, acoustic transducers are used to generate ultrasonic pulses.[12] When the pulse wave passes through concrete, it undergoes various reflections at the boundaries of materials with different properties within the concrete body. The velocity of the pulse waves is often independent of the geometrical shapes of the materials through which they pass. The pulse velocity test is a common method to assess structural concrete. The actual pulse velocity wave obtained depends mainly on the materials and mixture of concrete.

After traveling a known path length (*L*) in the concrete, the pulse is converted into an electrical signal by a second electro-acoustical transducer, and an electronic timing circuit enables the transfer time (*T*) of the pulse to be recorded. The pulse wave velocity (*V*) is obtained by

$$V = \frac{L}{t} \tag{1}$$

where *V*/(km/s) pulse wave velocity, /cm length of path, and /μs transfer time

The longitudinal ultrasonic pulse waves that leave the transmitter travel in the direction normal to the transducer surface according to BS 1881 [13]. To make a reasonably accurate and relevant assessment of the uniformity of the concrete strength in existing walls in this study, the ultrasonic pulse velocity test was used as a non-destructive test method. Ultrasonic pulse velocity (UPV) tests on the walls at 21 d were performed using Pundit equipment [14]. The pulse velocity measurements were taken directly through the thickness of the walls at the grid locations indicated in **Figure 2**. The UPV test locations included 21 points, which were located at the top, middle and bottom levels at heights of (175, 100 and 25) cm, respectively, above the bottom surface of the walls. These locations were chosen to test different levels within the walls while satisfying the minimum edge distance and spacing requirements and avoiding reinforcing steel.

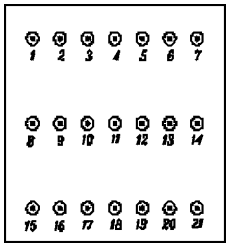

Figure 2: Test positions on the walls
Slika 2: Mesta preizkusov v stenah

Table 4: Hardened properties
Tabela 4: Lastnosti strjenih vzorcev

Mix Type	Compressive Strength (MPa)				Ultrasonic Pulse Velocity (km/s)			
	3 days	7 days	14 days	28 days	3 days	7 days	14 days	28 days
NC	14.2	19.4	23.3	29.0	3.61	3.78	3.89	3.98
SSCC	26.9	29.1	29.8	33.0	3.96	4.08	4.11	4.27
NSCC	30.3	32.3	33.8	35.5	4.26	4.27	4.31	4.36
SLWSCC	22.5	23.4	24.0	25.3	4.04	4.08	4.09	4.14
NLWSCC	24.0	26.8	27.2	27.0	4.07	4.18	4.21	4.22

4 RESULTS AND DISCUSSION

4.1 Compressive strength

To obtain the compressive strength and UPV, the walls were tested at the ages of (3, 7, 14 and 28) d. The compressive strengths of five 100 mm cube specimens were tested at the ages of (3, 7, 14 and 28) d. All results were the average of five 100 mm cubes. The UPV measurements were repeated three times for each cube specimen. The values found for the compressive strength and UPV tests of the mixtures at different ages are tabulated in **Table 4**.

4.2 The relationship between the ultrasonic pulse velocity and the compressive strength

From the data listed in **Table 4**, which shows the averages of the compressive strength and UPV test results, a regression analysis for the pulse velocity versus compressive strength of the cube samples for each mixture was performed. The correlations were established using an exponential curve model. The pulse velocity functions and the correlation coefficient (R^2) are presented in **Table 5**. The high correlation coefficient of the numerical formula indicates the suitability of the functions.

Table 5: Relationships between compressive strength and in-place test results
Tabela 5: Odvisnost med tlačno trdnostjo in rezultati *in situ* preizkusov

Mixture Type	Regression equations	
	Pulse velocity function	Correlation coefficient (R^2)
NC	$f'c = 0.0204\ e^{1.8142V}$	0.9217
SSCC	$f'c = 1.906\ e^{0.6679V}$	0.9412
NSCC	$f'c = 0.0801\ e^{1.3998V}$	0.8914
SLWSCC	$f'c = 0.1857\ e^{1.1872V}$	0.9873
NSLWSCC	$f'c = 0.7731\ e^{0.845V}$	0.9646

4.3 Distribution of the concrete strength within concrete walls

The results of ultrasonic pulse velocity measurements at different test points at the age of 28 d are presented in **Figure 3**. The concrete compressive strength of the reinforced concrete walls was determined by measuring the ultrasonic pulse velocity along the wall thickness and converting it to the cube compressive strength using the relevant function. The average of the ultrasonic pulse velocity measurements and the estimated compressive strength using the pulse velocity functions are summarized in **Table 6**.

The strength distribution of the concrete at the levels of (25, 100 and 175) cm from the bottom of the walls was studied. For all mixes, the strength variation in the walls showed that the bottom regions of the walls were stronger than the top regions. Some trends were also previously observed in structural members of normal and lightweight concrete and self-compacting concrete.[5–11] The phenomenon of strength reduction along the height of the members was probably due to several factors. Toosi et al. studied the strength variation of normal concrete and showed that local segregation and bleeding occur under aggregates, which leads to microcracks and voids beneath the aggregate surface. Therefore, the paste-aggregate bond is weakened. They also showed bond improvement because of the increase of the pressure head in the lower layers.[8] In the case of lightweight concrete, a nonuniform density distribution also occurs because of the porosity and floating of the lightweight aggregates in fresh concrete. Consequently, lightweight aggregates tend to move to the upper levels of concrete

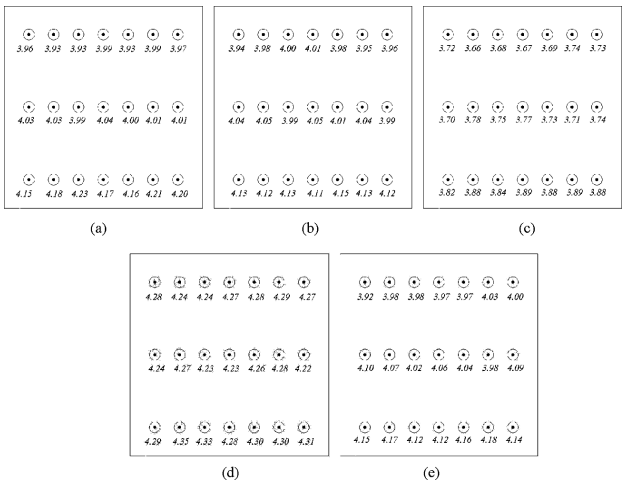

Figure 3: Ultrasonic pulse velocity measurements in different test points of the reinforced concrete walls: (a) SSCC, (b) SLWSCC, (c) NC, (d) NSCC and (e) NLWSCC
Slika 3: Meritve hitrost ultrazvoka v različnih točkah ojačenih betonskih sten: (a) SSCC, (b) SLWSCC, (c) NC, (d) NSCC, in (e) NLWSCC

Table 6: Estimated in situ strengths and test results (28 days)
Tabela 6: Ocenjene *in situ* trdnosti in rezultati preizkusov (28 d)

Level of walls	NC		SSCC		NSCC		SLWSCC		NLWSCC	
	f'_c (MPa)	UPV measurements (km/s)	f'_c (MPa)	UPV measurements (km/s)	f'_c (MPa)	UPV measurements (km/s)	f'_c (MPa)	UPV measurements (km/s)	f'_c (MPa)	UPV measurements (km/s)
Top	16.7	3.70	26.8	3.95	31.5	4.27	20.7	3.97	22.3	3.98
Middle	18.3	3.74	27.9	4.01	30.7	4.25	22.0	4.02	23.7	4.05
Bottom	23.2	3.87	31.2	4.19	33.4	4.31	24.9	4.12	25.8	4.15
Average	19.4	3.77	28.6	4.05	31.8	4.27	22.5	4.03	23.9	4.06

Note: f'_c = Cube compressive strength.

members. This phenomenon is more intense if coarse lightweight aggregate is used.[15] Previous research has shown that the tendency of segregation decreases with increasing the mineral admixtures contents.[16] The relative concrete strength variation at different levels with respect to the concrete strength at the bottom level of the mixtures is shown in **Figure 4**.

Figure 4 shows that the strength of middle and upper levels in comparison to the lower level decreased by 8 % and 14 % for NLWSCC, 10 % and 8 % for NSCC, 11.4 % and 16.5 % for SLWSCC, 11 % and 14.5 % for SSCC and 21 % and 28 % for normal concrete. The results indicated a similar trend for the normal weight self-compacting concrete mixes (SSCC and NSCC) and lightweight self-compacting concrete (SLWSCC and NLWSCC), and there was a significant discrepancy between the self-compacted mixtures and the normal concrete mix. It is possible that the results could be different due to the use of more Leca, especially coarse aggregates. As predicted, because of the use of mineral admixtures and a fine lightweight aggregate in this study, a lower tendency of segregation was observed in the SLWSCC and NLWSCC mixtures. In other words, lightweight self-compacting concrete had greater homogeneity than the normal concrete, but compared with normal self-compacting concrete, it showed less homogeneity.

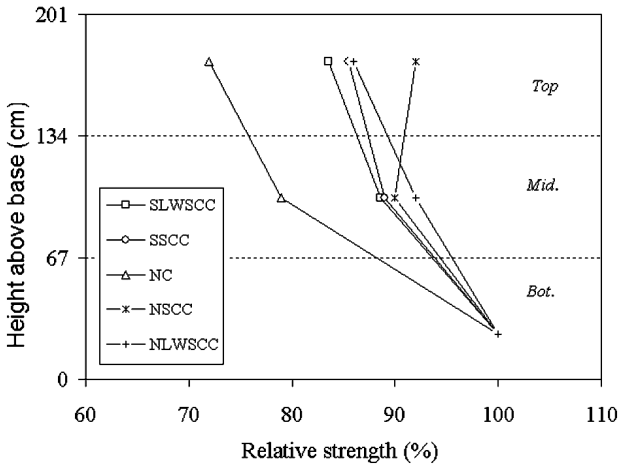

Figure 4: In situ strength variations across the height of the walls
Slika 4: Variacije *in situ* trdnosti po višini sten

Because self-compacted mixtures contain a lower coarse aggregate volume of smaller sizes compared to NC, the size and quantity of microcracks are much lower in self-compacted mixtures, which leads to paste-aggregate bond improvement. As mentioned above, the effects of head pressure and local segregation on the strength variation are much lower in self-compacted mixes than in NC. Some previous reports indicated considerable statistical discrepancies in the homogeneity of properties.[10,11] However, in this study significant differences in strength variation between self-compacted concrete and NC were observed. Khayat showed a similar trend of changes in the

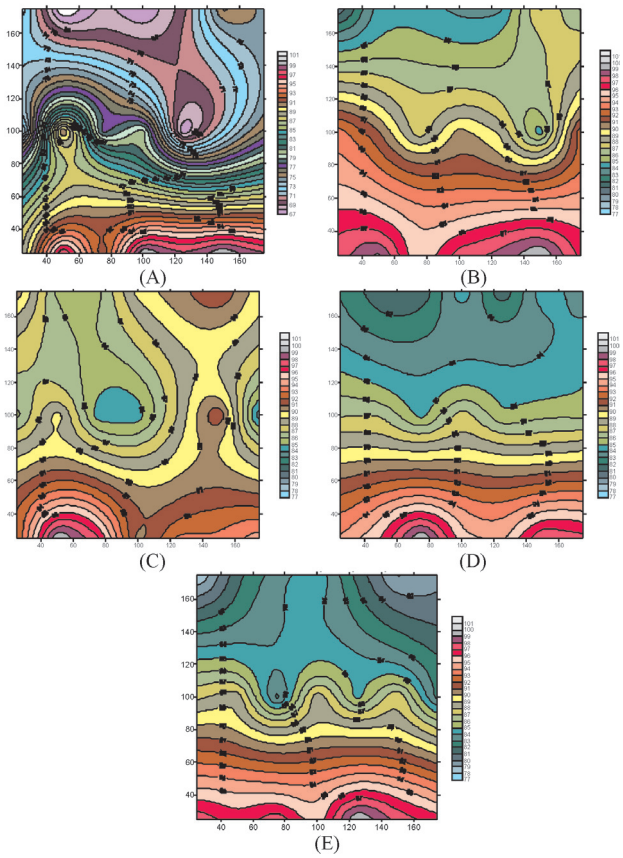

Figure 5: Stress contour plots based on 28-d UPV measurements: (a) NC, (b) NLWSCC, (c) NSCC, (d) SSCC, and (e) SLWSCC
Slika 5: Porazdelitev napetosti na podlagi 28-dnevnih meritev UPV: (a) NC, (b) NLWSCC, (c) NSCC, (d) SSCC in (e) SLWSCC

Table 7: Comparison of cube strengths and estimated in situ strengths
Tabela 7: Primerjava trdnosti kock in ocenjenih *in situ* trdnosti

Mixture type	Level	f: Estimated in situ cube strength (MPa)	f'_c: 28 day standard cube strength in wet-cured condition (MPa)	$\frac{f}{f'_c}$
NC	Top	16.7	27.0	0.62
	Mid.	18.3		0.64
	Bot.	23.2		0.86
SSCC	Top	26.8	32.8	0.82
	Mid.	27.9		0.85
	Bot.	31.2		0.95
NSCC	Top	31.5	32.7	0.96
	Mid.	30.7		0.94
	Bot.	33.4		1.02
SLWSCC	Top	20.7	25.5	0.81
	Mid.	22		0.86
	Bot.	24.9		0.97
NLWSCC	Top	22.3	28.0	0.97
	Mid.	23.7		0.84
	Bot.	25.8		0.92

concrete strength of normal self-compacting and normal concrete walls.[11] However, the walls that Khayat considered were not full scale or reinforced. Hence, the effects of the reinforcement configurations on compaction were not considered, and more studies are necessary. The in situ strength variability is shown in the contour plot of **Figure 5**. This contour plot provides further comparison of the strength variation within the walls both across their height and their length. Random variation along the member length was noted. **Figure 6** shows the strength changes with specific trends along the wall height. However, this trend varied for different mixtures. The NC wall exhibited more intensive discrepancies because of the effect of the internal vibration on the compaction of the concrete.

In **Table 7**, the wet-cured standard cubic compressive strengths are compared with equal cubic strengths at different levels of the walls. Figure 6 shows that the in situ strength varied from 81 % to 102 % of the wet-cured standard 28 d strength for all four self-compacted concrete walls. However, this difference was about 62 % to 86 % for the normal concrete wall. The main reason for the differences between the in situ and standard 28 d strengths is the low sensitivity of self-compacted mixtures to curing conditions. This observation was previously reported by Pera et al.[17] On the other hand, the high discrepancy between the lightweight self-compacting concretes and NC might be because the high initial moisture content of the lightweight aggregates led to typical internal curing. Thus, low sensitivity to the curing regime can be expected for lightweight self-compacting concretes.

A previous study showed 75 % to 90 % differences between the standard cube and in situ 28 d strengths for the SCC mixture.[11]

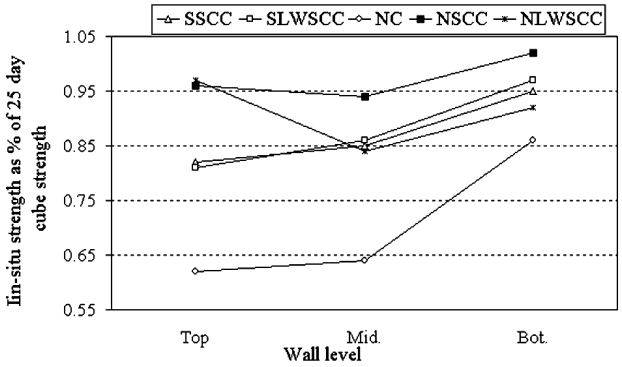

Figure 6: In situ compressive strength in walls in relation to standard 28 d strength
Slika 6: *In situ* tlačna trdnost v stenah v odvisnosti od standardne 28-dnevne trdnosti

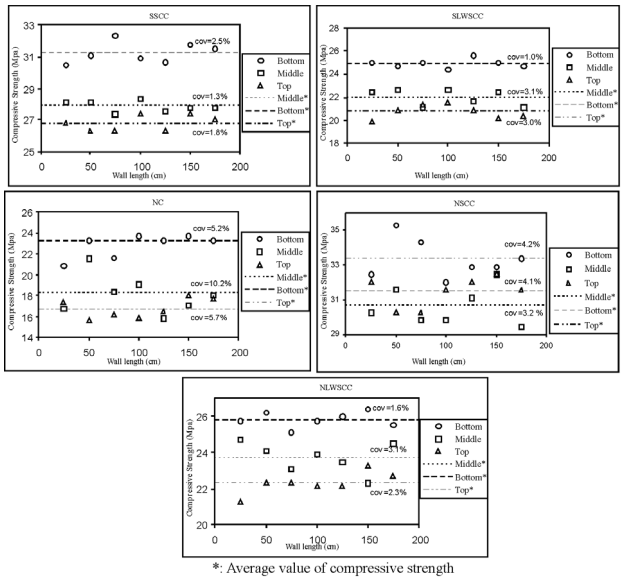

*: Average value of compressive strength

*: Average value of compressive strength
Figure 7: Strength variations along the length of the walls with respect to the average value of each level
Slika 7: Variacije trdnosti po dolžini sten v razmerju s povprečno vrednostjo na vsakem nivoju

4.4 Distribution of concrete strength along the walls

Figure 7 indicates the coefficient of variation (COV) of strength for different heights along the experimental walls. The COV of strength measurements ranged from 1 % to 4.1 % for self-compacted mixes and were limited to 10.2 % for the NC mix. Therefore, the self-compacted mixtures had better uniformity along the length of the walls.

5 CONCLUSIONS

The following conclusions were drawn from the results presented in this paper concerning the variation of

factors such as strength level, type of lightweight aggregate and admixture content.

1. Strength variations across the height of the reinforced concrete walls followed the general pattern of a reasonably uniform distribution from top to bottom, with the top region having a lower strength than the bottom region. However, the magnitude of this variation varied according to the concrete type.
2. The low in situ strength variations of all self-compacted mixtures showed greater strength uniformity than that of the NC mixture along the height of the walls.
3. Due to the low sensitivity of self-compacted mixes to curing conditions, smaller differences were observed in the self-compacted mixes than the normal concrete mix.
4. The COV of the strength measurements showed better uniformity for all normal self-compacting and lightweight self-compacting mixtures.
5. By replacing the silica fume with nano-sized SiO_2 as the admixture, no considerable changes were observed in strength variation trends.

6 REFERENCES

[1] Skarendahl, A., Petersson, O. Self compacting concrete: state-of-the-art report of RILEM TC 174-SCC, Report 23, RILEM Publishers, Cachan, France, **2000**

[2] Koyata, H., Comman, C. R. 2005. Workability measurement and developing robust SCC mixture designs. In proceeding if Second north American conference on the design and use of self consolidating concrete (SCC) and the fourth International RILEM Symposium on self compacting concrete. Addison, IL, USA: Hanley Wood Publishers, (**2005**), 799–805

[3] N'ielsson, I., Wallevik, O.H. In: Wallevik O, Nielsson I., **2003**. Rheologycal evaluation of some empirical test methods – preliminary results proceedings of the 3rd international RILEM symposium Reykjavik, Iceland. RILEM Publishers PRO, 33 (**2003**), 59–68

[4] Videla C., Lopez, M. Effect of lightweight aggregate intrinsic strength on lightweight concrete compressive strength and modulus of elasticity. Mater de construction, 52 (**2002**), 23–27

[5] Madandoust, R. Strength assessment of lightweight concrete. PhD thesis, The University of Liverpool; **1990**

[6] Bungey J. H., Madandoust R. Strength variation in lightweight concrete beams. Cem Concr Res., 34 (**2004**),1259–63

[7] Toosi, M., Houde, J. Evaluation of strength variation due to height of concrete members. Cem. Concr. Res., 11 (**1981**), 519–529

[8] Toosi, M. Variation of concrete strength due to pressure exerted on fresh concrete. Cem. Concr. Res., 10 (**1980**), 845–852

[9] Kumar, R., Bhattacharjee, B. Porosity, pore size distribution and in situ strength of concrete. Cem. Concr. Res., 33 (**2002**), 155–164

[10] Zho, W., Gibbs, J. C., Bartos, J. M., Uniformity of in situ properties of self compacting concrete in full- scale structural element, Cem. Concr. Compos., 23 (**2001**), 57–64

[11] Khayat, K. H, Manai, K., Trudel, A. In situ mechanical properties of walls elements cast using self consolidating concrete, ACI Mater J., 941 (**1997**), 491–500

[12] Malhotra, V. M., Carino, N. J. CRC handbook on non-destructive testing of concrete. CRC Press, **1997**

[13] Bungey, J. The testing of concrete in structures. London, Uk: Surrey university Press, **1989**

[14] PUNDIT Ultrasonic concrete tester. C. N. S. Electronics LTD, 61–63 Holms road, London, NW5, England

[15] Mindess, S., Young, J.F, Darwin, D. Concrete 2nd Prentice Hall, **2003**

[16] Demirboğa, R., Örüng, I, Gül, R. Effect of expanded perlite aggregate and mineral admixtures on compressive strength of low density concrete. Cem. Concr. Res., 31 (**2001**), 1627–32

[17] Pera, J., Husson, S., Guilhot, B. Influence of finely ground limestone on cement hydration. Cem. Concr. Res. 21 (**1999**), 99–105

UDK 621.791.05:669.1
Original scientific article/Izvirni znanstveni članek

ISSN 1580-2949
MTAEC9, 45(6)579(2011)

THE INFLUENCE OF BUFFER LAYER ON THE PROPERTIES OF SURFACE WELDED JOINT OF HIGH-CARBON STEEL

VPLIV VMESNE PLASTI NA LASTNOSTI POVRŠINSKIH ZVAROV JEKLA Z VELIKO OGLJIKA

Olivera Popović[1], Radica Prokić - Cvetković[1], Aleksandar Sedmak[1], Galip Buyukyildrim[2], Aleksandar Bukvić[3]

[1]Faculty of Mechanical Engineering, University of Belgrade, 11000 Belgrade, Serbia
[2]EWE, Istanbul, Turkey
[3]Ministry of defense, 11000 Belgrade, Serbia
opopovic@mas.bg.ac.rs

Prejem rokopisa – received: 2011-02-02; sprejem za objavo – accepted for publication: 2011-06-02

Surface welding with buffer layer is often in use because of its well-known properties of plasticity, or ability to slow crack growth initiated. However, in modern surface welding technologies, buffer layer is rarely used. New classes of flux-cored and self-shielded wires are recently developed and it is possible to achieve the requested properties of welded joints without buffer layer. In this paper, for comparison, the high-carbon steel surface was welded with and without buffer layer. In both cases, it has been used same surface process, but with different filler materials and equal heat input. The mechanical properties, total impact energy, as its components, the fatigue threshold value of ΔK_{th}, and the crack growth rate da/dN were determined. The results obtained at room temperature show better properties of the sample surface welded with the buffer layer, but, with temperature decrease a sharp decrease of toughness of the sample welded with buffer layer occured. Also, buffer layer didn't change the property of initiated crack in terms of crack growth rate. The construction from high-carbon steel are exposed to low exploitation temperature and are used for prolong working time, thus the use of buffer layer in modern surface welding technologies is not recommended.

Keywords: surface welding, buffer layer, welded joint, toughness, crack growth parameters

Površinsko varjenje z vmesno (buffer) plastjo se večkrat uporablja zaradi dobre plastičnosti in sposobnosti za preprečevanje rasti nastale razpoke. Vendar se redkeje uporablja pri sodobnih tehnologijah površinskega varjenja. Nove vrste polnjene in samozaščitne žice so bile razvite in je bilo tako mogoče doseči zahtevane lastnosti zvarov brez vmesne plasti. V tem delu je opisana zavarjena površina jekla z veliko ogljika z vmesno plastjo in brez nje. V obeh primerih je bil uporabljen enak proces z enakim vnosom toplote, vendar z različnim varilnim materialom. Določene so bile mehanske lastnosti, skupna žilavost in njene komponente, prag utrujenosti ΔK_{th} in hitrost napredovanja razpoke da/dN. Lastnosti pri sobni temperaturi so boljše pri vzorcu površine, ki je bil zavarjen z vmesno plastjo, vendar se je pri znižanju temperature hitro zmanjšala žilavost vzorca, ki je bil zvarjen z vmesno plastjo. Tudi vmesna plast ni spremenila hitrosti rasti začete razpoke. Konstrukcije iz jekla z veliko ogljika obratujejo pri nizki temperaturi in se uporabljajo dolgo časa. Zato ni priporočena uporaba vmesne plasti pri modernih tehnologijah varjenja površine.

Ključne besede: varjenje površine, vmesna plast, zvar, žilavost, parametri rasti razpoke

1 INTRODUCTION

The main properties of high-carbon steels are high hardness and strength and having a pearlitic microstructure, have a typically low toughness and crack growth resistance also. Since in exploitation they are often exposed to wear and rolling contact fatigue, parts become unfit for service due to unacceptable profiles, cracking, spalling etc. Surface welding is maintenance way to prolong the exploitation life of damaged parts.[1] For surface welding are mostly in use semi-automatic arc welding processes, with flux-cored and self-shielded wires. Basic difference between them is that the first requires an external shielding gas. In both cases, core material acts as a deoxidizer, helping to purify the weld metal, generate slag formers and by adding alloying elements to the core, it is possible to increase the strength and provide other desirable weld metal properties.[2,3] These processes have replaced slowly MMA process and they almost ideal for outdoors in heavy winds. The result of flux-cored wire application are higher quality welds, faster welding and maximizing a certain area of welding performance.[4] The number of layers in surface welded joint depends of the damage degree, most frequently it's consists of three layers, sometimes with buffer layer, also. The buffer layer is applied for the crack sensitive materials, what high carbon steel certainly is (high CE). The function of buffer layer is to slow down the growth of initiated crack with its own plasticity. Constructions, like railways, are exposed to cyclic load and wear in exploatation, that the crack initiate. Sometimes it is necessary to use a buffer layer, which besides good affects, may have drawbacks, also. Namely, the use of buffer layer slows down significantly the surface welding process, due to replacement of wires and settings of other welding parameters. Since, as already noted, for surface welding are used mainly semi-automatic and automatic processes, it significantly

extends the working time. New classes of flux-cored and self-shielded wires are developed recently, and it is possible to achieve the requested properties of welded joints without buffer layer.

2 EXPERIMENTAL PROCEDURE

The investigation was carried out with high carbon steel with 0.52C-0.39Si-1.06Mn-0.042P-0.038S-0.011Cu-0.006Al, having initial pearlitic microstructure and tensile strength of 680–830 N/ mm^2.

The surface welding of the testing plates was perfomed with a semi-automatic process. As the filler material, the self-shielded wire (FCAW-S) and flux-cored wires (FCAW) with chemical compositions and mechanical properties given in **Table 1**, were used. The plates were surface welded in three layers; sample 1 with FCAW-S without buffer layer; sample 2 with FCAW with buffer layer, as shown in **Table 1**.

Since the *CE*-equivalent was *CE* = 0.64[4], the heat input during welding was of 10 kJ/cm, the preheating temperature was of 230 °C, and the controlled interpass temperature was of 250 °C. Sample 1 was surfaced with one type of filler material (self-shielded wire), while for surfacing of sample 2 two types of wires were used, but both flux-cored: one for the buffer layer and the second for the last two layers. As shielded gas for welding of sample 2, CO_2 was used. To evaluate the mechanical properties, specimens for further investigation were cut from surface welded joints.

3 HARDNESS

Hardness measurements were performed using the 100 Pa load. The hardness profiles of surface welded joints are shown in **Figure 1**. The lowest hardness is for the base metal (250–300 HV), being the hardness of naturally cooled standard rails.[5,6] In HAZ hardness increase is noticable in both samples, due to complex heat treatment and grain refinement.[4] In sample 2 in the first surfaced layer, i.e. in buffer layer the hardness is decreased sharply. The function of buffer layer is to stop the growth crack initiates with own plasticity and lower hardness. The hardness of II and III welded layers of both samples are the highest and similar, due to influence of alloying

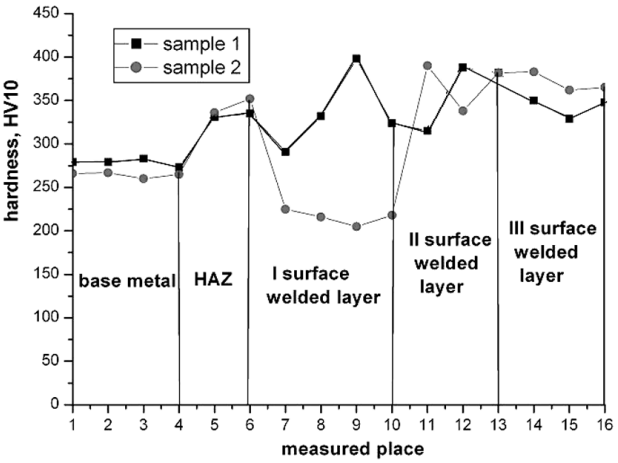

Figure 1: Hardness profiles along the joint cross-section of samples
Slika 1: Profili trdote na prečnem prerezu vzorcev

elements in filler materials, which shift transformation points to bainitic region.[4] The maximum hardness level of 350–390 HV is reached in surface welded layers and it provides improvement of mechanical properties and wear resistance.[4]

4 TENSILE TESTS

The tensile tests were performed on a 2 mm thick specimens. The room temperature mechanical properties (ultimate tensile strength, UTS) of the surface welding layers are shown in **Figure 2**. The basic requirement in

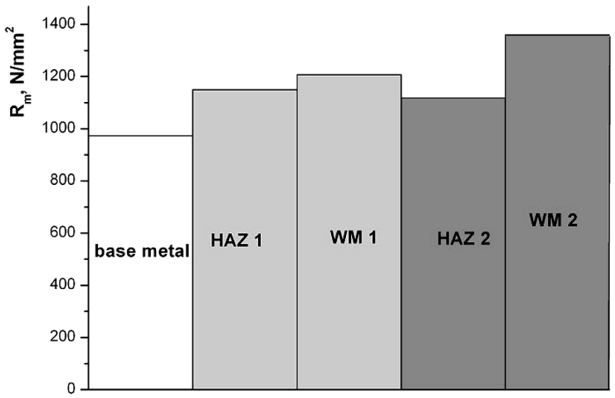

Figure 2: Ultimate tensile strength of the surface welded joints
Slika 2: Raztržna trdnost površinskih zvarov

Table 1: Chemical composition of filler materials
Tabela 1: Kemična sestava varilnih materialov

Sample No.	Wire designation		Wire diam. *d*/mm	Chemical composition, mass fractions, *w*/%							Hardness, HRC
				C	Si	Mn	Cr	Mo	Ni	Al	
Sample 1	OK Tubrodur 15.43 (self-shielded wire)		1.6	0.15	<0.5	1.1	1.0	0.5	2.3	1.6	30–40
Sample 2	1.layer (buffer layer)	Filtub 12B (flux-cored wire)	1.2	0.05	0.35	1.4	-	-	-	-	-
	2. and 3. layer	Filtub dur 12 (flux-cored wire)	1.6	0.12	0.6	1.5	5.5	1.0	-	-	37–42

welded structures design is to assure the required strength. In most welded structures this is obtained with superior strength of WM compared to BM (overmatching effect), and in tested case this is achieved[7,8]. The highest UTS was found for the weld metal of sample 2 (1210 MPa), due to solid state strengthening by alloying elements.[9]

5 IMPACT TESTING

The impact testing was performed according to EN 10045-1, i.e ASTM E23-95, with Charpy V notched specimens on the instrumented machine SCHENCK TREBEL 150 J. Impact testing results are given in **Table 2, 3** and in **Figure 3** for base metal and HAZ at all testing temperatures. The total impact energy, as well as crack initiation and crack propagation energies, for weld metal of both samples at all testing temperatures are presented in **Table 4** and in F**igure 4**.

The total energy of base metal is very low (5 J), due to very hard and very brittle cementite lamellae in pearlite microstructure,[4] while the toughness of HAZ is higher (11–12 J) and is similar for both samples at all testing temperatures.

Table 2: Instrumented impact testing results of Charpy V specimens for base metal and HAZ at all testing temperatures
Tabela 2: Rezultati instrumentiranih Charpyjevih preizkusov za osnovni material in HAZ pri vseh temperaturah preizkušanja

	Total impact energy, E_u/ J		
	20 °C	–20 °C	–40 °C
base metal	5	3	3
sample 1-HAZ 1	12	11	10
sample 2-HAZ 2	11	10	9

Table 3: Instrumented impact testing results of Charpy V surface weld metal specimens at all testing temperatures
Tabela 3: Rezultati instrumentiranih Charpyjevih preizkusov za vzorce V površinskih zvarov pri vseh temperaturah preizkušanja

	sample 1-WM1			sample 2-WM2		
	20 °C	–20 °C	–40 °C	20 °C	–20 °C	–40 °C
Total impact energy, E_u/ J	29	23	17	34	14	11
Crack initiation energy, E_{in}/ J	20	16	15	12	10	10
Crack propagation energy, E_{pr}/ J	9	7	2	22	4	1

The total impact energy of samples 1 and 2 at room temperature are significantly higher (29 J and 34 J) than in base metal (5 J), as consequence of appropriate choice of alloying elements in the filler material. The presence of Ni, Mn and Mo promotes the formation of needled bainitic microstructure and grain refinements, and increases the strength and toughness also[9]. By analyzing the impact energy values of sample 1, a change of toughness in continuity is observed, with no marked drop of toughness, and for all tested temperatures, crack initiation energy is higher than crack propagation energy. This

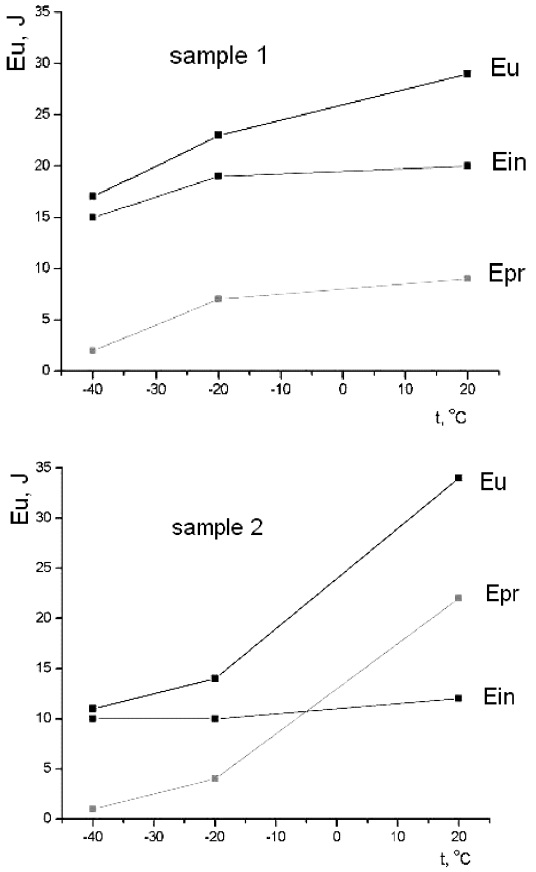

Figure 3: Dependence total impact energy, crack initiation and crack propagation energy vs.temperature for a) weld metal of sample 1 and b)weld metal of sample 2
Slika 3: Odvisnost skupne žilavosti ter energije začetka in napredovanja razpoke od temperature za zvar vzorca 1 in zvar vzorca 2

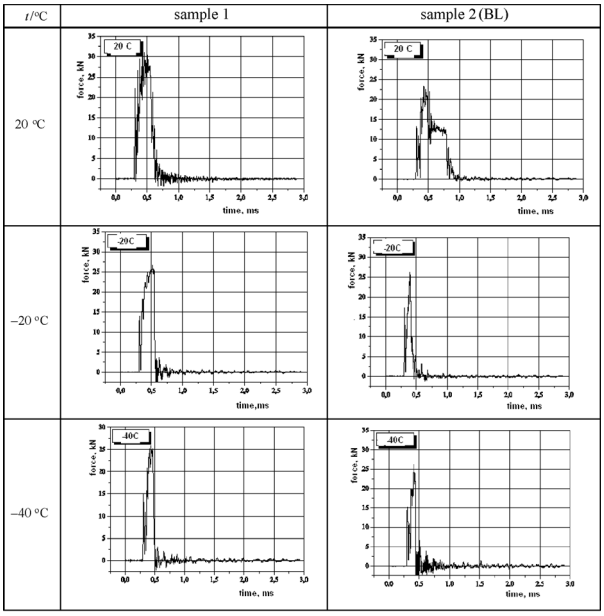

Figure 4: Diagrams force-time, obtained by instrumented Charpy pendulum for sample 1 and sample 2
Slika 4: Odvisnost sile od časa, določena z instrumentalnim Charpyjevim kladivom za vzorca 1 in 2

is the reason for the absence of significant decrease of toughness. The highest value of total impact energy was found for the sample 2 at room temperaure (34 J), which is the only case when the initiation energy is lower than propagation energy (12 J and 22 J, respectivelly). This shown practically the buffer layer function. Namely, the initiated crack during propagation comes to plastic buffer layer, which slows down crack further growth. For this reason, the crack propagation energy is the largest part of total impact energy. However, at –20 °C, significant drop of total impact energy is noticable (14 J) due to losing of buffer layer plastic properties at lower temperatures. The low-carbon wire (0.05 % C and 1.4 % Mn) has excellent toughness, but and marked rapid drop on S-curve (dependence toughness vs. temperature). Transition temperature of this material above –20 °C is confirmed by the obtained impact toughness results. The use of buffer layer is reasonable if the exploatation temperature is above –5 °C; on the contrary, at lower temperatures, buffer layer is losing its function and the toughess is decreased.

Diagrams force-time, obtained by instrumented Charpy pendulum, are given in **Figure 5**. As can be seen, for the sample 1 the character of diagrams force-time changed little by lower temperature. Namely, this material at room temperature has diagram with marked rapid drop, as consequence of unstable crack growth. After the maximum load, a very fast crack growth is started, and it is confirmed by the low value of crack propagation energy.[10] On the contrary, on the sample 2 diagram at room temperature, the presence of buffer layer is clearly shown. The initiated crack, during its growth, comes to buffer layer which temporary stops the further crack growth and changes crack growth rate. The obtained experimental diagram doesn't belong to any type, according to standard EN 10045-1. This leads to toughness increase, primarily crack propagation energy, and it is also here the only case when the crack initiation energy is lower than crack propagation energy.

6 CRACK GROWTH RATE

A basic contribution of fracture mechanics in fatigue analysis is the division of fracture process to crack initiation period and the growth period to critical size for fast fracture[7]. Fatigue crack growth tests had been performed on the CRACKTRONIC dynamic testing device in FRACTOMAT system, with standard Charpy size specimens, at room temperature, and the ratio $R = 0.1$. A standard 2 mm V notch was located in third layer of WM, for the estimation of parameters for WM and HAZ, since initiated crack will propagate through those zones. Crack was initiated from surface (WM) and propagated into HAZ, enabling calculation of crack growth rate da/dN and fatigue treshold ΔK_{th}.[4] The results of crack growth resistance parameters, i.e., obtained relationship da/dN vs. ΔK for sample 1 and for sample 2 are given in **Figure 6**. Parameters C and m in Paris law, fatigue threshold ΔK_{th} and crack growth rate values are given in **Table 5** for both samples as obtained from relationships given in **Figure 6**, for corresponding ΔK values.

The behaviour of welded joint and its constituents should affect the change of curve slope in the part of validity of the Paris law. Materials of lower fatigue-crack growth rate have lower slope in the diagram da/dN *vs.* ΔK.[7] For comparison of the properties of surface welded joint constituents the crack growth rates are calculated for different values of stress-intensity factor range ΔK. Bearing in mind that the weld metal consists of two lay-

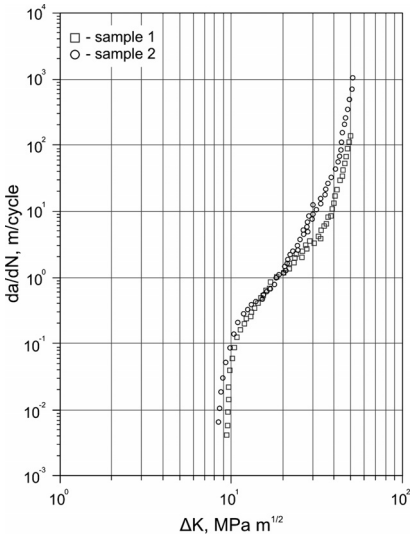

Figure 6: Diagram da/dN vs. ΔK for sample 1 and sample 2
Slika 6: Diagram da/dN za vzorca 1 in 2

Table 4: Parameters C, m, ΔK_{th} and crack growth rate values for all zones of surface welded joints
Tabela 4: Parametri C, m, ΔK_{th} in hitrost rasti razpoke za vse dele površinsko zvarjenih vzorcev

	Zone of surface welded joint	Fatigue threshold ΔK_{th}/ (MPa m$^{1/2}$)	Parameter C	Parameter m	Crack growth rate (da/dN)/m		
					ΔK = 15 MPa m$^{1/2}$	ΔK = 20 MPa m$^{1/2}$	ΔK = 30 MPa m$^{1/2}$
sample 1	WM 1	9,5	$4.45 \cdot 10^{-13}$	3.74	$1.11 \cdot 10^{-8}$	-	-
	WM 2		$3.78 \cdot 10^{-13}$	3.61	-	$1.88 \cdot 10^{-8}$	-
	HAZ		$4.07 \cdot 10^{-13}$	3.79	-	-	$1{,}61 \cdot 10^{-7}$
sample 2	WM 1	8,9	$4.63 \cdot 10^{-13}$	3.87	$1.65 \cdot 10^{-8}$	-	-
	WM 2		$3.85 \cdot 10^{-13}$	3.88	-	$2.07 \cdot 10^{-7}$	-
	HAZ		$3.76 \cdot 10^{-13}$	3.93	-	-	$1.18 \cdot 10^{-6}$

ers (third layer is used for V notch), as referent values of ΔK were taken: ΔK = 15 MPa m$^{1/2}$ for WM1, ΔK = 20 MPa m$^{1/2}$ for WM2, and ΔK = 30 MPa m$^{1/2}$ for HAZ. It's important that all the selected values are within the middle part of the diagram, where Paris law is applied. In all three zones of surface welded joint (WM2, WM1 and HAZ), the sample 2 with buffer layer has a higher crack growth rate than sample 1, i.e. the growth of initiated crack will be slower in sample 1. This means that for the same value of stress intensity factor ΔK, the specimen of sample 2 needs less number of cycles of variable amplitude than the specimen of sample 1, for the same crack increment.[9] The maximum fatigue crack growth rate is achieved in HAZ for both samples, when stress intensity factor range approaches to plane strain fracture toughness.

If a structural component is continuously exposed to variable loads, fatigue crack may initiate and propagate from severe stress raisers if the stress intensity factor range at fatigue threshold ΔK_{th} is exceeded.[7] The fatigue treshold value ΔK_{th} for sample 2 (ΔK_{th} = 8.9 MPa m$^{1/2}$) is lower than that for sample 1 (ΔK_{th} = 9.5 MPa m$^{1/2}$). This means that the crack in sample 2 will be initiated earlier, i.e. after less number of cycles, than in sample 1.

Values of fatigue threshold and crack growth rates corespond to initiation and propagation energies in impact testing, and in this case, good corelation is achieved.[9] Sample 1 has higher crack initiation energy (20 J) and higher ΔK_{th} (ΔK_{th} = 9.5 MPa m$^{1/2}$ for sample 1 and ΔK_{th} = 8.9 MPa m$^{1/2}$ for sample 2). With comparation of crack propagation energy and crack growth rate, it is hard to establish the precise analogy, as toughness was estimated for the surface weld metal, whereas crack growth rate for each surface welded layer. Generally, buffer layer didn't show slow,, the initiated crack growth, with aspect of crack growth rate, while this effect is obvious in the case of toughness, i.e. crack propagation energy.

7 CONCLUSIONS

On the base of obtained experimental results and their analysis, the following is concluded:

1. The experimental investigation of surface welded joints with different weld procedures has shown, as expected, significant differences on their performance in terms of mechanical properties. But, in both cases, it was shown, that in spite of poor weldability of high carbon steel, they can be successfully welded.
2. The maximal hardness level of 350–390 HV is reached in surface welded layers of both samples, with equal hardness of base metal (250–300 HV). The main difference appears in the first deposition layer, where as expected, in sample 2 the hardness is significantly lower (buffer layer). The obtained hardness values ensure simultaneously the improvement of mechanical and wear properties, and in the case of a rail, represents maximal hardness preventing the wheel wear.[4] Similar results are obtained by tensile testing. Sample 2 has slightly higher ultimate tensile strength (1360 MPa) than sample 1 (1210 MPa) due to solid solution strengthening by alloying elements.
3. The greatest differences are found in impact properties. The highest value of total impact energy of sample 2 at room temperaure (34 J) was obtained only in the case when the initiation energy was lower than propagation energy (12 J and 22 J, respectivelly). However, at –20 °C, the drop of total impact energy is significant (14 J), due to lowering of buffer layer plastic properties at lower temperatures. The transition temperature of this material is above –20 °C, and it was confirmed by obtained impact toughness results. The use of buffer layer is beneficial for exploatation temperature above –5 °C. On the contrary, at lower temperatures, buffer layer loses its function and toughess decreases. On the contrary, for sample 1 the change of toughness is continous and without marked drop of toughness (29 J at 20 °C and 23 J at –20 °C). At all tested temperatures, the crack initiation energy is higher than crack propagation energy. This may be the reason for the absence of significant decrease of toughness and that should be kept in mind during design and exploitation.
4. Results show that sample 2 has higher crack growth rate ($1.65 \cdot 10^{-8}$) than sample 1 ($1.11 \cdot 10^{-8}$), and lower fatigue treshold value ΔK_{th} (8.9 MPa m$^{1/2}$ for sample 2 and 9.5 MPa m$^{1/2}$ for sample 1). This means that the crack in sample 2 will be initiated earlier, i.e. after less number of cycles, than in sample 1, and that a less number of cycles is needed to reach the critical size.
5. Values of fatigue threshold and crack growth rates corespond to initiation and propagation energies in impact testing. In the case of fatigue treshold and crack initiation energy, good correlation was achieved. Sample 1 has higher crack initiation energy (20 J) and higher ΔK_{th} (9.5 MPa m$^{1/2}$) than sample 2 (12 J and ΔK_{th} = 8.9 MPa m$^{1/2}$). On the contrary, buffer layer didn't show decrease of initiated crack growth rate, as this effect is obvious in the case of toughness, i.e. crack propagation energy. Since the constructions from high-carbon steel are used at low temperature, and bearing in mind the extended working time, in modern surface welding technologies, the use of buffer layer is not recommended.

Acknowledgement

The research was performed in the frame of the national project TR 35024 financed by Ministry of Science of the Republic of Serbia.

8 REFERENCES

[1] O. Popovic, R. Prokic - Cvetkovic, A. Sedmak, R. Jovicic, Proceedings of 12thIntern. Conf. Trends in the Development of Machinery and Associated Technology TMT 2008, Turkey, 2008, 1157–1160

[2] K. Lee, Increase productivity with optimized FCAW wire, Welding design & Fabrication, 74 (**2001**) 9, 30

[3] H. Sadler, Including welding Engineer, Welding design & Fabrication, 70 (**1997**) 6, 74

[4] O. Popovic et al, Characterisation of high-carbon steel surface welded layer, Journal of Mechanical Engineering 56 (**2010**) 5, 295–300

[5] U. P. Singh, B. Roy, S. Jha, S. K. Bhattacharyya, Microstructure and mechanical properties of as rolled high strength bainitic rail steels, Materials Science and Technology, 17 (**2001**) 1, 33–38

[6] K. Lee, A. Polycarpou, Wear of conventional pearlitic and improved bainitic rail steels, Wear, 259 (**2005**), 391–399

[7] M. Burzić, Ž. Adamović, Experimental analysis of crack initiation and growth in welded joint of steel for elevated temperature, Mater. Tehnol., 42 (**2008**) 6, 263–271

[8] M. Manjgo, M. Behmen, F. Islamović, Z. Burzić, Behaviour of cracks in microalloyed steel welded joint, Structural integrity and life, 10 (**2010**) 3, 235–238

[9] O. Popovic, Ph. D. Thesis, University of Belgrade, Faculty of Mechanical Engineering, (**2006**)

[10] V. Grabulov, I. Blačić, A. Radović, S. Sedmak, Toughness and ductility of high strength steels welded joints, Structural integrity and life, 8 (**2008**) 3, 181–190

UDK 669.35'6:620.193
Original scientific article/Izvirni znanstveni članek

ISSN 1580-2949
MTAEC9, 45(6)585(2011)

CORROSION STABILITY OF DIFFERENT BRONZES IN SIMULATED URBAN RAIN

KOROZIJSKA STABILNOST RAZLIČNIH BRONOV V UMETNEM KISLEM DEŽJU

Erika Švara Fabjan, Tadeja Kosec, Viljem Kuhar, Andraž Legat

National Building and Civil Engineering Institute, Dimičeva 12, 1000 Ljubljana, Slovenia
erika.svara@zag.si

Prejem rokopisa – received: 2011-04-16; sprejem za objavo – accepted for publication: 2011-06-06

Copper and high copper alloys tend to passivate in humid air. In clean humid air, cuprite slowly transforms to black tenorite. If atmosphere contains aggressive species, acid rain might effect the formation of different corrosion products. The patina that forms upon exposure to urban acid rain also depends of the composition of the base alloy. In the present study three different alloys were investigated: leaded bronze, usually used for sculptures, unleaded bronze as an alloy without an impact on the environment, and new type of bronze alloy, silicon bronze.
The electrochemical measurements were performed to investigate the different bronze properties in simulated urban acid rain that contained carbonates, sulphates and nitrates, acidified to pH 5. Morphological characteristics of the three different bronzes were studied and SEM/EDX analysis of the corrosion products was performed.
It was found that silicon bronze has higher corrosion resistivity than unleaded bronze, the former having higher corrosion resistivity than leaded bronze. In addition, time dependant electrochemical impedance spectroscopy measurements showed that polarization resistances for silicon bronze and unleaded increased with time, whereas it decreased for leaded bronze. The corrosion layer on silicon bronze is more compact and thinner due to homogeneous microstructure.

Keywords: bronze, metallography, corrosion, simulated urban rain

Baker ter bakrove zlitine se na vlažnem zraku pasivirajo, prihaja do nastanka t. i. patin. Najprej se tvori rdečkast kuprit, ki se nato počasi spreminja v črn tenorit. Če pa so v atmosferi agresivne zvrsti, lahko nastali kisli dež vpliva na tvorbo različnih korozijskih produktov. Patina, ki se tvori zaradi izpostavitve kislemu dežju, je odvisna tudi od sestave zlitine. V študiji smo preiskovali tri različne vrste bronastih zlitin: bron z vsebnostjo svinca, pogosto uporabljen pri ulivanju večjih bronastih spomenikov, bron brez vsebnosti svinca ter novo vrsto brona s silicijem.
Elektrokemijske preiskave smo izvedli v simulirani raztopini kislega dežja, ki je vsebovala sulfate, karbonate in nitrate. Določili smo mikrostrukturne značilnosti posameznih bronov ter morfologijo korozijskih produktov.
Ugotovili smo, da je najbolj korozijsko odporna zlitina bakra s silicijem, sledi recentna zlitina brez svinca, najslabše korozijske lastnosti pa ima zlitina s svincem. Nadalje smo z elektrokemijsko impedančno spektroskopijo pokazali, da se korozijske lastnosti zlitine s svincem s časom slabšajo, korozijske lastnosti zlitine brez svinca ter bron s silicijem pa se s časom izboljšujejo. Korozijski produkti na silicijevi zlitini so kompaktni predvsem zaradi homogene mikrostrukture.

Ključne besede: bron, metalografija, korozija, simulirana raztopina kislega dežja

1 INTRODUCTION

Copper and copper alloys may corrode different ways depending on the type of atmosphere that the bronze objects are exposed to. In rural areas where atmosphere is clean, the bronze surface first turns reddish forming cuprite and finally it transforms to black tenorite. In general, urban and marine atmosphere are more aggressive, and versatile corrosion products form on non protected copper or bronze. Numerous studies have been involved in the subject [1–28].

The bronze problematics is very wide in its area, it covers studies of different bronze types [3,7,11,20] and natural patinas that form on copper or bronze [1,8–10,19,24,25,28]. The main concern in some studies is protection of natural and synthetic artificial patinas [4,5,14,15,18,19]. Much work is devoted to different corrosion inhibitors [5,14,16–18,27] next to different basic electrochemical studies [6,22,23].

The corrosion products that form in particular type of bronze are strongly dependant on the type of bronze, the type of the atmosphere, the chemical and physical preparation of surface, patinations and protections. The two scientific works were result of EUREKA– 2210 Eurocare bronzart project, where different cast bronzes for production of bronze artworks were studied [7,11].

The seven different types of bronze with different contents of copper, tin, zinc, lead, silicon and nickel were employed in the study by Gallese et al. [11]. It was shown that the bronze alloy with minimal content of Pb (Cu–4Sn–5Zn) showed very good characteristics, as well as the bronze alloy with less zinc and more tin (Cu–9Sn–1.5 Zn) and alloy with the presence of Ni (Cu–9Sn–2Zn–3Ni). All these alloys showed improved corrosion characteristics when compared to reference alloy (Cu–5Sn–4Zn–5Pb). This traditional alloy that contains lead is recognized as problematic due to lead toxicity.

In another study, the electrochemical properties of alloy Cu–5Sn–5Zn–5Pb (G85) were compared to SI3 (Cu–8Sn–3Si) in simulated acid rain and the corrosion characteristics were evaluated after exposure in simulated urban–industrial and marine environment. It was found out that silicon bronze exhibited better corrosion resistance in more aggressive marine environment [7].

It is of big importance to develop and investigate bronzes that would perform well in different corrosive environments. The information could provide more knowledge and appropriate selection of suitable materials for the application in the field of Cultural Heritage. The selection of proper alloy in different environments could be improved to minimize visual change of bronze surface as well as unwanted appearance of corrosion products. Novelty feature of this study is the evaluation of the difference in corrosion performance of older and newer type of alloys.

The main objectives of the present study were to electrochemically investigate the difference of the three different bronze types: Cu–Zn–Sn and Cu–Zn–Sn–Pb and Cu–Sn–Si. Potentiodynamic techniques as well as electrochemical impedance spectroscopy were used for the study of electrochemical behaviour and passive layers that formed in simulated urban rain at open circuit potential. The morphological examination was performed. The SEM/EDX spectroscopic investigation was made in order to examine the corrosion products that had formed during 35 days immersion in simulated urban rain solution.

2 EXPERIMENTAL

2.1 Material and surface preparation

The bronze samples were cast in a sand mould of dimension of (100 × 100 × 5) mm. Three different bronzes were chosen to be investigated: CuSnZn, CuSnZnPb and CuSnSi. CuSnZn bronze is currently used for casting of big bronze sculptures, bronze CuSnZnPb contains some lead, which is advised to be omitted in newly casted sculptures, and new type of bronze that contains silicon: CuSnSi. The composition of the three different bronzes, determinated by portable X-ray fluorescence analysers X-MET5100, Oxford Instruments, UK, is given in **Table 1**.

Samples were sectioned from 5 mm plates in the form of discs of 15 mm diameter used as working electrodes. Prior to measurement, the specimens were abraded with 800 and 1000 grid emery paper. Finally, the samples were ultrasonically cleaned in distilled water and then well dried.

2.2 Electrochemical measurements

The electrochemical measurements were performed in a solution of 0.2 g/L Na_2SO_4, 0.2 g/L $NaHCO_3$ and 0.2 g/L $NaNO_3$. It was acidified with H_2SO_4 to pH 5 in order to simulate the acid rain which is frequently found in polluted urban environments (this atmosphere was designated: "simulated urban rain"). Four different electrochemical measurements were done for three different types of bronzes.

A three–electrode corrosion cell was used with a volume of 350 cm^3. The working electrode was embedded in a Teflon holder, and had an exposed area of 0.785 cm^2. Saturated calomel electrode (SCE, E = 0.2415 V) was used as reference electrode and two stainless steal rods served as a counter electrode. For electrochemical tests a Gamry 600 potentiostat/galvanostat, expanded with a Gamry Instruments framework module was used.

Following initial 1 h stabilization at open circuit potential (OCP), linear polarization measurements at ±20 mV vs. OCP with a scan rate 0.1 mV/s were performed. Finally, electrochemical impedance measurements, the frequency range ranged from 65 kHz to 5 MHz at 10 cycles per decade, with an ac amplitude of ±10 mV, were monitored. The absolute impedance and phase angle were measured at each frequency. The impedance measurements were carried out after different times of immersion (1 h, 4 h, 8 h and 12 h) in the electrolyte. All potentials are reported with respect to the SCE scale.

2.3 SEM/EDX analysis

For SEM/EDX analysis the different alloys were immersed in a simulated urban rain, pH 5 for 35 d under stationary conditions. At the end of exposure, the specimens were taken from the solutions, rinsed with distilled water and dried. Surface morphology was inspected and analyzed with a low vacuum scanning electron microscope (SEM, JSM 5500 LV, JOEL, Japan) at acceleration voltage of 20 kV. The microscope was equipped with energy dispersive spectrometer (Inca, Oxford Instruments Analytical, UK). EDS analysis was performed at an acceleration voltage of 20 kV.

2.4 Metalographic examination

Samples were first grounded up to grades 2000, then they were polished up to 4000 and finally 0.5 μm paste was used. Etching for uncovering the microstructure was performed using solution of ammonium and hydrogen peroxide for 3 min. The sample was then immediately rinsed with alcohol and dried with air.

Table 1: The composition of the three different bronzes in mole fractions, *x*/%
Tabela 1: Sestava različnih bronastih zlitin v molskih deležih, *x*/%

Bronze alloy / Composition	Cu	Sn	Zn	Pb	Si	Al	P	Fe	the rest
CuSnZn	87.0	5.5	3.6	0.1	–	0.6	–	0.1	3.1
CuSnZnPb	87.1	6.6	1.1	5.0	–	–	0.1	0.1	0
CuSnSi	85.5	9.6	0.1	0.1	2.5	–	0.1	0.1	2.0

A CARL ZEISS AXIO Imager M2m optical metallographic microscope was used to inspect the microstructure of specimens. Metallographic specimens were prepared and investigated in the longitudinal and transverse direction of castings.

3 RESULTS AND DISCUSSION

3.1 Metalographic examination

Unleaded bronze, CuZnSn, revealed a non–homogeneous material consisting of dendrites of β–tin and zinc eutectics in the matrix of α–copper. CuSnZn bronze many microstructural imperfections, such as shrinkage cavities, pores and non–uniform dendrite distribution (**Figure 1a and 1b**).

Microstructure of CuSnZnPb bronze consisted of similar eutectics and matrix as CuSnZn bronze. Lead produced by the eutectic reaction was distributed inter–dendritically in copper as small globules. Some shrinkage cavities (black inter–dendritic network) could be observed in the microstructure (**Figure 1c and 1d**).

Silicon bronze, denoted as CuSnSi, is a very homogeneous material in both longitudinal and transverse direction (**Figure 1e and 1f**). It consisted of dendrites of silicon and β–tin eutectics in matrix of α–copper. It was reported that higher tin content in the alloy might improve corrosion resistance of the bronze [7].

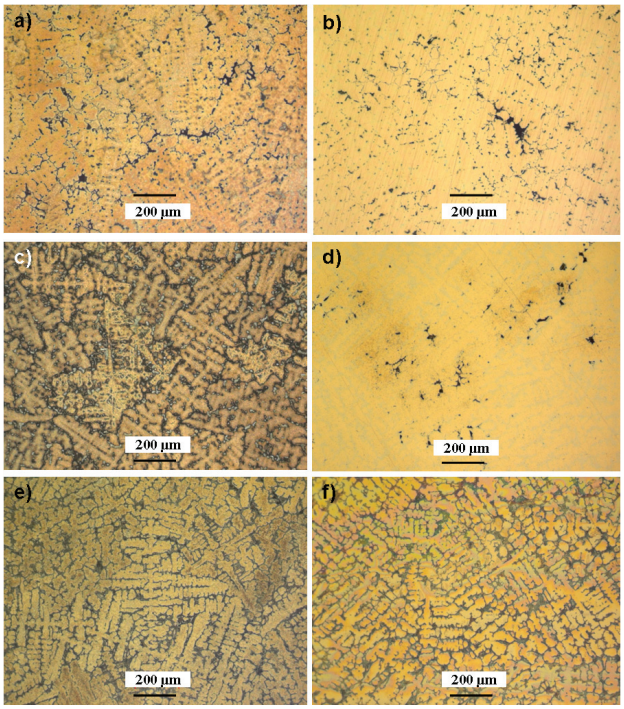

Figure 1: Metalographic images of the three different bronzes (CuSnZnPb– a and b, CuSnSi–c and d and CuSnZn– e and f), exposed surface direction–longitudinal (a, c, e) and cross–sections–transverse side (b, c, f). All shown images are etched, except b) and f), which are polished.

Slika 1: Metalografski posnetki treh različnih vrst brona (CuSnZnPb– a in b, CuSnSi–c in d ter CuSnZn– e in f). Longitudinalna smer je izpostavljena površina brona (a, c, e) in prerez brona (b, c, f). Broni na prikazanih posnetkih so jedkani, razen na posnetkih b) in f), kjer je prikazana brušena površina.

3.2 Electrochemical measurements

In order to evaluate corrosion properties of the three different bronzes, electrochemical experiments were conducted in a simulated urban rain, pH 5. For further evaluation of corrosion behaviour, the samples were immersed in the simulated urban rain solution for 35 d. After that, the surface was examined by EDX/SEM technique.

3.2.1 Open circle potential measurement

During the stabilization process, the open circuit potential was measured as a function of time. **Figure 2** represents open circuit potential curves of all three investigated bronzes, immersed in the urban rain solution with pH 5. All curves show a similar electrochemical behaviour. The corrosion potential, E_{OC} at the beginning of exposure (up to 500 s) did not change much with time for CuSnZn and CuSnSi. For leaded bronze CuSnZnPb it moved to slightly more positive values at the beginning of exposure. Then, the corrosion potential in all cases moved to more negative values of potentials. After one hour of immersion it stabilized at –0.025 V for bronze CuSnZn and at a slightly more positive potential for bronze CuSnZnPb at –0.020 V. Corrosion potential for CuSnSi stabilized at –0.030 V after 1 h of immersion. The observed decrease of the value of E_{OC} in time might be a result of formation of adsorbed layer at interface bronze/electrolyte due to carbonate, sulphate and nitrate ions in simulated urban rain. However, *E*oc evolution is quite regular, indicating a stable process occurring through a relative stable layers that formed on investigated bronze surfaces.

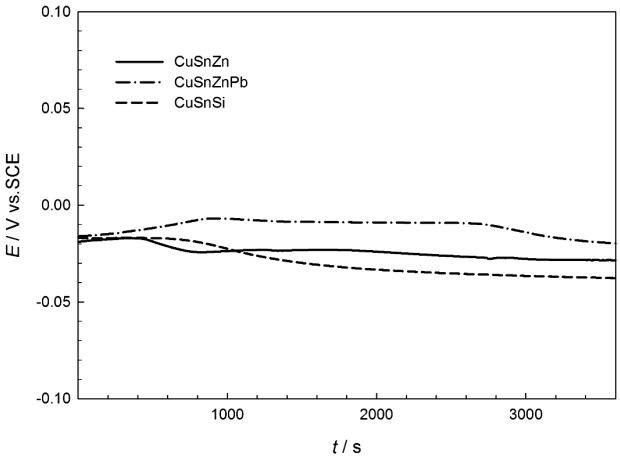

Figure 2: Open circuit potential measurements for the three different bronzes: CuSnZn, CuSnZnPb and CuSnSi, immersed in simulated urban rain solution, pH 5.

Slika 2: Meritve pri potencialu odprtega kroga za tri različne brone CuSnZn, CuSnZnPb in CuSnSi, potopljene v simulirano raztopino mestnega dežja, pH 5.

3.2.2 Polarization resistance (R_p) measurements

One hour after immersion of CuSnZn, CuSnZnPb and CuSnSi in simulated urban rain, pH 5, the linear polarization measurements at a scan rate of 0.1 mV/s were executed (**Figure 3**). The slope of the curve potential–current is the polarization resistance value as described in Stearn Geary equation (1):

$$R_{\mathrm{p}(\Delta E \to 0)} = \frac{\Delta E}{\Delta j} \quad (1)$$

The average measured values for the three bronzes are presented in **Table 2**. The lowest value of polarization resistance (R_p = 2.3 kΩ cm^2) corresponded to leaded bronze, CuSnZnPb and the highest value of polarization resistance corresponded to silicon bronze, CuSnZnSi (R_p = 4.6 kΩ cm^2). The lowest value of polarization resistance for CuSnZnPb exhibited the highest corrosion susceptibility of leaded bronze, whereas values for Silicon bronze CuSnSi showed higher corrosion resistance in simulated urban rain than leaded bronze and bronze CuSnZn. Similar observation was found by Chiavari and coworkers [7]. In their study, leaded bronze and silicon bronze exhibited similar electrochemical behaviour at initial stages but after 7 d, the corrosion rate of leaded bronze was decreased. It was ascribed to formation of uniform and stable passive layer on silicon bronze in comparison with passive layer on leaded bronze. Namely, the passive layer on silicon bronze hindered the oxygen diffusion to the copper surface.

3.2.3 Electrochemical impedance spectroscopy (EIS) measurements

Figure 4 represents the Nyquist diagrams for the three different bronze samples: CuSnZn, CuSnZnPb and CuSnSi at different immersion times during 12 h of immersion in simulated urban rain solution with pH 5.

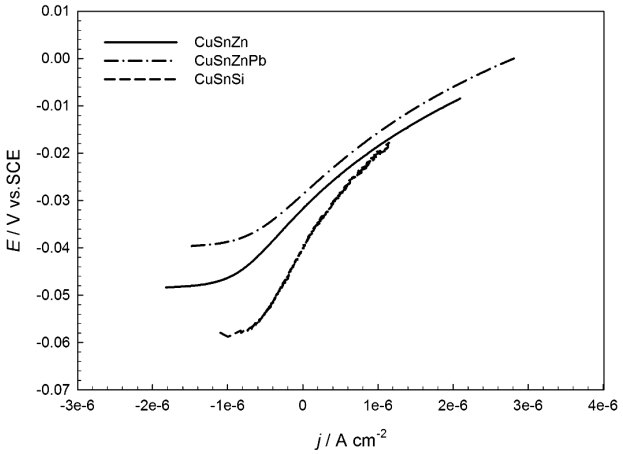

Figure 3: Polarization resistance curves for CuSnZn, CuSnZnPb and CuSnSi immersed in simulated urban rain, pH 5 at a scan rate 0.1 mV/s

Slika 3: Meritve linearne upornosti za CuSnZn, CuSnZnPb in CuSnSi, potopljene v simulirano raztopino mestnega dežja, pH 5, pri hitrosti preleta 0,1 mV/s

Table 2: Corrosion potential, E_{corr} and polarization resistance values, R_p, deduced from linear polarization measurements

Tabela 2: Korozijski potencial E_{kor} in vrednosti polarizacijskih upornosti R_p, dobljenih iz meritev linearne upornosti

Material	E_{corr} /V	R_p/(kΩ cm^2)
CuSnZn	–0.032	3.2
CuSnZnPb	–0.029	2.3
CuSnSi	–0.038	4.6

Table 3: The estimated polarization resistance from EIS measurements in dependence of the time, values of R_p/(kΩ cm^2)

Tabela 3: Ocenjene vrednosti polarizacijskih upornosti iz meritev EIS v različnih časovnih obdobjih R_p/(kΩ cm^2)

Immersion time	1 h	4 h	8 h	12 h
$R_{p\ (CuSnZn)}$	15	13	23	25
$R_{p\ (CuSnZnPb)}$	3.4	3.4	3.1	2.9
$R_{p\ (CuSnSi)}$	5.2	5.0	5.9	9.2

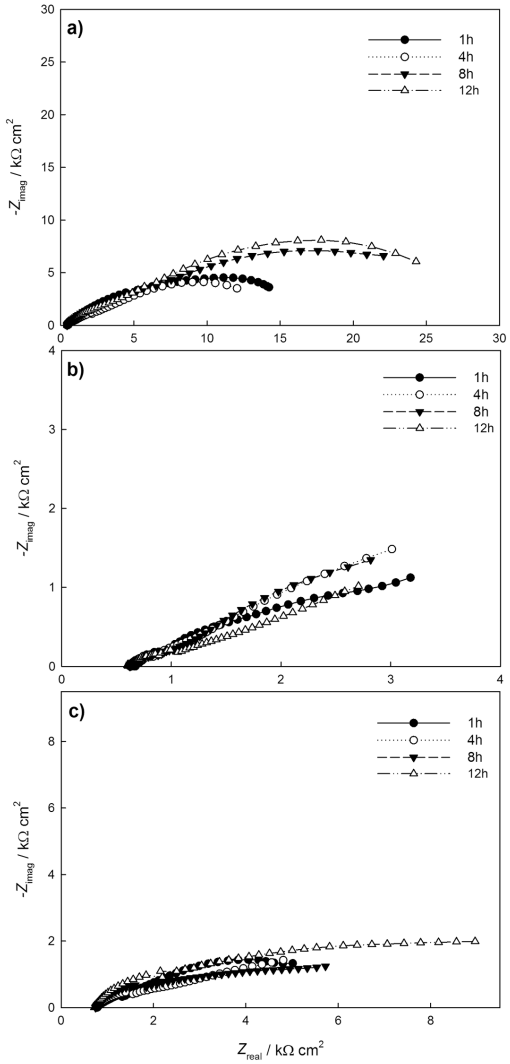

Figure 4: EIS response as Nyquist plots for different bronzes: a) CuSnZn, b) CuSnZnPb and c) CuSnSi after different immersion times in a simulated urban rain solution, pH 5.

Slika 4: EIS-odziv v obliki Nyquistovih diagramov za različne brone CuSnZn, CuSnZnPb in CuSnSi po različnih časih potopitve v simulirano raztopino mestnega dežja, pH 5.

Nyquist diagram corresponding to bronze CuSnZn was characterized by high frequency intercept at the abscise axis and broad and semi-depressed loop at lower frequencies (**Figure 3**). One time constant was observed at 1 h immersion which then evolves with two clearly resolved time constants at 12 h immersion time. Estimated polarization resistances (R_p) were determinated from impedance modulus at the lowest value of frequencies, as presented in **Table 3**. During 12 h immersion, impedance values for bronze CuSnZn increased with time. Thus, the estimated polarization resistance increased with immersion time. Stable layer of protective products had formed.

The Nyquist diagram for CuSnZnPb (**Figure 4**) was characterized by high frequency intercept at the absise axis, broad depressed loop at middle frequencies and straight line at low frequencies. The high frequency intercept is relatively high due to low conductivity of the urban acid rain solution. The shape of impedance response indicated the undefined time constant as observed from Bode diagrams (not shown). Also, the phase shift is very low for all times of immersion. Impedance response is not highly dependant of the immersion time, but a slight decrease is observed, as also presented in **Table 3**. Nyquist diagram for CuSnSi showed similar impedance behaviour to the sample CuSnZn including similar diagram shape and increasing value of impedance response. Also, the estimated polarization resistance value increased with immersion time (**Table 3**).

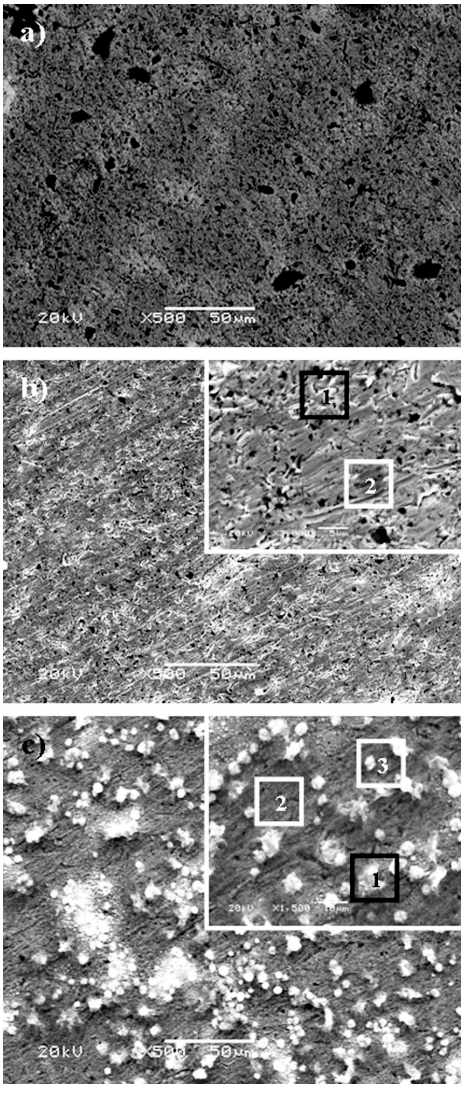

Figure 5: SEM image of a) CuSnZn b) CuSnZnPb and c) CuSnSi after 35 d of immersion in simulated urban rain solution pH 5
Slika 5: SEM-prikaz a) CuSnZn b) CuSnZnPb and c) CuSnSi po 35 d izpostavitve v simulirani raztopini mestnega dežja, pH 5

Thus, our results showed that the corrosion rate of unleaded bronze and silicon bronze decreased with time, whereas corrosion rate for leaded bronze increased with time. Impedance spectroscopy results show that unleaded bronze showed slightly better corrosion characteristics due to bigger estimated polarization resistances when compared to silicon bronze. However, the appearance of silicon bronze corrosion products is favourable over unleaded bronze, as shown in the next chapter of results.

Our results are similar to results reported by Chiavari *et al.* [7]. They investigated the silicon bronze (3 % Si) and leaded bronze (5 % Pb) in acid rain solution pH 3.1 by conducting different electrochemical measurements at different immersion times in acid rain solution pH 3.1. They found out that corrosion rate of silicon bronze decreased after long immersion time due to formation of stable layer of protective corrosion product, whereas in the case of leaded bronze the corrosion rate increased.

3.3 Surface characterization by SEM / EDX analysis

After 35–day immersion in simulated acid rain solution pH 5 under stagnant conditions, the samples of CuSnZn, CuSnZnPb and CuSnSi were examined by Scanning Electron Microscopy (SEM) and quantitatively analysed by EDS analysis (**Figure 5**). Differences of patina formation were observed already with a naked eye (not shown). Patina on unleaded bronze CuSnZn exhibited orange type compact corrosion product, whereas patina on leaded bronze after 35 day immersion in urban acid rain was brown–reddish and uneven. Patina that formed on silicon Bronze CuSnSi looked like smoky brown colour and very compact and thin.

The SEM image of sample CuSnZn after 35 d of exposure to urban acid rain (**Figure 5a**) showed homogeneously coated surface with corrosion products. The EDS analysis indicated the presence of mainly copper, oxygen and carbon (mole fractions x: 41 %, 35 % and 10 %), whereas Zn, Sn, S, Si were present as minor elements. Due to high percentage of oxygen in the analysed layer, the bronze surface presumably contained other corrosion products apart from cuprite, Cu_2O. The possible proposed mineral was brochantite [16]. The SEM image of leaded bronze, CuSnZnPb (**Figure 5b**), after 35 day immersion in acid rain solution exhibited two different

areas, denoted as area No. 1b and area No. 2b. Area No. 1b contained mainly carbon, less oxygen and copper, and nitrogen and lead in trace amounts. That indicated to copper carbonate as possible corrosion product. Whereas darker area, denoted as area No. 2b, was rich in copper (*x*/% : 51 % Cu, 2 % Sn, 27 % C, 9 % N and 11 % O) and contain more tin than area No. 1. The darker area could be the base alloy, not yet entirely covered by corrosion products. Cuprite and SnO_2 were proposed as the most possible oxidation products.

The SEM micrograph of CuSnSi (**Figure 5c**) showed three different areas, denoted as Area No. 1c, Area No. 2c and Area No. 3c. All analysed areas examined contained similar elements but in different ratios. Corrosion products in the shape of white spherical particles (Area No. 1) are rich in oxygen, carbon, nitrogen and sulphur. The formation of sulphates (brohantite $Cu_4SO_4(OH)_6$ or naukarite $Cu_4(SO_4)_4(CO_3)(OH)_6{\cdot}48\ H_2O$) was proposed. Grey coloured area, denoted as Area No.2c, is rich in tin, silicon and copper and less rich in oxygen and sulphur, indicated the formation of SiO_2 and SnO_2. Area No.3c is in composition similar to area No. 1c, but contained less sulphur.

It is difficult to unambiguously differentiate the corrosion products, grown during 35 d immersion in urban acid rain on the three different bronzes as the corrosion layers are too thin to detect the EDS signal just from corrosion products. However, the visual inspection of the patina layers on the three different bronzes showed that the patinas were different as the result of the base alloy composition.

Chiavari et al [7] who studied leaded bronze and silicon bronze in climatic chamber with chlorides and sulphates, showed that the main corrosion product on leaded bronze was brochantite, and that the layer on Silicon bronze was thinner and more compact. Also, similarly to our case, the corrosion products on leaded bronze were more non-homogeneous and thicker.

As the result of microstructural characteristics of the three different bronzes, it can be concluded that surface imperfections, non homogeneous distribution of corrosion products formed in the case of leaded bronze CuSnZnPb. Even distribution of corrosion products on Silicon bronze is also a result of homogeneous distribution of metallographic phases on silicon bronze, whereas unleaded bronze CuSnZn behaved somehow in between.

4 CONCLUSIONS

Three different bronzes were investigated in simulated urban rain solution, pH 5: recent bronze CuSnZn, leaded bronze CuSnZnPb and newer representative of bronzes, silicon bronze CuSnSi.

Microstructural investigation showed that recent bronze CuSnZn consisted of β–tin and zinc eutectics in α–copper. Inter dendritic network of shrinkage cavities were observed as an alloy imperfection. Similar observation occurred for leaded bronze, where lead as globules intermixed in α–copper of the bronze alloy. Silicon bronze has extremely oriented microstructure which is very regular. It consisted of dendrites of silicon and β–tin eutectics in matrix of α–copper.

Electrochemical investigation of different bronzes in simulated urban rain solution showed that the leaded bronze is most likely to corrode the most, followed by recent bronze CuSnZn. The highest corrosion resistivity among the bronzes was found for silicon bronze, CuSnSi.

Time dependence during 12 h immersion was followed by electrochemical impedance spectroscopy measurements. It was showed that corrosion resistance decreased with time for leaded bronze, whereas it increased for unleaded bronze CuSnZn and silicon bronze CuZnSi.

Morphological observation of corrosion products that formed during 35 d immersion in stagnant solution of urban acid rain showed that the patina layer is different for the three different bronzes. It is non–homogeneous for leaded bronze and very thin and compact for silicon bronze. It is believed that alloy composition and micro-structural characteristic have a great impact on electrochemical behaviour and formation of oxidation products–bronze patina layer. It affects visual appearance as well as chemical composition of corrosion products.

Unleaded bronze can successfully replace the use of leaded bronze where also better corrosion characteristics were found. Silicon bronze can be used in environments where only small changes of appearance of corrosion products are expected.

5 REFERENCES

[1] Ammeloot, F.; Fiaud, C.; Sutter, E. M. M., Characterization of the oxide layers on a Cu-13Sn alloy in a NaCl aqueous solution without and with 0.1 M benzotriazole. Electrochemical and photoelectrochemical contributions. Electrochimica Acta, 44 (**1999**) 15, 2549–2558

[2] Bendezu, R. D.; Goncalves, R. P.; Neiva, A. C.; de Melo, H. G., EIS and microstructural characterization of artificial nitrate patina layers produced at room temperature on copper and bronze. Journal of the Brazilian Chemical Society, 18 (**2007**) 1, 54–64

[3] Bernardi, E.; Chiavari, C.; Lenza, B.; Martini, C.; Morselli, L.; Ospitali, F.; Robbiola, L., The atmospheric corrosion of quaternary bronzes: The leaching action of acid rain. Corrosion Science, 51 (**2009**) 1, 159–170

[4] Bierwagen, G.; Shedlosky, T. J.; Stanek, K., Developing and testing a new generation of protective coatings for outdoor bronze sculpture. Progress in Organic Coatings, 48 (**2003**) 2–4, 289–296

[5] Brunoro, G.; Frignani, A.; Colledan, A.; Chiavari, C., Organic films for protection of copper and bronze against acid rain corrosion. Corrosion Science, 45 (**2003**) 10, 2219–2231

[6] Cano, E.; Polo, J. L.; La Iglesia, A.; Bastidas, J. M., Rate control for copper tarnishing. Corrosion Science, 47 (**2005**) 4, 977–987

[7] Chiavari, C.; Colledan, A.; Frignani, A.; Brunoro, G., Corrosion evaluation of traditional and new bronzes for artistic castings. Materials Chemistry and Physics, 95 (**2006**) 2–3, 252–259

[8] Chiavari, C.; Rahmouni, K.; Takenouti, H.; Joiret, S.; Vermaut, P.; Robbiola, L., Composition and electrochemical properties of natural patinas of outdoor bronze monuments. Electrochimica Acta, 52 (**2007**) 27, 7760–7769

[9] Cicileo, G. P.; Crespo, M. A.; Rosales, B. M., Comparative study of patinas formed on statuary alloys by means of electrochemical and surface analysis techniques. Corrosion Science, 46 (**2004**) 4, 929–953

[10] de la Fuente, D.; Simancas, J.; Morcillo, M., Morphological study of 16–year patinas formed on copper in a wide range of atmospheric exposures. Corrosion Science, 50 (**2008**) 1, 268–285

[11] Gallese, F.; Laguzzi, G.; Luvidi, L.; Ferrari, V.; Takacs, S.; Venturi Pagani Cesa, G., Comparative investigation into the corrosion of different bronze alloys suitable for outdoor sculptures. Corrosion Science, 50 (**2008**) 4, 954–961

[12] Hayez, V.; Costa, V.; Guillaume, J.; Terryn, H.; Hubin, A., Micro Raman spectroscopy used for the study of corrosion products on copper alloys: study of the chemical composition of artificial patinas used for restoration purposes. Analyst, 130 (**2005**) 4, 550–556

[13] Hernandez, R. P. B.; Paszti, Z.; de Melo, H. G.; Aoki, I. V., Chemical characterization and anticorrosion properties of corrosion products formed on pure copper in synthetic rainwater of Rio de Janeiro and Sao Paulo. Corrosion Science, 52 (**2010**) 3, 826–837

[14] Marusic, K.; Otmacic–Curkovic, H.; Horvat–Kurbegovic, S.; Takenouti, H.; Stupnisek–Lisac, E., Comparative studies of chemical and electrochemical preparation of artificial bronze patinas and their protection by corrosion inhibitor. Electrochimica Acta, 54 (**2009**), 27, 7106–7113

[15] Muresan, L.; Varvara, S.; Stupnisek–Lisac, E.; Otmacic, H.; Marusic, K.; Horvat–Kurbegovic, S.; Robbiola, L.; Rahmouni, K.; Takenouti, H., Protection of bronze covered with patina by innoxious organic substances. Electrochimica Acta, 52 (**2007**) 27, 7770–7779

[16] Otmačić Ćurković H, Kosec T., Legat A, Stupinšek–Lisac E, Improvement of corrosion stability of patinated bronze. Corrosion Engineering, Science and Technology, 45 (**2010**) 327–333

[17] Otmacic, H.; Stupnisek–Lisac, E., Copper corrosion inhibitors in near neutral media. Electrochimica Acta, 48 (**2003**) 8, 985–991

[18] Rahmouni, K.; Takenouti, H.; Hajjaji, N.; Srhiri, A.; Robbiola, L., Protection of ancient and historic bronzes by triazole derivatives. Electrochimica Acta, 54 (**2009**) 22, 5206–5215

[19] Robbiola, L.; Blengino, J. M.; Fiaud, C., Morphology and mechanisms of formation of natural patinas on archaeological Cu–Sn alloys. Corrosion Science, 40 (**1998**) 12, 2083–2111

[20] Rosales, B. M.; Vera, R. M.; Hidalgo, J. P., Characterisation and properties of synthetic patina on copper base sculptural alloys. Corrosion Science 52 (**2010**) 10, 3212–3224

[21] Schweitzer, P. A., Fundamentals of metallic corrosion : Atmosferic and Media Corrosion of Metals, Corrosion Engineering Handbook, 2nd Ed. RC Press/Taylor & Francis Group: Boca Raton, FL., 2007

[22] Serghini–Idrissi, M.; Bernard, M. C.; Harrif, F. Z.; Joiret, S.; Rahmouni, K.; Srhiri, A.; Takenouti, H.; Vivier, V.; Ziani, M., Electrochemical and spectroscopic characterizations of patinas formed on an archaeological bronze coin. Electrochimica Acta, 50 (**2005**) 24, 4699–4709

[23] Sidot, E.; Souissi, N.; Bousselmi, L.; Triki, E.; Robbiola, L., Study of the corrosion behaviour of Cu–10Sn bronze in aerated Na2SO4 aqueous solution. Corrosion Science, 48 (**2006**) 8, 2241–2257

[24] Strandberg, H., Reactions of copper patina compounds–II. influence of sodium chloride in the presence of some air pollutants. Atmospheric Environment, 32 (**1998**) 20, 3521–3526

[25] Strandberg, H., Reactions of copper patina compounds–I. Influence of some air pollutants. Atmospheric Environment, 32 (**1998**) 20, 3511–3520

[26] Strehblow, H. H.; Titze, B., The investigation of the passive behaviour of copper in weakly acid and alkaline solutions and the examination of the passive film by esca and ISS. Electrochimica Acta, 25 (**1980**) 6, 839–850

[27] Varvara, S.; Muresan, L. M.; Rahmouni, K.; Takenouti, H., Evaluation of some non–toxic thiadiazole derivatives as bronze corrosion inhibitors in aqueous solution. Corrosion Science, 50 (**2008**) 9, 2596–2604

[28] Watanabe, M.; Toyoda, E.; Handa, T.; Ichino, T.; Kuwaki, N.; Higashi, Y.; Tanaka, T., Evolution of patinas on copper exposed in a suburban area. Corrosion Science, 49 (**2007**) 2, 766–780

UDK 669.71:620.193:621.9
Original scientific article/Izvirni znanstveni članek

ISSN 1580-2949
MTAEC9, 45(6)593(2011)

MORPHOLOGY AND CORROSION PROPERTIES PVD Cr-N COATINGS DEPOSITED ON ALUMINIUM ALLOYS

MORFOLOGIJA IN KOROZIJSKE LASTNOSTI CrN PVD-PREVLEK, NANESENIH NA ALUMINIJEVE ZLITINE

Darja Kek Merl[1], Ingrid Milošev[1], Peter Panjan[1], Franc Zupanič[2]

[1]Jožef Stefan Institute, Jamova 39, 1000 Ljubljana, Slovenia
[2]University of Maribor, Faculty of Mechanical Engineering, Smetanova 17, 2000 Maribor, Slovenija
darja.kek@ijs.si

Prejem rokopisa – received:2011-04-07; sprejem za objavo – accepted for publication: 2011-05-30

The attempt to find an alternative coating for corrosion protection of Al- alloys was made. PVD coatings are one of the possible alternatives for replacement of ecological unfriendly chromate coatings. Chromium-nitride (Cr-N) and Ni/Cr-N coatings were sputtered on aluminium substrates (AA7075 and cladded AA2024). Surface and sub-surface characterizations were performed by AFM and SEM. Special attention was given to defects incorporated into coatings, since they play important role in the corrosion protection of the coating/substrate systems. The cross-sections through the typical defects were performed by ion beam milling incorporated into the SEM. The Vickers hardness of the Cr-N with and without layer of Ni on both substrates was determined. After the coatings deposition, the values of Vickers hardness (10 mN load) increase for 10 to 100-fold compared to the substrates. The corrosion behaviour of Cr-N and Ni/Cr-N thin films was investigated in near neutral 0.1 M solution of NaCl using potentiodynamics electrochemical measurement. Cr-N and Ni/Cr-N coatings shift the corrosion potentials to more positive values. The best corrosion resistance among the tested coating/substrate systems were found for Ni/Cr-N on AA7075 substrate.

Keywords: Al-alloys, corrosion properties, CrN films, FIB, PVD coatings

Ena od možnih alternativ za zamenjavo ekološko neprijaznih kromatnih prevlek na aluminijevih zlitinah so PVD-prevleke. V prispevku opisujemo pripravo in karakterizacijo prevlek Cr-N in Ni/Cr-N na aluminijeve podlage (AA7075 in AA2024). Površinsko in podpovršinsko karakterizacijo CrN-prevlek smo izvedli z vrstično elektronsko mikroskopijo (SEM) in mikroskopom na atomsko silo (AFM). Posebna pozornost je bila namenjena karakterizaciji defektov v prevlekah, saj igrajo pomembno vlogo pri korozijski zaščiti sistema prevleka/podlaga. Defekte smo karakterizirali z vrstičnim mikroskopom (SEM), ki je dodatno opremljen s fokusiranim ionskim curkom (FIB) za odstranjevanje materiala. Določili smo trdoto prevlek po Vickersu na obeh vrstah aluminijevih podlag. Korozijske lastnosti prevlek smo merili v 0,1 M raztopini NaCl s potenciodinamskimi krivuljami. Cr-N- in Ni/Cr-N-prevleke premaknejo korozijski potencial proti pozitivnim vrednostim. Zaščita aluminijevih zlitin je boljša z dvojno prevleko Ni/CrN kot samo s prevleko CrN.

Ključne besede: Al-zlitina, korozijske lastnosti, CrN, FIB, PVD-prevleke

1 INTRODUCTION

Aluminium alloys are very important engineering materials employed in a variety of applications, which include automotive, constructive, chemical, petrochemical, cryogenics, transportation equipment, etc. Among other attractive properties, these materials exhibit relatively high strength to weight ratio, good corrosion resistance and high thermal conductivity. However, due to their low hardness, wear and abrasion resistance, the application of these materials to sliding part is quite limited. Conventionally, the improvement of the surface properties of aluminium alloys, particularly those involved in aircraft and aerospace application, like AA2024 and AA7075, has been the use of electrolytic hard chromium deposition and conversion chromate coating. However, the strong environmental regulations issued in the past few years to decrease significantly the emissions of the highly toxic hexavalent chromium, have led to the development of different technologies also able to improve the surface properties of such materials, but more friendly from the environmental point of view.[1–5] On the other hand, conversion chromate coating possesses advantageous properties, like self-healing effect in case of mechanical coatings damage.

PVD technologies offer a promising alternative for the production of cost-effective, quality coatings with dry, clean and environment-friendly technology fully supported by legislation on environmental protection. The properties of various PVD coatings (metals, alloys, nitrides and oxides, carbides) have been well documented and systematically presented.[6,7] Ceramic materials have oriented covalent bonds; such materials are hard, brittle, chemical inert and with high melting-point temperature. Their wear resistance is excellent. Because of these properties, PVD coatings are in many cases a serious alternative to electrochemical coatings. For example, 1–5 μm thick layer of PVD coatings can replace 250 μm thick layer of hard chrome.

In the recent years, many efforts have been oriented to the development of anticorrosive coatings deposited by reactive sputtering in order to protect aluminium alloys like AA2024 and AA7075 used in aircraft application. Among conventional nitride and carbide PVD hard coatings, TiN and AlN sputtered on aluminium alloys were investigated. Diesselberg *et al.*[8] sputtered

TiN_x varying concentration of nitrogen and bias voltage to get different microstructructure of TiN_x. The lower concentration of nitrogen and the deposition at higher bias shows a positive effect on the corrosion protection. AlN_x sputtered coatings were investigated by Schafer and Stock[9]. AlN_x coatings on Al-substrate with higher concentration of nitrogen shift the pitting potential to more positive values. However, salt spray test showed opposite effect of nitrogen concentration; the coatings with less concentration of nitrogen are more stable. Liu *et al.* [10] studied effect of nitrogen ion implanted into aluminium substrate on the mechanical properties of TiN films. Implantation of nitrogen ion, increase the adhesion of TiN coating, therefore improve surface properties of aluminium by forming 80 nm thick AlN gradient layers. Corrosion properties were not reported.

On the other hand, sputtered chromium and reactively sputtered chromium nitride (CrN) act as very promising candidates due to their high internal resistance to corrosion, which arises from the instant formation of an oxide layer on the surface at room temperature.[11,12,13] In this paper, we present the investigation of PVD coating CrN and Ni/CrN for corrosion protection of aluminium alloys AA2024-cladded and AA7075. CrN thin films on aluminium substrates were prepared by sputtered deposition at low temperature. Surface and sub-surface characterization were performed on the coatings. Mechanical properties such as hardness and roughness were determined for each coating. The corrosion testing of PVD coatings, using electrochemical methods (potentiodynamic measurement), were performed in the 0.1M solution of NaCl.

2 EXPERIMENTAL

2.1 Substrate preparation

As substrates, the disks of aluminium alloys (AA2024 cladded and AA7075) were used. All the Al-substrates were chemically cleaned with a mildly alkaline cleaner Ridoline 1 % in an ultrasonic bath at 60 °C for 4 min, followed with distilled water bath and ethanol bath and drying with N_2. To study the effects of the surface preparation on corrosion performance of PVD coatings, the grinding (1000 and 4000 SiC papers) and polishing (0.25 μm diamond paste) of the substrate surface were performed in some cases. Ion etching to remove native oxide layer usng Ar + H_2 mixture (15 min) in vacuum chamber was performed in some cases.

2.2 Coating depositions

All coatings were prepared by sputtering at 150 °C in the depositing system with termionic arc (Sputron, Balzers). Cr-N and Ni/Cr-N were deposited on the substrates with and without ion etching. Additional interface layer of amorphous carbon (a-C) were performed to reduce the roughness of the substrates. The thickness of Cr-N coatings was ≈2,5 μm and Ni/Cr-N coating about 3 μm.

The vacuum chamber was evacuated to a base pressure of approximately 2 mPa. Nitrogen (purity 99.995 %) flow remained constant at 9.5 cm^3. During deposition the bias voltage and the substrate temperature were -30 V and 150 °C

2.3 Characterisation

Field emission scanning electron microscope (Zeiss Supra 35 VP) was used for study of the defect morphology in planar surface view and cross-sectional fracture view.

Focused ion beam (FIB) workstation[14] was used to prepare cross-section through the defects. We used FIB integrated in FEI QUANTA 200 3D microscope. Ion beam was used to remove precise sections of material (close to the selected defect) from the specimen surface by sputtering.

The surface morphology and roughness of the substrates and coating/substrate systems was also examined by atomic force microscope (Solver PRO).

Hardness was determined using the nanoindenter Fischerscope H100C. The load was varied between 10–1000 mN.

The electrochemical corrosion behaviour was studied using potentiodynamic polarisation tests in a solution of 0.1 M NaCl. Autolab three-electrode corrosion cell was used, with the working electrode embedded in a Teflon holder. An Ag/AgCl electrode served as a reference electrode and carbon rods as counter electrodes. The working electrode (WE) was a substrate with an area of 0.785 cm^2 that was coated with Cr-N and Ni/Cr-N. The polarisation curves were measured after 1 h of stabilization at the corrosion potential so that a quasi-stable potential was reached. The curves were obtained by sweeping the potential from the cathode to the anode. The sweep-rate setting was 1 mV/s using an EG&Par PC-controlled potentiostat /galvanostat Model 263 and Powersuite software.

3 RESULTS AND DISCUSSION

3.1 Microstructure

A typical surface morphology of PVD-hard coatings Ni/CrN on AA-7075 alloy is shown on **Figure 1a**. Top-view image is possible to distinguish typically growth defects for PVD-coatings: a) spherical droplets-cone structure, coming above the surface, typical wide size from 1 to few μm, b) pin- holes apparently going to the substrate, reaching the size up to the few μm c) big, not deep craters of wide size of 10–40 μm.

High surface roughness of Al-alloy substrate is shown on cross section image on **Figure 1b**. Surface roughness of AA-7075 substrate measured by AFM was $R_a \approx 14$ nm, AA2024–cladd $R_a \approx 11.3$ nm. After

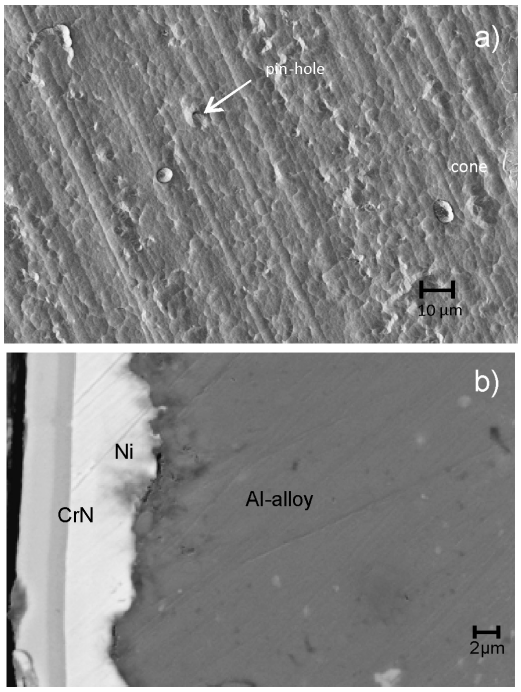

Figure 1: A top view of a) Cr-N coating on aluminium alloy AA2024 cladded substrate b) cross-section of Ni/Cr-N/Al-alloys
Slika 1: SEM posnetek a) mikrostrukture površine Cr-N-prevleke na aluminijevi zlitini AA2024, b) prereza Ni/CrN/Al-zlitina

deposition surface roughness increased for around $R_a \approx$ 34 nm on AA7075 substrate and $R_a \approx$ 26 nm on AA2024-cladd.

Microstructure characteristics of PVD-coatings, where surface defects have to be taken into account, play important role in the determination of corrosion properties of thin films. A few authors pay attention to the defect density and try to explain the origin of the growth defect on the PVD-coatings. To determine the origin of the defects the FIB cross section analysis were made on the two typical defects shown on **Figure 2**. The first defect (**Figure 2a–d**) has the form of a cone, while the second one (**Figure 2e–h**) resembles a pinhole. The question was weather these defects extend through the whole coating or not, and what is the origin for their nucleation. After consecutive serial sectioning, we found

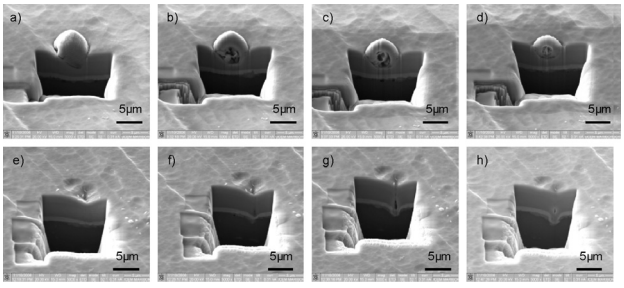

Figure 2: FIB cross section analysis were made on the two typical defects of coatings a-d) cone structure and e-h) pin-hole
Slika 2: SEM posnetek prerezov (narejenih s FIB) dveh tipičnih napak v prevleki; a)–d) konusna oblika napake in e)–h) luknjica (pin-hole)

that the first defect started to grow in the middle of the coating due to the incorporation of a foreign particle. **Figure 2c** shows that the region under the cone is not completely filled with material. The second defect extends through the whole coating and originates in a small hole in the substrate (**Figure 2e**). It is well known that PVD processes have a poor ability to cover a small hole due to shadowing effect. **Figure 2e–h** clearly shows that a small crater on the substrate surface cannot be covered completely and that a pinhole extending through the whole coating was formed. The corrosion takes place on such defects, while solution can reach the base material. The origin of the pinholes could be the corrosion products (wet cleaning) or dust particles that they are not removed from the substrate surface during the deposition. The high roughness of selected substrates could result the same effects. The cone microstructure, appearing quite an accident anywhere in the growing layer, (**Figure 2b**) are due to inclusions coming on the growing layer from the vacuum chamber, i.e. drops of metal target.

The origin of the big not deep craters (**Figure 1a**) can be explained by the falling away of the particles (corrosion products due to wet cleaning, dust particles) from the surface, soon after the starting the deposition.

3.2 Mechanical characterization

The Vickers hardness of the Cr-N, Ni and Ni/Cr-N coating, with deposited on AA2024 cladd and AA7075 substrates was determined. The bare substrate

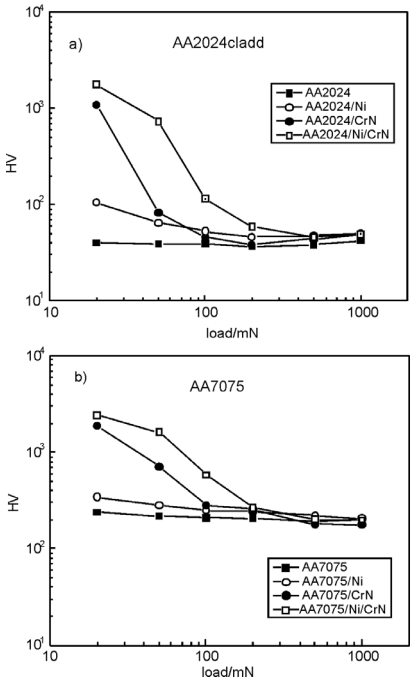

Figure 3: Hardness of the substrates and coatings for a) AA2024-cladded b) AA7075
Slika 3: Trdote po Vickersu pripravljenih prevlek: a) podlaga Al-AA2024, b) podlaga Al-AA7075

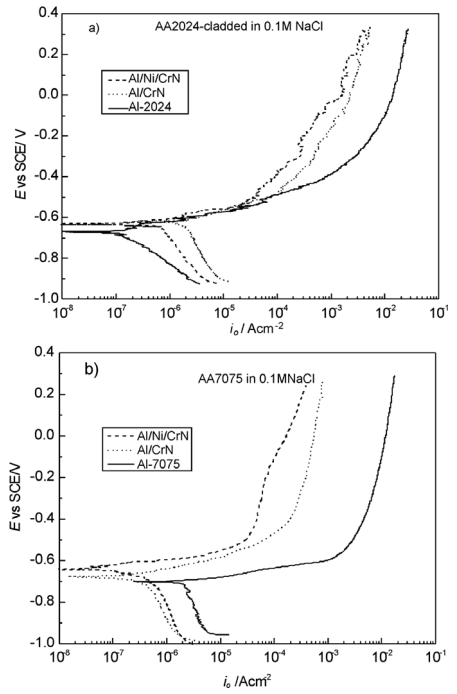

Figure 4: PD curves of various coatings, as indicated on figures, for a) AA2024-cladded substrate b) AA7075 substrate

Slika 4: PD-krivulje prevlek, označenih na sliki za a) podlage Al-AA2024, b) podlage Al-AA7075

Table 1: Corrosion potential (E_{corr}) and corrosion current density (i_o) after 1 h stabilisation for uncoated and coated substrates on **Figure 4**.

material	E_{corr}/V	i_o/(μA cm^{-2})
AA7075	–0.707	2.10
AA7075/CrN	–0.679	0.99
AA7075/Ni/NiCrN	–0.645	0.41
AA2024-cladd	–0.674	0.18
AA2024-cladd /CrN	–0.631	0.38
AA2024-cladd /Ni/NiCrN	–0.624	2.80

AA2024-cladd (**Figure 3a**) has a hardness of 40 HV and AA7075 substrates of 200 HV (**Figure 3b**). After the coating deposition, the values of Vickers hardness, measured at 10 mN, increase for 10 to almost 100-fold compare the substrates and then progressively diminishes at higher loads. In both cases, this is only a surface effect due to small thickness of the coatings (**Figure 3a and Figure 3b**).

3.3 Corrosion characterisation

The results from the potentiodynamic measurements of the CrN and Ni/Cr-N coatings on the substrates of aluminium alloys (AA2024-cladd and AA7075) in the 0.1M aqueous sodium chloride solution are shown in **Figure 4**. After 1 h of stabilization at the open-circuit potential, the corrosion potential (E_{corr}) for the AA2024-cladd substrate in was approximately –0.67 V (**Figure 4a**). Following the Tafel region, the alloy

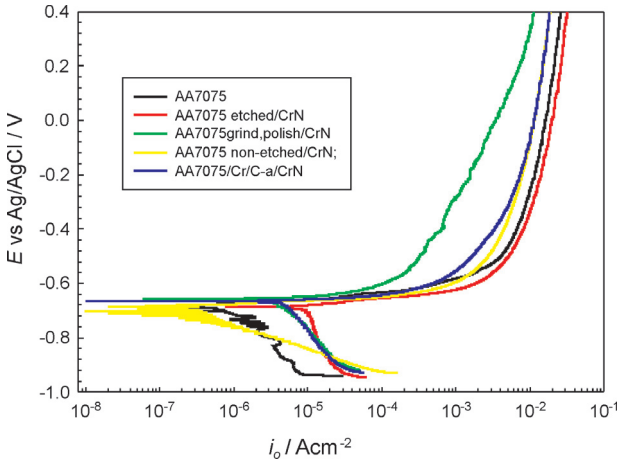

Figure 5: PD curves of Cr-N coating with the different surface substrate preparation as indicate in the figure

Slika 5: PD-krivulje Cr-N z različno predpripravo podlag, kot so označene na sliki

exhibited a narrow range of passivation, with breakdown potential E_b of about –0.63V, due to native oxide layer formed on pure (cladded) aluminium. In the case of the AA7075, the E_{corr} in 0.1 M NaCl was approximately –0.70V.

E_{corr} shifted to a more positive potential with the application of the Cr-N and Ni/Cr-N coatings, reaching -0.62 V and -0.63 V versus on the AA2024-cladd (**Figure 4a**). The E_{corr} of the CrN and Ni/Cr-N coatings on the AA7075 reached a value of -0.67 V and -0.64 V (**Figure 4b**).

The corrosion current density is often used as an important parameter to evaluate the kinetics of corrosion reactions. Corrosion protection is normally proportional to the corrosion current density (i_o) measured via polarization. In our case, where PVD coatings of Cr-N are chemically not reactive, the corrosion current density indicates pores in the coatings, where the electrochemical reaction of the substrate takes place. The i_o values from **Figure 4** show that the Cr-N coating on on both Al-alloys corroded faster than the Ni/CrN coating under open-circuit conditions; this means that the active area of the substrate due to coating porosity is higher in the case of Cr-N than in the case of Ni/Cr-N coatings. However, the overall corrosion process was still dominated by locally active dissolution, which occurred as the substrate was exposed via coating porosity.

Cr-N coating did not improve the corrosion properties for aluminium substrates in the extent as is well known for corrosion protection of steel substrate[6]. The effects of the surface preparation (grinding, polishing, etching) and interface layers were investigated further on AA7075 as is shown on **Figure 5**. Performance of Cr-N coatings can be slightly improved with the proper surface preparation (grinding, polishing) as is shown with the green curves (green and yellow curves). No effect of etched and non-etched substrate, with (Ar+H_2) plasma in the vacuum chamber before the deposition, was observed

on the PD performance of Cr-N protective layer (**Figure 5**). The deposition of an interface layer could influence the performance of the coatings as well. Thin interface layer of a-C (amorphous carbon) was sputtered in order to reduce the high roughness of the substrate. A slight improvement was observed. PD curves show that although there is some effect of surface preparation on the corrosion performance of Cr-N, Cr-N alone is not suitable coating for corrosion protection of soft aluminium substrates.

4 SUMMARY

The deposition of Cr-N and Ni/Cr-N was carried out. Physical, surface analytical and electrochemical measurements were performed on coated and uncoated AA2024-cladded and AA7075 substrates. Cr-N and Ni/Cr-N coatings increase the surface hardness of both Al-alloys substrates to 10-fold. At the measure loads of 10 mN.

FIB cross section analyses were made on the two typical defects of coatings (cone structure and pin-hole). Cone microstructure, appearing quite an accident in the growing layer, are due to inclusions coming on the growing layer from vacuum chamber (drops of metal target, dust, etc). A small crater (probably due to surface roughness) on the substrate surface cannot be covered completely due to shadowing effect and that a pinhole extending through the whole coating was formed. The corrosion takes place on such defects, while solution can reach the base material.

Corrosion behaviour of Cr-N and Ni/Cr-N thin films was investigated in near neutral 0.1 M solution of NaCl using potentiodynamics electrochemical measurement. Cr-N and Ni/Cr-N coatings shift the corrosion potentials to the more positive values. The best corrosion resistance among the tested coating/substrate systems were found for Ni/Cr-N on AA7075 substrate.

Acknowledgements

The work was supported by the Slovenian Research Agency (project No. L2-9189).

5 REFERENCES

[1] B. Meyers, S. Lynn, ASM Handbook, Surface Engineering, vol. 5, ASM International, Materials Park, OH, 1994
[2] K. O. Legg, M. Graham, P. Chang, F. Rastagar, A. Gonzales, B. D. Sartwll, Surf. Coat.Technol., 81 (**1996**), 99
[3] R. L. Twite, G. P. Bierwagen, Prog . Org. Coat., 33 (**1998**), 91
[4] P. M. Natishan, S. H. Lawrence, R. L. Foster, J. Lewis, B. D. Sartwell, Surf. Coat.Technol., 130 (**2000**), 218
[5] H. J. Gibb, P. S. J. Lees, P. F. Pinsky, C. B. Rooney, Am. J. Ind. Med., 38 (**2000**), 15
[6] B. Blushan, B. K. Gupta, Hard Coating, Handbook of Tribology, McGraw Hill, New York, 1991, Chapter 14
[7] G. Jetson, Handbook of Thin Film Process Technology, Institute of Physics, Bristol, 1996
[8] M. Diesselberg, H-R. Stock, P. Mayr, Surf. Coat.Technol., 177–178 (**2004**), 399
[9] H Schaefer, H-R. Stock, Corr. Sci., 547 (**2000**), 953
[10] Y. Liu, L. Li, M. Xu, Q. Chen, Y. Hu, X. Cai, P. K. Chu, Surf. Coat. Technol., 200 (**2006**), 2672
[11] B. Navinšek, P. Panjan, I. Milošev, Surf. Coat.Technol., 116–119 (**1999**), 476
[12] D. K. Merl, M. Cekada, P. Panjan, M. Macek, Electrochimica Acta, 49 (**2004**), 1527
[13] M. Čekada, P. Panjan, D. Kek Merl, M. Maček, Mater. Tehnol., 37 (**2003**) 5, 213–216
[14] J. M. Cairney, P. R. Munroe, M. Hoffman, Surf. Coat.Technol., 198 (**2005**), 165

UDK 621.74.047:669.14.018
Professional article/Strokovni članek

ISSN 1580-2949
MTAEC9, 45(6)599(2011)

THE EFFECT OF ELECTROMAGNETIC STIRRING ON THE CRYSTALLIZATION OF CONCAST BILLETS – II.

VPLIV ELEKTROMAGNETNEGA MEŠANJA NA KRISTALIZACIJO KONTINUIRNO ULITIH GREDIC – II.

Frantisek Kavicka[1], Karel Stransky[1], Bohumil Sekanina[1], Josef Stetina[1], Vasilij Gontarev[2], Tomas Mauder[1], Milos Masarik[3]

[1]Brno Technological University, Technicka 2, 616 69 Brno, Czech Rep.
[2]University of Ljubljana, Aškerčeva 12, 1000 Ljubljana, Slovenia
[3]EVRAZ VITKOVICE STEEL, a. s., Stramberska 2871/47, 709 00 Ostrava, Czech Rep.
kavicka@fme.vutbr.cz

Prejem rokopisa – received:2011-02-01 ; sprejem za objavo – accepted for publicatio: 2011-03-03

The solidification and cooling of a continuously cast slab and the simultaneous heating of the mold is a very complicated problem of three-dimensional (3D) transient heat and mass transfer. The solving of such a problem is impossible without numerical models of the temperature field of the concasting processed through the concasting machine. Experimental research and measurements have to take place simultaneously with the numerical computation, to be confronted with the numerical model and make it more accurate throughout the process. An important area of the caster is the secondary cooling zone, which is subdivided into thirteen sections. In this zone, where the slab is beginning to straighten, the breakout of the shell can occur at points of increased local chemical and temperature heterogeneity for the steel, from increased tension as a result of the bending of the slab and also from a high local concentration of non-metal and slag inclusions. The changes in the chemical composition of the steel during the actual concasting are particularly dangerous. In the case of two melts, one immediately after the other, this could lead to an immediate interruption in the concasting and a breakout. The material, physical, chemical and technological parameters, which differed in both melts, were determined. If the dimensionless analysis is applied for assessing and reducing the number of these parameters, then it is possible to express the level of risk of the breakout as a function of five dimensionless criteria.

Keywords: concast slabs, oscillation marks, hooks, chemical composition, breakout, criteria, electromagnetic stirring, crystallization

Strjevanje in ohlajevanje kontinuirno ulitega slaba in istočasno ogrevanje kokile je zelo zapleten problem pri tridimenzionalnem (3D) prenosu toplote in mase. Rešitev takega problema je nemogoča brez uporabe numeričnih modelov temperaturnega polja pri kontinuirnem ulivanju. Eksperimentalne raziskave in meritve se morajo dogajati istočasno z numeričnim računom, ne le zaradi primerjave z numeričnim modelom, ampak tudi zaradi večje natančnosti samega procesa. Pomembno področje livnega stroja je t. i. sekundarna hladilna cona, ki je razdeljena v trinajst presekov. V sekundarni hladilni coni lahko nastane preboj skorje zaradi povečane lokalne kemijske in temperaturne heterogenosti jekla, porasta napetosti v slabu zaradi upogibanja in velikih lokalnih koncentracij nekovinskih vključkov in vključkov žlindre. Posebno nevarne so spremembe kemijske sestave jekla med dejanskim kontinuirnim ulivanjem. V primeru dveh talin, ki sledita ena takoj za drugo, lahko nastane takojšnja prekinitve kontiulivanja in preboja. Določeni so bili fizikalni, kemijski in tehnološki parametri snovi, v katerih se obe talini razlikujeta. Z uporabo brezdimenzijske analize za ocenitev in zmanjšanje števila teh parametrov, je mogoče izraziti stopnjo tveganja preboja kot funkcijo petih brezdimenzijskih meril.

Ključne besede: kontinuirno uliti drogovi, nihajoče oznake, kemijska sestava, preboj, merila, elektromagnetno mešanje, kristalizacija

1 INTRODUCTION

Oscillation marks are transverse grooves forming on the surface of the solidifying shell of a concast slab. The course of the individual marks is rough and perpendicular to the direction of the movement of the slab. The formation of the marks is sometimes the result of the bending of the solidifying shell during the oscillation of the mould, which depends on the frequency and the amplitude of the oscillation and on the casting speed. The hooks are solidified, microscopically thin, surface layers of steel [1–3] covered with oxides and slag, and their microstructures are different to that of the solidifying shell. The formation of the oscillation marks and hooks is related. The depth of the oscillation marks and also the shape, size and the microstructure of the hooks vary irregularly. An increasing extent of these changes leads to a defect in the shape of a crack, which reduces the thickness of the solidified shell of the slab upon its exit from the mould and causes a dangerous notch. In the secondary-cooling zone, where the slab is beginning to straighten out, a breakout of the steel can occur at points of increased local chemical and temperature heterogeneity of the steel, from increased tension as a result of the bending of the slab and also a high local concentration of non-metal, slag inclusions. The changes in the chemical composition of the steel during the actual concasting are particularly dangerous. The consequences of this immediate operational change in the chemical composition of the steel, which are not prevented by a breakout system directly inside the mould, could lead to an immediate interruption of the concasting and a

breakout at a greater distance from the mould than usual, thus leading to a significant material loss and downtime.

2 INTERRUPTION OF CONCASTING

This case was recorded during the process of concasting of (250 × 1530) mm steel slabs of quality A with the mass fractions of carbon content 0.41 % and 9.95 % chromium content (melts 1 to 3) and quality B steel with 0.17 % carbon content and 0.70 % chromium content (melt 4). The casting of the first two melts of quality A took place without any significant problems, after the casting of the third melt of quality A, the fourth melt of quality B followed. The change in the chemical compositions of the steels of both qualities was carried out very quickly by changing the tundish. Inside the mould, steel B mixed with steel A of the previous melt. The pouring continued for another 20 min, but then, after, in the unbending point of the slab, at a distance of 14.15 m away from the level of the melt inside the mould, there occurred a breakout between the 7th and 8th segments and the caster stopped. The difference in the height between the level inside the mould and the breakout point was 8.605 m. This tear in the shell occurred on the small radius of the caster. A 250-mm-thick sample was taken from the breakout area using a longitudinal axial cut (**Figure. 1**). The structure of this sample was examined and using the Bauman print the distribution of sulphur was analyzed too. The numbers 1 to 11 indicate the positions of the samples in the places around the breakout intended for the analysis. Simultaneously, significant 25-mm sulphide segregations were discovered (see **Figure 1, position 6**) – very heterogeneous areas created by the original base material of the slab (melt 3), the new material of the slab (melt 4) and between them and also by the areas of mixed composition. Beneath the surface of the slab, at a depth of 75–85 mm, there were cracks and a zone of columnar crystals oriented towards the surface of the slab on the small radius. This was identical to the orientation of the groove, which gradually turned into a crack (**Figure 1 – direction 4–6**) and, on the opposite surface of the slab, the hook which was covered by the melt (position 8). In the first phase of the analyses, the aim was to determine the material, physical, chemical and technological parameters, for which both melts 3 and 4 differed (besides the already introduced chemical composition). **Table 1** contains the individual parameters of both melts.

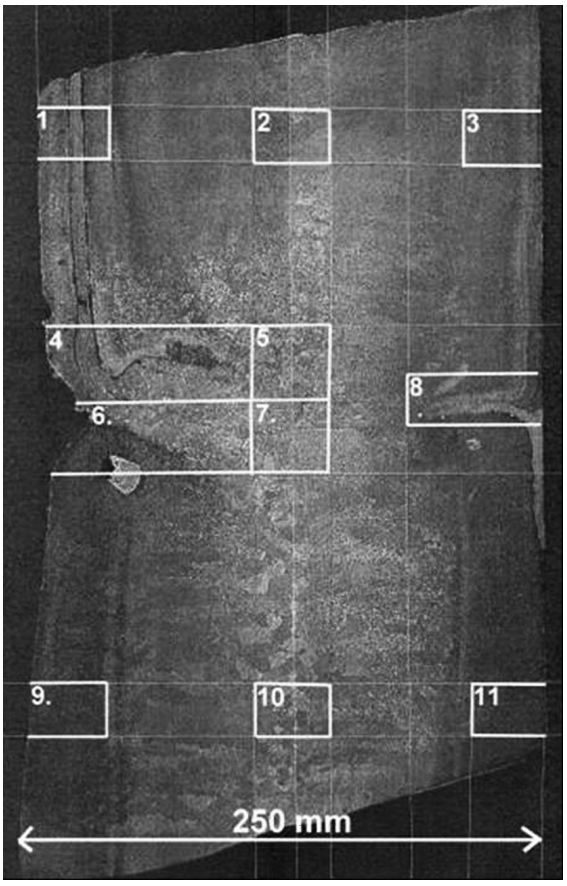

Figure1: Macrostructure of breakout
Slika 1: Makrostruktura zloma

3 DIMENSIONLESS CRITERIA

If the method of dimensionless analysis is applied for assessing and reducing the number of parameters in **Table 1** in the first approximation, then it is possible to express the level of risk of breakout as a function of the five dimensionless criteria contained in **Table 2** (units m, kg, s, K).

4 SUSCEPTIBILITY TO BREAKOUT – BREAKOUT RISK

The risk of breakout grows in accordance with the first criterion in direct proportion to the latent heat L released from the mushy zone and inversely proportionally to its dynamic viscosity η. The second criterion, i.e., the Strouhal number, includes transient, oscillation movement, including the amplitude of the mould and also, implicitly, a susceptibility to marks and hooks, which precede the breakout. The third criterion has a similar significance but, in addition, also includes the dynamic viscosity. The first three criteria increase the risk of breakout with melt 4 more than with melt 3. The fourth criterion characterizes the reduction of the load-bearing cross-section of the slab (by 28.1 % in melt 3 and by 21.4 % in melt 4) by creating a mushy zone, which indicates a greater risk of breakout in melt 3. The last criterion considers the effect of the mixture zone of melt 3 and a common effect of the mixture zone of melts 3 and 4. The first three criteria are of a dynamic nature and their product in melt 3 is 1.044 × 10^6, while in the fourth melt it is 1.502 × 10^6, i.e., the mixture melt has a 50 % greater risk of breakout. The product of all five criteria of the melts 3 and 4,

Table 1: Parameters characterizing the concasting of melt 3 (quality A) and melt 4 (quality B)
Tabela 1: Parametri, ki karakterizirajo kontiulivanje taline 3 (kakovost A) in taline 4 (kakovost B)

Item #	Parameter	Symbol	Units	A – melt 3	B – melt 4
1	Pouring speed	w	m s^{-1}	0.0130	0.0126
2	Dynamic viscosity	η	m^{-1} kg s^{-1}	0.00570 T_L	0.00562 T_L
		$\eta = \rho \cdot \nu$	m^{-1} kg s^{-1}	0.00772 T_S	0.00615 T_S
3	Density	ρ	kg m^{-3}	7560.7	7600.9
4	Latent heat of the phase change	L	m^2 kg s^{-2}	246×10^3	259×10^3
5	Specific heat capacity	c_p	m^2 s^{-2} K^{-1}	632.6	611.0
6	Mould oscillation amplitude	ΔS	m	0.006 ± 0.003	0.006 ± 0.003
7	Oscillation frequency	f	s^{-1}	1.533	1.533
8	Solidus temperature	T_S	°C	1427.0	1480.6
9	Liquidus temperature	T_L	°C	1493.9	1512.3
10	Difference between the liquidus and solidus temperatures	$T_L - T_S$	°C	66.9	31.7
11	Max. length of the isosolidus curve from the level*	h_S^{max}	m	21.07	19.72
12	Min. length of the isosolidus curve from the level**	h_S^{min}	m	19.92	18.69
13	Max. length of the isoliquidus curve from the level*	h_L^{max}	m	14.50	16.20
14	Min. length of the isoliquidus curve from the level**	h_L^{min}	m	13.70	15.20
15	The area of the mushy zone on half of the cross-section of the breakout [+]	F_{mushy}	m^2	0.05366	0.04100
16	The surface temperature of the slab[++]	T_{surf}	°C	934	1097

Note (continued from table above): *) of the steel inside the mould to a position 0.650 m from the edges of the 1.53 m wide slab; **) of the steel inside the mould to the centre of the slab; [+]) the overall area of half of the cross-section is F_{slab} = 0,19125 m^2 ; [++]) in the material 15 mm around the groove (**Figure 1**). The data in Table 1 were established a) on the caster after breakout; b) from archived on-line results of the temperature model; c) by off-line modelling of the temperature field of melts 3 and 4 [5].

Table 2: Dimensionless criteria characterizing the breakout
Tabela 2: Brezdimenzijska merila, ki označujejo zlom

Criterion	$\frac{L \cdot f}{c_p \eta T_L \Delta S}$	$\frac{\Delta S \cdot f}{w}$	$\frac{\rho \Delta S^2 \cdot f}{\eta}$	$\frac{F_{slab}}{F_{slab} - F_{mushy}}$	$\frac{T_L - T_S}{T_L}$
steel A	5124.78	1.179	172.77	1.3900	0.044782
steel B	6237.96	1.217	197.87	1.2729	0.056404*

Note: *) The maximum temperature difference inside the mixture zone $(T_{L-B} - T_{S-A})/T_{L-B}$

Table 3: Ductility testing at 1093.0 °C and 914.5 °C [5]
Tabela 3: Preizkusi gnetljivosti pri 1093.0 °C in 914.5 °C [5]

Sample	Testing temperature	Tensile strength	Strength	Diameter	Contraction	Deformation before breaking	Breaking Work
	°C	N	MPa	mm	%	mm	J
1	1093	817	28.9	3.90	58.0	12.0	7
2	914.5	1247	44.1	5.35	21.5	5.5	6

considering their partial homogenization, is 1.078×10^5 in melt 4 and 6.498×10^4 in melt 3. The quotient of the product for melts 3 and 4 is 0.603, which predicts a reduced risk of breakout in melt 3. If the influence of temperature on the surface of the slab in melt 3 and in the place of the groove in melt 4, it is clear that the effect of the groove during the straightening out of the slab is connected with the tensile stress, then in the place of the groove (**Figure 1**) the effect must have been compensated for at a temperature of 1097 °C, i.e., at a temperature that is 163 °C higher than that of a completely straight surface of the slab of melt 3. The data was obtained from the investigation into the causes behind a transversal crack that occurred in a different steel slab [4]. In order to clarify this, it was necessary to conduct a series of ductility tests at temperatures ranging from 20 °C to the solidus temperature. **Table 3** contains the test results from temperatures that are close to the temperatures in row 16 of **Table 2**. A comparison of the mechanical values indicates that the tensile strength at 914.5 °C and the pulling force are 1.5 times greater than at 1093.0 °C. In addition to this, there was a 8 605 m column of melt working on the mushy zone at the point of the breakout, where the mushy zone reached h_S^{max} = 21.07 m from the level in the mould, i.e., at least 6.92 m beyond the breakout point. It is therefore possible to assume that the main factor that significantly increased the risk of breakout was the superposition of the causing

effects of the parameters occurring in the first four criteria of **Table 2**.

5 DISCUSSION

Following a rapid change of the tundish, there was a period of 20 min when there was a mixture of quality A and quality B steels. The liquidus temperature 1493.9 °C of quality A increased to 1512.3 °C and, simultaneously, the latent heat of the phase change increased from 246 kJ/kg (quality A) to 259 kJ/kg (quality B). This led to an increase in the temperature of the melt and to the re-melting of the solidified shell of the original quality A steel. Furthermore, there was an increase in the length of the mushy zone (up to $h^{\max}_{S-3\,t.melt} - h^{\min}_{S-3.melt}$ = 21.07 – 13.70 = 7.37 m) and also in its temperature heterogeneity. The temperature of the mushy zone – following the mixing of both qualities – could find itself anywhere between the maximum temperature of the liquidus of quality A and the minimum temperature of the solidus of quality B (i.e., within the interval $T_{L-B} - T_{S-A}$= 1512.3 – 1427.0 = 85.3 °C. During the 20 min of pouring of the quality B steel (the 4th melt), which began immediately after the quality A steel (the 3rd melt), marks and hooks formed as a result of the oscillation of the mould and continued to form during the unbending of the slab (**Figure 1** – where the groove is 50 mm wide and 15–16 mm deep with an opening angle of 115°). The tensile forces in the vicinity of this groove and the re-melting of the solidified shell brought about the breakout in the wall of the small radius of the slab in the unbending point.

6 CONCLUSION

The changes in the chemical composition of the steel during the actual concasting are particularly dangerous. One way of reducing the risk of breakout and the consequent shutdown of the caster is to modify the values of the dimensionless criteria characterizing the breakout, i.e., to select two consecutive melts of such chemical compositions and the corresponding physical and chemical parameters (from which the dimensionless criteria are determined) that the criteria predict zero-breakthrough.

Acknowledgements

GACR projects No. 106/08/0606, 106/09/0940, 106/09/0969 and P107/11/1566.

7 REFERENCES

[1] Badri A. et al.: A mold simulator for continuous casting of steel. part ii. the formation of oscillation marks during the continuous casting of low carbon steel. Metallurgical and Materials Transactions B, 36 (**2005**), 373–383

[2] Thomas, B. G., J. Sengupta, Ojeda, C. Mechanism of hook and oscillation mark formation in ultra-low carbon steel. In Second Baosteel Biennial Conference, (May 25–26, 2006, Shanghai, PRC), 1 (**2006**), 112–117

[3] Ojeda, C. et al.: Mathematical modeling of thermal-fluid flow in the meniscus region during an oscillation cycle. AISTech Proceedings, 1 (**2006**), 1017–1028

[4] Dobrovska, J. et al.: Analysis of a transversal crack in a steel slab. Materials Science Forum, 567–568 (**2007**), 105–108 ©2008 Trans Tech Publications, Switzerland

[5] Stetina, J. et al.: Optimization of a casting technology of a steel slab via numerical models. Proceedings 22nd Canadian Congress of Applied Mechanics, Dalhousie University Halifax, Nova Scotia, Canada, May **2009**, 4

UDK 669.1:620.193:620.1/.2
Professional article/Strokovni članek

ISSN 1580-2949
MTAEC9, 45(6)603(2011)

WEAR OF REFRACTORY MATERIALS FOR CERAMIC FILTERS OF DIFFERENT POROSITY IN CONTACT WITH HOT METAL

OBRABA OGNJEVZDRŽNEGA MATERIALA KERAMIČNIH FILTROV Z RAZLIČNO POROZNOSTJO V STIKU Z VROČO KOVINO

Jiří Bažan[1], Ladislav Socha[1], Ludvík Martínek[2], Pavel Fila[2], Martin Balcar[2], Jaroslav Chmelař[3]

[1]VŠB - Technical University of Ostrava, FMME, Department of Metallurgy, 17. listopadu 15/2172, 708 33 Ostrava-Poruba, Czech Republic
[2]ŽĎAS, a. s., Strojírenská 6, 591 71 Žďár nad Sázavou, Czech Republic
[3]KERAMTECH, s.r.o., Horská 139, 542 01 Žacléř, Czech Republic
jiri.bazan@vsb.cz

Prejem rokopisa – received: 2011-05-31; sprejem za objavo – accepted for publication: 2011-09-02

This paper deals with an investigation of the development of refractory materials for the fabrication of ceramic filters for the filtration of steel. Ceramic filters are used for increasing the cleanliness of steel and they must meet several strict requirements, such as the ability to remove impurities, a resistance to sudden changes in temperature, a resistance to corrosion and erosion by metal. The use of filters must not lead to an excessive reduction of the steel's temperature, as this may lead to solidification of steel and thus to filter clogging. That is why a special refractory material has been developed with reduced thermal capacity caused by increased porosity. Tests were made in a laboratory of the Department of Metallurgy at VŠB-TUO in order to simulate the industrial conditions of the filtration of steel with a focus on the evaluation of the erosion and corrosion effects and also on a determination of the resistance and service life of ceramic filters.

Keywords: steel, ceramic filter, refractory material, corrosion and erosion, porosity

V članku je opisano raziskovanje v zvezi z razvojem ognjevzdržnih materialov za keramične filtre za filtriranje železa. Te filtre se uporablja za izboljšanje čistosti jekla, zato morajo izpolnjevati več strogih zahtev, kot npr.: odstranitev nečistoč, odpornost proti sunkovitim spremembam temperature in odpornost proti koroziji in eroziji zaradi kovine. Uporaba filtra ne sme preveč znižati temperature jekla in povzročiti njegovega strjevanja ter zato tudi mašenja filtra. Zato je bilo razvit poseben ognjevzdržen material, ki ima zmanjšano termično kapaciteto zaradi povečane poroznosti. Preizkusi so bili opravljeni v laboratoriju Oddelka za metalurgijo VŠB-TUO, da bi simulirali industrijske razmere filtriranja jekla s poudarkom na oceni korozijskih in erozijskih učinkov in za določitev odpornosti in dobe uporabe keramičnih filtrov.

Ključne besede: jeklo, keramika, ognjevzdržni material, korozija, erozija, poroznost

1 INTRODUCTION

The technology of filtration, i.e., the use of ceramic filters in a gating system, is one of the possibilities for enhancing the cleanliness of steel and the quality of as-cast ingots. This makes it possible to achieve an increase of the steel's purity, a reduction of the occurrence of non-metallic inclusions, a reduction of the costs of repairs of defects, etc.

Ceramic filters are exposed to extreme working conditions, such as sudden changes of temperature, the resistance to corrosion and erosion caused by hot metal or molten slags, etc. Ceramic filters are currently commonly used for increasing the cleanliness of steel in steel shops, where filtration is used for the removal of non-metallic inclusions, particularly those of an exogenous character and of the rest of slide valve nozzle fill, e.g., during uphill casting, but also in the tundish during the continuous casting of steel. Nowadays, a whole series of structurally different types of ceramic filters for the filtration of metals are manufactured. The most commonly used types are strainer and foam filters [1]. The paper concentrates on the influence of the porosity of refractory materials on their density and thus on the reduction of their thermal capacity.

2 USE OF CERAMIC FILTERS DURING THE CASTING OF STEEL INGOTS

The technology of the filtration of steel was tested in industrial conditions in a steel shop at the company ŽĎAS, a. s., during the uphill casting of ingots through a gating system in order to eliminate the occurrence of inclusions and to ensure an improved purity of the steel. The system for the casting of ingots consisted of a gate stick, a stool and an ingot mould with a shrink head (**Figure 1**). The application of the filtration system for the casting of ingots consisted of the use of a series of filters situated in a ceramic cartridge arranged in succession. The cartridge is placed in the gating system in the broadened channel of the stool (**Figure 2**).

The steel shop of ŽĎAS, a. s., participated in the design and realisation of the technical solution, including

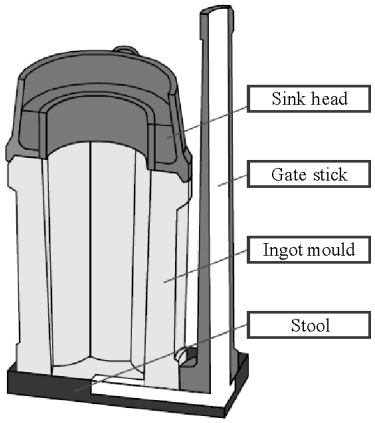

Figure 1: Cross-section of system for casting of ingots
Slika 1: Prerez sistema za litje ingotov

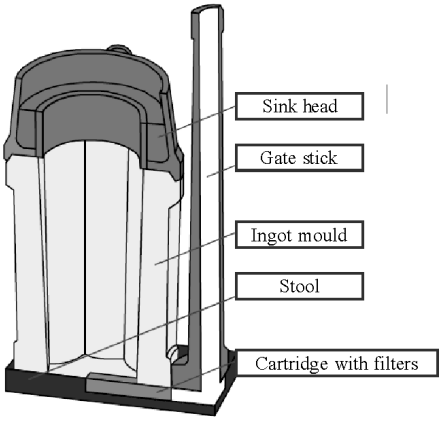

Figure 2: Cross-section of casting system with the application of a filtration cartridge
Slika 2: Prerez sistema za litje ingotov s filtrirnim tulcem

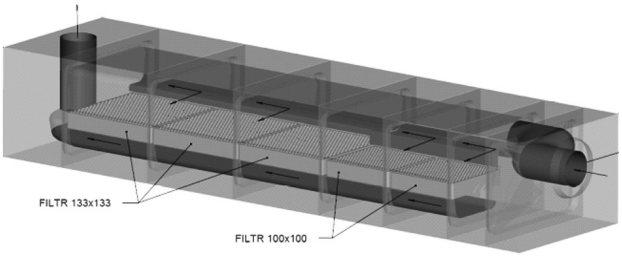

Figure 3: Filtration cartridge
Slika 3: Filtrirni tulec

the manufacture of cartridges and filters. Ceramic foam filters of 150 mm × 150 mm × 30 mm made of material based on ZrO_2, SiO_2 + SiC, as well as of material based on carbon, Al_2O_3 and SiO_2 were then tested in this steel shop. Due to problems during pouring (mechanical damage and freezing of the metal) in the next stage the filtration cartridges were modified and ceramic strainer filters based on mullite with dimensions of 100 mm × 100 mm × 20 mm and 133 mm × 133 mm × 20 mm were used. The filtration cartridge was made of fireclay material with the share of the mass fraction of Al_2O_3 > 61 % (**Figure 3**).

It was ascertained during industrial applications that this arrangement is satisfactory; however, in this case too during the flow of steel through the filter channels, the steel was cooled and problems with its freezing occurred as well. Subsequently, in order to minimise this problem, the company KERAMTECH, s. r. o., developed and tested a refractory material, in which its porosity was purposefully increased (up to 10 % of material), which led to a reduction of its mass and cooling effect.

3 DEVELOPMENT AND TESTING OF REFRACTORY MATERIALS FOR NEW CERAMIC FILTERS

The refractory material was developed by the company KERAMTECH, s. r. o., and a refractory material consisting of a mullite-corundum mass with higher contents of Al_2O_3 was chosen for the modification. **Table 1** gives the chemical composition of this material. The porosity of this material was increased by the addition of organic mass in portions of (3, 5, 7.5 and 10) % in order to reduce the material's thermal capacity.

Table 1: Chemical composition of modified refractory material
Tabela 1: Kemična sestava modificiranega ognjevzdržnega materiala v masnih deležih, *w*/%

Chemical composition in mass fractions (*w*/%)							
SiO_2	Al_2O_3	Fe_2O_3	TiO_2	K_2O	CaO	MgO	Na_2O
21.0	75.0	0.8	0.6	0.8	less than 0.5		

The specific thermal capacity of ordinary material is 1800 kJ K^{-1} kg^{-1}. The addition of 1 % of organic mass to the basic material reduces, by increased porosity, the mass of the final product by 2 %, and thus also its thermal capacity.

The modified refractory materials with increased porosity were tested with experimental heats in a laboratory of VŠB – Technical University of Ostrava to verify the erosion and corrosion effects and to determine the resistance and service life of the new ceramic filters. These experimental heats were supposed to simulate the conditions during the industrial filtration of hot metal. Two types of steel were used for all the experimental heats, i.e., ordinary carbon steel and high-manganese steel. **Table 2** gives the chemical compositions of both these steels, including the liquidus temperature.

Table 2: Chemical compositions of the used steels with liquidus temperatures
Tabela 2: Kemična sestava uporabljenih jekel in likvidusna temperatura

Type of steel	Chemical composition (*w*/%)					T_l/°C
	C	Si	Mn	P	S	
Carbon steel	0.44	0.23	0.67	0.019	0.016	1495
Manganese steel	1.1-1.5	max. 0.70	12.0-14.0	max. 0.10	max. 0.050	1375

Samples with dimensions 10 mm × 10 mm × 100 mm were made from the modified refractory material. For the simulation of the usual industrial conditions, prior to their insertion into the hot metal the samples were pre-heated to a temperature of 350 °C for 10 min. This tempering of the samples simulates the heating of the casting system in industrial conditions. Before their insertion into the reheating furnace and the start of the experiment, the samples were weighed in order to determine the mass loss. A comparison of the results showed that the re-heating of the samples did not cause any loss of mass. Afterwards, experimental heats were carried out. The induction furnace served as a melting unit. For the evaluation of corrosion and erosion phenomena, the experiments were made afterwards with use of both carbon and manganese steel at temperatures of 1560 °C, 1600 °C and 1680 °C for 20 min, while the porosity of the tested refractory materials was increased by the addition of various organic masses 10 wt.%.

4 EVALUATION OF REFRACTORY MATERIALS

The evaluation of the exposed samples was made in several steps. It started with a visual evaluation (photographs of the whole samples taken after the experiment) followed by an evaluation of cross-sections with a focus on the structure and the surface (edge) of the samples.

4.1 Visual evaluation of erosion and corrosion

With the experiments the refractory materials were tested from the point of view of the influence on carbon and manganese steels at the extreme temperature of 1680 °C for 20 min with contents of organic mass in the refractory material in volumes of (3, 5, 7.5 and 10) %. **Figure 4** shows the results of the first series of experiments.

It is evident from this figure that the addition of organic mass in the quantity up to approx. 3 % had no significant influence on the wear of the refractory materials. However, larger additions of organic mass up to 10 % brought about a distinct wear and deformation of refractory material in both the carbon and manganese steels. It is also evident that in the case of use of manganese steel, the corrosion effects of refractory materials were substantially higher than for the heats of the carbon steel.

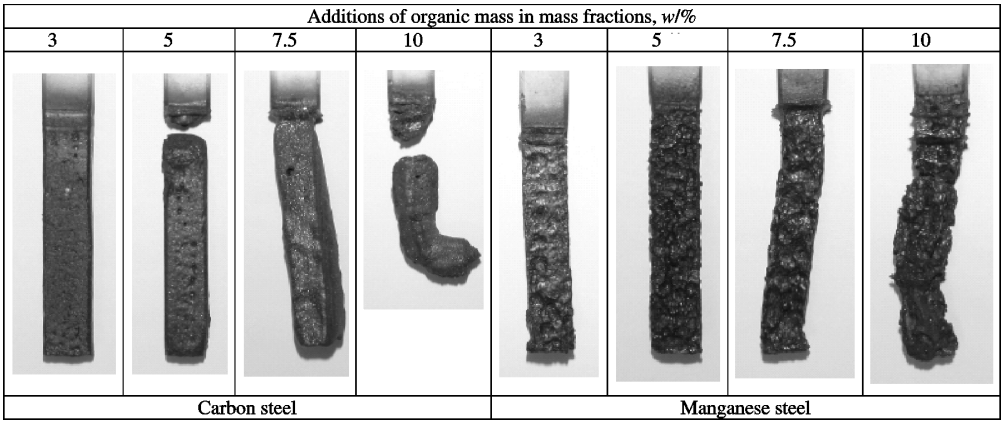

Figure 4: Pictures of refractory material after exposition in carbon and manganese steel at a temperature of 1680 °C for a period of 20 min
Slika 4: Posnetki ognjevzdržnega materiala po 20-minutni izpostavi ogljikovemu in manganovemu jeklu pri temperaturi 1680 °C

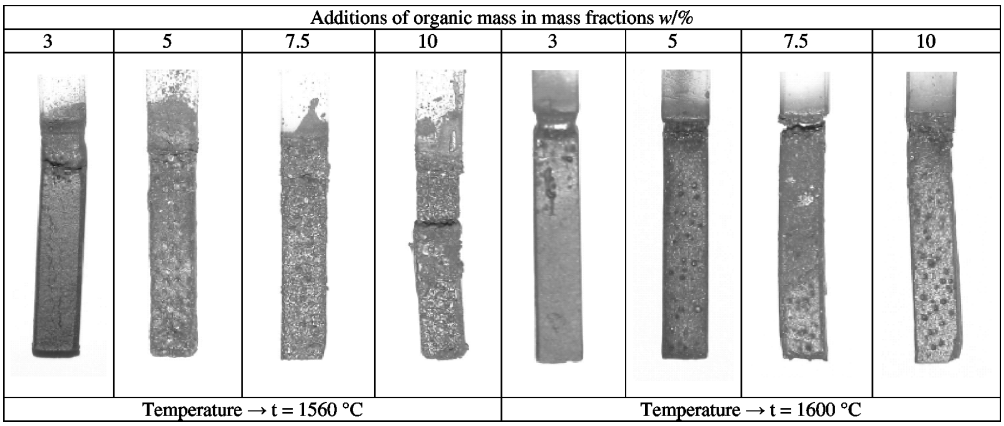

Figure 5: Pictures of refractory material after exposition in carbon steel at temperatures of 1560 °C and 1600 °C for a period of 20 min
Slika 5: Posnetki ognjevzdržnega materiala po 20-minutni izpostavi ogljikovemu jeklu pri temperaturah 1560 °C in 1600 °C

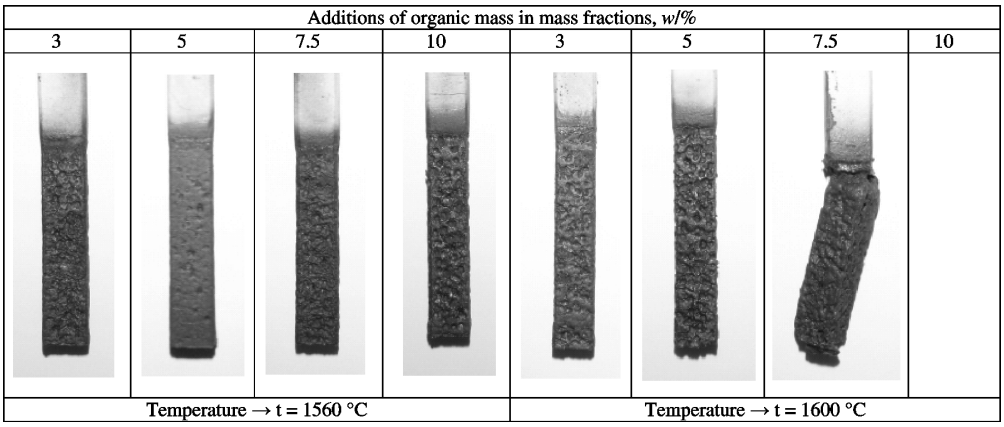

Figure 6: Pictures of refractory material after exposition in manganese steel at temperatures of 1560 °C and 1600 °C for a period of 20 min
Slika 6: Posnetki ognjevzdržnega materiala po 20-minutni izpostavi manganovemu jeklu pri temperaturah 1560 °C in 1600 °C

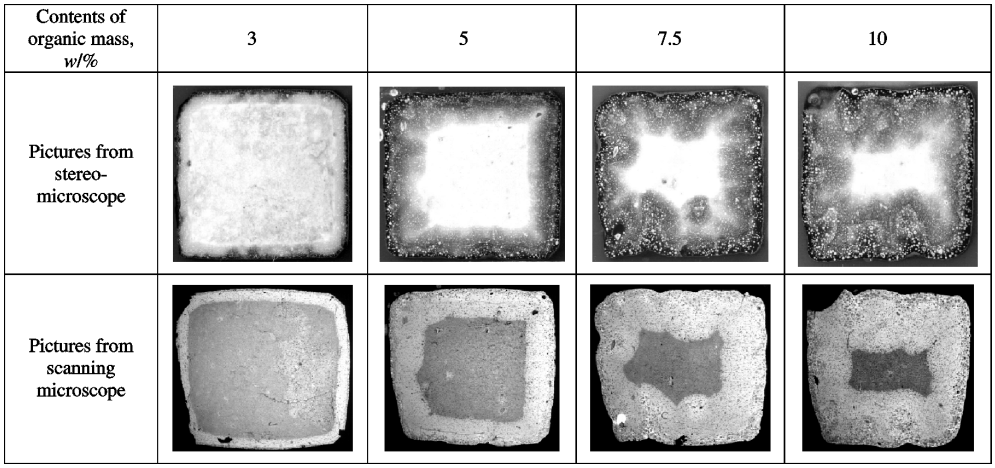

Figure 7: Comparison of pictures of cross-sections stressed at the temperature of 1600 °C in carbon steel taken with stereo-microscope and scanning electron microscope
Slika 7: Primerjava posnetkov prereza, obremenjenega pri temperaturi 1600 °C v ogljikovem jeklu, pripravljenih s stereomikroskopom in z vrstičnim elektronskim mikroskopom

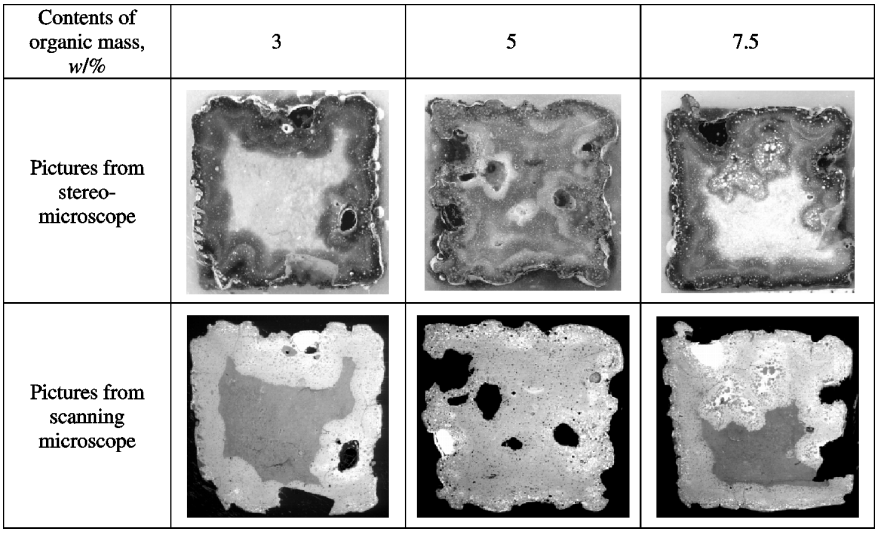

Figure 8: Comparison of pictures of cross-sections stressed at the temperature of 1600 °C in manganese steel taken with stereo-microscope and scanning electron microscope
Slika 8: Primerjava posnetkov prereza, obremenjenega pri temperaturi 1600 °C v manganovem jeklu, pripravljenih s stereomikroskopom in z vrstičnim elektronskim mikroskopom

On the basis of previous results the experiments were carried out under modified conditions, again with refractory materials with contents of organic mass of (3, 5, 7.5 and 10) % with use of carbon and manganese steel with an interaction time of 20 min, but at temperatures of 1560 °C and 1600 °C. The objective of these tests was to simulate the temperatures in practical conditions of the uphill casting of steels into ingot moulds, as well as to test the influence of various additions of organic mass on the wear at these reduced temperatures. The results of the experiments are shown in **Figures 5 and 6**.

An analysis of these figures revealed that a temperature of 1560 °C seems to be too low for carbon steels. The liquidus temperature calculated on the basis of the chemical composition of the steel is 1495 °C (see **Table 2**). In this case freezing of the steel on the walls of the ceramic samples occurred during testing. In the case of an industrial application this would require an increase in the pouring temperature from the usual 1560 °C (pouring temperature used at ŽĎAS, a. s.) to approximately 1570–1575 °C (i.e., by about 10–15 °C).

However, with the same steel and temperature of 1600 °C, the refractory materials showed, with contents of 5 % of organic mass, only minimum wear, and slightly higher wear for a content of 7.5 %. Nevertheless, higher contents of organic mass up to 10 % already had a negative impact at this temperature. During the use of manganese steel at the temperature of 1560 °C and at calculated liquidus temperature of 1375 °C (see **Table 2**) the degree of wear was higher for contents of organic mass higher than 7.5 %. For this reason, experiments at a temperature of 1600 °C were made without the sample containing 10 % of organic mass. At the temperature of 1600 °C a minimum loss was determined in the same (manganese) steel for the contents of 3 % of organic mass in the refractory material [2].

4.2 Evaluation of cross-sections

Apart from a visual evaluation of the samples after the experiments, their cross-sections were evaluated as well. The evaluation itself was made on the basis of a visual comparison of images taken using an Olympus stereo-microscope and Tescan Vega scanning microscope operating in the "fish eye" mode. The photos taken with the stereo-microscope make it possible to determine the depth of penetration, the material structure and also the losses of material. The pictures taken with the scanning microscope enable a determination of the cracks, fissures, structure failures, and in some cases, also the depth of the penetration. For an illustration, only the samples with use of carbon and manganese steels for 20 min at the temperature of 1600 °C were used, with the contents of organic mass in the refractory materials of (3, 5, 7.5 and 10) %.

The photographs of the cross-sections taken with the stereomicroscope and the scanning microscope of the carbon steel at the temperature of 1600 °C are shown in **Figure 7**. The images show that the character and morphology of the surfaces of the refractory materials are similar. Refractory materials with contents of organic mass up to 5 % showed minimum wear, and a slightly higher wear was observed for the contents from 7.5 %. **Figure 8** shows pictures of the cross-sections taken with the stereo-microscope and the scanning microscope of the manganese steel at the temperature of 1600 °C. The pictures show that for this steel the addition of organic mass >5 % at the temperature of 1600 °C had a negative impact, and it influenced not only the surface layers of the refractory material, but also its central parts. Larger additions had a very negative impact on the material's structure.

5 CONCLUSIONS

With the development of new ceramic filters intended for the filtration of steel in the gating system during the casting of ingots, experiments were carried out in laboratory conditions with a focus on the verification of the influence of porosity in refractory materials on the erosion and corrosion caused by the steel. Afterwards, various pictures were visually evaluated. This evaluation made it possible to assess the influence of the additions of the organic mass on the degree of wear of the refractory material under various operating conditions. The following conclusions may be drawn on the basis of the results of the laboratory experiments:

- it is obvious from the results obtained in both series that the manganese steel had a much greater corrosive impact on the tested refractory materials than the carbon steel,
- for the tested samples in the first part during the contact with carbon and manganese steel at the temperature of 1680 °C for 20 min, the addition of organic mass up to approx. 3 % had no significant influence on the wear of the refractory materials. However, larger additions of organic mass up to 10 % caused a distinct wear and deformation of the refractory material,
- the samples of refractory materials in the second part were in contact with the carbon and manganese steel for 20 min, but at temperatures of 1560 °C and 1600 °C. The temperature of the experiments at 1560 °C was too low for the carbon steel, since freezing of the steel on the walls of the samples occurred during testing. In the case of the same steel and a temperature of 1600 °C the samples showed up to the contents of 5 % of organic mass only a minimal amount of wear. However, larger contents of organic mass of 10 % had a negative influence at the temperature of 1600 °C,
- for the manganese steel and a temperature of 1560 °C an increased degree of wear was found for contents of organic mass exceeding 7.5 %. For this reason, the experiments at the temperature of 1600

°C were realised without the sample containing 10 % of organic mass. The samples showed for the same steel a minimum loss of refractory material at the temperature of 1600 °C and contents of 3 % of organic mass,

– it was determined from the pictures of the cross-sections for the carbon steel and the temperature of 1600 °C, that up to the contents of 5 % of organic mass the refractory materials showed only minimal wear, while at the contents of 7.5 % and more of organic mass they showed slightly increased wear. However, the manganese steel had a negative impact during the addition of organic mass >5 %, and this phenomenon influenced not only the surface layers, but also the central areas of the refractory material,
– on the basis of the obtained results the company KERAMTECH, s. r. o., produces ceramic filters with the addition of 5 % of organic mass under the designation RK-5/5.

Acknowledgement

This work was carried out within the project EUREKA MICROST OE08009 and the project FR-TI1/222.

6 REFERENCES

[1] Stránský, K., Bažan, J., Horáková, D. *Filtrace taveni železa v průmyslové praxi [Filtration of molten steel in practice]*. Editor. Ostrava, VŠB-TU Ostrava, 2008, 113 pp. ISBN 978-80-248-1844-3

[2] Bažan, J., Socha, L., Martínek, L., Fila, P., Balcar, M., Lev, P. Effect of Refractory Materials Porosity on Erosion and Corrosion of Ceramic Filters by Molten Steel Treatment. *Hutnické listy*, 63 (**2010**) 2, 20–2

UDK 622.349.1:666.32/.36
Professional article/Strokovni članek

ISSN 1580-2949
MTAEC9, 45(6)609(2011)

THE INFLUENCE OF THE MINERAL CONTENT OF CLAY FROM THE WHITE BAUXITE MINE ON THE PROPERTIES OF THE SINTERED PRODUCT

VPLIV VSEBNOSTI MINERALA GLINE IZ RUDNIKA BELEGA BOKSITA NA LASTNOSTI SINTRANEGA PROIZVODA

Milun Krgović[1], Ivana Bošković[1], Mira Vukčević[1], Radomir Zejak[2], Miloš Knežević[2], Ratko Mitrović[2], Biljana Zlatičanin[1], Nataša Jaćimović[1]

[1]University of Montenegro, Faculty of Metallurgy and Technology, Dž. Vašingtona bb, 81000 Podgorica, Montenegro
[2]University of Montenegro, Faculty of Civil Engineering, Džordža Vašingtona bb, 20000 Podgorica, Montenegro
milun@ac.me

Prejem rokopisa – received: 2011-05-30; sprejem za objavo – accepted for publication: 2011-08-24

An investigation of the influence of the mineral content of clay from the White Bauxite Mine on the properties of the sintered product is presented. The whole area of the white bauxite deposit (the "Bijele Poljane" mine) is characterized by the presence of clays. To investigate the properties of the sintered product, two of the most present types of clays were used (marked as "B" and "C"). The investigations of the properties of the sintered products on the basis of these clays involved the linear and volume shrinkage, the total porosity and the compression strength. The sintering process was conducted at temperatures of 1000 °C, 1100 °C, 1200 °C, 1300 °C and 1400 °C.

Key words: clay, linear shrinkage, total shrinkage, compression strength, sintering, porosity

Raziskava vpliva vsebnosti minerala gline iz Rudnika belega boksita je predstavljena v tem delu. Karakteristična za celotno področje ležišča belega boksita (rudnik Bele Poljane) je prisotnost gline. Lastnosti sintranega proizvoda so bile izvršene pri dveh največ prisotnih vrstah gline (označbi B in C). Določene so bile naslednje lastnosti sintranih proizvodov teh glin: linearno in volumensko krčenje, celotna poroznost in tlačna trdnost. Sintranje je bilo izvršeno pri temperaturah (1000, 1100, 1200, 1300 in 1400) °C.

Ključne besede: glina, linearno krčenje, skupno krčenje, tlačna trdnost, sintranje, poroznost

1 INTRODUCTION

The investigated clay types from the White Bauxite Mine appear in layers and have different mineral contents:

– clays with bauxite minerals,
– illite-kaolinite clays,
– clays with a very heterogeneous mineral content.

This mineral content gives us the possibility to obtain different ceramic products [1]. The most important differences in the mineral content are related mostly to the content of bauxite minerals, clay minerals, iron compounds, quartz and calcite [2]. Depending on the sintering temperature, this mineral content of the clays influences the solid-state reactions, the polymorphic transformations of the quartz and the liquid-phase formation[3]. Apart from the degree of the sintering of the ceramic mass, i.e., the firing regime, the mineral content of the raw material also has an important influence on the relations between particular microstructural elements. [4] The new crystal phases, i.e., the compounds formed within the solid-state reactions during sintering, are determined by the mineral content of the clays, as well as by the previously mentioned factors. [5,6] It causes important differences in the mineral content of the sintered products. The content of bauxite minerals (boehmite, gibbsite), iron compounds (hematite), clay minerals (kaolinite, illite) in the investigated clay types primarily determines the properties of the sintered products.[7,8] According to their refractoriness, the investigated clay types are refractory (the refractoriness is over 1500 °C).[1,9] Neither flux, as a component that decreases shrinkage, nor electrolytes were used for the raw-material mixture formation, because the aim of the investigation was to determine the influence of the mineral content of the investigated clays on the properties of the sintered product.

2 EXPERIMENTAL

The samples were formed by shaping of a plastic mass in a mould corresponding to a parallelepiped with dimensions of 7.7 cm × 3.9 cm × 1.6 cm. The characterization of the investigated clays was made by a determination of the mineral content, the chemical content, the density, the humidity and the granulometry. The chemical content was determined with a Perkin Elmer 4000 atomic absorption spectrophotometer. The granulometry of the clays was determined on a "Microsizer 201C" VA INSTALT instrument. For the raw, non-sintered products the linear and volume shrinkage during the drying in air and in a dryer, to a constant

Table 1: Chemical composition of clay "B" and "C" in mass fractions, *w*/%
Tabela 1: Kemična sestava glin "A" in "B" v masnih deležih, *w*/%

Oxides	SiO_2	Fe_2O_3	Al_2O_3	CaO	MgO	K_2O	TiO_2	lg. loss
Clay "B"	63,2	2,2	25,2	1,2	1,3	0,9	0,8	4,1
Clay "C"	64,2	2,3	24,8	1,3	1,4	1,0	0,7	3,8

mass, at a temperature of 110 °C was determined. The samples were sintered at (1000, 1100, 1200, 1300 and 1400) °C.

For the sintered products the linear and volume shrinkage during sintering, the total porosity and the compression strength were determined. The volume shrinkage was determined using the following equation:

$$C_{\mathrm{v}} = \frac{V_0 - V_i}{V_0} \cdot 100(\%)$$

V_0/m^3 – the volume before shrinkage
V_i/m^3 – the volume after shrinkage

The total porosity was determined using the following equation:

$$TP = \frac{\rho_0 - \rho_{\mathrm{v}}}{\rho_0} \cdot 100(\%)$$

ρ/(kg m^{-3}) – the sample's density
ρ_{v}/(kg m^{-3}) – the sample's volume mass

The compression strength was determined on a novopress HPM 400 and the X-ray analysis was performed on a Difractometer PHILIPS PW 1710. The microscopic analysis of the sintered products was made by scanning electron microscopy on a JEOL-JSM 6460LV-DEU (BAL-TEC SCD 005-SPVTTER COATER).

3 RESULTS AND DISCUSSION

The results of the chemical analysis (**Table 1**) show a slightly higher content of oxides, i.e., CaO and MgO, in the clay "C" as a consequence of the higher content of carbonates. The clay "C" contains more Fe_2O_3 in the mass fraction, *w* (*w* = 2.3 %), with respect to the clay "B" (*w* = 2.2 %). The content of TiO_2 in clay "B" is slightly higher (*w* = 0.8 %) compared to the clay "C" (*w* = 0.7 %).

The mineral content of the clay "B", determined by the X-ray analysis (**Figure 1**), shows the presence of kaolinite, gibbsite, boehmite and anatase. The X-ray analysis shows the presence of the following minerals in the clay "C" (**Figure 2**): kaolinite, gibbsite, boehmite, anatase, hematite, illite and clinochlore.

The results of the granulometric analysis show an average grain size of 69.32 μm in the samples on the basis of clay "B", while in the samples on the basis of clay "C" the average grain size is 63.25 μm, under the same milling conditions. The clay "B" has a higher average grain size with respect to the clay "C" under the same milling conditions, which is a consequence of the mineral content of the clays.

The volume shrinkage of the products during sintering (**Figure 3**) grows with the increase of the temperature as a consequence of solid-state reactions, polymorphic transformations of the quartz, the carbonates' dissolution, the glass-phase formation and the closure of pores during sintering. The content of K_2O in clay "C" is slightly higher (1.0 %) with respect to clay "B" (0.9 %) and it can be concluded that it does not have an important influence on the differences in the liquid-phase content, which accelerates the solid-state reactions (the diffusion coefficient increases).

The granulometric content of clays "B" and "C" also has an important influence on the volume shrinkage. The average grain size is greater in clay "B".

The content of Fe_2O_3 also has an influence on the volume shrinkage during sintering, and the content of Fe_2O_3 in the clay „C" (2.3 %) is slightly higher compared to the clay "B" (2.2 %).

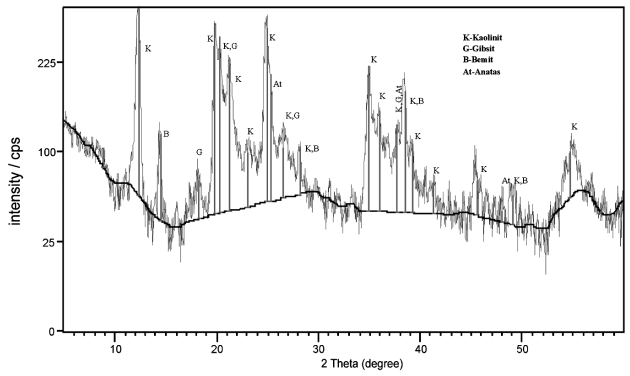

Figure 1: X-ray diffractogram of "B" clay
Slika 1: Rentgenski difraktogram gline "B"

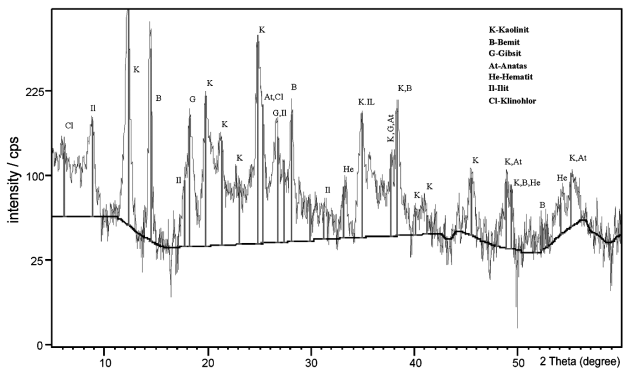

Figure 2: X-ray diffractogram of "C" clay
Slika 2: Rentgenski difraktogram gline "C"

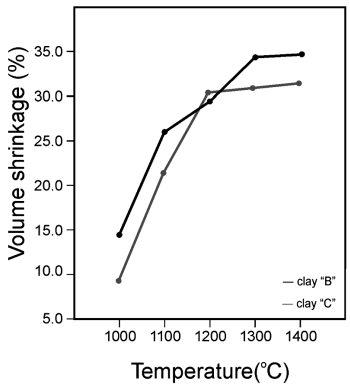

Figure 3: Volume shrinkage of product during sintering (clay "B" and clay "C")
Slika 3: Volumensko krčenje med sintranjem (glini "B" in "C")

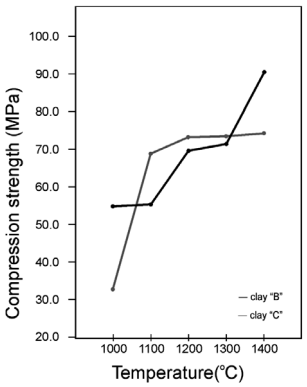

Figure 5: Compression strength of product during sintering (clay "B" and clay "C")
Slika 5: Tlačna trdnost sintranca med sintranjem (glina "B" in "C")

The volume shrinkage increases with the increase of the sintering temperature and the growth is more evident in samples on the basis of clay "B" at higher temperatures (1300 °C and 1400 °C), which can be explained by the differences in the mineral and granulometric contents of the clays and solid-state reactions (X-ray analysis of sintered product at T = 1300 °C and 1400 °C, see **Figure 6 and Figure 7**).

The total porosity during sintering decreases with the increase of the temperature (**Figure 4**). Apart from the intense solid-state reactions at higher temperatures (liquid-phase formation, diffusion coefficient increase), the decisive factors for the decrease of the porosity at higher temperatures are the chemical, mineral and granulometric contents of the raw material. The granulometric analysis shows that clay "B" has a larger average grain size with respect to the clay "C".

Considering the small difference in the content of alkali, they do not decisively influence the total porosity. The total porosity at 1400 °C has smaller values in the samples on the basis of clay "C", which is probably a consequence of the grain fraction (smaller average grain size) and the relations between the microstructural elements.

Clay "B" has a higher average grain size with respect to clay "C", which increases the total porosity and in this way the granulometric content of the clays influences indirectly on the compression strength. For the samples on the basis of clay "B" at (1100, 1200, 1300 and 1400) °C it is evident that there is an almost linear dependence of the compression strength of the sintering temperature, while in samples on the basis of clay "C" the compression strength value at temperatures of (1100, 1200, 1300 and 1400) °C (**Figure 5**) increases only slightly, which can be explained by the mineral content . In the samples on the basis of clay "B" with an increase

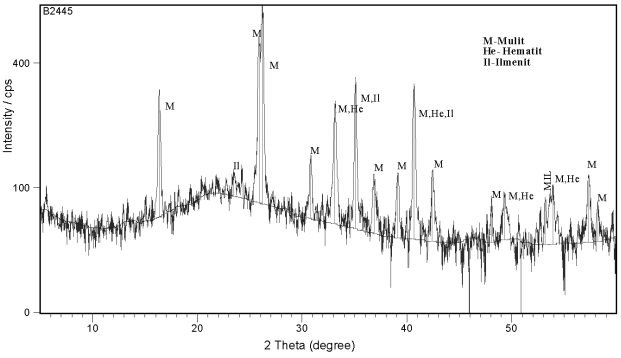

Figure 6: X-ray diffractogram of sintered product (clay "B", T = 1300 °C)
Slika 6: Rengenski difraktogram sintranca (gline "B", T = 1300 °C)

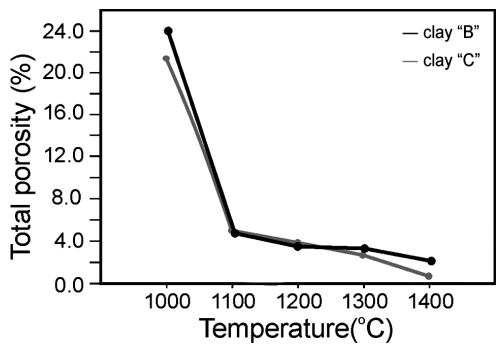

Figure 4: Total porosity of products during sintering (clay "B" and clay "C")
Slika 4: Skupna poroznost med sintranjem (glina "B" in "C")

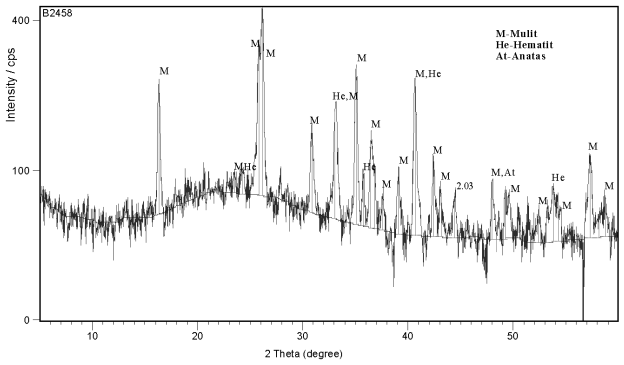

Figure 7: X-ray diffractogram of sintered product (clay "C", T = 1300 °C)
Slika 7: Rentgenski difraktogram sintranca (gline "C", T = 1300 °C)

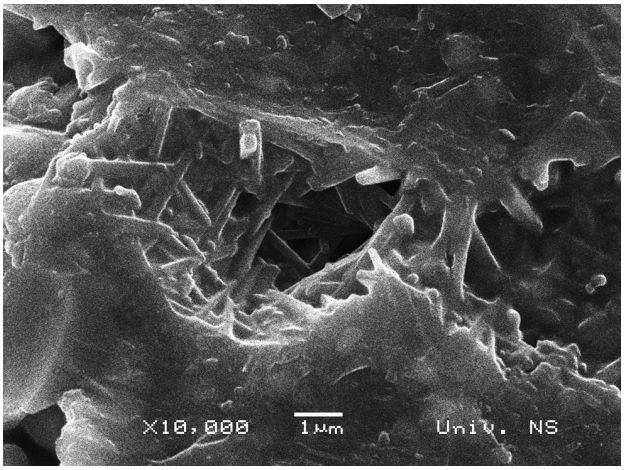

Figure 8: Microstructure of sintered product (clay "B", *T* = 1300 °C, magn. 10 000-times)

Slika 8: Mikrostruktura sintranca (gline "B", *T* = 1300 °C, pov. 10 000-kratna)

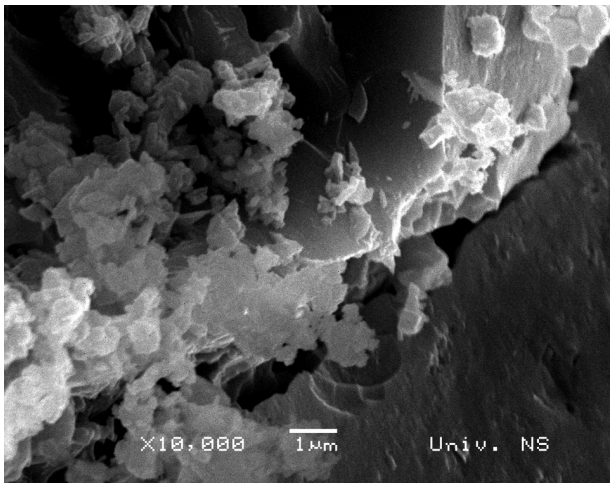

Figure 9: Microstructure of sintered product (clay "C", *T* = 1300 °C, magn. 10 000-times)

Slika 9: Mikrostruktura sintranca (gline "C", *T* = 1300 °C, pov. 10 000-kratna)

of the temperature up to 1400 °C a high compression strength can be obtained (above 90 MPa). With an increase of the sintering temperature in samples on the basis of clay "C" above 1200 °C the compression strength increases slightly.

The X-ray structure analyses of the sintered products in the samples on the basis of clay "B" and "C" show important differences in the mineral content (**Figure 6 and Figure 7**). The crystal phases at the temperature of 1300 °C for samples on the basis of clay "B" are mullite, hematite and ilmenit, while for samples on the basis of clay "C" they are mullite, hematite and anatase. Mullite and hematite, as crystal phases, are present in sintered products even at temperatures of (1100, 1200 and 1400) °C. The presence of the crystal phases is a consequence of the solid-state reactions at these temperatures. The microstructural analysis of the sintered products (**Figure 8** and **Figure 9**, 10,000 × magnification) shows the complexity of the structure (glass phase, crystal phase, unreacted grains and pores).

4 CONCLUSIONS

On the basis of the performed investigations of the influence of the mineral content of clays from the White Bauxite Mine it is concluded that:

- The investigated clay types are very different for in terms of their mineral and chemical compositions,
- the volume shrinkage is greater for samples on the basis of clay "B" and this is explained by the difference in mineral and granulometric content of the clays and the solid-state reactions,
- the differences in the total porosity of the sintered products on the basis of the investigated clays are not significant,
- the values of the compression strengths of the sintered products are very different: in the samples on basis of clay "B", important values of the compression strength are noted only at temperatures above 1300 °C, while in samples on the basis of clay "C" this is already above 1100 °C.

On the basis of the volume shrinkage, the total porosity and the compression strength it is concluded that a quality ceramic product can be obtained by sintering clays from the White Bauxite Mine.

5 REFERENCES

[1] Lj. Kostić-Gvozdenović, R. Ninković, *Inorganic Technology*, Faculty of Technology and Metallurgy, University of Belgrade, Belgrade (**1997**)

[2] N. Jaćimović, The Influence of the Mineral Composition of clay from the Mine "Bijele Poljane" on the Characteristics of Sintered Products, *Master Thesis,*University of Montenegro, Podgorica (**2010**), 4–15

[3] M. Tecilazić - Stevanović, *Principles of Ceramic Technology*, Faculty of Technology and Metallurgy, University of Belgrade, Belgrade (**1990**)

[4] M. Krgović, M. Knežević, M. Ivanović, I. Bošković, M. Vukčević, R. Zejak, B. Zlatičanin, S. Đurković, The properties of a sintered product based on electrofilter ash, *Mater. Tehnol.,* 43 (**2009**) 6, 327–331

[5] B. Živanović, R. Vasić, O. Janjić, *Ceramic Tiles*, *Monography*, Institute of Materials in Serbia, Belgrade (**1985**), 12–17

[6] M. Krgović, N. Z. Blagojević, Ž. Jaćimović, R. Zejak, Possibilities of using red mud as raw materials mixture component for production of bricks, *Research Journal of Chemistry and Environment,* 8 (**2004**), 73–76

[7] M. Krgović, N. Marstijepović, M. Ivanović, R. Zejak, M. Knežević, S. Đurković, The influence of illite-kaolinite clays mineral content on the products shrinkage during drying and firing, *Mater. Tehnol.*, 41 (**2007**) 4, 189–192

[8] S. Đurković, The Possibilities of using Electrofilter Ash TE "Pljevlja" as Raw Materials component Mixture for producting sintered product, Master Thesis, University of Montenegro, Podgorica (**2008**), 4–5

[9] J. Griffiths, Minerals in Foundry Casting, *Ind. Min.*, 272 (**1990**), 35–40

UDK 669.715:539.3:519.68
Professional article/Strokovni članek

ISSN 1580-2949
MTAEC9, 45(6)613(2011)

EFFECT OF PRE-STRAINING ON THE SPRINGBACK BEHAVIOR OF THE AA5754-0 ALLOY

VPLIV PRENAPENJANJA NA POVRATNO ELASTIČNO IZRAVNAVO ZLITINE AA5754-0

Serkan Toros, Mahmut Alkan, Remzi Ecmel Ece, Fahrettin Ozturk*

Department of Mechanical Engineering, Nigde University, Nigde, 51245, Turkey
fahrettin@nigde.edu.tr

Prejem rokopisa – received:2011-03-31 ; sprejem za objavo – accepted for publication: 2011-09-20

This study presents the effect of pre-straining on the springback behavior of the AA5754-0 aluminum-magnesium (Al-Mg) alloy sheet under V bending by an experimental and finite-element simulation studies. Pre-straining ranges from 0 % to 11 % were applied to the samples, which were bent on a 60° V-shaped die for the springback evaluation. Commercially available finite-element software, ETA/Dynaform, was used to simulate the 60° V-die bending process. The dynamic explicit finite-element method for pressing and the static implicit finite-element method for the unloading phase were used for the simulations. The results from both the experiment and the simulation indicate that the pre-straining has no positive effect on the springback compensation.

Keywords: pre-straining; springback; Al-Mg alloy; AA5754-O alloy

Delo obravnava vpliv prenapenjanja na povratno elastično izravnavo pločevine iz aluminij magnezijeve zlitine AA5754-0 pri V-upogibu eksperimentalno in s simulacijo s končnimi elementi. Za oceno povratne elastične izravnave so bili prednapetosti v razponu od 0 % do 11 % izpostavljeni vzorci, ki so bili upognjeni v V-utopu. Uporabljen je bil komercialno dosegljiv softver ETA Dyna form za simuliranje upogibanja v 60° V-utopu. Za simulacijo sta bili uporabljeni eksplicitna metoda končnih elementov za fazo tlačenja in statična implicitna metoda končnih elementov za razbremenitev. Rezultati preizkusov in simulacije kažejo, da prenapetost nima pozitivnega vpliva na kompenzacijo izravnave.

Ključne besede: prednapetost, povratna izravnava, AlMg zlitina, zlitina AA5754-O

1 INTRODUCTION

In recent years, lightweight structures have been a key target for automotive manufacturers in order to reduce fuel consumption and carbon dioxide emissions without sacrificing vehicle safety and performance. Therefore, lightweight materials, particularly aluminum alloys, have found more applications in auto-body structures. Many industries, such as aerospace, defense and ship building, prefer aluminum alloys because of their relatively light weight to high strength ratios and corrosion resistance [1–5]. However, there are some limitations in the usage of these materials in terms of low formability at room temperature (RT) and springback. The springback issue is the most common problem in the forming operations of these lightweight materials because of their low Young's modulus. It can lead to significant problems during assembly if the phenomenon is not well controlled, and so the manufacturing costs will increase [6–8]. In bending operations, after the release of the load, an elastic recovery occurs. The geometry of the part becomes quite different than the desired shape. The springback issue has been studied over the years to compensate for the undesired shape errors and to identify the effect of major factors, such as material parameters, tooling geometry, and process parameters, on the amount of springback, both experimentally and numerically. Asnafi [9] examined the effects of process parameters on the springback in the V-bending process by developing theoretical models for stainless-steel sheets. Asnafi [10] also studied the springback characterization of steel and aluminum sheets in double-curved autobody panels, both experimentally and theoretically. He reported that this springback could be reduced by increasing the blank holder force (BHF), sheet thickness, and die radius and decreasing the yield strength. One of the most important material parameters that affect the amount of springback is the Bauschinger effect. The Bauschinger effect is normally associated with conditions where the yield strength of a metal decreases when the direction of the strain is changed. The basic mechanism for the Bauschinger effect is related to the dislocation structure in the cold-worked metal. Gau and Kinzel [11] experimentally investigated the Bauschinger effect in steel and aluminum alloys using a simple bending process. They showed that the Baushinger effect on the springback of an aluminum alloy (AA6111-T4) is very significant. Chun et al. [12,13] also studied the Bauschinger effect on a sheet-metal forming process that was subjected to cyclic loading conditions for different hardening rules. Moreover, a similar method was also used by Xue et al. [14,15]. They developed a new analytical procedure to predict the springback of circular and square metal sheets after a double-curvature forming operation [14,15].

In recent years, finite-element analysis (FEA) software packages have become very popular as a rapid and

cost-effective tool for sheet-metal forming processes. The developed models for the materials which are used in FEA software have significant effects on the accurate prediction of the forming results. For a numerical simulation of a springback analysis, the appropriate hardening model and the plastic yield criterion that properly describe the material behavior at a large strain are needed. There have been several studies in the literature to predict the springback of materials by using FEA programs based on the different hardening models, i.e., isotropic, kinematic, and mixed hardening models for different yield criteria and tool geometry, material properties, forming conditions, etc. [16–22]. Laurent et al. [22] compared several plastic yield criteria to show their relevance with respect to predicting the springback behavior for a AA5754-0 aluminum alloy, both experimentally and numerically. In their study, the effectiveness of the isotropic and kinematic hardening models, which are combined with one of the following plasticity criteria – von Mises, Hill'48 and Barlat'91 – are analyzed.

In the present study, the effects of pre-straining on the flow stress and the springback behavior of the 5754-O Al-Mg alloy were investigated. In addition to the experimental work, finite-element (FE) simulations were also used for the springback predictions and the comparison.

2 MATERIAL AND EXPERIMENTAL WORK

In this study, as-received Alcan 5754-O Al-Mg alloy sheet in the O-temper with a thickness of 1.88 mm was evaluated. The chemical composition of the material is given in **Table 1**.

Table 1: Chemical composition of 5754 Al-Mg alloy (in mass fractions, *w*/%)
Tabela 1: Kemična sestava AlMg zlitine 5754 (v masnih deležih, *w*/%)

Mg	Si	Mn	Fe	Cu	Al
3.17	0.112	0.51	0.1613	0.01	Balance

Initial material properties are given in **Table 2**.

Tensile and pre-straining tests were performed on a Shimadzu Autograph 100 kN testing machine with a data-acquisition system maintained by a digital interface board utilizing a specialized computer program. The material deformation was measured with a video-extensometer measurement system for tensile-test specimens with a 50-mm initial gauge length. Tensile-test samples were prepared according to the ASTM E8 standard in the rolling, "diagonal" and transverse directions. The tests were conducted at room temperature and a strain rate of 0.0083 s^{-1} (25 mm/min) in order to determine the initial properties of the material, which are shown in **Table 2**. The specimens in the rolling direction were also pre-strained by the tensile testing machine for six different pre-straining levels, ranging from 1 % to 11%, by an increment of 2 %. The pre-straining was performed at a constant deformation rate of 3 mm/min and then unloaded at the same deformation rate. It is generally known that the alloy shows serrated hardening curves, as commonly observed for 5XXX series aluminum alloy sheets [23]. The yield strength of the material was determined based on the 0.2 % proof stress. As mentioned before, the Young's modulus of the material has considerable affects on the springback behavior of the materials. However, determining the Young's modulus by performing tensile tests is very difficult because of the machine competence and software limitations. Research in the literature shows that the Young's modulus varies with the plastic deformation and therefore using a constant Young's modulus in springback calculations and simulations means less accurate results [24,25].

The 60° V-shaped die bending test samples were also prepared at a rolling direction in a rectangular shape of 30 mm × 200 mm. They were all pre-stained using the

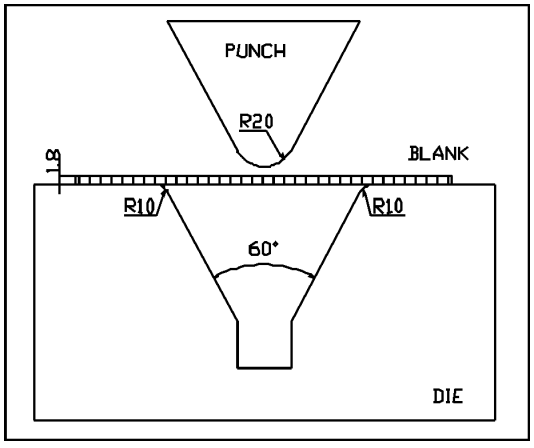

Figure 1: 60° V-shaped bending setup
Slika 1: 60° V-utop za upogibanje

Table 2: Initial material properties of 5754 Al-Mg alloy
Tabela 2: Začetne lastnosti AlMg zlitine 5754

	YS (0.2 %)/MPa	*UTS*/MPa	*UE*/%	*TE*/%	*r*	Lankford Parameter	*n*	*K*/MPa
Rolling (0°)	118	296	19.5	22.3	0.712	0.7325	0.306	492.2
Diagonal (45°)	106	234	23.2	26.2	0.754		0.304	462.5
Transverse (90°)	108	234	21.8	24.3	0.710		0.302	464.7

UE: Uniform elongation; TE: Total tensile elongation

tensile testing machine, in the same way as the tensile test samples.

In this study the springback evaluation was made by a 60° V-shaped die bending test, as shown in **Figure 1**.

The bending tests were performed at a 25 mm/min deformation speed. The precision of the displacement and force measurements of the punch are 0.001 mm and ±2 N, respectively. No lubrication was applied to the die and blank surfaces. The punch was released after the forming. No soak time was assigned. The springback angle ($\Delta\theta$) was measured by a Mitutoyo 187-907 universal bevel protractor that has a ±5min measurement accuracy.

3 FINITE-ELEMENT STUDY

There have been many numerical approaches to defining the springback characterization of materials for bending operations. In general, these approaches are directly related to the material properties, which are the strain hardening coefficient (n), strength coefficient (K), thickness (t), anisotropy (R), Young's modulus (E), Baushinger effects, hardening models, etc. In this research, finite-element modeling was considered in addition to the experimental study.

The material properties, i.e., Young's modulus (E), yield stress (Y) and strength coefficient (K), were obtained from uniaxial tensile test and modified for the plane strain conditions using von Mises criterion. The bending process was also analyzed based on a consideration of the plane strain condition. Plane strain bending is a major sheet-forming process and it is practiced as air bending, U- and V-shaped die bending. The deformation in a bending process can be pronounced as a plane strain deformation. In a plane strain deformation, the sheet usually extends only in one direction. For this reason, the plane strain condition was also studied and compared with the tensile deformation in order to see the effect of the deformation mode.

The new E', Y', and K' for the plane strain calculation are as follows:

$$E^{l} = \frac{E}{1-\nu^{2}}$$

$$Y^{l} = \frac{2Y}{\sqrt{3}}$$

$$K^{l} = \frac{2K}{\sqrt{3}}$$

In the calculations and simulations it was assumed that the n values that were obtained under prescribed pre-straining conditions during the uniaxial tensile tests do not change with the uniaxial and plane strain conditions.

The 60° V-shaped bending process was modeled using a commercially available ETA/Dynaform finite-element simulation program, as shown in **Figure 2**. In

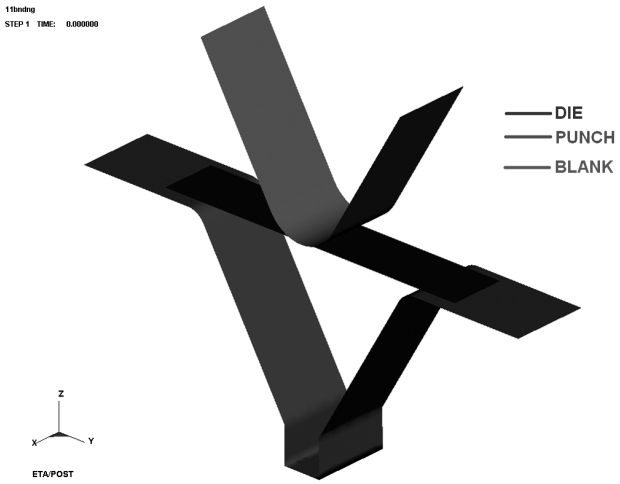

Figure 2: Finite element modeling of V bending process
Slika 2: Modeliranje V-upogibanja s končnimi elementi

the model, the die and punch were considered as rigid bodies, and the blank was a deformable body. A Belytschko-TSAY shell element was used for the blank and rigid tools in order to improve the effectiveness of the nonlinear numerical computation.

Besides the element type, the number of elements can also affect the accuracy of the simulation results. In the study, 4012 elements were used with five integration points through the thickness of the deformable sheet. An adaptive mesh option was also used in order to reduce the errors during the calculation of the springback. In the adaptive mesh method the elements are subdivided into smaller elements during the analysis. This subdivision of the elements provides improved accuracy and in the study a two-times adaptivity was applied to the model.

The implicit and explicit solutions are two methods that are used for the springback simulations. In the simulation, the explicit loading and implicit unloading approaches were used to predict the springback characterization of the material. The implicit solution is realized by applying a reverse nodal force and an equivalent iteration. Due to the large deformations in the sheet-metal forming operations, the amount of springback is relatively large so the implicit solution is able to meet these kinds of convergence forming operations. When the accuracy of the stress field after the forming is poor, the convergence problem becomes more serious [26].

As a material model, the material Type 36 (MAT_3-PARAMETER_BARLAT) was used. This model was developed by Barlat and Lian [27] in 1989 for the modeling of anisotropic materials under plane stress-strain conditions. This material allows the use of Lankford parameters [28] for the definition of anisotropy. The criterion can be expressed as:

$$a|K_1 + K_2|^m + b|K_1 - K_2|^m + c|2K_2|^m = 2\sigma_e{}^m$$

where a, b and c are the material constants that depend on the anisotropy, K_1 and K_2 are the invariants of the stress tensor and m is the stress exponent that is

Table 3: Summary of material properties
Tabela 3: Povzetek lastnosti materiala

Pre-straining (%)	*Y*/MPa	*UTS*/MPa	*E*/MPa	*K*/MPa	*n*
0	118.56	296.80	47.17	492.2	0.310
1	125.66	296.80	57.46	516.3	0.323
3	174.62	297.75	58.61	512.6	0.328
5	204.89	296.53	61.34	497.4	0.305
7	225.81	306.30	65.55	482.8	0.297
9	245.85	308.56	74.72	455.1	0.263
11	259.18	300.94	81.24	449	0.260

calculated based on the crystallographic texture and is equal to 8 for FCC materials.

4 RESULTS AND DISCUSSION

In the experimental study, the pre-straining was applied to 5754-O Al-Mg alloy sheets at the prescribed values. The tensile load and extension data were converted to true stress vs. true strain data, which were obtained at different pre-straining values. The true stress vs. true strain diagrams were plotted, as seen in **Figure 3**. Each pre-straining path can be seen on the graph. The mechanical properties were measured for all pre-strained conditions at RT and a 0.0083 s^{-1} strain rate. The data was tabulated as seen in **Table 3**. As also seen in **Table 3**, the yield strength of the material was significantly increased from 118 MPa to 259 MPa. The change is twice that of the initial value. It is known that if the ratio of UTS/Y is high, a high springback is generally observed. Increased pre-straining creates a high elastic energy, which is the opposite to steels, is thought to be the major reason for a high springback observation. The change in UTS is not a large amount. It has an increasing tendency up to 9 % pre-straining, then it starts to decrease.

E is the one of the most important material properties that affects the springback of the materials. Some researchers have pointed out the effects of a variable Young's modulus on the formability of the materials [29–33]. The change in Young's modulus was plotted with respect to the pre-straining value, as shown in **Figure 4**. As seen from **Table 3**, the value was much lower than the known value. Normally, it is very difficult to determine the Young's modulus with a tensile test. The purpose of the study is to evaluate the springback variation with pre-straining relatively. For this reason it is not paid attention to the values. The same procedure was applied for each condition, which means it does not make any significant changes for the final outcome. The important point is that the tendency of the *E* based on pre-straining was determined. **Figure 4** indicates two linear curves and their equations. Although the Young's modulus of the material shows fluctuation with prescribed pre-straining levels, the trend of the values is increasing with plastic deformation.

Figures 5 and 6 show the variations of *K* and *n* with respect to the prescribed pre-straining.

Similar behaviors were observed in **Figures 5 and 6**. A minor increase was seen up to 3 % pre-straining and a minor decrease was seen after that. *K* has the highest value at 3 % pre-staining. As seen from the results, it is very complicated to clarify the changes. It may be

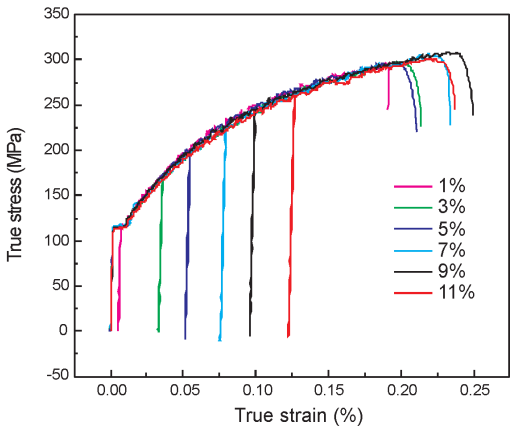

Figure 3: True stress vs. true strain curves for the 5754 Al-Mg alloy
Slika 3: Odvisnosti prava napetost – prava deformacija za zlitino AlMg 5754

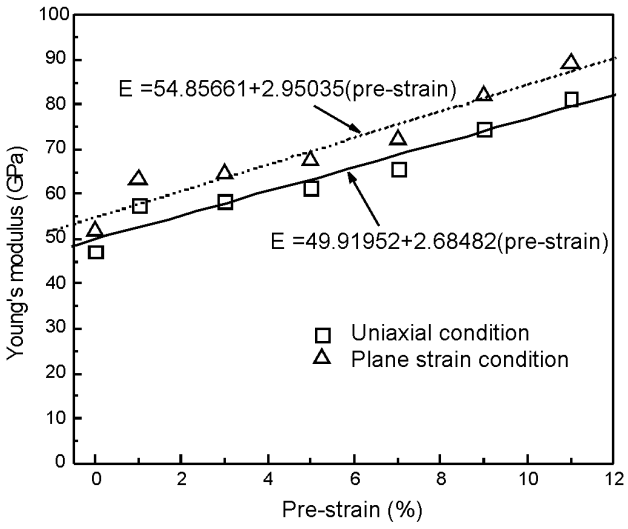

Figure 4: Variation of the Young's modulus vs. pre-straining
Slika 4: Sprememba Youngovega modula v odvisnosti od prednapetosti

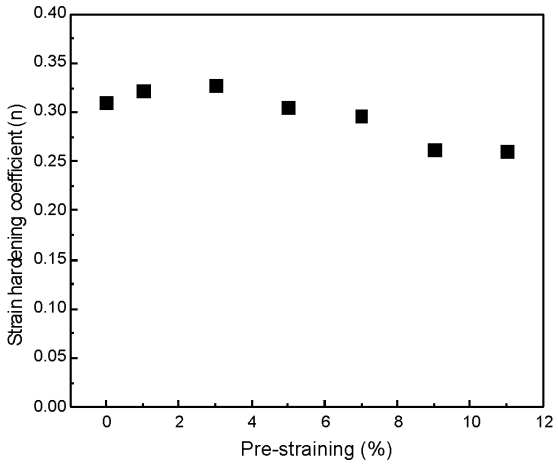

Figure 5: Variation of the strain hardening coefficient vs. pre-straining
Slika 5: Sprememba koeficienta deformacijske utrditve v odvisnosti od prenapetosti

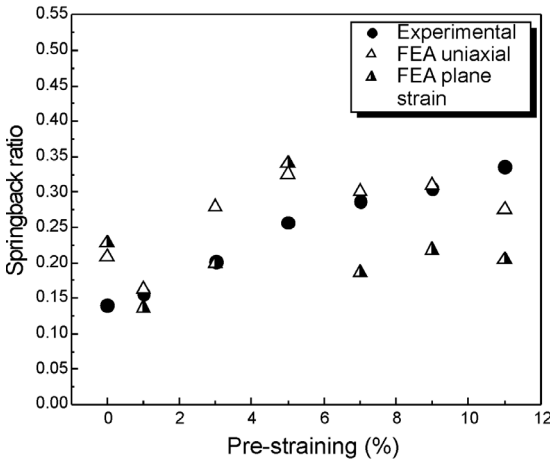

Figure 7: Variation of the springback with pre-straining
Slika 7: Sprememba povratne izravnave v odvisnosti od prednapetosti

explained with the changes in the microstructure, including the dislocation mechanism, porosities, inclusion, and deformation rate, etc.

Finally, the evaluation of the springback was investigated by experiment and finite-element methods. All the results were plotted on the same graph and displayed in **Figure 7**. The reference curve is the experimental curve. Any prediction that is close to this curve is considered to be a most accurate prediction.

The experimental data in **Figure 7** reveals that the springback is linearly increasing with increasing pre-straining. Pre-straining has no positive contribution on the springback compensation. It is related to the increasing elastic energy during the pre-straining.

Finite-element predictions were determined for the uniaxial and plane strain conditions. They were different from each other. The predictions at 1 % pre-straining were in good agreement with the experiments. But the predictions at no pre-straining and 5 % were higher than the experiments. At 3 % pre-straining, the FE prediction for the plane strain condition is almost the same as the experiment. At 7 % and over, the FE predictions for uniaxial were in accord with the experiment, except for the 11 % pre-straining. But the FE prediction for plane stress condition was lower than the experiments. In general, the FE predictions were close to the experimental results. The simulation results that were obtained for (1, 7 and 9) % pre-straining were close to the experimental results for the uniaxial strain condition. All these findings suggest that the pre-straining does not help the springback compensation.

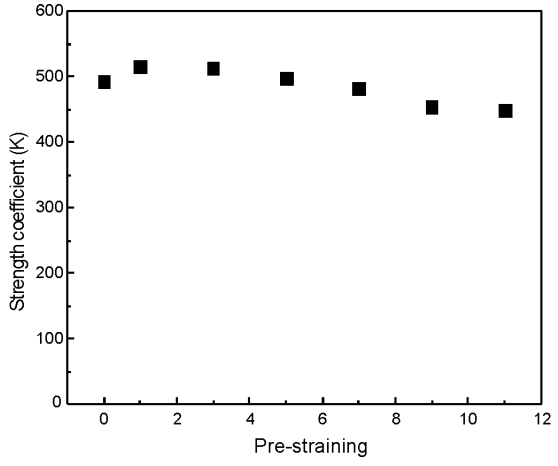

Figure 6: Variation of the strength coefficient vs. pre-straining
Slika 6: Sprememba koeficienta trdnosti v odvisnosti od prednapetosti

5 CONCLUSION

In this study, the effect of pre-straining on springback was investigated for a 5754-O Al-Mg alloy, both experimentally and numerically. It was found that the springback was increased with increasing pre-straining. The finite-element predictions were in partially good agreement with the experimental data.

Acknowledgement

This work is supported by The Scientific and Technological Research Council of Turkey (TÜBİTAK). Project Number: 106M058, Title: "Experimental and Theoretical Investigations of The Effects of Temperature and Deformation Speed on Formability". TÜBİTAK's support is gratefully acknowledged.

6 REFERENCES

[1] Naka, T.,Yoshida F., Deep drawability of type 5083 aluminium-magnesium alloy sheet under various conditions of temperature and forming speed, J Mater Process Tech, 89–90 (**1999**), 19–23
[2] Keum, Y. T., Han, B. Y., Springback of FCC sheet in warm forming, J Ceram Process Res, 3 (**2002**), 159–165
[3] Miller, W. S., Zhuang, L., Bottema, J., Wittebrood, A. J., De Smet, P., Haszler, A., Vieregge, A., Recent development in aluminium

alloys for the automotive industry, Mater Sci Eng A, 280 (**2000**), 37–49

[4] Fridlyander, I. N., Sister, V. G., Grushko, O. E., Berstenev, V. V., Sheveleva, L. M. Ivanova L. A., Aluminum alloys: Promising materials in the automotive industry, Met Sci Heat Treat, 44 (**2002**), 365–370

[5] Mildenberger, U., Khare, A., Planning for an environment-friendly car, Technovation, 20 (**2000**), 205–214

[6] Li K. P., Carden W. P, Wagoner R.H., Simulation of springback. Inter J Mech Sci, 44 (**2002**), 103–122

[7] Gan W., Wagoner R. H., Die design method for sheet springback. Inter J Mech Sci., 46 (**2004**), 1097–1113

[8] Carden W. D., Geng L. M., Matlock D. K., Wagoner R. H., Measurement of springback. Inter J Mech Sci., 44 (**2002**), 79–101

[9] Asnafi N., Springback and fracture in v-die air bending of thick stainless steel sheets, Mater Design, 21 (**2000**), 217–236

[10] Asnafi N., On springback of double-curved autobody panels, Inter J Mech Sci, 43 (**2001**), 5–37

[11] Gau, J.-T., Kinzel, G. L., An experimental investigation of the influence of the Bauschinger effect on springback predictions," J. Mater. Process. Technol., 108 (**2001**), 369–375

[12] Chun, K. B., Jinn, T. J., Lee, K. J., Modeling the Bauschinger effect for sheet metals, Part I: theory, Inter J Plasticity, 18 (**2002**), 571–595

[13] Chun, K. B, Jinn, T. J., Lee, K. J., Modeling the Bauschinger effect for sheet metals, part II: applications, Inter J Plasticity, 18 (**2002**), 597–616

[14] Xue P., Yu T. X., Chu E., An energy approach for predicting springback of metal sheets after double-curvature forming, Part I: axisymmetric stamping, Inter J Mech Sci, 43 (**2001**), 1893–1914

[15] Xue P., Yu T. X., Chu E., An energy approach for predicting springback of metal sheets after double-curvature forming Part II: Unequal double-curvature forming, Inter J Mech Sci, 43 (**2001**), 1915–1924

[16] Lee G. M., Kim D., Kim C., Wenner L. M., Wagoner H. R., Chung, K., Spring-back evaluation of automotive sheets based on isotropic-kinematic hardening laws and non-quadratic anisotropic yield functions Part II: characterization of material properties, Inter J Plasticity, 21 (**2005**), 883–914

[17] Lee G. M., Kim D., Kim C., Wenner L. M., Chung, K., Spring-back evaluation of automotive sheets based on isotropic–kinematic hardening laws and non-quadratic anisotropic yield functions, Part III: applications, Inter J Plasticity, 21 (**2005**) 915–953

[18] Fei, D., Hodgson, P., Experimental and numerical studies of springback in air V-bending process for cold rolled TRIP steels, Nuclear Eng Design, 236 (**2006**), 1847–1851

[19] Meinders T., Burchitz I. A., Bonte M. H. A, Lingbeek R. A. Numerical product design: Springback prediction, compensation and optimization, Inter J Machine Tools Manufacture, 48 (**2008**), 499–514

[20] Borah U., Venugopal S., Nagarajan R., Sivaprasad P. V., Venugopal S., Raj B., Estimation of springback in double-curvature forming of plates: Experimental evaluation and process modeling, Inter J Mech Sci., 50 (**2008**), 704–718

[21] Morestin, F., Boivin, M., Silva, C., Elasto plastic formulation using a kinematic hardening model for springback analysis in sheet metal forming. J. Mater. Proc. Tech, 56 (**1996**), 619–630

[22] Laurent H., Grežze R., Manach P. Y., Thuillier S., Influence of constitutive model in springback prediction using the split-ring test, Inter J Mech Sci, 51 (**2009**), 233–245

[23] Lee G. M., Kim D., Kim C., Wenner L. M., Wagoner H. R., Chung K., Spring-back evaluation of automotive sheets based on isotropic-kinematik hardening laws and non-quadratic anisotropic yield functions PartII: characterization of material properties, J. Plasticity, 21 (**2005**), 883–914

[24] Devin L. J., Streppl A. H., A process model for air bending. J Mater Process Tech, 57 (**1996**), 48–54

[25] Shima S., Yang M., A study of accuracy in an intelligent V-bending process for sheet metals. Material, 44 (**1995**), 578–583

[26] Xu W. L., Ma C. H., Li C. H., Feng W. J., Sensitive factors in springback simulation for sheet metal forming, J Mater Process Tech 151 (**2004**), 217–222

[27] Barlat F., Lian J., Plastic behavior and stretchability of sheet metals. Part I. A yield function for orthotropic sheets under plane stress conditions. Inter J Plast., 5 (**1989**), 51–66

[28] Ls-dyna keyword user's manual version 971 Livermore Software Technology Corporation (LSTC), (**2007**), 1556–1562

[29] Gan W., Babu S. S., Kapustka N., Wagoner R. H., Microstructural effects on the springback of advanced high-strength steel, Metall. Mater. Trans. A, 37 (**2006**), 3221–3231

[30] Ledbetter H. M., Kim S. A., Low temperature elastic constants of deformed polycrystalline copper, Mater Sci Eng, 101 (**1988**), 87–92

[31] Cleveland R. M., Ghosh A. K., Inelastic effects on springback in metals, Inter J Plasticity, 18 (**2002**), 769–785

[32] Li X. C., Yang Y. Y., Wang Y. Z., et al., Effect of the material hardening mode on the springback simulation accuracy of V-free bending, J Mater Process Tech, 123 (**2002**), 209–211

[33] Zang S.-L., Guo C., Wei G-J., et al., A new model to describe effect of plastic deformation on elastic modulus of aluminum alloy, Trans. Nonferrous Met Soc China, 16 (**2006**), 1314–1318

UDK 669.14.018.298:621.785:620.17
Professional article/Strokovni članek

ISSN 1580-2949
MTAEC9, 45(6)619(2011)

HEAT TREATMENT AND MECHANICAL PROPERTIES OF HEAVY FORGINGS FROM A694–F60 STEEL

TOPLOTNA OBDELAVA IN MEHANSKE LASTNOSTI TEŽKIH IZKOVKOV IZ JEKLA A694-F60

Martin Balcar[1], Jaroslav Novák[1], Libor Sochor[1], Pavel Fila[1], Ludvík Martínek[1], Jiří Bažan[2], Ladislav Socha[2], Danijela Anica Skobir Balantič[3], Matjaž Godec[3]

[1]ŽĎAS, a. s., Strojírenská 6, 591 71 Žďár nad Sázavou, Czech Republic
[2]VŠB TU Ostrava – FMMI, 17. listopadu 15/2172, 708 33 Ostrava-Poruba, Czech Republic
[3]Institute of Metals and Technology, Lepi pot 11, 1000 Ljubljana, Slovenia
martin.balcar@zdas.cz

Prejem rokopisa – received: 2011-05-31; sprejem za objavo – accepted for publication: 2011-09-21

The production of heavy steel forgings of micro-alloyed steels gives the possibility to obtain advantages associated with the benefit of the application of micro-alloying elements and thermomechanical treatments for improving the mechanical properties of forgings to level by sheets, strips and tubes. The paper presents the influence of quenching temperature on the mechanical properties and microstructure of F60 steel according to ASTM A694. The verification of the influence of quenching temperature contributes to an optimization of the method of micro-alloyed steel heat treatment. The steel's microstructure and mechanical properties after quenching constitute the initial and basic criteria to achieve the required mechanical properties after a properly chosen tempering temperature.

Keywords: HSLA steel, A694 F605, quenching and tempering

Proizvodnja težkih izkovkov iz mikrolegiranih jekel omogoča, da se uporabijo prednosti mikrolegiranja in termomehanske obdelave za doseganje mehanskih lastnosti pri trakovih, ploščah in ceveh. V članku je predstavljen vpliv temperature kaljenja na mehanske lastnosti in mikrostrukturo. Preveritev vpliva temperature kaljenja je del procesa opredelitve in optimizacije metode toplotne obdelave mikrolegiranega jekla. Mikrostruktura in mehanske lastnosti po toplotni obdelavi so osnovni pogoj za doseganje predpisanih lastnosti.

Ključne besede: HSLA-jeklo, A694 F605, kaljenje in popuščanje

1 INTRODUCTION

As the requirements for the properties of structural steel are increasing, the development of the use of micro-alloying elements, even in the field of the production of forgings and castings, takes place. The production of heavy steel forgings of micro-alloyed steels does not allow the use of the advantages associated with the benefit of the application of micro-alloying elements and thermomechanical treatment known from the production of sheets, strips and tubes. The production of steel forgings involves forming and heat-treatment processes, which are significantly different than those for thin-walled products (sheets, strips, tubes).

The development and verification of F60 steel production and treatment technology according to ASTM A694 in ZDAS, Inc. conditions constituted a number of technological changes and the introduction of new process elements in the field of steel making and thermomechanical treatment. The verification of the influence of the quenching temperature on the properties and the microstructure of F60 forged steel contributes to the optimization of the HSLA steel-making technology at ZDAS, Inc.

2 EXPERIMENTAL MATERIAL

The verification of the influence of quenching temperature on the microstructure and mechanical properties of modified F60 steel according to ASTM A694 made by EOP/LF/VD technology was carried out on forged samples with dimensions 100 mm × 100 mm × 150 mm. The basic chemical composition of the steel is shown in **Table 1**.

The F60 steel modified according to ASTM A694 is a typical low-carbon steel with the addition of the alloying elements, manganese, nickel and molybdenum. Moreover, the steel is micro-alloyed with vanadium, aluminium and niobium. The content of other elements is at the level of residuals.

Table 1: Basic chemical composition of HSLA steel F60 in mass fraction, w/%
Tabela 1: Osnovna kemična sestava HSLA jekla F60 v masnih deležih, w/%

C	Mn	Si	P	S	Cr	Ni	Mo	V	Al	Nb	N
0.10	1.08	0.33	0.003	0.001	0.16	0.77	0.27	0.04	0.027	0.034	0.0037

After the forming process, the forgings were "anti-flake" annealed at a temperature of 650 °C for a period of 10 h and then normalized at a temperature of 930 °C with air cooling.

3 LABORATORY HEAT TREATMENT

The heat treatment was carried out on forged steel samples in the laboratory. The verification of the influence of the austenitization–quenching temperature (T_A) on the microstructure and mechanical properties was performed for the temperature range of 880 °C to 940 °C with water quenching, tempering T_P = 620 °C and air cooling. The sample markings and heat treatment were carried out as follows:

Sample L1: T_A = 880 °C/6 h/water + T_P = 620 °C/8 h/air
Sample L2: T_A = 890 °C/6 h/water + T_P = 620 °C/8 h/air
Sample L3: T_A = 900 °C/6 h/water + T_P = 620 °C/8 h/air
Sample L4: T_A = 910 °C/6 h/water + T_P = 620 °C/8 h/air
Sample L5: T_A = 920 °C/6 h/water + T_P = 620 °C/8 h/air
Sample L6: T_A = 930 °C/6 h/water + T_P = 620 °C/8 h/air
Sample L7: T_A = 940 °C/6 h/water + T_P = 620 °C/8 h/air

Figure 1: Forging specimen - 100 mm × 100 mm × 150 mm
Slika 1: Odkovek, 100 mm × 100 mm ×150 mm

4 MECHANICAL PROPERTIES OF F60 HSLA STEEL

The samples for determining the achieved mechanical properties and to evaluate the microstructure were taken from the central zone of the forgings in the longitudinal direction. In table 2 the requested level and attained values of the mechanical properties of individual F60 steel samples are shown.

The influence of the austenitization temperature on the change in the mechanical properties of forged, quenched and tempered F60 steel is visible from **Table 2**. It is obvious that the steel's strength increases and a significant toughness drop occurs with an increase of the austenitization temperature. An austenitization temperature of over 910 °C causes the steel to become brittle.

5 MICROSTRUCTURE OF SAMPLES OF HSLA STEEL ASTM A694 F60

Like in the case of the mechanical properties, the steel microstructure was evaluated in the control zone of samples.

The steel microstructure for the heat-treatment states (T_A = (880, 900, 920, 940) °C) is shown in **Figure 2 to 5**:

After quenching and tempering, the microstructures of all the sample forgings are practically the same and it consists of ferrite, bainite, granular pearlite and sorbite. It is evident from the micrographs where the secondary grain size can be compared more easily, that the secondary grain size does not change noticeably with an increase of the quenching temperature. This is confirmed

Table 3: Austenitic grain size - HSLA steel F60 -ASTM E 112 – LECO IA32
Tabela 3: HSLA-jeklo F 60 - ASTM E 112 - LECO IA32

	T_A/°C	Grain size /µm
L1	880	11.3 ± 0.4
L2	890	11.2 ± 0.4
L3	900	10.7 ± 0.3
L4	910	11.3 ± 0.5
L5	920	11.4 ± 0.2
L6	930	9.4 ± 0.6
L7	940	10.3 ± 0.4

Table 2: Mechanical properties HSLA steel F60 after different austenization temperatures
Tabela 2: Mehanske lastnosti HSLA-jekla F 60 po avstenitizacij pri različnih temperaturah

	T_A/°C	R_e/MPa	R_m/MPa	A5/%	Z/%	KV$_{-46\ °C}$/J			AVG KV$_{-46\ °C}$/J
		415–565	520–760	min. 20	min. 35	ø KV min. 63			ø KV min. 63
L1	880	548	639	21.6	76.0	299	300	217	272
L2	890	550	653	22.2	75.0	255	229	286	257
L3	900	561	653	21.8	75.0	213	217	218	216
L4	910	573	667	22.2	75.0	101	214	89	135
L5	920	576	662	23.0	76.0	189	137	27	118
L6	930	576	672	22.8	74.0	124	204	238	189
L7	940	576	671	22.4	75.0	86	153	31	90

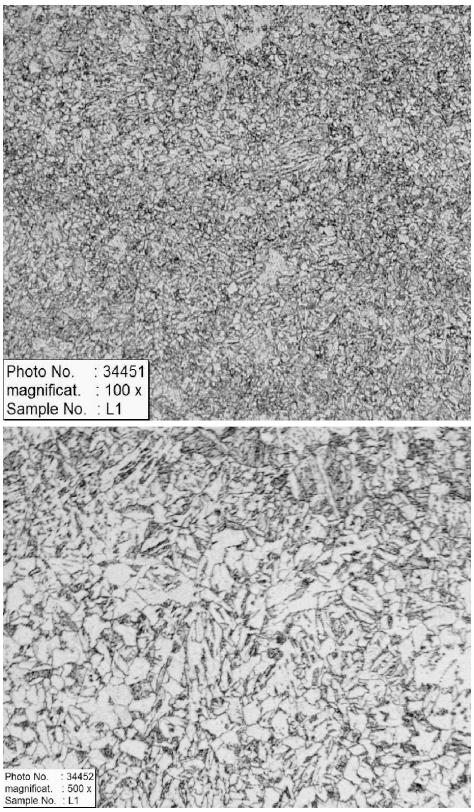

Figure 2: Sample L1: T_A = 880 °C/6 h/water + T_P = 620 °C/8 h/air
Slika 2: Vzorec L1: T_A = 880 °C/ 6 h/ voda + T_p = 620 °C/ 8 h/zrak

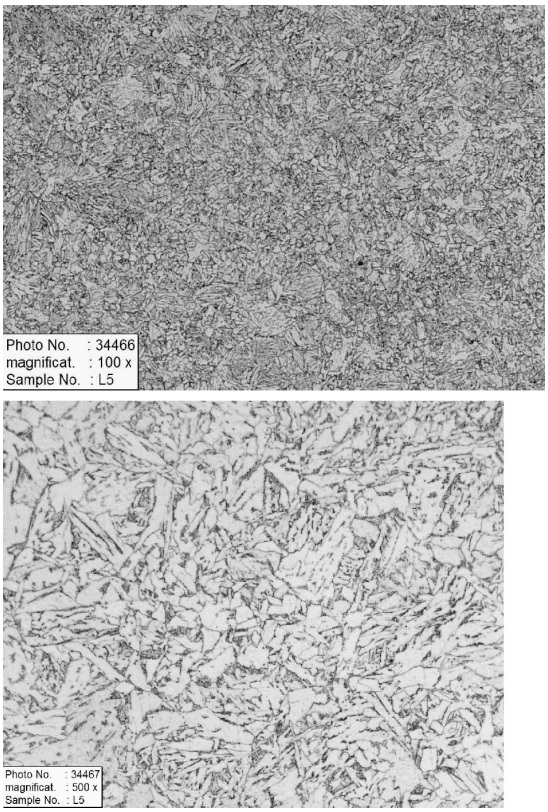

Figure 4: Sample L5: T_A = 920 °C/6 h/water + T_P = 620 °C/8 h/air
Slika 4: Vzorec L5: T_A = 920 °C/ 6 h/ voda + T_p = 620 °C/ 8 h/zrak

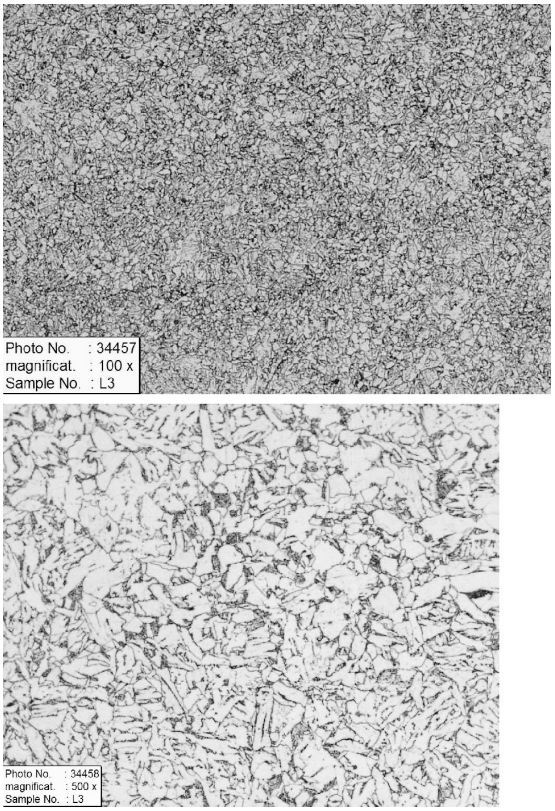

Figure 3: Sample L3: T_A = 900 °C/6 h/water + T_P = 620 °C/8 h/air
Slika 3: Vzorec L3: T_A = 900 °C/ 6 h/ voda + T_p = 620 °C/8 h/zrak

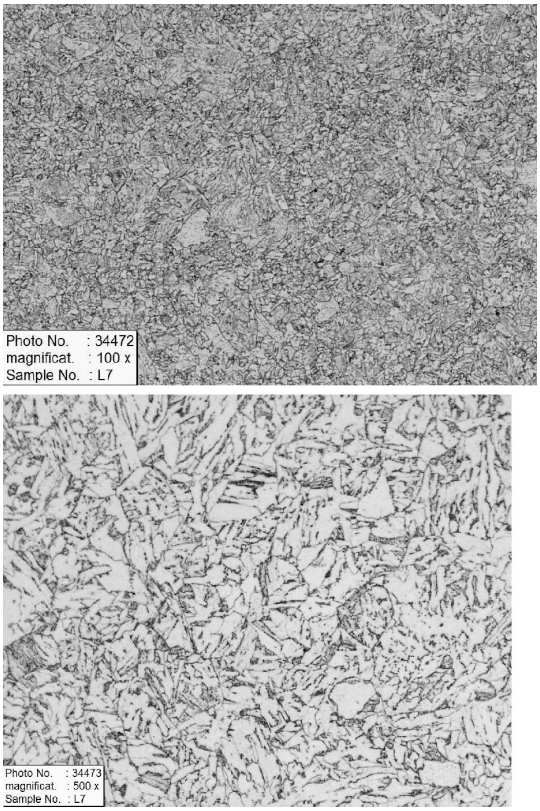

Figure 5: Sample L7: T_A = 940 °C/6 h/water + T_P = 620 °C/8 h/air
Slika 5: Vzorec L7: T_A = 940 °C/ 6 h/ voda + T_p = 620 °C/8 h/zrak

by the results of the assessment of the austenite grain size by the oxidation method according to ASTM E 112 – 97 using LECO IA32 image analysis. The results of the austenitic grain-size assessment are shown in **Table 3**.

From the results in **Table 3** it is not possible to establish the direct influence of quenching temperature on the austenite grain-size change as all the samples show a very fine grain size.

6 CONCLUSIONS

From the results of the experimental work we can see the direct influence of the quenching temperature on the mechanical properties of the F60 steel.

A slight increase of strength and a strong drop in impact value was found for an increase of the quenching temperature. The most favourable results of the mechanical properties were attained with the quenching temperatures 880 °C, 890 °C and 900 °C.

The steel microstructure after quenching and tempering is similar for all samples and consists of ferrite, bainite, granular pearlite and sorbite. The assessment of the austenite grain size by the oxidation method confirmed the grain-size uniformity, when comparing experimental samples, without any provable influence of the quenching to a temperature of 920 °C.

A further optimization of the steel's mechanization properties and microstructure is expected after a verification of the influence of the tempering temperature. Subsequently, it will be possible to determine a complex optimized heat-treatment process for the HSLA steel ASTM A694 F60.

In this paper the results obtained in the EUREKA programme of the E!4092 MICROST project are presented. The project was realized with the financial support of the Ministry of Education, Youth and Sport of the Czech Republic.

UDK 669.715:621.791
Professional article/Strokovni članek

ISSN 1580-2949
MTAEC9, 45(6)623(2011)

THE TENSILE BEHAVIOUR OF FRICTION-STIR-WELDED DISSIMILAR ALUMINIUM ALLOYS

NATEZNE ZNAČILNOSTI TORNIH POMIČNIH ZVAROV RAZLIČNIH ALUMINIJEVIH ZLITIN

R. Palanivel[1], P. Koshy Mathews[2]

[1]Faculty in Mechanical Engineering, Kalaivani College of Technology, Coimbatore, India
[2]Dean, Research and Development, Kalaivani College of Technology, Coimbatore, India
rpelmech@yahoo.co.in

Prejem rokopisa – received: 2011-04-01; sprejem za objavo – accepted for publication: 2011-07-27

Aluminium alloys generally have a low weldability with the traditional fusion-welding process. However, the development of Friction Stir Welding (FSW) has provided an alternative, improved way of producing aluminium joints, in a faster and more reliable manner. The FSW process has several advantages, in particular the possibility to weld dissimilar aluminium alloys. This study focuses on the tensile behaviour of dissimilar joints of AA6351-T6 alloy to AA5083-H111 alloy produced by friction stir welding. Five different tool pin profiles, such as Straight Square (SS), Tapered Square (TS), Straight Hexagon (SH), Straight Octagon (SO) and Tapered Octagon (TO), with three different welding speeds (50 mm/min, 63 mm/min, 75 mm/min) have been used to weld the joints. The effect of the pin profiles and the welding speed on the tensile properties was analyzed and it was found that the straight square pin profile with 63 mm/min produced a better tensile strength then the other tool pin profiles and welding speeds.

Key words: friction stir welding, aluminium alloys, tool pin profile, welding speed, tensile properties

Aluminijeve zlitine so slabo varive po tradicionalnih talilnih postopkih. Razvoj tornega pomičnega varjenja (FSW) je ponudil možnost priprave aluminijevih zvarov na hiter in zanesljiv način. Proces ima več prednosti, predvsem možnost varjenja različnih aluminijevih zlitin. Raziskava je bila osredinjena na natezno vedenje različnih zvarov zlitin AA6351-T6 in AA5083-H111, pripravljenih s tornim pomičnim varjenjem. Pet različnih profilov trna je bilo uporabljenih: raven kvadrat (SS), koničen kvadrat (TS), raven šestkokotnik (SH), raven osemkotnik (SO) in koničen osemkotnik (TO) s tremi različnimi hitrostmi varjenja (50 mm/min, 63 mm/min in 75 mm/min). Določen je bil vpliv oblike trna in hitrosti varjenja na natezne lastnosti. Ugotovljeno je, da raven kvadraten trn pri hitrosti 63 mm/min da boljšo trdnost kot drugi profili trna in druge hitrosti varjenja.

Ključne besede: pomično torno varjenje, aluminijeve zlitine, profil tornega trna, hitrost varjenja, natezne lastnosti

1 INTRODUCTION

Friction stir welding (FSW) is a solid-state welding process developed by The Welding Institute (UK) in 1991, and now being used increasingly for joining aluminium alloys, for which fusion welding is often difficult. FSW uses a rotating tool with a probe travelling along the weld path, and plastically deforms the surrounding material to form the weld. Since the material subjected to FSW does not melt and recast, the resultant weld offers advantages over conventional fusion welds, such as less distortion, lower residual stresses and fewer weld defects.[1–3] When developing such a technology, one of the most important factors is the possibility to join different aluminium alloys. [4] The development of sound joints between dissimilar materials is a very important consideration for many emerging applications, including ship building, aerospace, transportation, power generation, as well as the chemical, nuclear, and electronics industries [5]. However, the joining of dissimilar materials by conventional fusion welding is difficult because of the poor weldability arising from the different chemical, mechanical, and thermal properties of welded materials and the formation of hard and brittle intermetallic compounds (IMCs) on a large scale at the weld interface. The absence of melting in friction stir welding (FSW) provides a strong tendency to produce reliable dissimilar joints. Amancio-Filho et al.[6] determined the tensile strength of dissimilar friction stir welded AA2024-T351 and AA6056-T4 as 56 % of the AA2024-T351 and 90 % of the AA6056-T4. It is reported that the poor tensile strength observed in these joints is due to the thermal softening of the base metals, and the poor ductility observed in these joints is due to the stress concentration caused by the large difference in strength between the base metals leading to confined plasticity and failure. Cavaliere et al.[Š4Ć] investigated the tensile behaviour of dissimilar friction stir welded joints of the aluminium alloys 2024-T3 and 7075-T6 and reported that both the ultimate strength and the elongation of the dissimilar joints are lower than the base metals 2024-T3 and 7075-T6. From the above literature review we can conclude that very little research work has been carried out on the dissimilar FS welding of aluminium alloys and that the dissimilar friction stir welding of AA6351 and AA5083, which are widely used in aerospace, ship building, and other fabrication industries,[7] were not investigated. Hence, the present research work focuses

Table 1: Chemical composition of AA6351-T6
Tabela 1: Kemična sestava zlitine AA6351-T6

Name of the Element	Si	Zn	Mg	Mn	Fe	Cu	Ti	Sn	Ni	Al
Masss fractions, *w*/% (AA6351)	0.907	0.89	0.586	0.65	0.355	0.086	0.015	0.003	0.002	Balance

Table 2: Chemical composition of AA5083-H111
Tabela 2: Kemična sestava zlitine AA5083-H111

Element	Si	Zn	Mg	Mn	Fe	Cu	Ti	Al
Mass fracions, *w*/% (AA5083-H111)	0.045	0.04	4.76	0.56	0.14	0.02	0.054	Balance

on the tensile behaviour of dissimilar friction stir welded joints of the aluminium alloys AA6351 and AA5083.

2 EXPERIMENTAL PROCEDURE

2.1 Manufacturing of FSW tools

Five different tools made of High Carbon High Chromium steel (HCHCr) having different pin profiles of Straight Square (SS), Tapered Square (TS), Straight Hexagon (SH), Straight Octagon (SO) and Tapered Octagon (TO) without draft were used to weld the FSW joints. Each tool had a shoulder of diameter 18 mm, a pin diameter of 6 mm and a pin length of 5.6 mm. The shoulder–workpiece interference surface had 3 concentric circular equally spaced slots of 2 mm depth on all the tools. The FSW tools were manufactured using a CNC turning center and a wire cut EDM (WEDM) machine to get an accurate profile. The tools were oil hardened. The manufactured tools are shown in **Figure 1**.

2.2 Frictions stir welding of dissimilar aluminium alloys

The aluminium alloys AA6351-T6 and AA5083-H111 were selected for the dissimilar friction stir welding process. The chemical compositions of the materials AA6351-T6 and AA5083-H111 are presented in **Tables 1 and 2** and the mechanical properties of the materials are presented in **Table 3**. Test plates of size 100 mm × 50 mm × 6 mm were prepared from rolled sheets.

The experimental set up consists of a special-purpose machine shown in **Figure 2** with arrangements designed for the friction stir welding. The plate AA 6351-T6 was fixed with the advancing side and the AA5083 H-111 was fixed with the retreating side of the machine. The vertical tool head can be moved along the vertical guide ways (*Z*-axis). The horizontal table can be moved along the *X*- and *Y*-axes and consists of mechanical fixtures to hold the workpieces rigidly. The machine can be operated over a wide range of tool rotational speeds, welding speeds and tool axial forces. Five different tool-pin profiles were used to produce the joints. Using each tool, three joints at three different welding speed levels and in

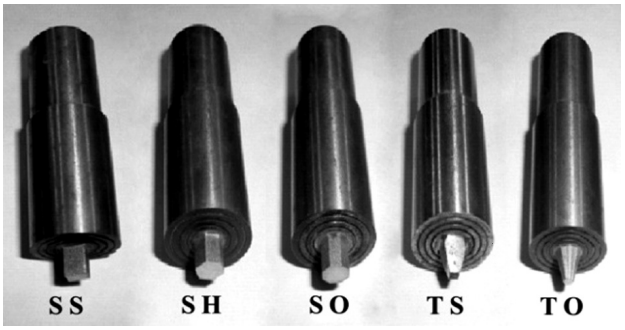

Figure 1: Manufactured tool for FSW (Straight Square (SS), Straight Hexagon (SH), Straight Octagon (SO), Tapered Square (TS), and Tapered Octagon (TO)
Slika 1: Trni za pomično torno varjenje: raven kvadrat (SS), koničen kvadrat (TS), raven šestokokotnik (SH), raven osmokotnik (SO) in koničen osmokotnik (TO)

Figure 2: Experimental setup
Slika 2: Eksperimentalna naprava

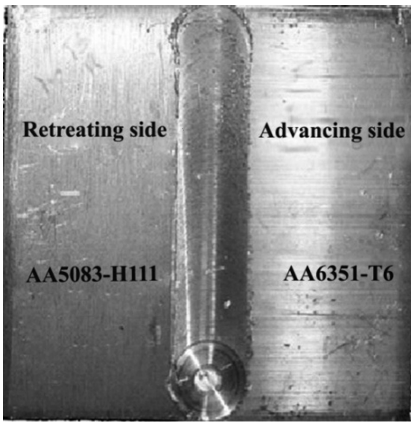

Figure 3: FS Welded sample (950 r/min, 1 t, 63 mm/min straight square pin profile)
Slika 3: Zvarjeni vzorec (950 r/min, 1 t, 63 mm/min, raven kvadraten profil)

Table 3: Mechanical properties of the AA6351 and AA5083-H111
Tabela 3: Mehanske lastnosti zlitin AA6351-T6 in AA5083-H111

Base Material	Tensile Strength (MPa)	Yield Strength (MPa)	Percentage of elongation
AA6351	310	285	14
AA5083-H111	308	273	23

Table 4: Welding process parameters
Tabela 4: Parametri procesa varjenja

Process parameter	Values
Tool rotational speed, r/min	950
Welding speed, mm/min	50,63,75
Axial force, t	1

total 15 joints (5 × 3) were produced in this study. The welding parameters are presented in **Table 4**. The joints were visually inspected for exterior weld defects and they were found to be free from any external defects. A sample of a friction stir welded plate is shown in **Figure 3**. The tensile test specimens were prepared according to

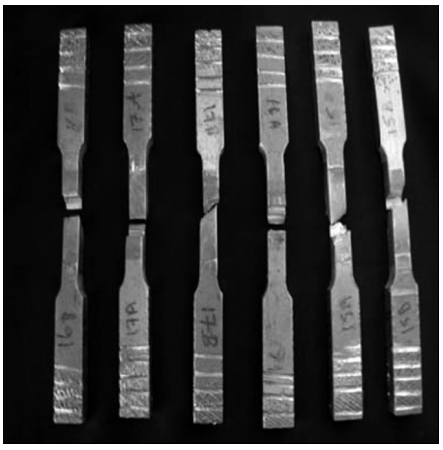

Figure 4: Tested specimen for tensile strength
Slika 4: Pretrgani natezni preizkušanci

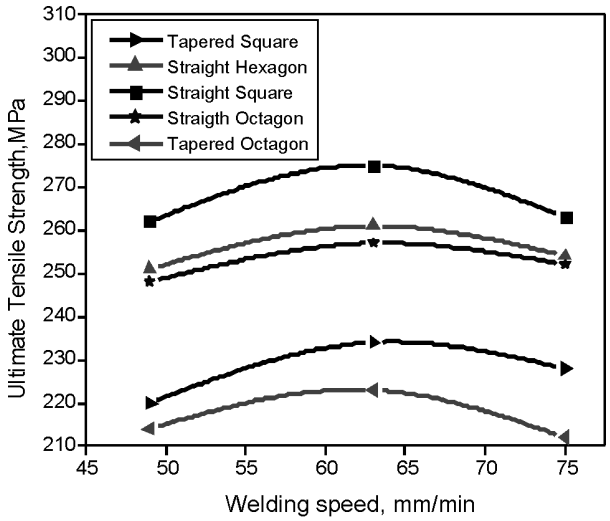

Figure 5: Effect of welding speed and pin profile
Slika 5: Vpliv hitrosti varjenja in profila trna

the ASTM E8 standard and the transverse tensile properties of the FS welded joints were evaluated using a computerized (Universal Testing Machine) UTM. For each welded plate, three specimens were prepared and tested. The fracture occurred either on the retreating side or the advancing side of the weld. **Figure 4** shows the fractured tensile specimen.

3 RESULTS

The effects of welding speed for various tool pin profiles are shown in **Figure 5**. At the lowest (50 mm/min) and the highest welding speeds (75 mm/min) a lower tensile strength was observed. This trend was common in all the joints, irrespective of the tool pin profile. The joint produced by the straight square pin profiled tool exhibits a high tensile strength when compared to the other joints. The joint produced by the tapered octagon pin profiled tool had the lowest tensile strength. The tensile strength of the joints welded using the straight hexagon and the straight octagon pin profiled tools did not differ significantly.

4 DISCUSSION

The increase in welding speed leads to an increase in the tensile strength up to a maximum value, while a further increase in the welding speed results in a decrease of the tensile strength of the FS welded joints. This is due to the increased frictional heat and insufficient frictional heat generated, respectively. [8] In general, FSW at higher welding speeds results in a short exposure time in the weld area with insufficient heat and a poor plastic flow of the metal and causes some void-like defects in the joints. The reduced plasticity and rates of diffusion in the material may have resulted in a weak interface. Higher welding speeds are associated with low

heat inputs, which result in faster cooling rates of the welded joint. This can significantly reduce the extent of the metallurgical transformations taking place during welding and the local strength of the individual regions across the weld zone. [9] The pin profile plays a crucial role in the material flow and in turn regulates the welding speed of the FSW process. The relationship between the static volume and the dynamic volume decides the path for the flow of plasticized material from the leading edge to the trailing edge of the rotating tool [10]. This ratio is equal to 1.56 for the straight square, 1.21 for the straight hexagon, 1.11 for the straight octagon, 2.04 for the tapered octagon and 3.51 for the tapered square pin profiles. In addition, these pin profiles produce a pulsating stirring action in the flowing material due to the flat faces. The square pin profile produces 63 pulses per second, the hexagon pin profile produces 95 pulses per second and the octagon pin profile produces 126 pulses per second, when the tool rotates at a speed of 950 r/min. There is not much pulsating action in the case of the octagonal and hexagonal pin profiled tool because it almost resembles a straight cylindrical pin profiled tool at this high rpm. In the tapered pin profiled tools, the same principle affects the material flow. Since the tapered square and tapered octagon pin profile sweeps less material when compared to that of the straight square pin tool, this joint exhibit less tensile properties.

5 CONCLUSION

Among the fifteen joints produced in this investigation, the joints produced using the straight square pin profiled tool at a welding speed of 63 mm/min showed the best tensile properties.

6 REFERENCES

[1] R. S. Mishraa, Z. Y. Ma, Frictions stir welding and processing. Materials Science and Engineering R, Reports, 50 (**2005**) 1–2, 1–78

[2] R. Nandan, T. DebRoy, H. K. D. H. Bhadeshia, Recent advances in friction-stir welding process, weldment structure and properties. Progress in Material Science, 53 (**2008**) 6, 980–1023

[3] Y. Uematsu , K. Tokaji, H. Shibata, Y. Tozaki, T. Ohmune, Fatigue behavior of friction stir welds without neither welding flash nor flaw in several aluminium alloys. International Journal of Fatigue, 31 (**2009**) 10, 1443–1453

[4] P. Cavaliere, E. Cerri, A. Squillace, Mechanical response of 2024-7075 aluminium alloys joined by friction stir welding. Journal of Material Science, 40 (**2005**) 14, 3669–76

[5] T. Saeid, A. Abdollah-zadeh, B. Sazgari, Weldability and mechanical properties of dissimilar aluminum–copper lap joints made by friction stir welding. Journal of Alloys and Compounds, 490 (**2010**) 1–2, 652–655

[6] S. Tamancio-Filho, S. Sheikhi, J. F. Dos Santos, C. Balfarini. Preliminary study on the microstructure and mechanical properties of dissimilar friction stir welds in aircraft aluminium alloys 2024-T351 and 6056-T4. Journal of Material processing Technology, 206 (**2008**) 1–3, 32–42

[7] H. D. Chandler, J. V. Bee, Cyclic strain induced precipitation in a solution treated aluminum alloy. Acta Metallurgica, 35 (**1987**) 10, 2503–2510

[8] Kevin J. Colligan, Paul J. Konkol, James, J. Fisher, Joseph R. Pickens, Friction stir welding demonstrated for combat vehicle construction. Welding Journal, 82 (**2003**) 3, 1–6

[9] A. V. Strombeck, J. F. D. Santos, F. Torster, P. Laureano, M. Kocak. Fracture toughness behavior of FSW joints on aluminum alloys, Proceedings of the First International Symposium on Friction Stir Welding California, USA, 1999, Paper No. S9-P1

[10] K. Elangovan, V. Balasubramanian, S. Babu, Predicting tensile strength of friction stir welded 6061 aluminium alloy joints by mathematical model. Material and Design, 30 (**2009**) 1, 188–193

UDK 621.38:620.1/.2
Professional article/Strokovni članek

ISSN 1580-2949
MTAEC9, 45(6)627(2011)

SCREEN-PRINTED ELECTRICALLY CONDUCTIVE FUNCTIONALITIES IN PAPER SUBSTRATES

ELEKTROPREVODNE OBLIKE, PRIPRAVLJENE S SITOTISKOM NA PAPIRNIH PODLAGAH

Maša Žveglič[1], Nina Hauptman[1], Marijan Maček[2], Marta Klanjšek Gunde[1*]

[1]National Institute of Chemistry, Hajdrihova 19, Ljubljana, Slovenia
[2]University of Ljubljana, Faculty of Electrical Engineering, Tržaška 25, Ljubljana, Slovenia
marta.k.gunde@ki.si

Prejem rokopisa – received: 2011-05-11; sprejem za objavo – accepted for publication: 2011-07-08

The topological and electrical properties of screen-printed conductive lines, applying silver-based conductive ink are analyzed. The influence of the substrate, curing time and wet-to-wet overprinting is analyzed. The mechanical profilometer, optical microscope and SEM images did not give the same information about the topography of the prints. Areas without functional particles on the line boundaries could be seen on the SEM micrographs, whereas the profilometer and optical microscope could not support such information, and thus provide wider lines. Careful analysis confirms that the printing parameters influence the electrical resistivity of the printed products. Overprinting does not influence a great deal on the shape of lines; however, these lines have a smaller resistivity. The larger resistivity of the prints was obtained on a rough and porous substrate and was smaller on the smooth one. The influence of curing time was also shown.

Keywords: printed electronics, screen printing, conductive ink, electrical resistivity

Analizirali smo topološke in električne lastnosti linij, ki so bile natisnjene s sitotiskom prevodne tiskarske barve s srebrovimi delci. Ugotavljali smo vpliv tiskovne podlage, časa termičnega sušenja in večkratnega tiska mokro-na-mokro. Mehanski profilometer, optični in elektronski mikroskop ne dajejo nujno enakih podatkov o topografiji potiskanih oblik. Območja brez funkcionalnih delcev opazimo le na posnetkih elektronskega mikroskopa, optični mikroskop in profilometer pa taka območja ne ločita od funkcionalnih delov linij. Analiza je pokazala, da parametri tiska vplivajo na električne lastnosti izdelkov. Tisk mokro-na-mokro ima zanemarljiv vpliv na tiskane oblike, pač pa imajo taki odtisi manjšo električno upornost. Na hrapavi in porozni podlagi dobimo večje upornosti kot na gladki. Na upornost potiskanih linij vpliva tudi čas segrevanja pri sušenju odtisov.

Ključne besede: tiskana elektronika, sitotisk, prevodna tiskarska barva, električna prevodnost

1 INTRODUCTION

Printed electronics, i.e., fabricating an entire electronic device by printing, is expected to provide low-cost electronic systems on common surfaces such as paper, plastic and textiles. The simplified structures of electronic devices, printed by a minimal number of different printing inks, should provide the lowest possible target price, which was estimated to be below 0.2 € per piece [1].

All printed electronic devices require some printed conductor to replace the metal layers used in conventional electronics. Polymer inks containing electrically conductive particles are the most common choice for this purpose in the field of printed electronics. They consist of a suitable polymer resin with metal particles, which in most cases are silver, gold, copper, nickel, platinum or carbon [2–6]. These conductive inks have various resistivities; the lowest was obtained with silver particles. Specific physical properties, such as viscosity, suitable rheology characteristics and appropriate curing, are demanded for each printing technology to obtain feasible prints of acceptable quality [7–9].

Conductive inks are available on the market for conventional technologies, i.e., screen printing, offset, and pad-printing. In most cases the producers provide resistivity data for a layer with a specified thickness prepared by a recommended application (printing) method and drying conditions. However, the resistivity of a shape, printed by a particle-based conductive printing ink, depends on the internal microstructure of the printed lines. This structure could be influenced by several parameters that may affect the functional properties of the final application [5–7,9].

The objective of our research was to analyze the influence of the printing parameters on the resistivity of screen-printed lines using a silver-based conductive ink. Two flexible substrates were used, the gloss-coated paper and the clear matt film. The topology of screen-printed lines was examined with several techniques. The resistivity of the test structures was measured and the influence of printing parameters was analyzed thoroughly.

2 EXPERIMENTAL

Electrodag PM-470 conductive screen-printable ink (Acheson Colloiden B.V., Netherlands) was used. It contains finely distributed silver particles in a thermoplastic resin. Its density is about 2140 kg/m^3 and the solid content 58–62 %. The manufacturer specifies the Broofield

viscosity of the ink to be 11 000–140 000 mPa s (30 °C, 20 r/min) and the sheet resistance of a 25-µm-thick layer at a sheet resistance of 0.008–0.015 Ω/□. This corresponds to a specific resistivity of 2.0–3.75 · 10^{-5} Ω cm.

The print form contained suitable structures for resistivity measurements and several horizontal and vertical lines (in series of four equally separated strips) with a width from 5 mm to 0.5 mm. The shape of narrowest lines (500 µm width on print form) was evaluated in detail.

The ink was screen printed by applying the SEFAR® high-modulus monofilament polyester plain weave mesh 43/80Y and a squeegee with a hardness of 75 °Sh. Two substrates were used, i.e., clear matt film (thermally and antistatically treated for transfer printing) and gloss-coated paper. Single and double layer prints (wet-on-wet) were made. The off-prints were cured at 120 °C for 4, 9 and 13 min. In all cases, dry prints were obtained.

The thickness and profile of the lines were measured with a Talysurf profilometer (Rank Taylor Hobson Series 2). The microtexture and profile of the narrow lines were monitored with a scanning electron microscope SEM – 6060 LV (JEOL, Japan). The shape of the edges, the degree of wicking and the width of narrowest line were also evaluated using a Nanometrics optical microscope (Olympus).

The electrical resistivity of the samples was measured by applying a four-terminal measurement method [5,6]. A constant DC-current source was used to force a current of ~1 µA through the outer contacts of the structure. The voltage drop was measured with an electronic voltmeter (FLUKE 289) on the inner contacts. In this way the contact resistance was completely eliminated and the results represent the pure resistance of the layer between the inner contacts. The specific electrical resistivity ρ of the printed layer with a thickness d was calculated using the measured voltage drop V_x and known current I according to the equation:

$$\rho = \frac{V_x}{I} \cdot \frac{W}{L} \cdot d \qquad (1)$$

where W and L denote the width and the length of the measured strip between the inner contacts.

The adhesion of printed layers on both substrates was evaluated using the standard cross-cut test, applying the Byko-cut universal inspection guage (Byk-Gardner Instruments, Germany). This method evaluates the coating resistance to separation from the substrate when a right-angle lattice pattern is cut up to the substrate. The micrographs of the prepared samples are then rated into classes with values 0–5, according to ISO 2409:1997.

3 RESULTS AND DISCUSSION

3.1 Print quality

The surfaces of all the printed lines clearly show silver flakes, which are not completely covered by the binder (**Figure 1**). This is the consequence of the very high solids content in the wet paint.

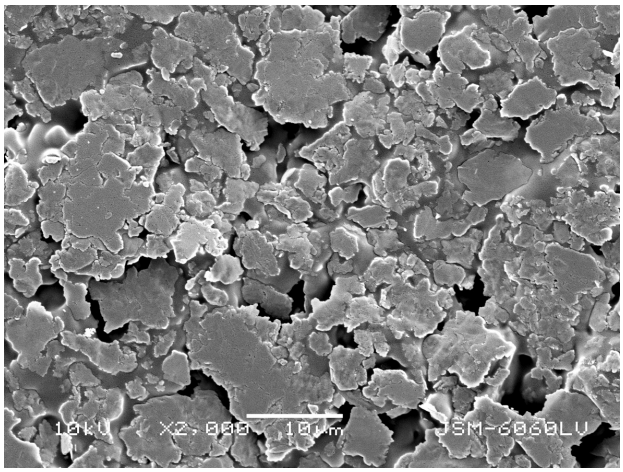

Figure 1: SEM micrograph of a typical front surface of printed conductive line. The silver flakes are not fully covered by the binder

Slika 1: SEM-posnetek površine tiskane prevodne linije. Srebrne luske niso popolnoma zakrite z vezivom

The dried, printed conductive lines were analyzed using line-profile measurements and an SEM image analysis. They are well separated. Surface-profile measurements show the different surface roughnesses of the two applied paper substrates and the similar roughnesses of the lines printed on them (**Figure 2**). Such results were obtained on all the prepared samples. These profiles were applied to determine the average thickness of the dry printed layers. In general, thinner layers were measured on the gloss-coated paper and thicker on the clear matt film. The wet-to-wet over-

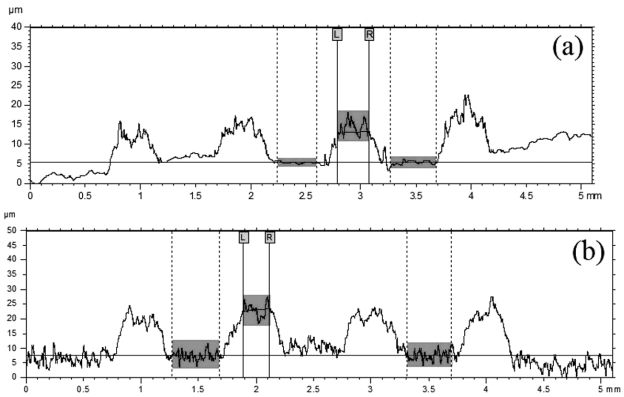

Figure 2: Surface profile of four parallel lines printed on gloss-coated paper (a) and clear matt film (b) as obtained by the profilometer. The lines are single-layer prints that were cured for 9 min. The average thickness is 9.1 µm and 15.5 µm, respectively. It was determined as the distance between the average lines of the substrate and top of the printed lines, determined on the marked regions.

Slika 2: Površinski profil štirih vzporednih črt, ki so bile natisnjene na sijajnem premazanem papirju (a) in na hrapavi foliji (b). Meritve so bile narejene na profilometeru. Črte so bile natisnjene z enkratnim prehodom in sušene 9 min. Povprečna debelina prikazanih linij je 9.1 µm (a) in 15.5 µm (b). Določena je kot razdalja med podlago in vrhom tiskanih linij; položaj vsake od teh je določen kot povprečna lega obarvanih področjih.

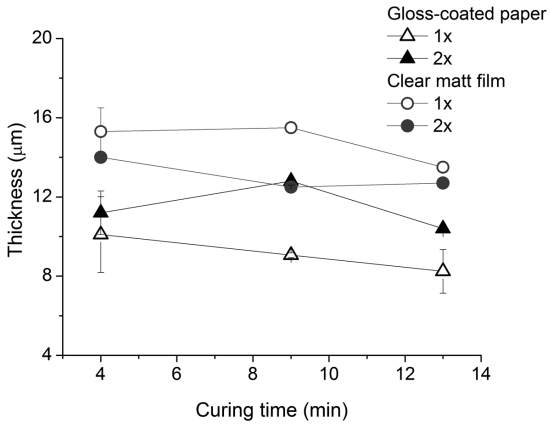

Figure 3: The thickness of strips single- (open signs) and double (solid signs) wet-to-wet overprinted on gloss coated paper (triangles) and clear matt film (circles) as a function of the curing time

Slika 3: Debelina črt natisnjenih z enkratnim (prazni znaki) in dvakratnim prehodom raklja (polni znaki) na sijajnem premazanem papirju (trikotniki) in na hrapavi foliji (krogi) v odvisnosti od časa sušenja

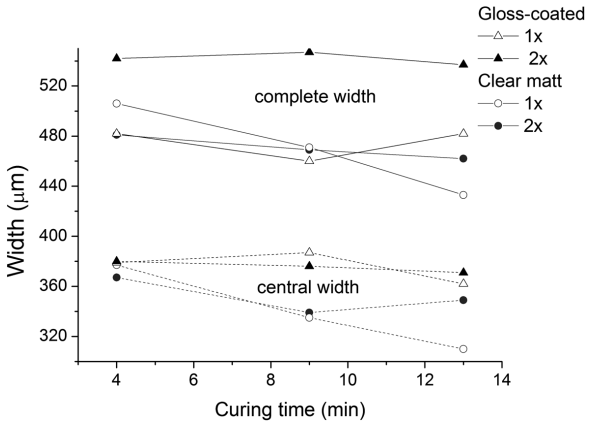

Figure 5: The fully functional width (central part of strips, broken lines) and the corresponding complete width (wicking area taking into account, full line) of strips printed by single- (open signs) and double (solid signs) wet-to-wet overprinting on gloss coated paper (triangles) and clear matt film (circles) as a function of the curing time.

Slika 5: Širina električno funkcionalnega dela črt (osrednji del, črtkane črte) in celotna širina (z upoštevanjem nagubanih robov, polne črte) v odvisnosti od časa sušenja. Črte so bile natisnjene z enkratnim (prazni znaki) in dvakratnim prehodom raklja (polni znaki) na sijajnem premazanem papirju (trikotniki) in hrapavi foliji (krogi).

printed layers are slightly thicker than the single-printed, but their thickness is much less than doubled. All the layers become thinner when longer curing was applied. The influence of curing time and overprinting is small (**Figure 3**).

The next important property is the width of the printed lines, which was evaluated with SEM and optical micrographs. The edges of the lines are not perfectly straight. A considerable amount of wicking was detected on the optical micrographs (**Figure 4a**). SEM micrographs show that such edges could lack conductive particles; some regions could also remain without any electrical functionality (**Figure 4b**). Therefore, the contribution of this region to the electrical conductivity is not the same as it is in the bulk of the printed shape.

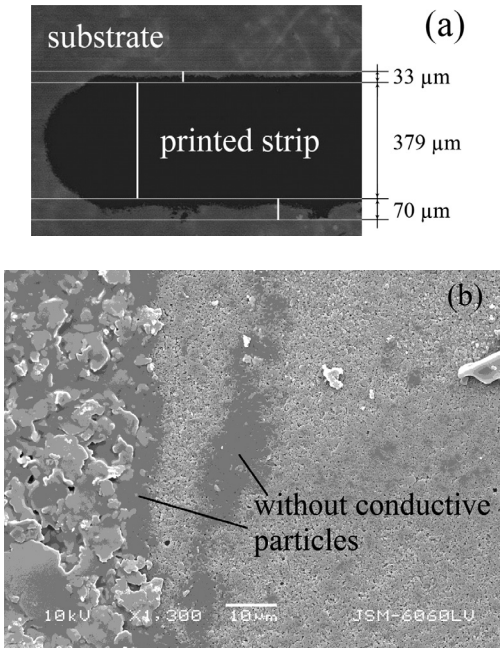

Figure 4: The edges of a printed line as observed by optical (a) and SEM micrographs (b). The width of the lines was evaluated from optical micrographs, taking into account the inner tangents. The printing squeegee was moved perpendicularly to the printed strip.

Slika 4: Robovi tiskanih črt, posneti z optičnim (a) in elektronskim mikroskopom (b). Širino črt smo določili med premicama, ki označujeta notranjost robov. Pri tisku se rakelj giblje v smeri od zgoraj navzdol.

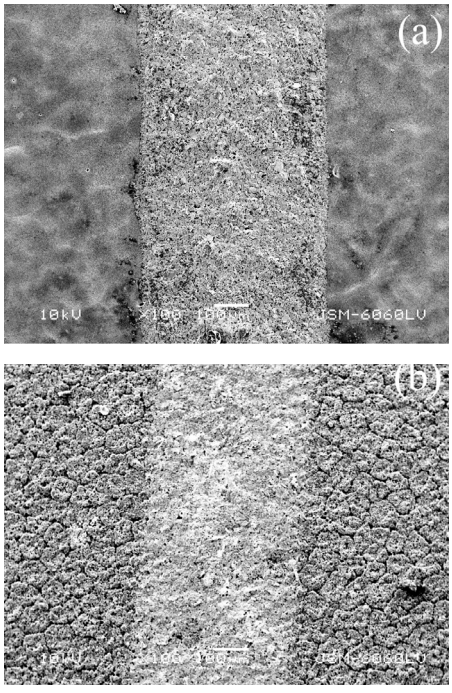

Figure 6: SEM micrograph of analyzed strip printed on gloss-coated paper (a) and clear matt film (b)

Slika 6: SEM-posnetek analizirane črte, natisnjene na sijajnem premazanem papirju (a) in hrapavi foliji (b)

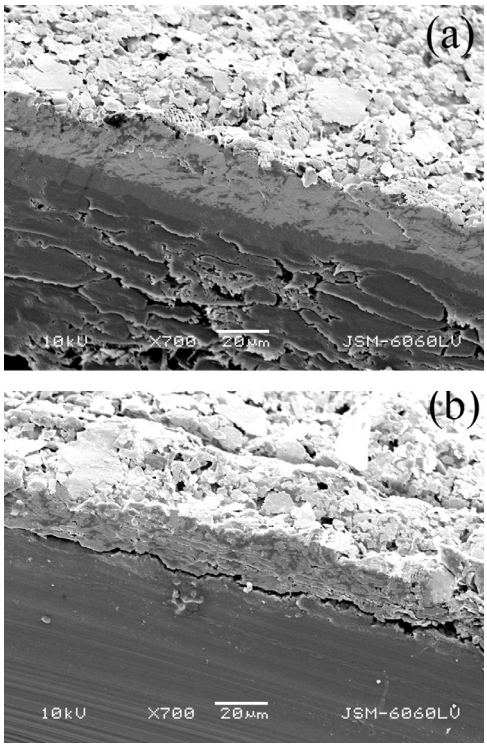

Figure 7: SEM micrographs of cross-sections of samples printed on gloss-coated paper (a) and clear matt film (b)

Slika7: SEM-posnetek prereza vzorcev, natisnjenih na sijajnem premazanem papirju (a) in hrapavi foliji (b)

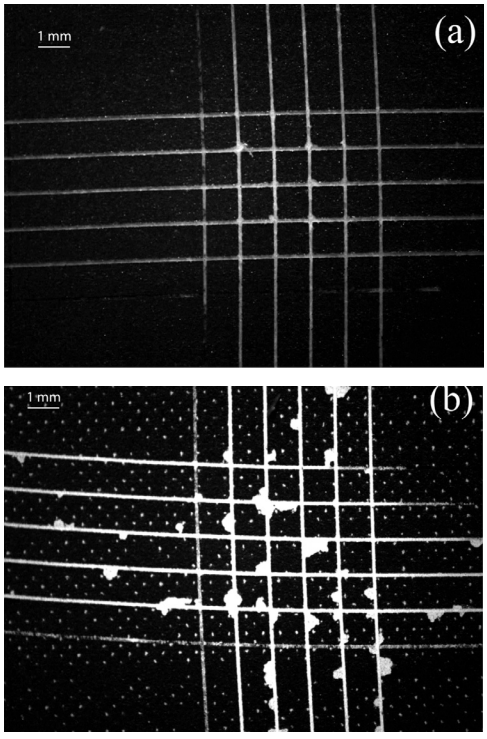

Figure 8: The cross-cut test of single-layer printed on gloss-coated paper (a, adhesion ISO class 1) and clear matt film (b, adhesion ISO class 3)

Slika 8: Metoda križnega reza enoslojne plasti, tiskane na sijajnem premazanem papirju (a, ISO adhezija razreda 1) in hrapavi foliji (b, ISO adhezija razreda 3)

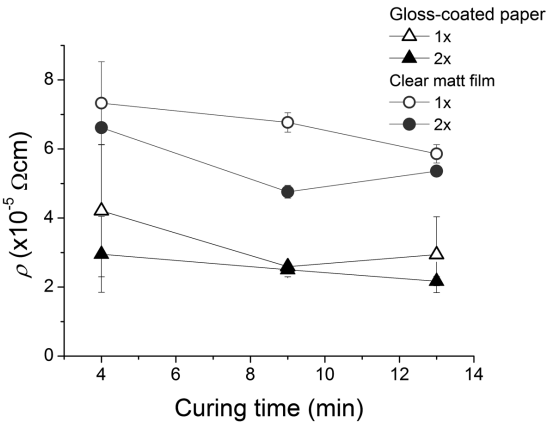

Figure 9: Specific resistivity of single- (open signs) and double-printed layers (solid signs) printed on clear matt film (circles) and gloss-coated paper (triangles)

Slika 9: Specifična upornost eno- (prazni znaki) in dvoplastnih linij (polni znaki), tiskanih na hrapavi foliji (krogi) in na sijajnem premazanem papirju (trikotniki)

The width of the wicking area was evaluated using two straight lines, limiting it on both sides of printed strip on the optical micrograph. Electrically, the fully functional width of the strips was determined between the inner tangents, whereas the rest was considered as the amount of wicking (**Figure 4a**). An about 10 % narrower wicking area was obtained on the top of the horizontally printed strips than on the opposite side. This is the consequence of the moving direction of the squeegee during the printing. The width of the central line (i.e., the fully functional shape) is larger on the gloss-coated paper and smaller on the clear matt film. It tends to diminish with curing time; however, the effect is observable on single-printed samples having a gloss-coated paper substrate, but could be neglected elsewhere (**Figure 5**). The complete width of the strips is the sum of the fully functional central part and the wicking area on both sides. It is about the corresponding width on the print form (i.e., 500 µm), being about 10 % broader when the shape was double printed on gloss-coated paper and could be up to about 10 % narrower elsewhere. In general, narrower lines were obtained on the gloss-coated paper and wider on the clear matt film (**Figure 5**).

A similar analysis was also performed on vertically printed strips; narrower lines were obtained in this case. The wicking area strongly depends on the direction of the printed shape with respect to the moving of the squeegee. This effect is known within the graphics industry [8]. The width of all the printed shapes is systematically broader when directed perpendicularly to the moving direction of the squeegee.

The dependence of the printed strips on the applied substrate can be attributed to the different roughness, porosity and the ability of the ink to diffuse into the substrate. The clear matt film has a very porous and rough surface, whereas the gloss-coated paper has much

smaller pores and a rather smooth surface (**Figure 6**). The smooth surface of the gloss-coated paper enables good orientation of the flakes, which gives thinner layers than the rough, clear matt film. The porosity of the substrates, together with the wettability (which was not evaluated here), influences the width of the printed strips. They are narrower on the gloss-coated paper and wider on the surface of the clear matt film. The additional difference between the prints on both substrates could be seen on the cross-sections. The layers printed on clear matt film do not adhere properly to the substrate (**Figure 7b**), while no such effect was observed on gloss-coated paper (**Figure 7a**). Most likely, this crack-like feature was created due to the large diffusion of liquid constituents of the ink through the pores of the substrate. Because the flakes are rather large, the polymer binder could not permeate sufficiently from the above positions, and therefore the layer and the substrate are not entirely merged. No such effects were observed on the gloss-coated paper (**Figure 7**). The existence of a partial separation between the printed layer and the substrate gives rise to poor adhesion. The effect was evaluated by cross-cut tests (**Figure 8**). The gloss-coated paper has a ISO class 1 (good adhesion, cross-cut area not significantly greater than 5 % is affected), while the clear matt film ISO class 3 (poorer adhesion, cross-cut area between 15 % and 35 % is affected).

3.2 Electrical resistivity

The specific resistivity of all the prepared prints is shown in **Figure 9**. Higher values were obtained for the conductive lines on the clear matt film and smaller on the gloss-coated paper. In general, single-printed layers have a higher resistivity and the double-printed, a lower. The specific resistivity also depends on the curing time: up to 9 min of curing, the resistivity diminishes and then this effect becomes smaller.

The electrical conductivity of composites having conductive particles in a dielectric medium (as with our silver-based printing ink) depends, among other parameters, on the concentration of particles and their orientation within the film [10]. It is well known that flaky particles orient preferably parallel to the substrate [11]. The distribution of silver flakes is influenced by the printing, overprinting and drying, giving rise to arrange, rearrange or distribute themselves evenly across the layer. The flakes are well oriented on the gloss-coated paper and more random on the clear matt film, according to their different surface roughness. This effect could explain the larger resistivity of the strips printed on clear matt film. During the curing process the volume of liquid components diminishes due to the evaporation of the solvents, due to the spreading of the strips and the penetration into the substrate; because of that the concentration of the flakes increases, which diminishes the specific resistivity. The last two processes are intensified on double-printed layers, which may explain the different specific resistivity of single- and double-printed strips on the same substrate: double-printed layers have a higher concentration of flakes.

4 CONCLUSIONS

A detailed analysis of screen-printed, silver-based, conductive lines with a target width of 500 μm for applications in printed electronics is shown here. The influence of the substrate, curing time and wet-to-wet overprinting were considered. While profilometer, optical microscope and SEM images do not give the same information about the topography of prints, the specific resistivity of printed layers has to be determined very carefully.

Two flexible substrates were applied, one with a smooth surface and the other with a rough and highly porous surface. The smooth substrate provides a well-merged interface between the layer and the substrate, whereas the porous substrate is not in full contact with the layer, giving rise to poor adhesion. Thinner and wider lines were obtained on the smooth surface, but thicker and narrower lines were seen on the rough one. All the lines have some wicking area where the content of the functional particles is, in general, much smaller than in its central part. Many of such features cannot contribute to the functional width of the printed line. The second wet-to-wet overprinted layer does not double the layer thickness but increases the width of the lines, especially the area with no proper functionality. These effects are stronger on the rough and porous substrate. Longer curing gives somewhat thinner and narrower strips.

The resistivity of the layers on smooth paper is smaller than that printed on the rough and porous surface. Wet-to-wet overprinting gives a smaller resistivity. It diminishes with a curing time up to 9 min. The specific resistivity depends on the concentration of flakes and the microstructure of printed line; it is influenced by the drying process, the surface roughness of the substrate and its porosity.

ACKNOWLEDGEMENTS

This research is supported by Slovenian Research Agency (Project No. L02-1097-0104-08). Maša Žveglič acknowledges the Slovenian Research Agency for young researchers' support.

5 REFERENCES

[1] Berggren, M., Nilsson, D., Robinson, N. D., Organic materials for printed electronics, Nature Materials, 2 (**2007**), 3–5

[2] Li, Y., Wong, C. P., Recent advances of conductive adhesives as a lead-free alternative in electronic packaging: materials, processing, reliability and applications, Material Science and Engineering, 51 (**2006**), 1–35

[3] Strűmpler, R., Glatz-Reichenbach, J., Conducting polymer composites, Journal of Electroceramics, 3 (**1999**), 329–346

[4] Park, B. K., Kim, D., Jeong, S., Moon, J., Kim, J. S., Direct writing of copper conductive patterns by ink-jet writing, Thin Solid Films, 515 (**2007**), 7706–7711

[5] Klanjšek Gunde, M., Hauptman, N., Maček M., Electrical properties of thin epoxy-based polymer layers filled with n-carbon black particles, Proceedings of SPIE 6882 (**2008**) 68820M-1-68820M-8.

[6] N. Hauptman, M. Žveglič, M. Maček, M. Klanjšek Gunde, Carbon based conductive photoresist, J. Mater. Sci., 44 (**2009**), 4625–4632

[7] Pudas, M., Halonen, N., Granat, P., Vähäkangas J., Gravure printing of conductive polymer inks on flexible substrates, Progress in Organic Coatings, 54 (**2005**), 310–316

[8] H. Kipphan, Handbook of Print Media, Berlin, Heidelberg: Springer **2001**

[9] M. Pudas, N. Halonen, P. Granat, J. Vähäkangas, Gravure printing of conductive polymer inks on flexible substrates, Progress in Organic Coatings, 54 (**2005**), 310–316

[10] I. Balberg, A comprehensive picture of the electrical phenomena in carbon black-polymer composites, Carbon, 40 (**2002**), 139–143

[11] M. Klanjšek Gunde, M. Kunaver, Infrared reflection-absorption spectra of metal-effect coatings, Applied Spectroscopy, 57 (**2003**), 1266–1272

UDK 629.1-46:669.721
Professional article/Strokovni članek

ISSN 1580-2949
MTAEC9, 45(6)633(2011)

RECENT GROWING DEMAND FOR MAGNESIUM IN THE AUTOMOTIVE INDUSTRY

RAST POVPRAŠEVANJA PO MAGNEZIJU V AVTOMOBILSKI INDUSTRIJI

María Josefa Freiría Gándara

Xunta de Galicia, Consellería de Educación e Ordenación Universitaria, 15704 Santiago de Compostela, La Coruña, Spain
josefa.freiria@yahoo.es

Prejem rokopisa – received: 2011-04-08; sprejem za objavo – accepted for publication: 2011-06-17

This article summarizes the importance of magnesium and magnesium alloys in the automotive industry. The resources and properties for magnesium, as well as for magnesium alloys, in manufacturing are concisely treated, taking the SF_6 emissions from magnesium production into account. Moreover, the possibilities of recycling magnesium and magnesium alloys are considered, ending with the expectations and problems in the wider application of magnesium in motor vehicles.

Keywords: Automotive industry, Mg Alloys, emission SF6, recycling, motor vehicle.

V članku je poudarjen pomen magnezija in magnezijevih zlitin v avtomobilski industriji. Viri in lastnosti magnezija in njegovih zlitin so na kratko predstavljeni z upoštevanjem emisije SF6 pri proizvodnji magnezija. Analizirane so tudi možnosti recikliranja magnezija in magnezijevih zlitin. Predstavljena so tudi pričakovanja in problemi večje uporabe magnezija v motornih vozilih.

Ključne besede: avtomobilska industrija, Mg-zlitine, emisija SF6, recikliranje, motorna vozila

1 INTRODUCTION

Although a small amount of magnesium has been used in automobiles for many years, its low density and the constant search for weight savings are encouraging subjects to evaluate more potential applications. The ease with which die castings can be produced makes it a favoured manufacturing route for most applications [1]. Current applications include seat frames, transmission system casings, air-bag housings and lock bodies. **Table 1** summarises the benefits of using magnesium die castings for seat frames.

Table 1: Benefits of using magnesium die castings for seat frames
Tabela 1: Prednosti pri uporabi tlačnih ulitkov magnezija za okvirje sedežev

Material choice:
• Lower specific weight than other options
• Better elongation than other die-casting metals
• 20–30 % shorter cycle times than aluminium die casting
• Longer die life (about double) than aluminium die casting
• ability to produce thinner walls than aluminium die casting
Economic choice:
• Magnesium price stability
• Investment cost reduction in comparison to current seats

Pure magnesium is about one-third lighter than aluminium, and two-thirds lighter than steel. A lighter weight translates into greater fuel efficiency, making magnesium-alloy parts very attractive to the auto industry. And these lighter parts come with good deformation properties, giving the products good dent and impact resistance, as well as fatigue resistance. The alloys also display good high-speed machinability and good thermal and electrical conductivity [2].

Magnesium is a silvery-white metal that is principally used as an alloying element for several non-ferrous metals (Al, Zn, Pb, etc.). Magnesium is among the lightest of all the metals and also the sixth most abundant on earth. The variety of applications of magnesium alloys in the automotive industry, aerospace engineering, chemical industry, etc. contribute to a rapid increase in the production of magnesium in the world [3].

The production of magnesium in the world increased from 20 000 t per year in 1937 up to 400 000 t per year in year 2000, of which China produced 170 000 t of magnesium in 2000. Magnesium alloys are predicted to continue to grow in popularity (about 15 % per year in the automotive industry alone), but the world's supply of magnesium, like every other natural resource, will be not

Table 2: US consumption of primary magnesium in 2007 by use
Tabela 2: Poraba proizvodov iz primarnega magnezija v ZDA v letu 2007

USE	kt
Magnesium casting	25.9
Magnesium wrought products	2.7
Alloying element with aluminium (specially in aluminium cans)	28.9
Iron and steel desulfurization	9.3
Others	5.4
Total	72.3

be unlimited forever. The solution is, logically, to recycle. Especially since anywhere between 30 % to 50 % of the metal handled by die casters ends up as scrap. For the end of life, a consequential approach is used: recycling the metal will significantly avoid the need to produce primary metal. To optimize the recycling of magnesium, an understanding of the current market of primary magnesium is essential [4]. **Table 2** is based on a publication of the US Geological Survey.

2 RESOURCES AND PROPERTIES OF PURE MG METAL. MANUFACTURING

The abundance of Mg in the Earth is considered to be the 4th highest metal, following iron, aluminium and silicon. The raw ores of Mg are dolomite ($MgCO_3$. $CaCO_3$) and magnesite ($MgCO_3$), and Mg is the second most abundant metal in seawater, following sodium. Therefore, it can be said that magnesium is an almost inexhaustible resource, and is distributed all over the world.

Magnesium is the lightest of all metals in practical use, and has a density (1.74 g/cm^3) of about 2/3 that of aluminium and 1/4 that of iron.

On the other hand, magnesium has shortcomings, such as insufficient strength, elongation and heat resistance, and a corrosion propensity. Its readiness to corrode has been found to be due to trace content of metals such as iron (Fe), nickel (Ni) and copper (Cu). The problem of corrosion has to be solved if the purity of the Mg is improved. However, its electrochemical potential indicates that magnesium will corrode by contact corrosion whenever it is in contact with any other metal. Therefore, magnesium is generally surface-treated before it is used.

The methods for manufacturing Mg can roughly be divided into electrolysis and thermal reduction. The electrolysis method involves extracting magnesium chloride from Mg ores and then reducing magnesium to its metallic form by electrolysis. Thermal reduction involves extracting magnesium oxide from Mg ores, adding a reducing agent such as ferro-silicon to it, and refining the resulting material by heating it to a high temperature under reduced pressure.

3 PROPERTIES OF MAGNESIUM IMPROVED WITH ALLOYING

The development of magnesium-alloy products has a long history that dates from 1945. Research has been conducted on the manufacture of various products, such as office goods, agricultural machines and tools, telecommunications equipment and sporting goods. Mg alloys have not yet been used as light structural materials for aircraft. However, they have been used for the gearbox housings of helicopters and other aircraft because they are good vibration dampers, a characteristic that has also brought them into use in the steering wheel cores of motor vehicles.

Alloying means altering a pure metal by melting it and adding other elements to it. This method is applied to almost all metals. Alloying magnesium improves its strength, heat resistance and creep resistance (creep is defined as deformation at a high temperature and under load). For example, AZ-based Mg alloys are well known materials produced by adding aluminium (Al) and zinc (Zn) to pure Mg. The appropriate amounts of additives may improve the strength, castability, workability, corrosion resistance and weldability of these alloys in a well-balanced way [5].

4 SF_6 EMISSIONS FROM MAGNESIUM PRODUCTION

The use of Mg alloys has recently increased. The surface-treatment techniques used to provide highly corrosion resistant Mg alloy products have already advanced on the same level as the die casting methods of some carbon steel plates and aluminium alloy products [6]. To put Mg alloy products to practical use, however, it is necessary to solve the critical problem that magnesium has a high activity in the presence of oxygen. For Mg, it is essential to prevent the formation of products of reaction with oxygen in the air. Currently, this is mainly accomplished with sulphur hexafloride (SF_6) gas, but is a potential greenhouse gas so alternatives that do not use SF_6 are now under investigation. The magnesium metal production and casting industry uses sulphur hexafluoride (SF_6) as a cover gas to prevent the violent oxidation of molten magnesium in the presence of air. SF_6 is a colourless, odourless, non-toxic, and non-flammable gas. The industry adopted the use of SF_6 to replace sulphur dioxide (SO_2), which is toxic and requires careful handling, to protect worker safety.

Historically, more than half of SF_6 emissions from the US magnesium industry have come from the primary magnesium industry, and the magnesium recycling industry, for the most part, continues to employ sulphur dioxide as a cover gas.

In 1999, EPA began the voluntary SF_6 Emission Reduction Partnership for the Magnesium Industry. SF_6 was introduced to replace SO_2, which corrodes casting equipment also. However, safer SO_2 handling procedures and the relatively low cost of SO_2 compared to SF_6 makes SO_2 more attractive [7].

5 MAGNESIUM TODAY

The magnesium industry is now experiencing a time of change with the die-casting segment characterized by rapid growth, both in the European and the North American markets. On the supply side, newcomers have started production, several projects are under consideration or at the pilot stage, while other suppliers have withdrawn from the business [8].

In today's marketplace, magnesium die-casting means the production of parts in compliance with the stringent requirements of high-purity alloy standards. This is the basis for the successful applications of die-cast parts for use in corrosive environments without complicated and cost-adding surface treatments. It is a paradox that magnesium die-cast alloys are melted in steel crucibles, when we know that iron is an impurity with a strong negative influence on corrosion. This can only be done when the whole production sequence, including the processing of ingots, is performed with close attention to the thermodynamic principles involved in keeping iron at an acceptable level throughout the process.

A number of applications, especially in the automotive field, require the ability to absorb energy without the formation of a fracture. Typical examples are provided by steering-wheel cores, instrument panels/cross-car beams, seat parts and door parts. These are typical examples where material properties, processing and design interact strongly in determining the properties of the product. The safe handling of magnesium requires an understanding of the basic processes that can cause hazardous events. The most common reactions involved are the following:

1) Burning/oxidation
   $2Mg + O_2 = 2MgO$
2) Rapid evaporation (expansion) of water entrapped by liquid magnesium
   $Mg(liq.) + H_2O(liq.) = H_2O(vap.) + Mg$
3) Water reaction/hydrogen explosion
   $Mg + H_2O = MgO + H_2$
   $2H_2 + O_2 = 2H_2O$
4) Thermite reaction
   $3Mg + Fe_2O_3 = 3MgO + 2Fe$
5) Silica reaction
   $2Mg + SiO_2 = 2MgO + Si$

There is a growing emphasis on environmental aspects when materials are selected. Magnesium, like aluminium, is an energy-intensive material to produce, and it is not obvious that use of this material will be beneficial. With a full analysis of the environmental impact of production, use and recycling, a life-cycle assessment (LCA) can be performed. Hydro magnesium has issued a comprehensive life cycle inventory (LCI) for the production of magnesium die-casting alloys. This inventory has been used to make a comparative analysis of the parts produced in die-cast magnesium alloys and other alloys. It follows that recyclability is a necessary prerequisite to release the full environmental benefits of using magnesium. Another important factor is to reduce or eliminate the consumption of the potent greenhouse gas SF_6. Recent research has shown that applying a dilute mixture of SO_2 in dry air is a viable method for replacing SF_6. SO_2 must be added as a 0.5–1.5 % mixture in dry air by using a well-designed gas distribution system supplied from a special mixing unit.

The rapid growth of magnesium alloy die-casting has triggered numerous developments of post-casting treatments. Equipment is readily available for trimming, vibratory finishing, blasting and machining. New, environmentally friendly conversion coatings have been developed, as well as improved painting and anodizing processes.

6 MAGNESIUM ALLOYS

Due to their low density (1.8 g/cm^3), magnesium alloys offer distinct advantages for weight saving in automotive applications [9]. It is fair to say that the 1990s have seen a growth of magnesium applications, among which are found steering-column assemblies, steering wheels, instrument panels, seat frames, valve covers and even a manual transmission-case application. The need for further weight reduction is extending the future use of magnesium to critical components such as transmission and engine parts. Magnesium faces a challenge in meeting the performance requirements of these components, for elevated-temperature (150 °C) strength and creep resistance, as well as adequate corrosion resistance. The most economic use of Mg in the automotive industry at the moment is in die-cast applications and this is because of the high productivity of the die-casting process, which upsets the cost of the magnesium metal.

The 1990s have seen renewed activity in the development of elevated-temperature Mg die-casting alloys. In 1994–1997 there have been patent applications on rare-earth and calcium containing alloys. These alloy systems have very good creep properties, such as creep-resistance and bolt-load retention, but contain the expensive rare-earth additions and their die-castability is not known. Also, in 1994-95 a cost-effective Mg-Al-Ca alloy system was developed and a patent application was filed.

There is presently an ongoing worldwide effort to develop more optimum elevated-temperature Mg alloys. Work is underway on the development of new alloys with a potential application in automotive parts requiring elevated temperature performance, such as engine components and automatic transmission cases. The commercial success of these alloys will require Mg producers to focus their efforts and address issues related to cost and recyclability. In collaboration with part producers and end users they will also need to address die-castability and manufaturability.

7 POSSIBILITIES FOR THE RECYCLING OF MAGNESIUM AND MAGNESIUM ALLOYS

Simultaneously with the increasing applications and consumption of magnesium, significant quantities of new scrap are generated; scrap from production as well as postconsumer scrap. As a result of this anticipated increase in new scrap generation, companies are planning new magnesium recycling plants or they are expanding

existing capacity. The principal long-term effect is that after an automobile is scrapped the magnesium-containing parts may be removed from the automobile and recycled. These additional magnesium-containing parts would result in additional quantities of old scrap as a source of supply. The projected increase in the use of magnesium in this application has prompted developed countries such as Germany, Japan, Great Britain, USA and Canada to install additional magnesium recycling capacity. In USA in 1998 the recycling efficiency rate for magnesium was estimated to be 33 %.

New magnesium-based scrap is typically categorized into one of the four types. Type I is high-grade scrap, generally materials such as gates, runners and drippings from die-casting operations that is uncontaminated with oils. Types II, III and IV are lower-graded materials. Type II is oil-contaminated scrap, type III is dross from magnesium-processing operations, and type IV is chips and fines. Old magnesium-based scrap or postconsumer scrap consists of such materials as automotive parts, helicopter parts, lawnmower decks, used tools and the like. This scrap is sold to scrap processors. In addition to magnesium-based scrap, significant quantities of magnesium are contained in aluminium alloys that can also be recycled. In particular, magnesium has a lower specific heat and a lower melting point than other metals. This gives the advantage of using less energy in recycling, with recycled Mg requiring as little as about 4 % of the energy required to manufacture new material. At present, however, recycling procedures are still not fully developed. For example, an experimental investigation of the processing of non oil-contaminated metal scrap based on magnesium and its alloys was carried out. Experimental investigations were conducted on a laboratory scale and the results were verified on an industrial scale. The investigations show that: processing of this kind of scrap is possible with a metal-extraction efficiency rate in range 45–90 %, depending on the quality of the scrap; and for the purpose of achieving satisfactory techno-economical effects it is necessary to have suitable processing technology, which includes the preparation, metallurgical processing, smelting and refining. An electrolytic process to recycle low-grade and post-consumer magnesium scrap was developed to recover magnesium from magnesium oxide, unlike the traditional electrolytic process that uses magnesium chloride as a feed material [10].

8 THE RECYCLING OF MAGNESIUM

Magnesium scrap is being melted and refined under strict control. After the removal of oxides and compositional adjustments, magnesium alloys of at least the same quality as primary metal are cast into ingots.

The magnesium die-casting industry has grown significantly over recent years and this growth is projected to continue with automotive applications leading the way. The current consumption of magnesium is about 2 kg per vehicle worldwide, and over the next 20 years, the automotive industry could use almost 100 kg per vehicle, or more than 50 times the current demand. This leads to significant amounts of magnesium scrap. Depending on the die-casting process used, and the design of the part, between 80 % to 100 % of the net weight of the casting can be scrap. To realize this growth, magnesium has to be economically and environmentally acceptable. All options for reusing pre- and post-consumer magnesium scrap in alternative markets, or for recycling, need to be evaluated. The growing demand for magnesium alloys in the automobile industry necessitates increasing recycling capacities. In this respect, the recycling process is today still basically related to the clean casting returns. However, there is an ever greater need to recycle other residual magnesium materials as well. The reuse or recycling of these residual materials continues to be a problem, in particular with regard to environmental issues. The re-melting of painted casting returns results in considerable quantities of dioxin. These must be recorded quantitatively and, using an appropriate filter, must be removed from the waste gases down to a content of 0.1 mg/m^3. This demands a relatively large investment in filter technology.

Today, the "dross" arising in the die-casting foundries is also recycled, i.e., the more or less salt-free magnesium scrapings that occur when the crucible surface is skimmed. The chips arising in the production process today are contaminated with either oil or oil-water emulsions. Even with long draining times, it is not possible to reduce the oil content to below 10 %. In this form, the chips cannot be re-melted using any of the melting techniques applied so far. They burn (to a greater or lesser extent), producing black oil-smoke clouds in the melting crucible, resulting in extreme emissions of dioxins, total C, HCl and Mg oxide, as well as scrapings that have to be disposed of in an expensive process. This is a very high-cost method of destroying magnesium chips. A technique was developed, it consists of pressing the magnesium chips in a hot condition at > 300 °C, which not only removes the oil thermally, but also causes the chips to cake in such a way that a re-melting process can be carried out without any major loss during red heat. Until now, this technique has only been applied rarely, and the quantities to be pressed per unit of time are relatively small.

In addition to protecting the environment, the main objective, of course, is to manufacture a clean alloy, which can be reused in the automobile industry and, if possible, has a high-purity (HP) quality. To achieve this it requires a type-specific separation and collection of the casting returns at the die caster's plant, and a fault-free handling/transport at the disposing/recycling company. If these prerequisites are satisfied, the recycling process will result in an alloy that complies with the standards. Today we distinguish between four different recycling categories:

1) "in-cell" recycling
2) "in-house" recycling
3) End of Life Vehicle (ELV) recycling
4) industrial (external) recycling/service.

Depending on the structure of the installation, the annual capacities of the recycling plants vary between 2 000 t per year and 10 000 t per year.

"In-cell" recycling takes place directly at the plant of the die-caster, who immediately puts the clean, initial castings into the melting crucible again. "In-house" recycling may become interesting for die-casters with high throughput quantities. ELV recycling still poses a challenge. By 2015, automobile manufacturers will be forced to reuse 95 percent of the materials used in the car and, what is more, in the same area of applications.

The traditional technology is melting and refining with salt, also called flux refining. The casting returns are melted down in an open steel crucible (heated by gas or electricity) while salt is added.

The Salt Furnace Technology was developed, using super-heated salt to melt the returns and cleaning the melt by settling in a multi-chamber furnace. In the one-furnace version of this technology, ingots are cast directly from the recycling furnace. There will be a constant increase in the demand for the recycling of residual magnesium materials. The statutory regulations will be ever more oriented towards a closed-loop cycle in which all the residual materials are, if at all possible, reused. The utilization of larger quantities of "post-consumer scrap" must be prepared and new applications must be created for the use of "non-HP alloys".

9 EXPECTATIONS AND PROBLEMS IN THE WIDER APPLICATION OF Mg TO MOTOR VEHICLES

Passenger transport accounted for about 60 % of the total energy consumption in the transport sector, and in particular the use of private cars contributed significantly to this consumption. To build a sustainable society in the future it will be necessary to reduce the weight of the structural materials used in transport equipment, especially private cars, both to conserve energy and to minimize global warming [11].Today, magnesium alloys are recognized alternatives to iron and aluminium for reducing the weight of structural elements [12]. On the other hand, motor vehicles tend to increase in weight as they are given additional functions, such as safety devices and electronic equipment. The challenge for the future is not only to offset weight increases due to performance enhancements, but also to reduce the overall weight of motor vehicles. Conventional weight reduction technologies have reduced the weight of motor vehicles by improving their structural design and thinning steel materials by increasing their strength. For the future, however, it is generally recognized that drastic changes in structural materials should be considered [13].

For passenger cars, the general rule is that about 86 % of their total lifetime energy use (from the time of production to the time of disuse or scrapping) is consumed by carrying their own weight and persons around. In Europe, the regulation governing CO_2 emissions from motor vehicles has been worked out, setting the standard that CO_2 emission shall not exceed 140 g/km in 2012 and 120 g/km in 2014. According to previous analysis, it will be necessary to reduce the mass of vehicles by about 10 %. To attain such a great reduction in mass, it will probably be necessary to replace steel with Mg alloys as the structural material. For this reason, much attention is now focused on Mg alloys as structural materials or parts for motor vehicles.

To work towards a sustainable society, it is absolutely necessary to develop energy-saving technologies that contribute to the reduction of CO_2 emissions. It is especially important to reduce the amount of energy that is consumed simply to enable a vehicle to carry its own weight around. Therefore, the weight reduction of transport equipment is one of the most important technical challenges. It is anticipated that activities will be accelerated to develop and commercialize Mg alloys that contribute to the weight reduction of structural materials for transport equipment.

Although Mg alloys possess a variety of desirable physical properties, including lightness, they have had a limited range of applications because they also have performance shortcomings, such as low strength, low heat resistance and low corrosion resistance. In recent years, however, advanced basic research on Mg alloys has enlarged the range of applications [14].

10 REFERENCES

[1] Zhi, D., Automotive Engineering, (**1991**), 1

[2] Luo, A. A., Nyberg, E. A., Sadayappan, K., Shi, W. Magnesium front end research and development: a Canada-China-USA collaboration. Presented at Magnesium Technology Conference, New Orleans, LA, USA, March 9–13, **2008**

[3] Liu, Z., Wang, Y.,Wang, Z., Li, F., Chinese Journal of Material Research, (**2000**), 5

[4] USGS, 2007 Annual Yearbook Magnesium (Advanced Release), http://minerals.usgs.gov./

[5] Wang, Q., Lu, Y., Zeng, X., Ding, W., Zhu, Y., Special Casting & Nonferrous Alloys, (**1999**), 1

[6] Fu, L., Automobile Technology & Material, (**2006**), 8

[7] Norsk Hydro (2008). Progress to eliminate SF_6 as a protective gas in magnesium diecasting. Hydro Magnesium, Brussels, **2008**

[8] Shukun, M., Xiuming, W., Jinxiang, X. China's magnesium industry development status in 2007. Presented at 65th World Magnesium Conference, Warsaw. Poland, May 18–20, **2008**

[9] Report of Investigation on the Technical Trend of Patent Applications in 2004: Automobile Weight reduction Technologies. Japan Patent Office, March **2005**

[10] Gesing, A. J., Dubreuil, A. Recycling of post-consumer Mg scrap . Presented at 65th Annual World Magnesium Conference, Warsaw, Poland, May 18–20, **2008**

[11] Energy consumption Trend in Transport Sector: 2-2-1. Analysis on private passenger cars' contribution to the total energy consumption. Home page provided by the Energy Conservation Center, Japan: http://www.eccj.or.jp/transportation/2-1-1.html

[12] Yan, Z., Hua, R., Automotive Engineering, (**1994**), 6

[13] Nyberg, E.A., Luo, A. A., Sadayappan, K., Shi, W., Advanced Materials & Process, 166 (**2008**) 10, 35–37

[14] Yan, Z., Automotive Engineering, (**1993**), 3

UDK 669.14.018.8:620.193
Professional article/Strokovni članek

ISSN 1580-2949
MTAEC9, 45(6)639(2011)

CONTACT WITH CHLORINATED WATER: SELECTION OF THE APPROPRIATE STEEL

KONTAKT S KLORIRANO VODO: IZBOR USTREZNEGA JEKLA

Leon Gosar[1,2], Darko Drev[1,3]

[1]Institute for Water of the Republic of Slovenia, Hajdrihova 28, 1000 Ljubljana, Slovenia
[2]University of Ljubljana, Faculty of Civil and Geodetic Engineering, Chair of Fluid Mechanics with Laboratory, Hajdrihova 28, 1000 Ljubljana, Slovenia
[3]University of Ljubljana, Faculty of Civil and Geodetic Engineering, Institute of Sanitary Engineering, Hajdrihova 28, 1000 Ljubljana, Slovenia
leon.gosar@izvrs.si

Prejem rokopisa – received: 2011-02-02; sprejem za objavo – accepted for publication: 2011-08-18

In water-supply systems and public swimming pools, the presence of highly chlorinated water can result in very aggressive corrosion. When choosing the appropriate type of steel, the extremely corrosive conditions that can occur are often forgotten. Under these conditions, corrosion-protection layers (zinc layer, polymer colour) can be quickly removed, and stainless-steel corrosion may occur as well. The high risk of the corrosion of galvanized steel pipes can also be caused by the improper implementation of disinfection. With aggressive disinfectants, the zinc layer is quickly dissolved, which leads to corrosion of the steel pipe. Therefore, we must select a particular type of stainless steel, thereby ensuring a much higher corrosion resistance than normal stainless steel. It is very important that the selection of materials is determined at the design stage of the project. In the contact of steel elements with swimming-pool water, in most cases extremely aggressive oscillations do not occur under normal operating conditions, because the content of chlorine and other elements that affect corrosion are mostly low and stable. However, even in these cases, from time to time, aggressive shocks may occur as a result of the cleaning treatment. Therefore, with the selection of the appropriate stainless steel the corrosion risk can be prevented. The contribution of the paper is mainly focused on experiences relating to the appropriate materials selection in the field of sanitary engineering.

Keywords: stainless steel, corrosion, sanitary engineering

Pri vodovodnih sistemih in javnih kopališčih se lahko pojavi močno klorirana voda, ki je korozijsko zelo agresivna. Ko izbiramo ustrezno vrsto jekla, pogosto pozabimo na ekstremne korozijske razmere, ki se lahko pojavijo. V njih se lahko zelo hitro odstranijo protikorozijski zaščitni sloji (cinkov sloj, polimerna barva), lahko pa se pojavi tudi korozija nerjavnega jekla. Veliko nevarnost za korozijo pocinkanih jeklenih cevi lahko npr. povzročimo z neustreznim izvajanjem dezinfekcije. Z agresivnimi dezinfekcijskimi sredstvi hitro raztopino zaščitni sloj cinka in povzročimo korozijo jeklene cevi. Zato je zelo pomembno, da se že v fazi projektiranja odločimo, katere materiale bomo izbrali ter na kakšen način se bo izvajala dezinfekcija. Pri izbiri jeklenih elementov, ki so v kontaktu z bazensko vodo, v večini primerov nimamo tako ekstremnih sprememb agresivnih razmer. Vsebnost klora in drugih sestavin, ki vplivajo na korozijo, je v kopalni vodi večinoma vedno nizka in stabilna. Kljub temu pa se lahko tudi v teh primerih pojavijo občasno agresivni šoki, ki lahko nastanejo v fazi čiščenja. Zato je treba z ustrezno izbiro nerjavnega jekla preprečiti nevarnost korozije. V prispevku je poudarek predvsem na izkušnjah pri izbiri ustreznega materiala s področja sanitarnega inženirstva.

Ključne besede: nerjavno jeklo, korozija, sanitarno inženirstvo

1 INTRODUCTION

In this paper we focus on facilities, which in addition to structural strength, also require sanitary adequacy. The latter requirement is particularly important for the selection of the stainless steel used in water-supply systems, public baths, food-processing facilities, kitchens, etc.[1] In these facilities, aggressive corrosive conditions in some parts of the water-supply systems may appear. [2] In the case of swimming pools, due to the presence of chlorinated water, the requirements for additional corrosion resistance need to be met.[3] Planners and designers often do not pay enough attention to the operating conditions in such facilities.

A particular case is the construction of a waterslide structure, where it is crucial for corrosion-resistant stainless steel to be selected to prevent endangering the stability of the structure. In addition, the surfaces must be completely smooth and free of corrosion effects, which is a sanitary requirement. This problem can be solved with the appropriate surface protection, [4] which may be questionable in the junctions,[5] if galvanic cells occur. Conversely, in the case of some steel surfaces (e.g., in food-processing facilities), contact with the surface where zinc is gradually being dissolved is prohibited. [6] Galvanized steel surfaces are resistant to corrosion by first dissolving the less-noble metals, e.g., zinc, thereby protecting the steel against corrosion. This method of corrosion protection is also used in galvanized-steel water-system pipes. However, in this case, corrosion protection is not only important for maintaining the stability of the installation, but also to ensure healthy drinking water.

The following types of steel corrosion can occur: [2]

– Uniform corrosion: the metal loss is uniform on the surface.
– Crevice corrosion: due to the specificity of the electrochemical process in crevices where the

changes in pH occur in the medium, the corrosion is progressing rapidly.
- Pitting corrosion: produced locally in the form of notches.
- Intergranular corrosion: localized attack along the grain boundaries, or immediately adjacent to the grain boundaries, while the bulk of the grains remains largely unaffected.
- Stress-corrosion cracking: unexpected sudden failure of normally metals subjected to in a environment.
- Hydrogen brittleness: arises from the destructive action of absorbed atomic hydrogen or hydrogen protons in the crystal lattice.
- Erosion corrosion: degradation of the material surface due to mechanical action, often by impinging liquid, abrasion by a slurry, particles suspended in fast-flowing liquid or gas, bubbles or droplets, s etc.

On steel surfaces, rust may occur as a result of chemical reactions in the steel. The characteristic brown colour appears in the presence of Fe^{+2} and Fe^{+3} iron compounds. Iron enters the Fe^{+2} and Fe^{+3} forms due to chemical reactions. However, these reactions occur more rapidly if the steel is not sufficiently "noble", e.g., it does not contain a sufficient amount of elements that are less susceptible to corrosion (nickel, chromium, cobalt, manganese, etc.).

The rate of the corrosion processes is affected by the steel composition, temperature, atmosphere, and the substances in contact with the steel construction (sheet metal). The purpose of corrosion-protection coatings is to reduce these processes to a minimum. If a connection with the moisture and the oxygen from the air is prevented, corrosion will progress very slowly. In this case, the necessary liquid electrolyte and the atmosphere that would enable an adequate decay rate of iron are absent. Since in the transformation of elemental iron in its compounds electrons are being emitted, this forms a galvanic cell. For the galvanic-cell formation to occur, both the electron donor and the recipient must be present. There exist several chemical reactions, where elemental iron passes over into its compounds. These compounds are of a brownish colour and can be seen on the outside as rust. [2]

$$Fe \rightarrow Fe^{2+} + 2e^{-} \quad O_2 + 2\,H_2O + 4e \rightarrow 4\,OH$$

$$Fe + H_2O + \tfrac{1}{2}\,O_2 \rightarrow Fe(OH)_2$$

$$Fe \cdot H_2O + 1/2\,H_2O + 1/2\,O_2 \rightarrow Fe(OH)_3$$

e.g. $\tfrac{1}{2}\,(Fe_2O_3 \cdot 3\,H_2O)$ ...

Purbaix [7] constructed the following potential/pH diagram (**Figure 1**). Based on this diagram, one can rapidly assess the corrosion resistance of various metals in water at 25 °C. He defined the possible equilibrium between the metal and H_2O. A simplified Pourbaix diagram indicates regions of "Immunity", "Corrosion" and "Passivation" and is a guide to the stability of a particular metal in a specific environment. Immunity means that the metal is not attacked, while shows that a general attack will occur. Passivation occurs when the metal forms a stable coating of an oxide or other salt on its surface.

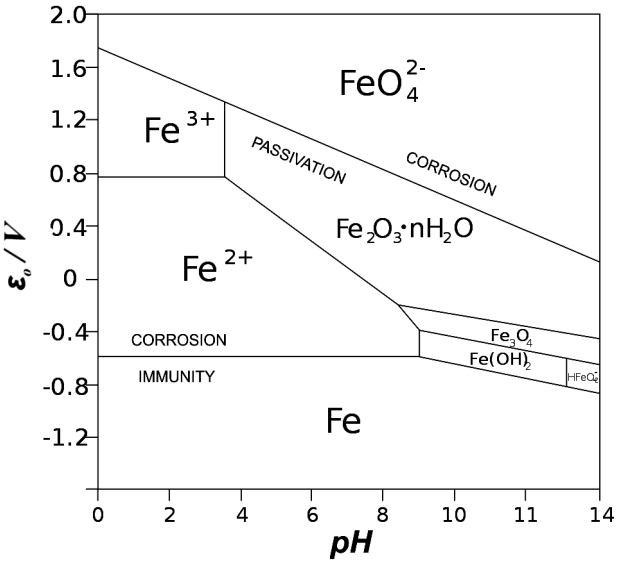

Figure 1: Purbaix diagram of iron [7]
Slika 1: Purbaix-ov diagram za železo [7]

In presence of chlorine ions, a high probability of the formation of porous or pitting corrosion exists. This result is the formation of small pits on the surface of the metal. Pitting corrosion is often difficult to differentiate from other, similar corrosive processes that may occur, such as crevice corrosion or the dissolution of zinc (both involve disparate mechanisms of corrosion). The critical pitting potential depends on the concentration of Cl-ions, the inhibitor potential of various anions in the solution, their concentration (OH^-, SO_4^{2-}, NO^{3-}, CrO_4^{2-}), as well as the temperature of the solution. In the case of swimming-pool water, we have a significant content of Cl^- and SO_4^{2-} ions and a relatively high water temperature. While this is conducive for the formation of pitting (porous) corrosion, a relevant microstructure of metals and their alloys need to be present as well.

In the case of drinking-water systems in the food industry, stainless steel should be selected. The same holds for waterslide structures and other facilities in and around swimming poles. However, it is important to note that even with the use of stainless steel, corrosion can still occur if:
- the stainless steel is not of adequate quality for the given conditions of use,
- the stainless steel forms a galvanic cell,
- there is contact with highly corrosive chemicals,
- the stainless-steel surface was not properly treated etc.

2 EXPERIMENTS AND RESULTS

We reviewed several examples of corrosion phenomena in steel and stainless steel in the field of sanitary

engineering (water-supply network, baths, spas, kitchens, etc). These were in most cases expert opinions and related research inquiries into the causes of corrosion in real-world structures. Due to the sensitive nature of these studies, we are not able to present specific details about the individual structures that were the focus of these investigations. Nevertheless, we are able to present all the relevant data and facts to support our findings and conclusions.

2.1 Corrosion in an internal water-supply network

When planning a complex, internal water-supply network, it is first necessary to determine the properties of the available water and what the purpose of the local water-distribution network will be. The designer must decide which materials to use in order to facilitate disinfection. If a specific type of disinfection is not prescribed in advance (e.g., by law), the materials have to be selected to allow the effective execution of a broad range of disinfection procedures. When using galvanized steel pipes and components made of stainless steel, copper and brass, the designer should take into account the possibility of galvanic cell formation and the removal of protective zinc coatings. Zinc layers can easily be dissolved by repeated disinfectant shocks. When using plastic pipes, the possibility of heat shocks must be considered. Heat shocks are often used to disinfect an internal water-supply system when the presence of Legionella bacteria is suspected. If heat shocks are implemented, the water pipes need to withstand temperatures up to 90 °C. In addition to water pipes, thermal stability is also expected for the seal components and other parts of the installed structure.

In the analyzed cases of the internal water-supply network, we found that multiple chlorine shocks and large concentrations of disinfectants (**Table 1**) resulted in the dissolution of zinc coatings on steel pipes. Corrosion also occurred inside stainless-steel water tanks (**Figure 2**).

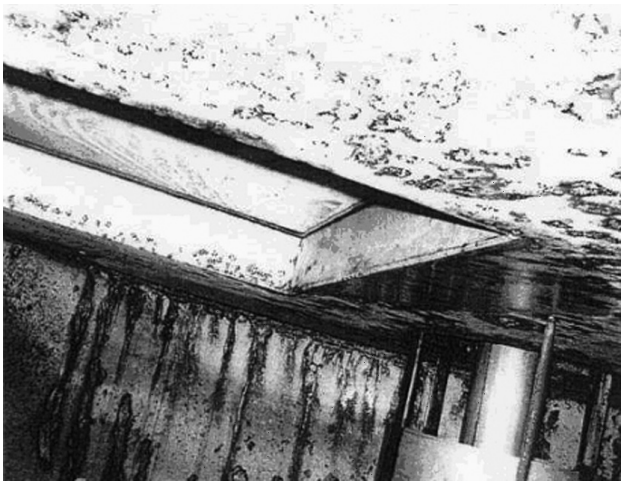

Figure 2: Corrosion inside a cold water reservoir
Slika 2: Korozija v notranjosti rezervoarja hladne vode

Table 1: Disinfectants recommended by the National Institute of Public Health of Slovenia for water supply systems.
Preglednica 1: Dezinfekcijska stredstva za vodovodne sisteme, ki jih priporoča IVZ

Disinfectant	Quantity / mg/l	Recommended resources for neutralization
Chlorine in gaseous form Cl_2	50 (Cl form)	Sulphur dioxide (SO_2) Sodium thiosulphate ($Na_2S_2O_3$)
Sodium hypochlorite NaClO	50 (Cl form)	Sulphur dioxide (SO_2) Sodium thiosulphate ($Na_2S_2O_3$)
Calcium hypochlorite $Ca(ClO)_2$	50 (Cl form)	Sulphur dioxide (SO_2) Sodium thiosulphate ($Na_2S_2O_3$)

Table 2: Conversion table for stainless steel AISI 304 tags to the European standard [8]
Preglednica 2: Tabela za pretvorbo oznake nerjavnega jekla AISI 304 v evropski standard [8]

Standard (Europe)	AISI	Chemical composition / %			
		C max	Cr	Ni	Mn max
X5 CrNi 18-10	304	0,07	17-19,5	8-10,5	2

In one of the internal water-supply network cases, the designer prescribed stainless steel AISI 304 (**Table 2**). In the lists of stainless steels for use in chlorinated water conditions, Deutsches Institut für Bautechnik recommends stainless steel with the same chemical composition as AISI 304, no. 1.4301.[8]

Extensive corrosion on all the surfaces of the reservoir has shown (**Figure 2**) that it could not result from conventional chlorine shocks alone, but instead required the presence of much higher concentrations of chlorine. This reservoir was constructed of stainless steel X5 CrNi 18-10 as recommended by the Deutsches Institut für Bautechnik for structures in contact with pool water that may be highly chlorinated. In the case of the water supply, disinfection with the recommended agents was employed to destroy the bacteria of the Legionella group (**Table 1**). Since this was not successful, the disinfection was repeated several times, each time with an increased concentration of disinfectants. When it was determined that the disinfectants were not appropriate, oxidizing agents effective for the removal of biological deposits and the destruction of Legionella bacteria were introduced into the system. This resulted in a corroded internal water-supply system and poor quality of the drinking water. However, by adding an oxidizing disinfectant based on hydrogen peroxide and small amounts of colloidal silver particles, one can indeed achieve microbiological water disinfection. However, this water will also likely be organoleptically and chemically unsuitable [9] due to the resulting water-pipe corrosion.

2.2 Stainless-steel corrosion in a public swimming pool

Swimming-pool water is always chlorinated to prevent the development of adverse microorganisms. Such water is very aggressive to metals and can easily

cause corrosion. Swimming-pool water also typically contains sulphates in addition to chlorine ions. In the presence of organic matter, chlorine forms chlorinated hydrocarbons, i.e., trihalomethanes, which are classified as carcinogenic substances.[10] This process can be prevented by the use of a large amount of Cl_2. The addition of a large quantity of Cl_2 is associated with a shortened contact time that prevents the formation of trihalomethanes. Residual chlorine can then be removed from the water by the addition of SO_2. This practice explains why SO_4^{-2} ions were detected in the water. However, it is important to note, that the concentration of the SO_4^{-2} in comparison with the chlorine is less important for corrosion.

Metals with a negative potential are easier to dissolve (corrode) than metals with a positive potential. It is clear that iron dissolves when in contact with chlorine. Chlorine is present in bathing water, as well as in various disinfectants and cleaning agents. The normal potential for iron is –0.44 V, while for chlorine it is +1.36 V, an absolute potential difference of 1.80 (**Table 3**).

One of the inspected cases was that of a waterslide. In its project documents, stainless-steel AISI 316 to AISI 316Ti was the prescribed material for the construction. AISI 316 stainless steel contains a chromium (Cr), nickel (Ni) and molybdenum (Mo) alloy of metals (**Tables 4 and 5** [13]). In addition, it contains small quantities of phosphorus (P), sulphur (S), as well as some other elements.

We note that in the table of stainless steels recommended for swimming-pool construction by the Deutsches Institut für Bautechnik, AISI 316 and AISI 316Ti are not listed. [8] This was overlooked by the designer, thus the resulting corrosion is not a coincidence and corrosion appeared on the stainless-steel nuts (**Figure 3**), which can endanger the the stability of structure. Due to the occurrence of corrosion, protective coatings were applied to the inappropriately chosen stainless steel. However, this did not ensure adequate protection; as shown in **Figure 4** the protective layer peeled off the protected surface and consequently the investor enforced the warranty for the waterslide structure.

Table 3: Metals typically used in construction [11,12]
Preglednica 3: Najbolj poznane konstrukcijske kovine [11,12]

Metal	Voltage /V	Metal	Voltage /V	Metal, nonmetal	Voltage /V
potassium	– 2.9	cadmium	– 0.40	silver	+ 0.80
sodium	– 2.7	cobalt	– 0.29	mercury	+ 0.86
manganese	– 2.34	nickel	– 0.25	gold	+ 1.68
aluminum	– 1.28	tin	– 0.14	platinum	+ 1.18
manganese	– 1.05	lead	– 0.12	sulphur	– 0.51
zinc	–0.76	antimony	+ 0.20	hydrogen	0.00
chromium	– 0.56	arsenic	+ 0.30	oxygen	+ 0.39
iron	– 0.44	copper	+ 0.34	chlorine	+ 1.36

Table 4: Features of the stainless steel prescribed by the designer
Preglednica 4: Lastnosti nerjavnega jekla, ki ga je predpisal projektant

W.Nr.	DIN	AISI	JUS
1.4436	X5CrNiMo 17 13 3	316	Č.45706
1.4571	X6CrNiMoTi 17 12 2	316Ti	Č.4574

Table 5: Conversion table for stainless steel AISI 316/316Ti tags to the European standard
Preglednica 5: Tebela za pretvorbo oznak nerjavnega jekla AISI 316/316Ti v evropske standardne oznake

Standards (Europe)	Chemical composition / %				
	P max	S max	Si max	Mo	Other elements
X5 CrNiMo 17-12-2	0,045	0,015	1	2-2,5	N 0,11 max
X6 CrNiMoTi 17-12-2	0,045	0,015	1	2-2,5	Ti=5 x C_{min}; 0,7 max

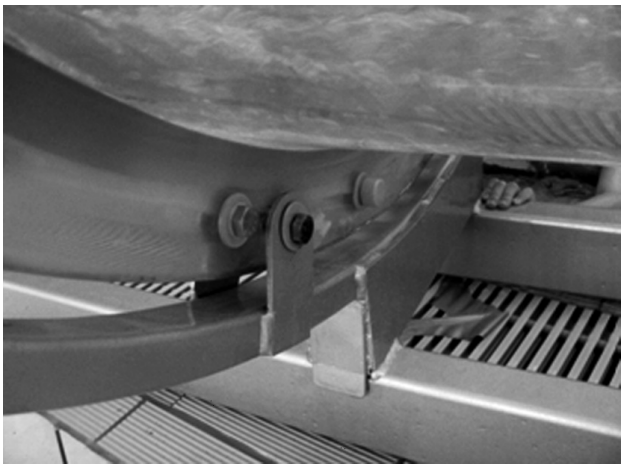

Figure 3: Corroded stainless steel nuts on the waterslide structure
Slika 3: Prikaz korozije na matici izdelani iz nerjavnega jekla na konstrukciji tobogana

Figure 4: Protective coating peeling off of stainless steel structure
Slika 4: Prikaz slabe površinske zaščite nerjaveče jeklene konstrukcije v kopalnem bazenu

3 DISCUSSION

The corrosion of stainless steel can be prevented by choosing an appropriate type of steel (steel alloys with a higher content of certain metals – Cr, Ni, Mo), by chemical treatment (pickling), thermal processing (annealing) and surface treatment (grinding, polishing). To avoid the corrosion of stainless steels, it is first necessary to respect the following rules:

- no use of tools (wrenches, pliers, vices) that were previously applied for work with non-corrosion-resistant steel,
- no use of abrasive wheels that were previously used for grinding or cutting non-corrosion-resistant steel,
- the filings of non-corrosion-resistant steel must not come into contact with the surface of the stainless steel,
- no use of cutting tools (saws, files, etc.) that were previously applied for work with non-corrosion-resistant steel,
- no use of sanding cloths and brushes that were previously used for processing non-corrosion-resistant steel.

The rules that define materials used in food processing and swimming-pool structures do not detail which materials must be used. Slovenian and EU rules define which materials can be used in facilities where they may come in contact with food. It is important to note that in this case water falls under the definition of food. Similarly, the Slovenian regulations for technical measures related to the safety of swimming pools [14] do not clearly define which materials may be used in the construction and operation of these facilities. The rules only simply state (Article 25) that.[15]

(1) All swimming pools and pool platforms must meet the requirements of SIST EN 13451, parts 1–9.
(2) Waterslides must be designed and constructed in accordance with SIST EN 1069-1 and SIST EN 1069-2.

SIST EN 13451 provides general safety requirements and test methods for swimming pools, while SIST EN 1069 -1 and SIST EN 1069 -2 prescribe safety requirements and test methods for waterslides.

4 CONCLUSION

It is evident from the cases presented that in the field of sanitary engineering the use of appropriate steel types is of paramount importance. However, even when the appropriate steel type is used and standard surface protection is applied, corrosion may still occur. In the example of the internal water-supply network shown, a protective layer of zinc had been removed due to the implementation of disinfection. A need for the repeated disinfection of the water-supply network arose from the contamination of the system with Legionella bacteria. Disinfection was executed by inappropriate methods and induced a significant corrosion of the water-supply system, while the contamination problem was not solved. Legionella bacteria could not be successfully destroyed, neither by chlorine shocks nor by thermal shocks. When inducing thermal shocks, it was not possible to reach a sufficient temperature in all the parts of the system simultaneously, thus the contamination was merely transmitted from the contaminated part to the decontaminated parts of the networks. Effective disinfection was later achieved by introducing oxidative disinfectants based on H_2O_2 and Ag into the system. However, this resulted in corrosion and lowering of the chemical and organoleptic quality of water. In the case of a public swimming pool, stainless steel of insufficient quality was used and corrosion became evident after only a few months of use. When the steel was protected with a plastic coating, this started to flake. The lesson is that stainless steel should be appropriately chosen, and protective coatings should be applied before installation.

By selecting appropriate protective coatings, corrosion can be prevented for the entire lifetime of a facility. Hot galvanized steel elements can adequately protect the steel for up to ten years or more, until the protective layer of zinc is dissolved. Polymeric coatings are also effective, but it is possible for corrosion to occur at the edges of the structural elements beneath the top layer. However, if an appropriate type of stainless steel is selected ex ante, we can remove the threat of corrosion altogether as long as the operation of the facility is performed in accordance with specified rules. The choice of high-grade stainless steel is associated with higher investment costs and lower operating costs. In the design and construction of sanitary engineering facilities, it is therefore necessary to think comprehensively about corrosion prevention, as the selection of appropriate steel types does not only provide structural strength; it can also ensure healthy drinking or bathing water, while reducing operational costs.

5 REFERENCES

[1] C. Jullien, T. Bénézech, B. Carpentier, V. Lebret, C. Faille, Identification of surface characteristics relevant to the hygienic status of stainless steel for the food industry, Journal of Food Engineering, 56 (**2003**) 1, 77–87

[2] G. Kreye, M. Schütze, Corrosion Handbook, John Wiley&Sons (**1998**)

[3] A. Sander, B. Berghult, A. Elfström Broo, E. Lind Johansson, T. Hedberg, Iron corrosion in drinking water distribution systems – The effect of pH, calcium and hydrogen carbonate, Corrosion Science, 38 (**1996**), 443–455

[4] W. F. Smith, Principles of Materials Science & Engeneering, 2.edt., Mc Graw Hill, New York, 1990

[5] G. Banerjee, T. K. Pal, N. Bandyopadhyay, D. Bhattacharjee, Effect of welding conditions on corrosion behaviour of spot welded coated steel sheets, Corrosion Engineering, Science and Technology, 46 (**2011**) 1, 64–69

[6] D. Jiasheng, C. Sihong, L. Manqi, Y. Ke, History and Current Status of Antibacterial Materials, Materials Chemistry and Physics, 89 (**2005**) 1, 38–48

[7] Pourbaix, M., Atlas of electrochemical equilibria in aqueous solutions. 2d English ed., Houston 1974

[8] Anstalt des öffentlichen Rechts, Allgemeine bauaufsichtliche Zulassung, Deutsches Institut für Bautechnik, Z-30.3.6. 2003

[9] S. D. Richardson, Disinfection by-products and other emerging contaminants in drinking water, TrAC Trends in Analytical Chemistry, 22 (**2003**) 10, 666–684

[10] M. Panyakapo, S. Soontornchai, P. Paopuree, Cancer risk assessment from exposure to trihalomethanes in tap water and swimming pool water, Journal of Environmental Sciences, 20 (**2008**) 3, 372–378

[11] P. Leskovar, Tehnologija gradiv, Technology Materials, Univerza v Ljubljani, Ljubljana 1970

[12] P. Leskovar, Gradiva, Del 2, Preizkušanje kovin, litje, važnejša nekovinska gradiva, korozija in površinska zaščita, Testing of metal, casting, more important non-metallic materials, corrosion and surface protection, Univerza v Ljubljani, Ljubljana 1986

[13] Rostfrei in Schwimmbädern, Merkblatt 831, Edelstahl 2000

[14] Pravilnik o tehničnih ukrepih in zahtevah za varno obratovanje kopališč in za varstvo pred utopitvami na kopališčih, Offical journal of RS No. 88/2003, 56/2006, 84/2007

[15] Standards SIST EN 1069-1, SIST EN 1069-2 and SIST EN 13451

MATERIALI IN TEHNOLOGIJE

MATERIALS AND TECHNOLOGY

Letnik / Volume 45 2011

ISSN 1580-2949

IMT Ljubljana, Lepi pot 11, 1000 Ljubljana, Slovenija

MATERIALI IN TEHNOLOGIJE / MATERIALS AND TECHNOLOGY

VSEBINA / CONTENTS
LETNIK / VOLUME 45, 2011/1, 2, 3, 4, 5, 6

MATERIALI IN TEHNOLOGIJE / MATERIALS AND TECHNOLOGY

AVTORSKO KAZALO / AUTHOR INDEX

LETNIK / VOLUME 45, 2011, 1–6, A–Ž

MATERIALI IN TEHNOLOGIJE / MATERIALS AND TECHNOLOGY

VSEBINSKO KAZALO / SUBJECT INDEX

LETNIK / VOLUME 45, 2011, 1–6

Kovinski materiali – Metallic materials

Anorganski materiali – Inorganic materials

Polimeri – Polymers

Vakuumska tehnika – Vacuum technique